Universidade de São Paulo
Instituto de Física

A opacidade do meio extragaláctico à radiação gama

Douglas Roberto de Matos Pimentel

Orientador: Prof. Dr. Edivaldo Moura Santos

Tese de doutorado apresentada ao Instituto de Física da Universidade de São Paulo, como requisito parcial para a obtenção do título de Doutor(a) em Ciências.

Banca Examinadora:
Prof. Dr. Edivaldo Moura Santos - Orientador - (IFUSP)
Prof. Dr. Luiz Vitor de Souza Filho - (IFSC/USP)
Prof. Dr. Laerte Sodré Junior - (IAG/USP)
Prof. Dr. Ulisses Barres de Almeida - (CBPF)
Prof. Dr. Rodrigo Nemmen da Silva - (IAG/USP)

São Paulo
2019

FICHA CATALOGRÁFICA
Preparada pelo Serviço de Biblioteca e Informação
do Instituto de Física da Universidade de São Paulo

Pimentel, Douglas Roberto de Matos

A opacidade do meio extragaláctico à radiação gama. São Paulo, 2019.

Tese (Doutorado) – Universidade de São Paulo. Instituto de Física. Depto. de Física Experimental

Orientador: Prof. Dr. Edivaldo Moura Santos
Área de Concentração: Física

Unitermos: 1. Radiação gama; 2. Núcleos ativos galácticos; 3. Astrofísica.

USP/IF/SBI-090/2019

University of São Paulo
Physics Institute

The opacity of the extragalactic medium to gamma radiation

Douglas Roberto de Matos Pimentel

Supervisor: Prof. Dr. Edivaldo Moura Santos

Thesis submitted to the Physics Institute of the University of São Paulo in partial fulfillment of the requirements for the degree of Doctor of Science.

Examining Committee:
Prof. Dr. Edivaldo Moura Santos - Supervisor - (IFUSP)
Prof. Dr. Luiz Vitor de Souza Filho - (IFSC/USP)
Prof. Dr. Laerte Sodré Junior - (IAG/USP)
Prof. Dr. Ulisses Barres de Almeida - (CBPF)
Prof. Dr. Rodrigo Nemmen da Silva - (IAG/USP)

São Paulo
2019

Dedico esse trabalho à minha
companheira Jessica e à minha filha Sophia.

Agradecimentos

Esse trabalho é o resultado de diversas interações durante esses anos de doutorado, portanto, gostaria de fazer aqui alguns agradecimentos.

Primeiramente ao meu orientador, Professor Edivaldo, pelas intensas discussões sobre física e por me dar a oportunidade da realização do trabalho aqui desenvolvido.

Aos meus pais, Nilda e Geraldo, que sempre me apoiaram e me guiaram nas minhas escolhas. Aos meus irmãos, Breno e Raissa, que sempre foram fundamentais na minha vida, inclusive durante esses anos de trabalho intenso.

À minha companheira de todas as horas, Jessica, que além de ser parte fundamental dessa minha caminhada, trouxe à vida o melhor presente que eu poderia imaginar, nossa filha Sophia.

Aos professores e amigos que fiz na USP, em especial ao Hendrik, Johnnier, Níkolas, Washington, Denis e à professora Ivone, com os quais pude discutir e aprender muita física nesse período.

Aos irmãos que fiz morando em São Paulo, na república Castelo, em especial ao Idelvan (Chewba), Julio (Fita), Gabriel (Minhoca), Lucas (Bituca), Fernando (Honda), Danilo (KLB) e Timóteo.

Aos grandes amigos que sempre estiveram presentes de alguma forma: Paulo, Diego (Pakita), Wilson, Douglas (Grilo), Pedro (Caconde), Jesus e Jeferson.

A todos do Colégio Vital Brazil, em especial, aos grandes professores e amigos Marcelo Barão e Carol Macedo.

À FAPESP (Fundação de Amparo à Pesquisa do Estado de São Paulo) pelo Projeto Temático processo número 2015/15897-1.

O presente trabalho foi realizado com apoio da Coordenação de Aperfeiçoamento de Pessoal de Nível Superior - Brasil (CAPES) - Código de Financiamento 001.

Pesquisa desenvolvida com o auxílio do CENAPAD-SP (Centro Nacional de Processamento de Alto Desempenho em São Paulo), projeto UNICAMP / FINEP - MCT.

Pesquisa desenvolvida com o auxílio dos recursos de HPC disponibilizados pela Superintendência de Tecnologia da Informação da Universidade de São Paulo.

Abstract

In this thesis a detailed study of the interaction between gamma-rays coming from active galactic nuclei (AGN) and the radiation field generated by the thermal emission from all the galaxies, the extragalactic background light (EBL), is performed. The development of the imaging air Cherenkov telescope (IACT) technique has been providing well determined spectral energy distributions (SED) of extragalactic sources and, in turn, allowing investigations of the attenuation processes of very high energy (VHE) radiation by the EBL. In 1997, a flare state of the blazar Markarian 501 (Mkn 501) provided flux measurements at energies up to ~ 20 TeV. We show that this spectrum is the one with the highest expected attenuation by the EBL dust component among the current known TeV emitters. Starting from an EBL model based on stellar and dust blackbody contributions, we were able to investigate the role of each EBL component in the attenuation of Mkn 501 SED. In such EBL model, dust is divided into three different grain types (polycyclic aromatic hydrocabons (PAH), small (SG) and large grains (LG)) and the importance of each one of these components to the opacity of the extragalactic medium for the Mkn 501 SED could be better understood. In particular, PAH molecules have a fundamental importance in the description of Mkn 501 spectrum, because its slope observed around 10 TeV can only be correctly described by this dust component. On the other hand, an effective model containing only PAH as dust can be excluded with a significance of at least 5σ, independently of the intrinsic spectrum assumed. Finally, a forecasting study is performed for the third generation of IACT, the Cherenkov Telescope Array (CTA). Through a maximum likelihood estimator we show that, already for a single source analysis, the PAH relative contribution can be determined with a good resolution for 50 hours of observation. The combination of several observations shows that 30 minutes of exposure time is enough to determine the PAH fraction with a reasonable resolution. The impact of the redshift uncertainties is also analyzed considering an a priori probability for this observable when determining the PAH fraction.

Keywords: Extragalactic background light; gamma radiation; active galactic nuclei.

Resumo

Nesta tese um estudo detalhado da interação entre raios gamas vindos de núcleos galácticos ativos (AGN) e o campo de radiação produzido pela emissão térmica das galáxias, a luz extragaláctica de fundo (EBL), é realizado. O desenvolvimento de técnicas de imageamento por telescópios de efeito Cherenkov na atmosfera (IACT) tem fornecido bem determinadas distribuições espectrais de energia (SED) de fontes extragalácticas e, por sua vez, permitido investigações do processo de atenuação de radiação de altíssima energia (VHE) por meio da EBL. Em 1997, um estado de *flare* do blazar Markarian 501 (Mkn 501) forneceu medidas de fluxos em energias até ~ 20 TeV. Nós mostramos que esse é o espectro com maior atenuação esperada por poeira dentre as fontes atualmente conhecidas que emitem em TeV. Partindo de um modelo de EBL baseado em contribuições de estrela e poeira que emitem como um corpo negro, nós investigamos o papel de cada componente da EBL na atenuação do SED da Mkn 501. Em tal modelo de EBL, a poeira é dividida em três diferentes tipos de grãos (hidrocabonetos aromáticos policíclicos (PAH), pequenos (SG) e grandes grãos (LG)) e a importância de cada uma dessas componentes para a opacidade do meio extragaláctico para o SED da Mkn 501 pôde ser melhor compreendida. Em particular, as moléculas de PAH têm uma importância fundamental na descrição do espectro da Mkn 501, pois sua inclinação observada em torno de 10 TeV somente pode ser corretamente descrita por essa componente da poeira. Por outro lado, um modelo efetivo contendo apenas PAH como poeira pode ser excluído com uma significância de pelo menos 5σ, independentemente do espectro intrínseco assumido. Finalmente, foi realizado um estudo de previsão para a terceira geração de IACT, o *Cherenkov Telescope Array* (CTA). Através de um estimador de máxima verossimilhança nós mostramos que, já para análises de uma única fonte, a contribuição relativa de PAH pode ser determinada com uma boa resolução para 50 horas de observação. A combinação de diversas observações mostra que 30 minutos de tempo de exposição é suficiente para determinar a fração das PAH com uma resolução razoável. O impacto das incertezas no redshift também é analisado considerando uma probabilidade a priori para esse observável na determinação da fração das PAH.

Palavras-chaves: Luz extragaláctica de fundo; radiação gama; núcleos galácticos ativos.

Contents

List of Figures

List of Tables

Acronyms

1FHL First Catalog of Hard Fermi-LAT Sources. 69

2FHL Second Catalog of Hard Fermi-LAT Sources. 68

3LAC Third catalog of active galactic nuclei detected by Fermi-LAT. 69

AEGIS All-wavelength Extended Groth Strip International Survey. 46

AGN Active Galaxy Nuclei. 51

CGRH Cosmic Gamma-Ray Horizon. 64

CMB Comisc Microwave Background. 30

COBE Cosmic Background Explorer. 32

CTA Cherenkov Telescope Array. 59

DIRBE Diffuse Infrared Background Experiment. 32

EBL Extragalactic Background Light. 30

EGRET Energetic Gamma Ray Experiment Telescope. 57

FRW Friedmann-Robertson-Walker metric. 31

FSRQ Flat Spectrum Radio Quasar. 54

GLF Gamma-ray Luminosity Function. 57

GRB Gamma-Ray Burst. 51

H-R Hertzsprung-Russell. 37

HEGRA High-Energy-Gamma-Ray Astronomy. 71

IACT Imaging Atmospheric (or Air) Cherenkov Telescope (or Technique). 51

IMF Initial Mass Function. 36

IR Infrared. 34

IRAS Infrared Astronomical Satellite. 32

IRF Instrument Response Function. 95

ISM Interstellar Medium. 36

LAT Large Area Telescope. 57

LF Luminosity Function. 33

MS Main Sequence. 37

NIRS Near Infrared Espectrometer. 32

OVV Optically Violently Variable. 52

PAH Polycyclic Aromatic Hydrocarbons. 38

PLE Pure Luminosity Evolution. 57

QED Quantum Electrodynamic. 59

QSO Quasi-Stellar Object. 52

ROI Region of Interest. 99

SED Spectral Energy Distribution. 46

SFR Star formation rate. 36

SSC Synchrotron Self-Compton. 54

SSP Simple Stellar Population. 38

SWIRE Spitzer Wide-Area Infrared Extragalactic Survey. 46

TS Test Statistic. 100

UV Ultraviolet. 34

XLF X-ray Luminosity Function. 57

Chapter 1

Introduction

Since the beginning of the universe up to now, many physical processes have released energy in radiation form and filled the universe with photon fields. In particular, low energy radiation fields, such as the Cosmic Microwave Background (CMB) and the Extragalactic Background Light, are of extreme importance in gamma-ray astronomy due to the quantum nature of the interaction between matter and radiation. In the standard cosmological model the CMB is treated as a relic of the Big Bang being created with a blackbody spectrum, resulting from the decoupling between matter and radiation after the cosmic plasma expanded adiabatically and its temperature dropped sufficiently so that photons could free stream [1]. It was first observed in 1964 by Wilson and Penzias through radio-telescopes, a discovery for which they received the Nobel Prize in Physics in 1978 [2]. Currently, its average temperature is 2.725 K with anisotropy levels of the order of 1/100000 and precise measurements of this radiation field led to an unprecedented understanding of the primordial universe. With more complicated spectral features, the EBL also presents fundamental information on the cosmological evolution of the universe. Its two main contributions are the direct stellar emission (expected to dominate at UV/visible wavelengths in comoving coordinates) and re-emission from cosmic dust, heated by part of the stellar emission, reaching maximal spectral intensity at IR wavelengths. It is believed that the production of this radiation began right after the end of the dark ages [1] and continues until today. In terms of total energy emission, the EBL is the second most intense background radiation, about 5% of the CMB, therefore it is a fundamental piece of information to the complete understanding of the universe's energy budget.

Low energy radiation fields are responsible for the level of opacity of the extragalactic medium to the very high energy photons. At TeV energies, e^-/e^+ pair production is expected to reduce the mean free path of gamma-rays emitted from extragalactic sources

[1] Epoch of the cosmological history during which there were no sources of radiation. It ocurred between the decoupling of matter and radiation and the emergence of the first gravitationally bound and nuclear fusion powered objects.

down to a few hundreds of Mpc [3, 4], and even though the current levels of EBL are uncertain, non-negligible attenuation effects have being observed. However, it is very hard to get direct measurements of the EBL due to the intense foregrounds coming from the zodiacal light and galactic emission. The direct measurements obtained have, in general, large uncertainties and are commonly treated as upper limits to the EBL energy density. Constraints on the EBL density are also obtained through resolved galaxy counts, imposing a lower limit to the EBL levels.

Very high energy processes in the astrophysical context are studied since 1912 when Hess [5] detected, for the first time, extremely energetic particles coming from outside the Earth's atmosphere. In this case, Hess detected charged particles bombarding the Earth, called cosmic-rays. Decades later, in 1989, Weekes [6] detected for the first time gamma-rays with energies at $\sim$ GeV - TeV coming from the Crab Nebula using the IACT technique. Gamma-ray detection is a hard experimental task due to many factors, for instance, the relatively low flux and the atmospheric opacity. Three techniques are used currently in gamma-ray observations: ground observatories (air shower arrays and Cherenkov telescopes) and detectors on-board satellites. Our atmosphere is opaque to these photons and for energies above ~ 10 MeV the main interaction between gamma-rays and atmospheric particles is the e^-/e^+ pair creation [7]. In order to get direct measurements, the atmosphere must be avoided, therefore detectors on-board satellites arise as an alternative method. With EGRET (Energetic Gamma Ray Experiment Telescope) on-board the Compton Gamma-Ray Observatory satellite [8] it was possible to measure photons with energy above 10 GeV. The state of the art for satellite-based measurements is the Fermi-LAT [9], it has a good energy resolution between 100 MeV up to 100 GeV, however, for photon energies above 100 GeV the flux is so low that its collection area becomes negligible. Air shower arrays reconstruct gamma-ray events based on the detection of extensive air showers produced by the interaction of primary particles with atoms at the top of the atmosphere. HAWC [10] and Tibet [11] observatories use this technique with water tanks located at high-altitude sites. The IACT telescopes are another way to detect gamma-rays with observatories on the ground. From the Cherenkov light emitted by showers produced from primary gamma-rays, telescopes can reconstruct primary photons with energies of $\gtrsim$ TeV.

Nowadays, the second generation of IACTs is in operation, being represented by three telescopes: H.E.S.S [12] located in Namibia, VERITAS [13] in the United States of America, and MAGIC [14] in Spain. However, a great effort of the astronomical community gave rise to a global consortium with the objective of building the third IACT generation, the CTA [15]. With two telescope arrays, one in the southern hemisphere at Paranal, Chile and another in the northern hemisphere at La Palma, Spain, an improvement by one order of magnitude in flux sensitivity is expected, fine angular and energy resolutions and an energy coverage of four decades ($\sim$ 0.01 to 100.0 TeV), allowing precise spectrum

measurements and the discovery of a whole new population of TeV sources. Extreme blazars, like Mkn 501, are one kind of these sources. Such AGNs can exhibit fluxes up to several TeV energies and must be seen as very faint objects from Earth. In addition, with a privileged view of the galactic center by the southern observatory it will be possible to investigate the high energy processes happening at the core of the Milk Way.

Extragalactic TeV sources have their measured spectra attenuated due to the opacity caused by the presence of the EBL during the propagation of gamma-rays. Here, we present a careful study of this process based on a combination of spectra of AGNs, mainly blazars, provided by IACTs and data-driven modeling of the EBL spectrum. Several works have investigated the EBL through the opacity to the gamma radiation, such as [16], [17] and [18]. Differently from these studies, here we have investigated each of the dominant contributions (stars and different dust grains) to the total EBL energy density separately. We show that the VHE photons from the currently detected population of AGNs interact mainly with the EBL stellar component that peaks around UV/optical wavelengths. Some well determined SEDs, however, like that of the flare state of the blazar Mkn 501, extending well above 1 TeV, allow us to investigate the attenuation by IR wavelength radiation, a region of the EBL spectrum dominated by the emission from cosmic dust. Furthermore, due to the large energy range expected to be covered by the CTA along with its high flux sensitivity in energies $\gtrsim 1$ TeV, especially in the CTA South array, this dust component will become essential for a correct description of the newly detected SEDs, opening up a window for investigating the contribution of dust to the EBL energy density. Such broad energy range covered by the CTA will also allow to access the attenuated and unattenuated parts of the SEDs, increasing the capability of EBL studies through CTA observations. Based on a maximum likelihood estimator, we show that CTA observations have a large potential in determining the relative contribution of dust grains with a good accuracy.

This thesis is organized as follows: in Chapter 2 a detailed description of the EBL is presented through the current constraints and some of the most commonly used models found in the literature. Such a detailed description was chosen in order to show the reader the main ingredients we had to consider when implementing from scratch some of these models in our simulation/analysis chain. A review of the main characteristics of extragalactic gamma-ray sources and the description of the attenuation process due to the interaction between EBL and gamma-rays are found in Chapter 3. At very high energies, around tens of TeV, the dust component of the EBL becomes important in the attenuation process and a careful study of the role of each dust grain type in this process, based on a well determined SED of a blazar (Mkn 501), is performed in the Chapter 4. Since the new generation of IACTs, represented by CTA, will observe photons up to $\sim$ 100 TeV, such an observatory has a clear potential for analyses of EBL attenuation, thus a forecast study is presented in Chapter 5. Finally, the main conclusions of this thesis are

presented in Chapter 6.

Chapter 2

The extragalactic background light

In this chapter we will present the theoretical development of the EBL and an explanation on the methods used to impose constraints in its intensity. Many models describing the EBL can be found in the literature, each one based on differents approaches. The motivation and construction of three of these EBL models are shown in detail here.

Since the formation of the first stars one assumes that the universe is transparent to all photons with energies below the hydrogen ionization energy (13.6 eV) and, as argued by Peebles [19], the radiation emitted by all galaxies should obey the following Boltzmann equation

$$\frac{dI(t,\lambda)}{dt} = -3\frac{\dot{a}}{a}I(t,\lambda) + c\,s(t,\lambda), \tag{2.1}$$

where $I(t,\lambda)$ is the brightness of all galaxies in units of $\mathrm{W\,m^{-2}\,Hz^{-1}\,sr^{-1}}$, a is the cosmological scale factor, c is the speed of light in vacuum and $s(t,\lambda)$ is the radiation source term. It is conveniently defined as $s(t,\lambda) = j(t,\lambda)/4\pi$, where $j(t,\lambda)$ is the luminosity density (i.e. emissivity) from the galaxies in units of $\mathrm{L_\odot Mpc^{-3}Hz^{-1}}$.[1]

Equation (2.1) shows that the evolution of the radiation field created by all galaxies depends on two contributions. The first term on the right hand side of equation 2.1 shows the dependence with the metric of the universe. The cosmological scale factor a gives the evolution of space, which several observational evidences have shown to be expanding in a accelerated way [1]. Therefore, this first term represents the dilution of the photon density. On the other hand the second term describes the rate at which radiation is injected by sources. An instructive example of application of the Boltzmann equation for the CMB case is presented in details in Appendix A. By solving (2.1) we obtain

$$I(t,\lambda) = \frac{c}{4\pi}\int_0^t dt' \left(\frac{a(t')}{a(t)}\right)^3 j(t',\lambda'). \tag{2.2}$$

So, we are able to get the solution to $I(t,\lambda)$ in terms of the comoving luminosity density

[1] $\mathrm{L_\odot} = 3.828 \times 10^{26}$ W.

$j_c(t,\lambda) = a^3(t) j(t,\lambda)$ as

$$I(t,\lambda) = \frac{c}{4\pi}\frac{1}{a(t)^3}\int_0^t dt' j_c(t',\lambda'). \tag{2.3}$$

Here it is convenient to change the variable from t to the redshift z using the relation

$$a(t) = \frac{1}{1+z} \tag{2.4}$$

where at the Big Bang we have $a(0) = 0$. This leads to

$$I(z,\lambda) = (1+z)^3\frac{c}{4\pi}\int_z^\infty j_c(z',\lambda')\left|\frac{dt'}{dz'}\right| dz'. \tag{2.5}$$

Assuming the Friedmann-Robertson-Walker metric (FRW), which describes a homogeneous and isotropic universe, dz/dt is given by

$$\frac{dt}{dz} = \frac{1}{(1+z)H_0\sqrt{(1+z)^4\Omega_r + (1+z)^3\Omega_m + (1+z)^2\Omega_k + \Omega_\Lambda}}, \tag{2.6}$$

which is a term dependent on the assumed cosmology. The cosmology is established by defining the energy density parameters Ω_m, Ω_r, Ω_k and Ω_Λ, corresponding to non-relativistic matter, radiation, curvature and dark energy, respectively. We will assume here a dark energy component in the form of a cosmological constant Λ. The density parameters must obey $\Omega_r + \Omega_m + \Omega_k + \Omega_\Lambda = 1$ [1] and are defined by

$$\Omega_i = \frac{\rho_i}{\rho_{cr}} \tag{2.7}$$

where $\rho_{cr} = 3H_0^2/8\pi G$ is the critical density of the universe. For the standard cosmological model and redshift interval of interest for EBL studies we take $\Omega_k = 0$, $\Omega_r \approx 0$, $\Omega_\Lambda = 0.7$, $\Omega_m = 0.3$ and the Hubble constant $H_0 = 70$ km s^{-1}Mpc^{-1} [1].

Therefore, with the cosmology set, once the galaxies emissivity is modeled, the EBL intensity can be finally calculated. However, this is not a simple task and there are more than one way to do it, either through semi-analytical models or data driven approaches. According to Domínguez et al. [20] these two paths give rise to four types of models:

(i) The Forward Evolution, which imposes initial cosmological conditions and then evolves them in time by semi-analytical models of galaxy formation [21–23];

(ii) The Backward Evolution, using as starting point current galaxy populations and extrapolating back in time [24–26];

(iii) The evolution of galaxy populations over a redshift range. The galactic evolution is described by some observational quantity like the star formation rate [27–29];

(iv) The evolution of galaxies contributing significantly to the EBL and directly observed in a certain redshift range [20, 30].

2.1 Limits on the EBL

Despite the difficulty due to the intense foregrounds, in the last decades some instruments carried out direct measurements of the EBL, such as the Infrared Astronomical Satellite (IRAS) [31], the Cosmic Background Explorer - Diffuse Infrared Background Experiment (COBE-DIRBE) [32] and the Near Infrared Spectrometer (NIRS) [33]. Dwek and Krennrich [34] used direct measurements to impose an upper limit on the EBL and measurements from resolved galaxy counts to define a lower limit. Figure 2.1 shows a plot with updated EBL data extracted from [35].

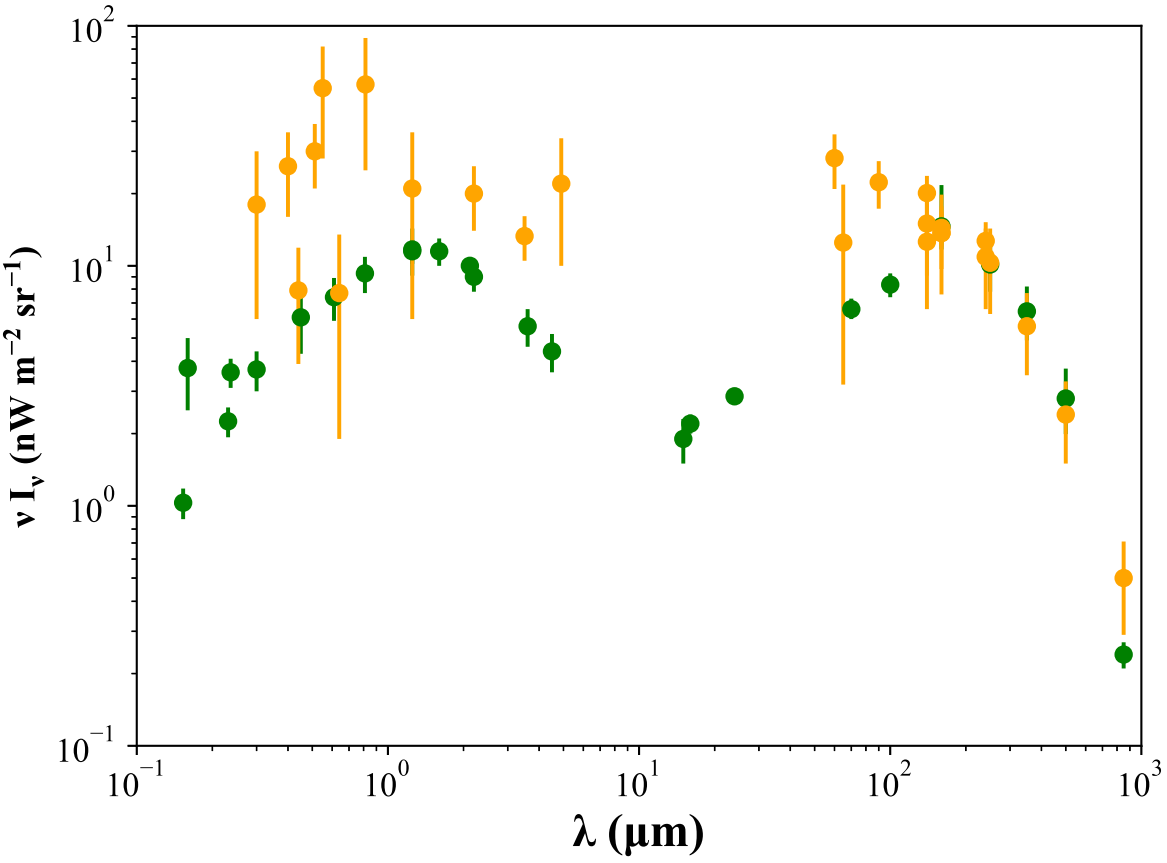

Figure 2.1: *Limits obtained to the EBL spectral intensity by direct measurements (yellow data) and resolved galaxy counts (green data) [35].*

Direct measurements present many challenges. Technically an absolute calibration of the instrument is necessary, so the sky brightness can be measured against a well established reference. Moreover, the careful subtraction of foregrounds such as dust particle emission and other galactic components is required, as well as corrections of atmospheric

effects. Radiation from local bright sources, like the Sun, the Moon and the Earth must be also eliminated from these observations [36].

The identification of astrophysical components is another fundamental piece for EBL direct measurements. In order to ensure that just extragalactic sources are being taken into account, foregrounds such as stellar and interstellar emission from our own galaxy and the zodiacal light, which is the radiation emitted from interplanetary dust particles, must be also removed. At long wavelengths, greater than ~ 400 μm, the CMB becomes dominant and must be subtracted from the observed flux [36].

A strict lower limit on the EBL intensity can be obtained considering the emission from all the resolved galaxies. This technique provides us a lower limit since faint unresolved galaxies are not detected and possible diffuse sources can be missed out [36].

As we can see in figure 2.1, the direct measurements (yellow points) and the resolved galaxy counts (green points) define a region on the spectrum where the EBL intensity should be found. The wavelength region around 10 μm is a difficult one from the observational point of view. As we will see, this region is dominated by emission from complex interstellar dust components and will be subject of analysis in future chapters.

2.2 Helgason and Kashlinsky's model

Helgason and Kashlinsky's model [30] is of type (iv) and uses measurements of luminosity function (LF) to reconstruct the comoving emissivity $j_c(z, \lambda)$. The luminosity function $\Phi(L_\nu, z)$ is the number of galaxies per comoving volume with luminosity between L_ν and $L_\nu + dL_\nu$. One can write

$$j_c(z, \lambda) = \int L_\nu \Phi(L_\nu, z) dL_\nu, \tag{2.8}$$

where L_ν is given in units of erg s^{-1} Hz^{-1}.

In 1976, Paul Schechter published a seminal paper where he presented an analytical expression to LF [37]. Based on data of galaxies and clusters he found a functional form that fits very well the observational data, except for extreme cases of low and high luminosities. The function found is written as

$$\Phi(L_\nu) = \left(\frac{\Phi^*}{L^*}\right)\left(\frac{L_\nu}{L^*}\right)^\alpha \exp\left(-L_\nu/L^*\right) \tag{2.9}$$

where Φ^* is a normalization, L^* is the characteristic luminosity and α is the faint-end slope, called the Schechter parameters. Inserting equation 2.9 in 2.8 one obtains

$$j_c = \Phi^* L^* \Gamma(\alpha + 2), \tag{2.10}$$

where $\Gamma(x)$ is the gamma function.

Using a library with 342 measurements of LF ranging from ultraviolet UV to infrared IR (0.15 - 25 μm) at several redshift bins, Helgason and Kashlinsky obtained 18 bins of rest-frame [2] wavelengths and were able to find the best-fit to the luminosity density using a 3-parameter function

$$\nu j_c(z) = a_\nu (1 + (z - z_0))^{b_\nu} \exp\left(-c_\nu (z - z_0)\right), \tag{2.11}$$

where $z_0 = 0.8$. Figures 2.2 and 2.3 show the best-fits found and their corresponding parameters. The motivation for using equation 2.11 to describe the emissivity comes from the good results obtained in [38] in describing the galaxy number counts at wavelengths ranging from 0.45 μm up to 4.5 μm. As noted by the authors in [30], this functional form is equivalent to Schechter expression obtained in equation 2.10 considering $L^* \propto (1 + (z - z_0))^{b_\lambda}$, $\Phi^* \propto \exp(-c_\lambda (z - z_0))$ and a redshift-independent α.

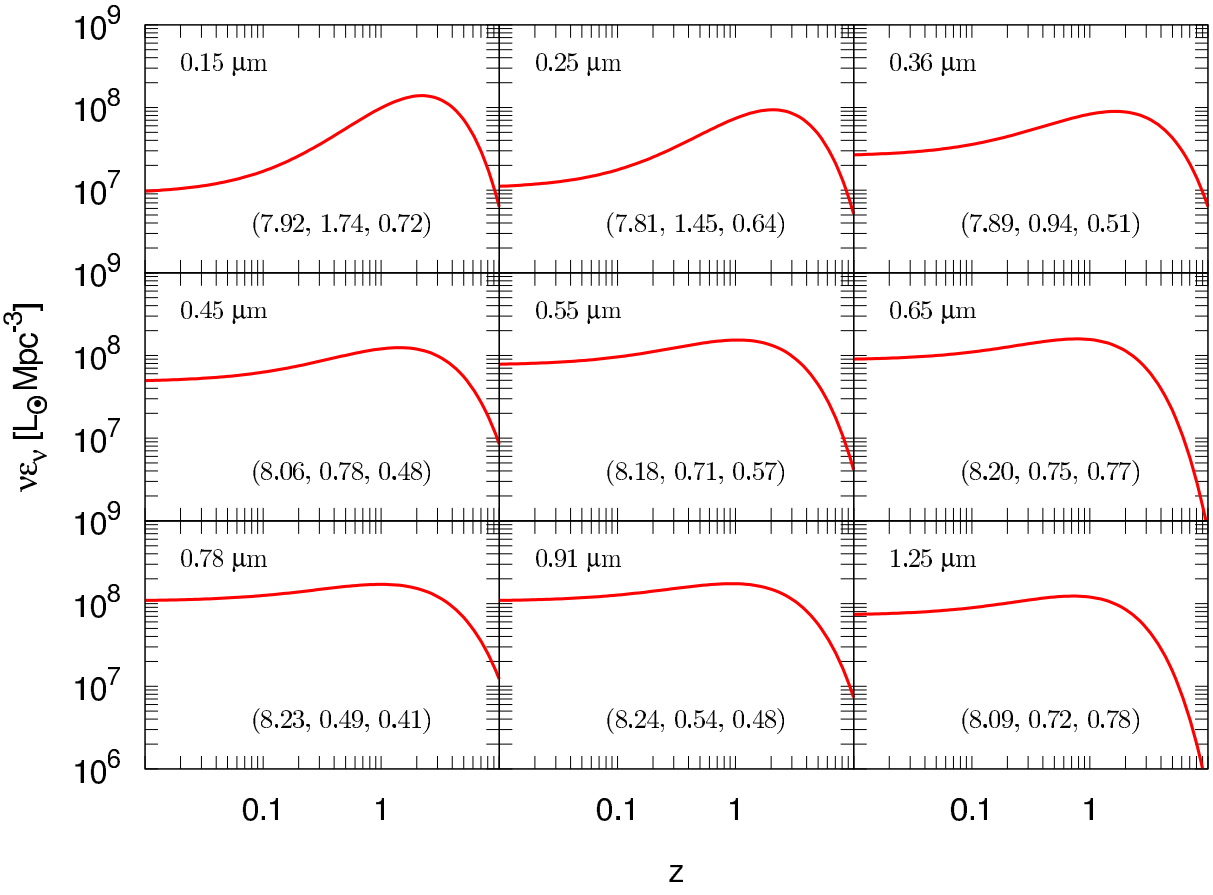

Figure 2.2: *Luminosity density (0.15 - 1.25 μm) found by Helgason's model [30]. Each plot shows the three parameters to the fits* $(\log a_\nu, b_\nu, c_\nu)$.

The parameters can then be interpolated in all wavelength range between 0.15 μm and 25 μm to get the luminosity density. However, it is important to notice that the emission drops to zero above a certain energy, due to the photon absorption by neutral

[2] The rest-frame is the reference frame of an observer located at the redshift of the source.

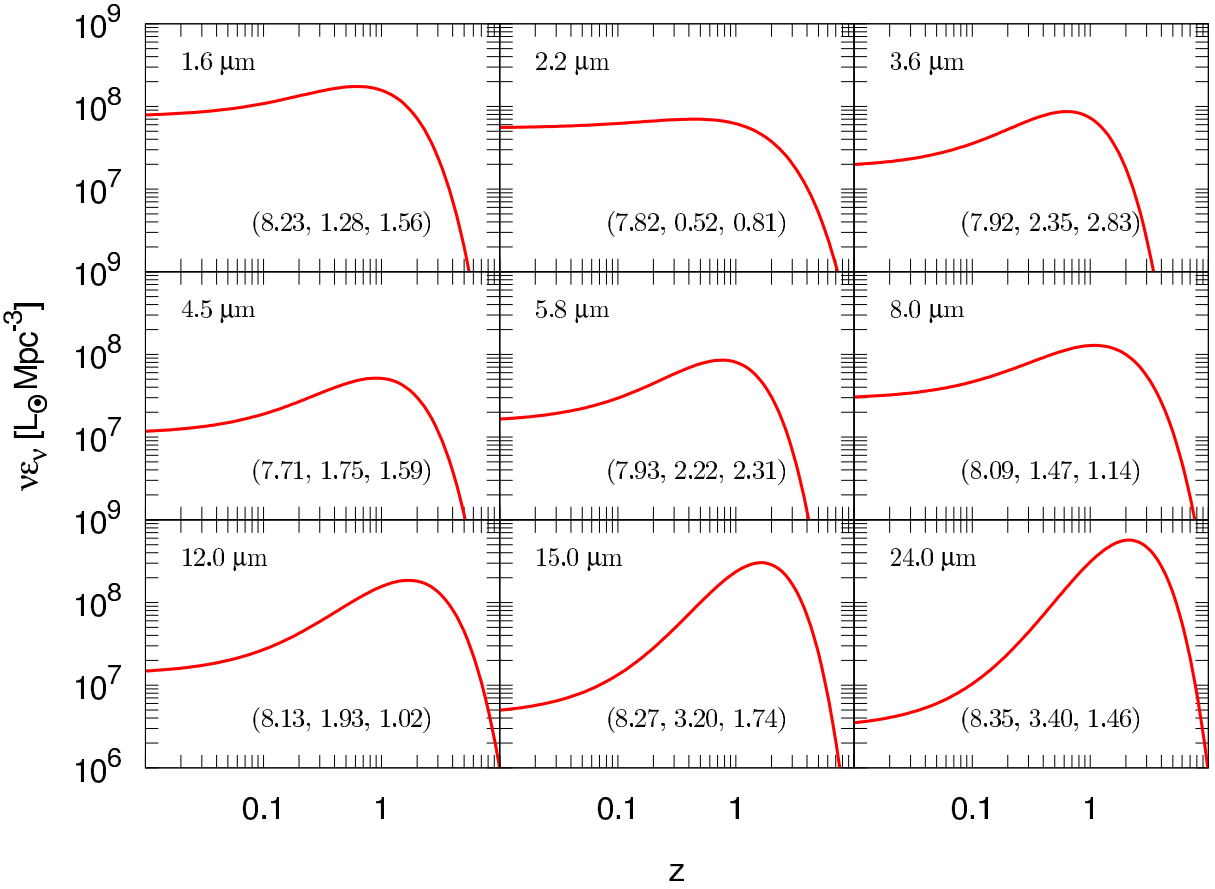

Figure 2.3: *Luminosity density (1.6 - 24 μm) found by Helgason's model [30]. Each plot shows the three parameters to the fits* $(\log a_\nu, b_\nu, c_\nu)$.

hydrogen in the source environment. Helgason and Kashlinsky [30] used two cutoffs to model this: the first absorption line of the Lyman series, at 13.6 eV (0.0912 μm), and the second absorption line, at 10.2 eV (0.1216 μm), each one representing different absorption efficiencies by intergalactic hydrogen. A linear extrapolation is used between 0.15 μm and the adopted cutoff.

We were able to calculate numerically the EBL intensity through equation 2.5. Figure 2.4 shows the EBL intensity measured by observers at different redshifts (in units of MJy s^{-1}) [3]. At some regions of the spectrum ($\lambda < 0.4\,\mu$m and $\lambda > 10\,\mu$m) one can see the EBL brightness at large redshifts overcoming the present value, showing a different rate of EBL production for different wavelengths. Figure 2.5 displays the spectrum of the EBL expected to be measured today, at $z = 0$. There are two curves in this figure, one for each cutoff discussed, where one can see the impact of the different choices of E_{cut} at small wavelengths. Superimposed to the expected EBL spectrum are the constraints imposed by resolved galaxy counts (lower limits) and direct measurements (upper limits) presented in section 2.1.

As argued by the authors in [30] this EBL construction presents a good agreement

[3] 1 Jy $= 10^{-26}$ W m^{-2} Hz^{-1}

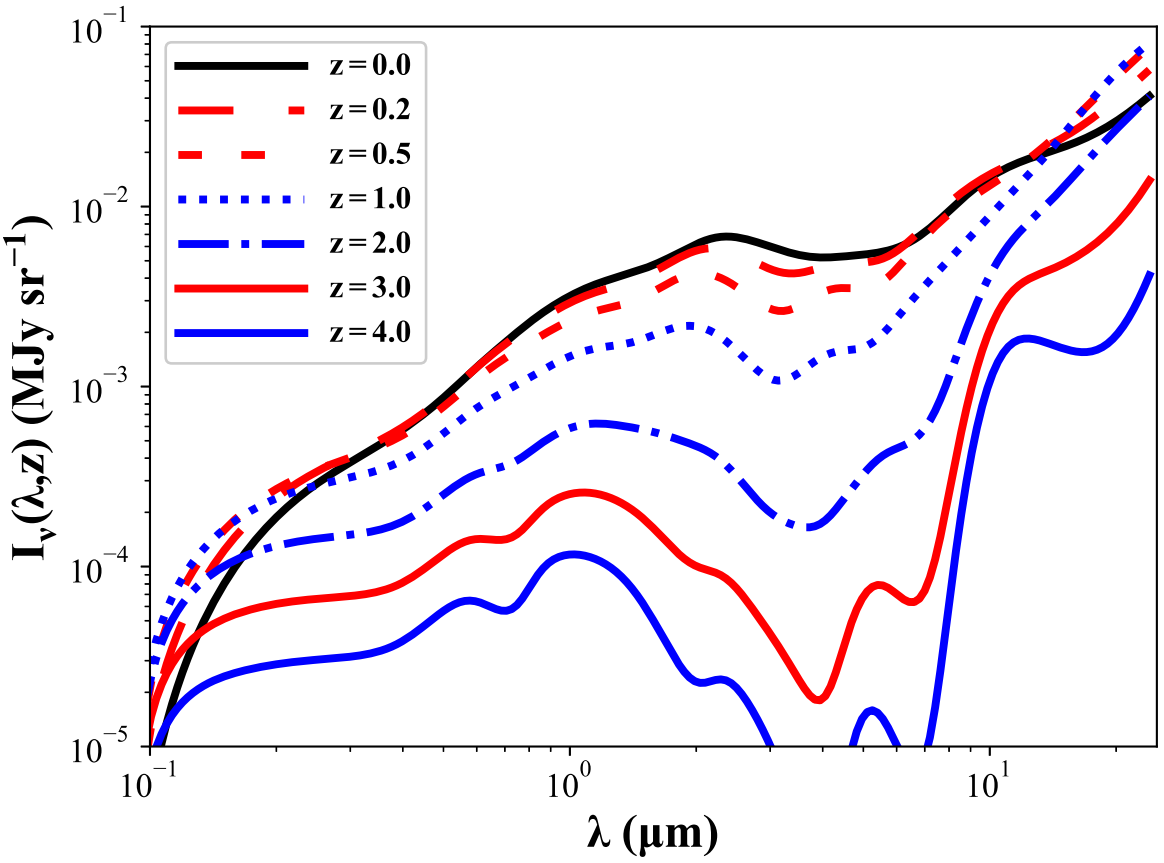

Figure 2.4: *Evolution of EBL spectrum according to Helgason and Kashlinsky's model with a cutoff at 13.6 eV. Each curve represent the EBL spectrum to a observer located at different redshifts, which is shown in the inset of the figure.*

up to ~ 6 μm, mainly with respect to the measurements from resolved galaxy counts, but above this wavelength the EBL becomes about 2 to 3 times more intense than the measurements. In fact, this spectral region deserves a special attention, since it marks the transition between the stellar and dust contributions. Moreover, one should keep in mind that the model does not cover the entire wavelength range relevant for attenuation studies of TeV photon sources. Due to the fact that it deals essentially with the stellar emission region, it will not predict the correct level of opacity of the extragalactic medium for sufficiently distant sources (the relation between EBL and opacity is discussed in detail in Chapter 3).

2.3 Finke et al. model

Another EBL model currently used is that elaborated by Finke et al. in 2010 (F10) [29]. This model is of type (iii) and describes the EBL evolution based on suitable models of star formation rate (SFR), initial mass function (IMF) and a photon escape function f_{esc}. The stars and cosmic dust in the interstellar medium (ISM) are the main contributions to the

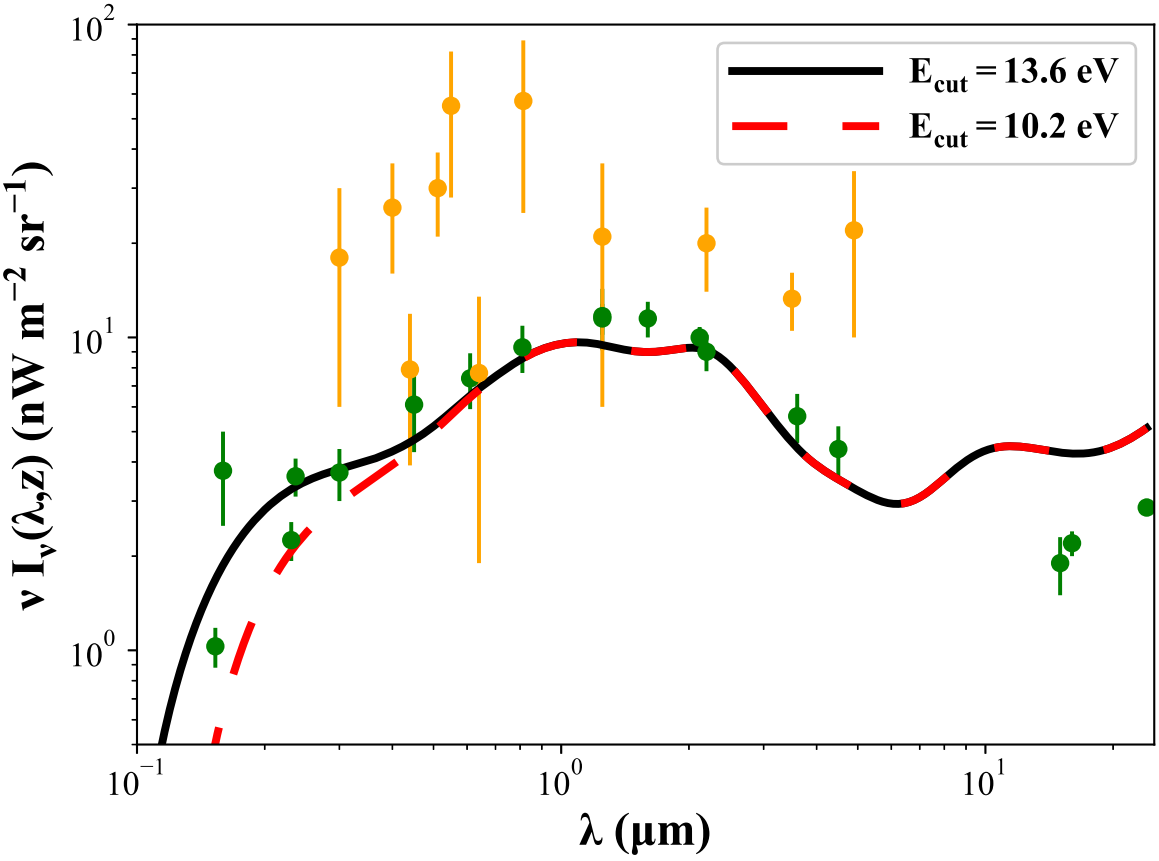

Figure 2.5: *EBL spectrum at $z = 0$ from Helgason and Kashlinsky's model using the two cutoffs discussed its construction. The green and yellow dots are limits coming from data from resolved galaxy counts and direct measurements, respectively.*

EBL spectrum. Each star is considered to emit like a blackbody having similar metallicity to the Sun, its temperature and radius depending on the stellar stage, which is given by its evolution through the Hertzsprung-Russell (H-R) diagram [39,40], as described in [41]. Dust emission occurs due to the heat up by a fraction of photons which cannot escape the environment. Therefore, with a function that describes the photon escape fraction from galaxies (f_{esc}) and the assumption that each astrophysical component (star and dust) emits like a blackbody, which will be presented in details in the next sections, it is possible to calculate separately the star and dust components of the EBL.

2.3.1 Stellar emission

Most of a star's life is spent in the main sequence (MS) and during this stage their spectra can be fairly well described by a blackbody. F10 [29] assumes this behavior for all of them throughout their lives. So, the photon density emitted by such a star in comoving coordinates is

$$n_\star = \frac{8\pi}{\lambda_C^3} \frac{\epsilon^2}{\exp(\epsilon/\Theta) - 1}, \tag{2.12}$$

where one defines the dimensionless energy $\epsilon = h\nu/m_e c^2$, $\lambda_C = h/m_e c$ is the Compton wavelength and $\Theta = k_B T/m_e c^2$ is the effective dimensionless temperature of the star. Therefore, the number of photons emitted per unit of time and energy is

$$\dot{N}_\star(\epsilon; m, t_\star) = \pi\, R(m, t_\star)^2\, c\, n_\star(\epsilon; \Theta(m, t_\star)), \tag{2.13}$$

where $R(m, t_\star)$ is the stellar radius and $t_\star$ is the age of the star. The effective temperature is given by

$$\Theta(m, t_\star) = \frac{k_B T_\odot}{m_e c^2} \left(\frac{L(m, t_\star)}{L_\odot}\right)^{1/4} \sqrt{\frac{R_\odot}{R(m, t_\star)}}, \tag{2.14}$$

where $T_\odot$, $L_\odot$ and $R_\odot$ [4] are, respectively, the temperature, luminosity and radius of the Sun. Following the prescription for the evolution across the H-R diagram from [41], it is possible to determine the effective temperature. Therefore, the luminosity density in comoving coordinates can be calculated by

$$\epsilon j_c^{star}(\epsilon; z) = m_e c^2 \epsilon^2 f_{esc}(\epsilon) \int_{m_{min}}^{m_{max}} dm\, \xi(m) \int_z^{z_{max}} dz_1 \left|\frac{dt_\star}{dz_1}\right| \psi_c(z_1) \dot{N}_\star(\epsilon; m, t_\star(z, z_1)), \tag{2.15}$$

where $f_{esc}(\epsilon)$ is the fraction of photons which escapes the stellar environment without being absorbed by dust and gas, $\psi_c(z)$ is the comoving SFR in units of $\mathrm{M}_\odot\ \mathrm{yr}^{-1}\ \mathrm{Mpc}^{-3}$ and $\xi(m)$ is the normalized IMF.

It is worth mentioning that the validity of the blackbody model to stars was tested in [29] for simple stellar populations (SSP's) for several ages. Comparing the blackbody approximation with SSPs at high spectral resolution calculated by [42], a fairly good agreement can be seen in the wavelength range of interest for EBL, as can be verified in figure 2.6.

2.3.2 Dust emission

As mentioned previously, part of the stellar radiation cannot escape from its host galaxy as it is absorbed by the cosmic dust, heating the grains up and causing them to reemit at longer wavelengths, giving rise to an additional component in the EBL spectrum. According to F10, the dust can be divided into three main components [43]: (1) large grains found in and around star-forming regions which absorb in the visible and reemit in the far infrared, (2) small grains located throughout the disk of spiral galaxies which absorb in the far UV and reemit in the near infrared, and (3) PAH emitting as broad lines.

For each dust component a blackbody spectrum is assumed and the total dust emis-

[4] $T_\odot = 5778$ K and $R_\odot = 6.960 \times 10^8$ m

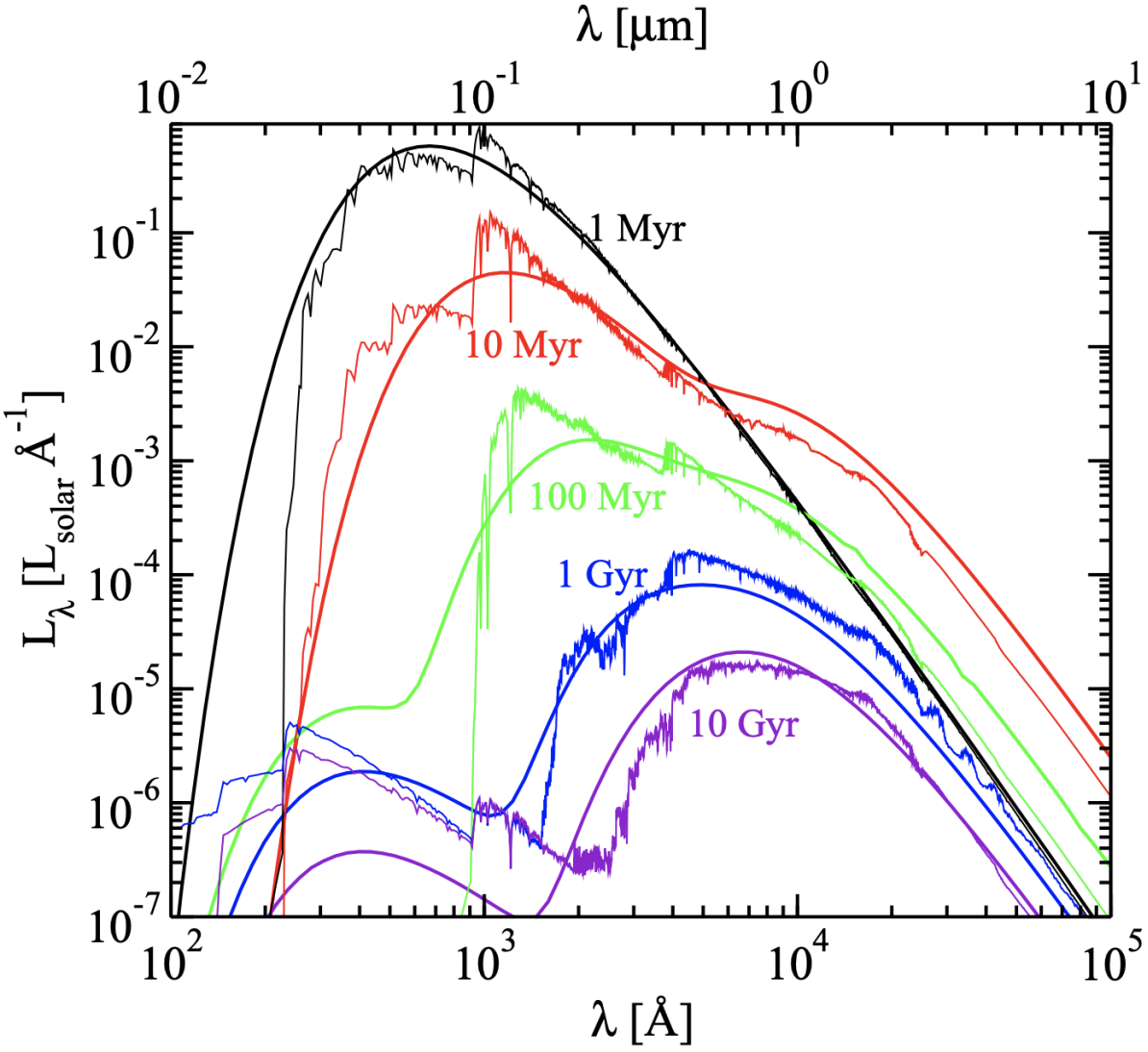

Figure 2.6: *Simple stellar population spectra for several ages. Figure extracted from [29].*

sivity is the combination of these three spectra. So, assuming that all absorbed radiation is reemitted, we write for dust

$$j_n = f_n(j^{total} - j^{star}), \tag{2.16}$$

which yields

$$f_n \int d\epsilon \left[\frac{1}{f_{esc}(\epsilon)} - 1\right] j_c^{star}(\epsilon; z) = \int d\epsilon\, j_n(\epsilon; \Theta_n), \tag{2.17}$$

where f_n is the relative contribution of a particular component, $\Theta_n = k_B T_n / m_e c^2$ is its effective dimensionless temperature and n is an index labeling each component ($n = 1, 2, 3$). It is worth mentioning here that the term $1/f_{esc}(\epsilon)$ does not cause any divergerce in the integral for $f_{esc} \to 0$ since, as we can see in equation 2.15, $j_c^{star}(\epsilon; z)$ is proportional to $f_{esc}(\epsilon)$.

The emissivity for each component is given by

$$j_n(\epsilon;\Theta_n) = j_n^0 \frac{\epsilon^3}{\exp(\epsilon/\Theta_n) - 1}, \tag{2.18}$$

replacing 2.18 in 2.17 it is possible to solve the integral on the right-hand side

$$\int_0^\infty d\epsilon j_n(\epsilon,\Theta_n) = \frac{\pi^4}{15} j_n^0 \Theta_n^4, \tag{2.19}$$

so, j_n^0 can be determined and the comoving luminosity density due to the cosmic dust can be written as

$$\epsilon j_c^{dust}(\epsilon;z) = \frac{15}{\pi^4} \int d\epsilon' \left[\frac{1}{f_{esc}(\epsilon')} - 1\right] j_c^{star}(\epsilon';z) \sum_{n=1}^{3} \frac{f_n}{\Theta_n^4} \frac{\epsilon^4}{\exp(\epsilon/\Theta_n) - 1}. \tag{2.20}$$

Therefore, once the luminosity density of stars has been determined, the dust component will be known as well.

It is hard to assess the applicability of the blackbody assumption to the cosmic dust emission. Unlike the stellar case, the physics of emission and absorption of dust in the ISM is difficult to model. In fact, from the observational point of view, the PAHs present a complex emission and absorption spectra at mid-IR mainly due to their vibrational and rotational modes [44].

2.3.3 Total emission

According to the previous discussion, one can calculate the emissivity from all galaxies if the photon escape fraction $f_{esc}(\epsilon)$, IMF $\xi(m)$, SFR $\psi_c(z)$ and the dust parameters f_n and Θ_n are defined.

In [45] the authors present a fit to $f_{esc}(\lambda)$ based on a model by Driver et al. [46] which uses a sample of $\sim 10^5$ galaxies. The segmented fit in power laws is given by

$$f_{esc}(\lambda) = \begin{cases} 0.688 + 0.556\log\lambda, & \lambda \leq 0.165 \\ 0.151 - 0.136\log\lambda, & 0.165 < \lambda \leq 0.22 \\ 1.0 + 1.148\log\lambda, & 0.22 < \lambda \leq 0.422 \\ 0.728 + 0.422\log\lambda, & \lambda > 0.422. \end{cases} \tag{2.21}$$

It is assumed that photons with energy above 13.6 eV are completely absorbed by interstellar and intergalactic HI gas. Figure 2.7 shows the behavior of $f_{esc}(\lambda)$. As we can see, from $\lambda \sim 4$ μm photons are no longer absorbed by interstelar dust. From $\lambda \sim 0.9$ μm to shorter wavelengths one can note the complete absorption by dust and HI gas.

The IMF models are, in general, powers of the mass like $\xi(m) \propto m^{-k}$, the classic

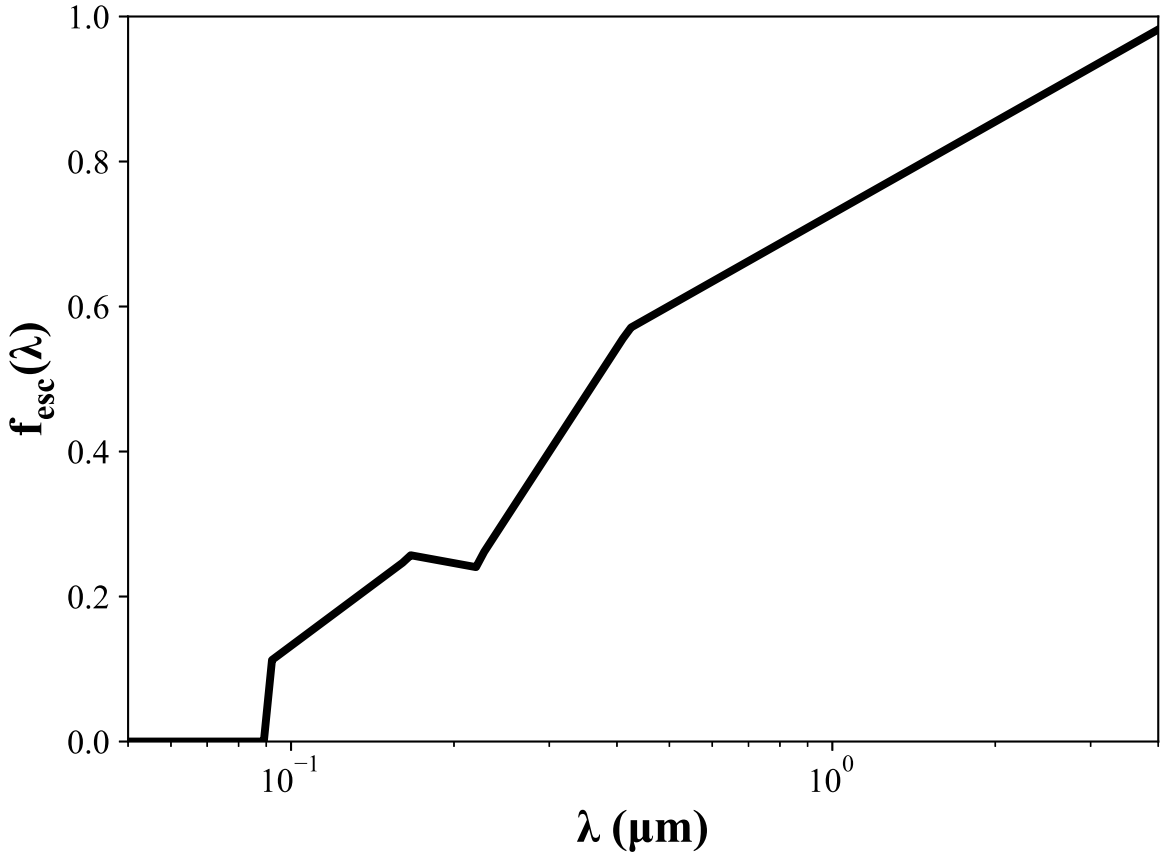

Figure 2.7: *Fraction of photons which escape their environment without being absorbed by dust or HI gas as a function of their wavelengths.*

Salpeter model uses $k = 2.35$ [47]. Here a variation of this model is used setting $k = 1.5$ to masses less than 0.5 $M_\odot$ and the Salpeter behavior to higher masses, and this model will be called "Salpeter A". Another alternative is the "Baldry-Glazebrook" model, that defines $k = 1.5$ to $m < 0.5$ $M_\odot$ and $k = 2.2$ to other masses. Figure 2.8 shows these models.

The star formation history and the number of stars at some given epoch of the universe are not independent physical quantities. It is necessary to assume a model to IMF in order to determine the parameters of SFR. Two functional forms to $\psi_c(z)$ are used here, one found by Cole et al. [48] given by

$$\psi_c(z) = h\frac{a + bz}{1 + \left(\frac{z}{c}\right)^d}, \tag{2.22}$$

where $h = 0.7$, and a, b, c and d are parameters that should be adjusted to each IMF model considered. Hopkins and Beacom [49] used equation 2.22 and formulated their own function, defined by pieces, given by

$$\psi_c(z) = 10^{a'}(1 + z)^{b'}, \tag{2.23}$$

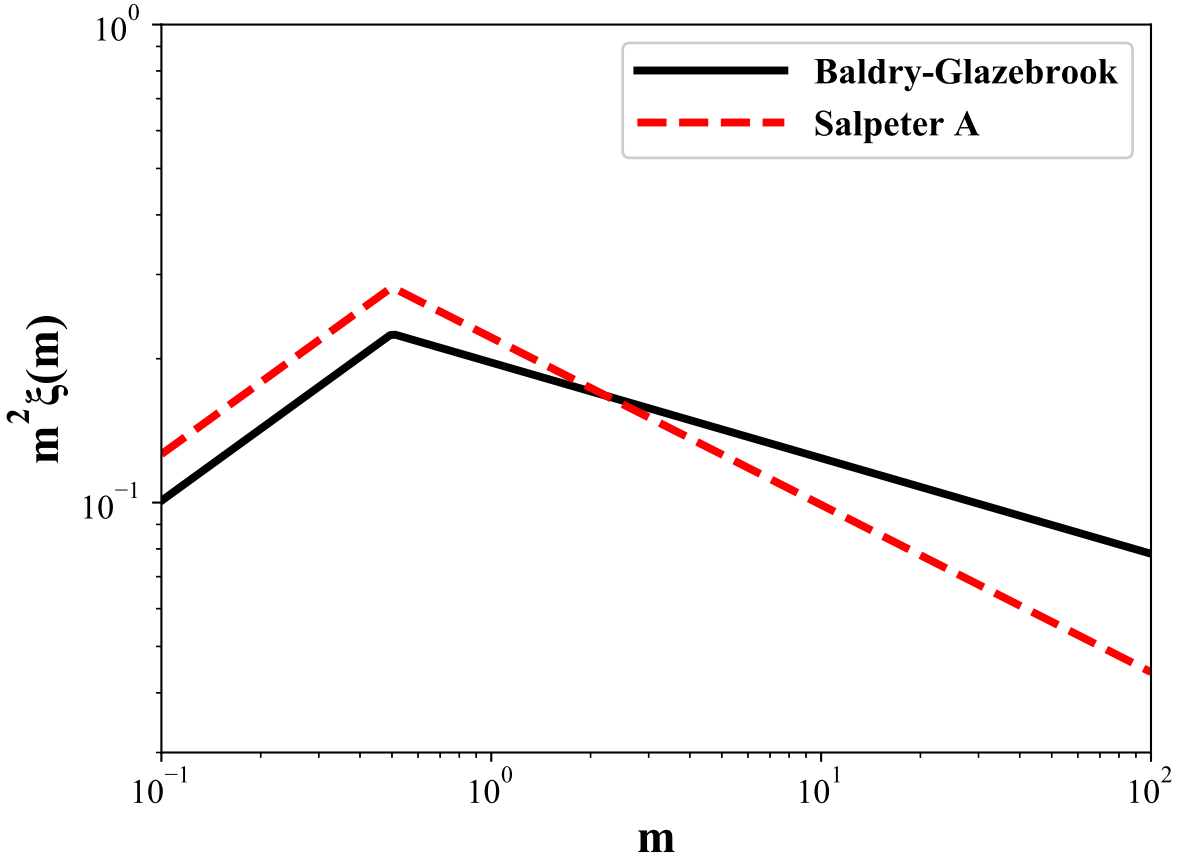

Figure 2.8: *Initial mass function normalized models utilized in [29] to describe the number of stars in terms of its mass. Here, the dimensionless mass $m = M/M_\odot$ is defined.*

where a' and b' take different values in distinct redshift intervals.

The parameters used in equations 2.22 and 2.23 are defined in [48] and [49]. So, it is possible to build five models used in [45] and [29]. Figure 2.9 shows the Madau diagram for the five SFR functions used.

The combinations of SRF and IMF are the following:

- Model A: SFR by Cole et al. [48] and the IMF Salpeter A,
- Model B: SFR by Cole et al. [48] changed by Hopkins and Beacom [49] and the IMF Salpeter A,
- Model C: SFR by Cole et al. [48] changed by Hopkins and Beacom [49] with the IMF from Baldry and Glazybrook [50],
- Model D: SFR by Hopkins and Beacom [49] with the IMF Salpeter A, and
- Model E: SFR by Hopkins and Beacom [49] with the IMF from Baldry and Glazybrook [50].

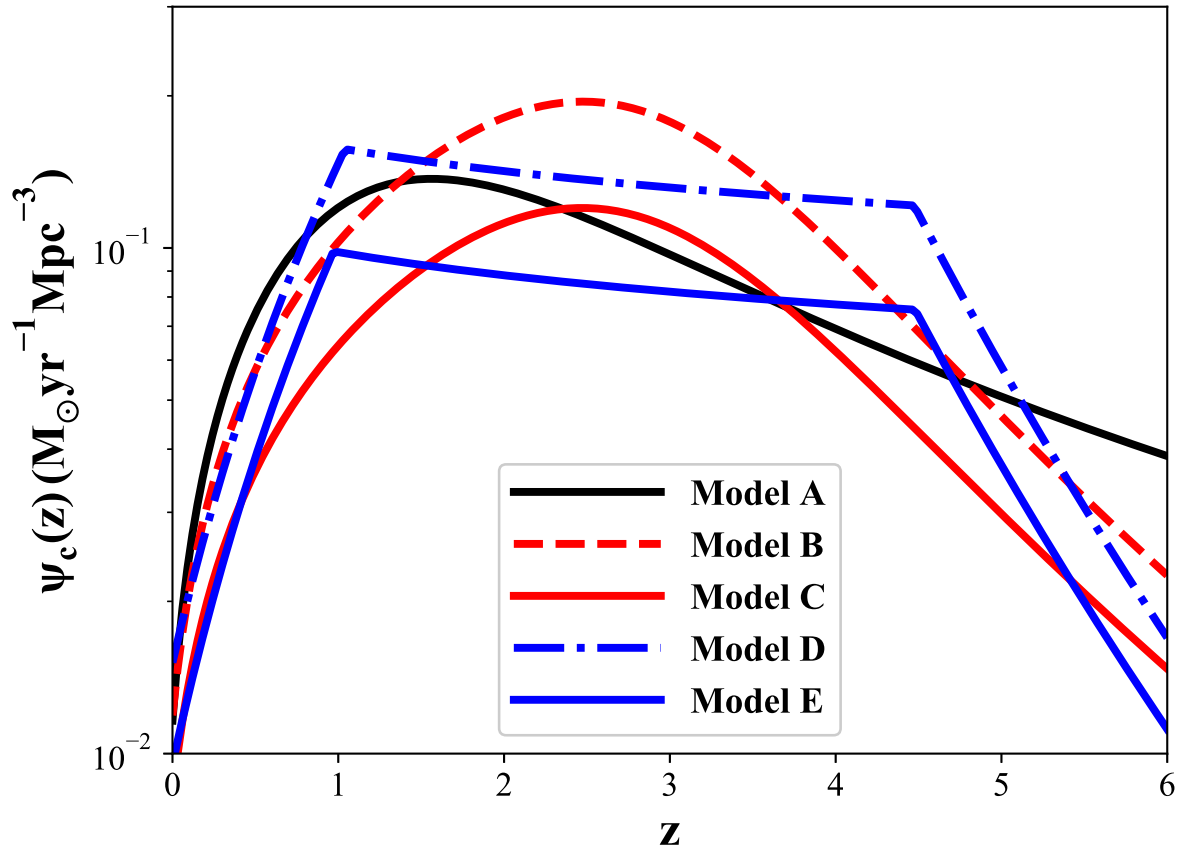

Figure 2.9: *Madau diagrams for the five models of star formation rate defined in [45] to describe the evolution of stars with the time given a specific universal initial mass function. The inset shows to which model each curve belongs.*

F10 model considers stars with masses between $m_{min} = 0.1$ and $m_{max} = 100$ and the maximum redshift $z_{max} = 6$. Comparing the luminosity density curves obtained from each one of the five models with the data available, the authors concluded that the model C is the one that best describes the stellar emissivity data at UV/optical band. As said before, once the stellar emissivity is determined, the dust luminosity density can be set just fixing the fraction contributions and temperatures of each grain type (f_n, Θ_n). These parameters are defined using IR LF data at $z = 0.0$ and $z = 0.1$ and the values are displayed in Table 2.1. Figures 2.10 and 2.11 show the luminosity density of model C in some redshifts. A direct comparison between model and data can be seen in [29].

Finally, we can calculate the EBL energy density u as a function of z and ϵ. The relation between energy density u and intensity I of the EBL is simply $\epsilon I(\epsilon; z) = \frac{c}{4\pi}\epsilon u(\epsilon; z)$. Therefore, in comoving coordinates, one can write

$$\epsilon\, u_c(\epsilon; z) = \int_z^{z_{\max}} dz_1 \frac{\epsilon' j_c(\epsilon'; z_1)}{(1+z_1)} \left|\frac{dt}{dz_1}\right| \tag{2.24}$$

Dust component	n	f_n	Θ_n $[10^{-9}]$
PAH	1	0.25	76
Small grains	2	0.05	12
Large grains	3	0.70	7

Table 2.1: *Summary of the dust parameters used in the calculations of this work. In order to reproduce the results obtained by F10, the values of PAH and large grains are slightly different from that shown by authors ($f_1 = 0.30$ and $f_3 = 0.65$)*

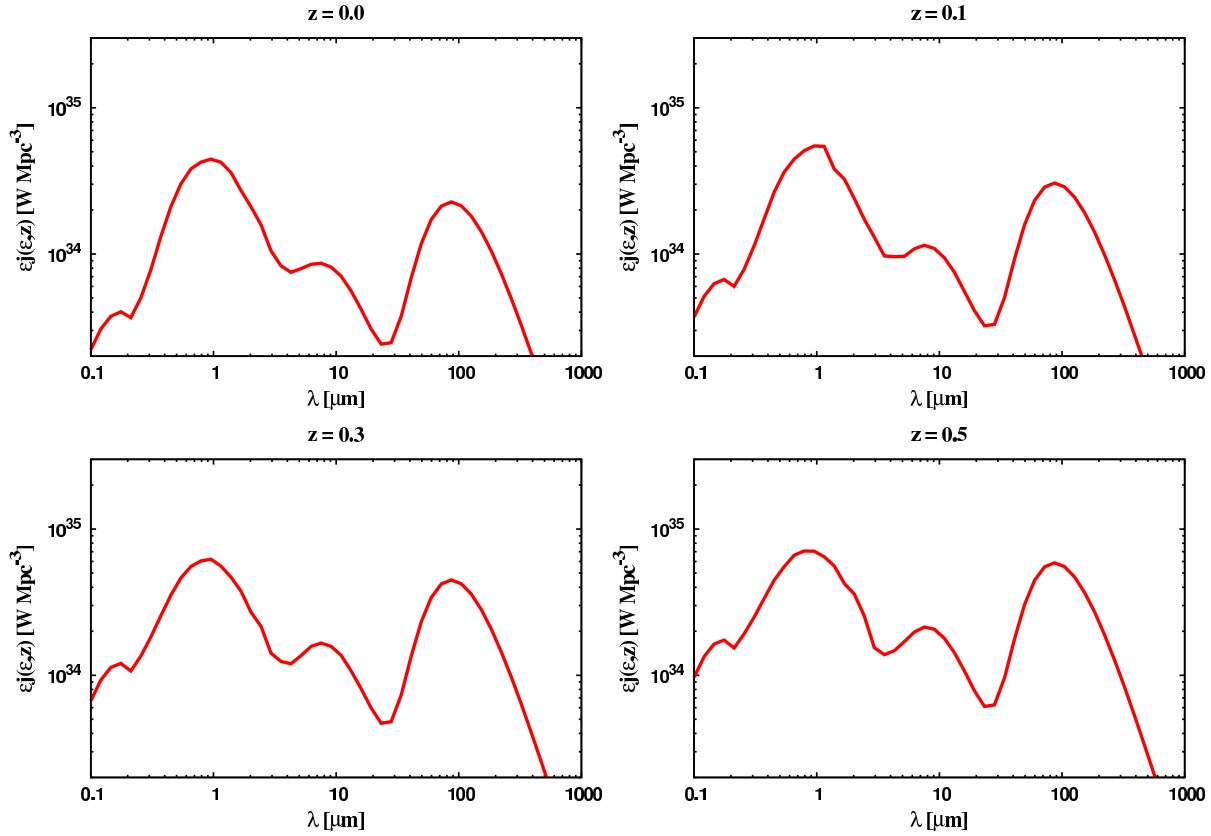

Figure 2.10: *Luminosity density calculated by model C from the F10 model [29]. The curves are to $z = 0.0$, 0.1, 0.3 and 0.5.*

where $\epsilon' = (1 + z_1)\epsilon$ is the photon energy at redshift z_1 and $j_c = j_c^{star} + j_c^{dust}$ is the total comoving emissivity of the sources. In this work we will be interested in analyzing the behaviour of each EBL contribution, therefore, each component (star + 3 dust) was calculated separately. As we can see in figure 2.12, the energy density of the EBL is displayed evincing each contribution. Superimposed we have the data representing the upper and lower limits. Clearly, F10 model is very close to the lower constraints. The temperature of each component determines the spectral region where it peaks. The values fixed in table 2.1 imply that the PAH component dominates at mid-IR ($\sim 10\,\mu$m) and the small and large grains dominate at far-IR, with main contribution coming from the large ones.

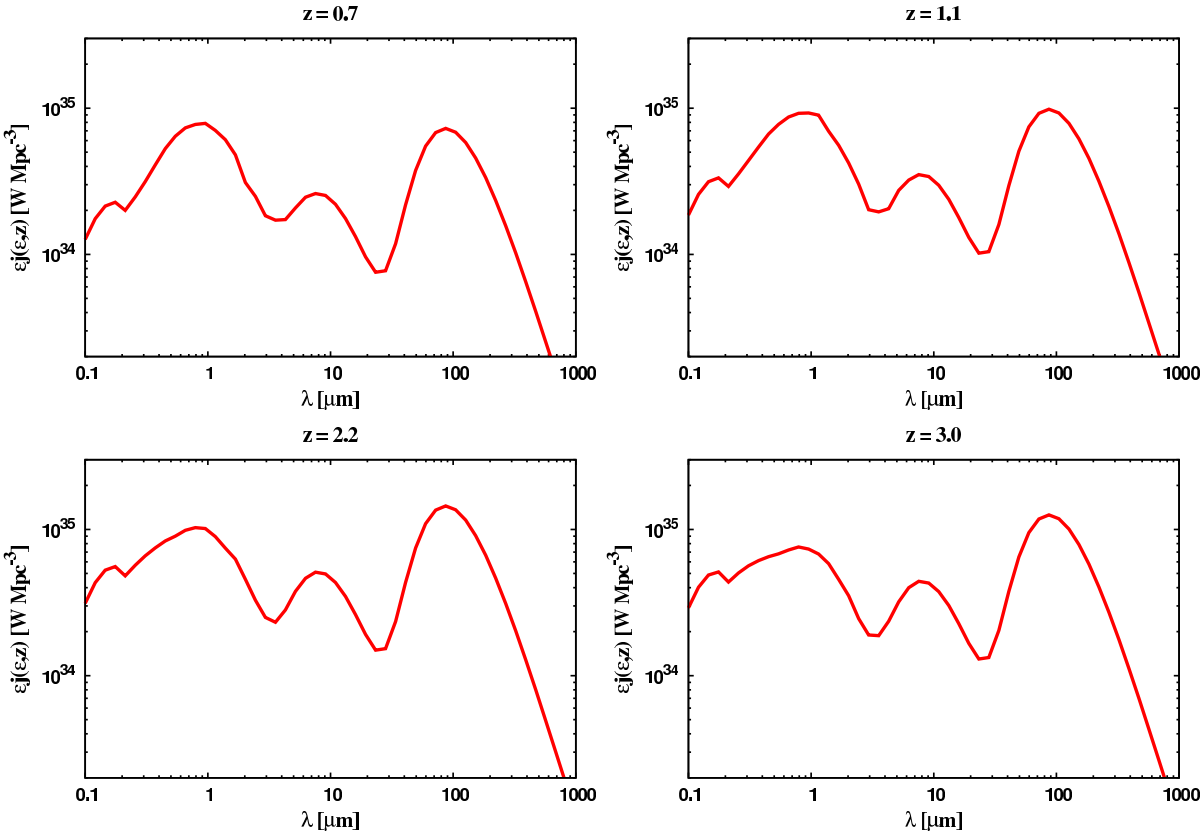

Figure 2.11: *Luminosity density calculated by model C from the F10 model [29]. The curves are to z = 0.7, 1.1, 2.2 e 3.0.*

The bolometric intensity is defined as the total output energy

$$I_{bol} = \int I d\nu, \tag{2.25}$$

given in units of W m^{-2} sr^{-1}. The EBL bolometric intensity calculated from F10 model corresponds to approximately 5% of CMB intensity. These integrated intensities to each component, total EBL and CMB are summarized in table 2.2.

Component	I_{bol} (nW m^{-2} sr^{-1})
Star	25.9
PAH	5.5
Small grains	1.1
Large grains	14.9
Total	47.4
CMB	1000.9

Table 2.2: *Bolometric intensity for each astrophysical component predicted by F10 model. It is also shown the total EBL and the CMB bolometric intensities.*

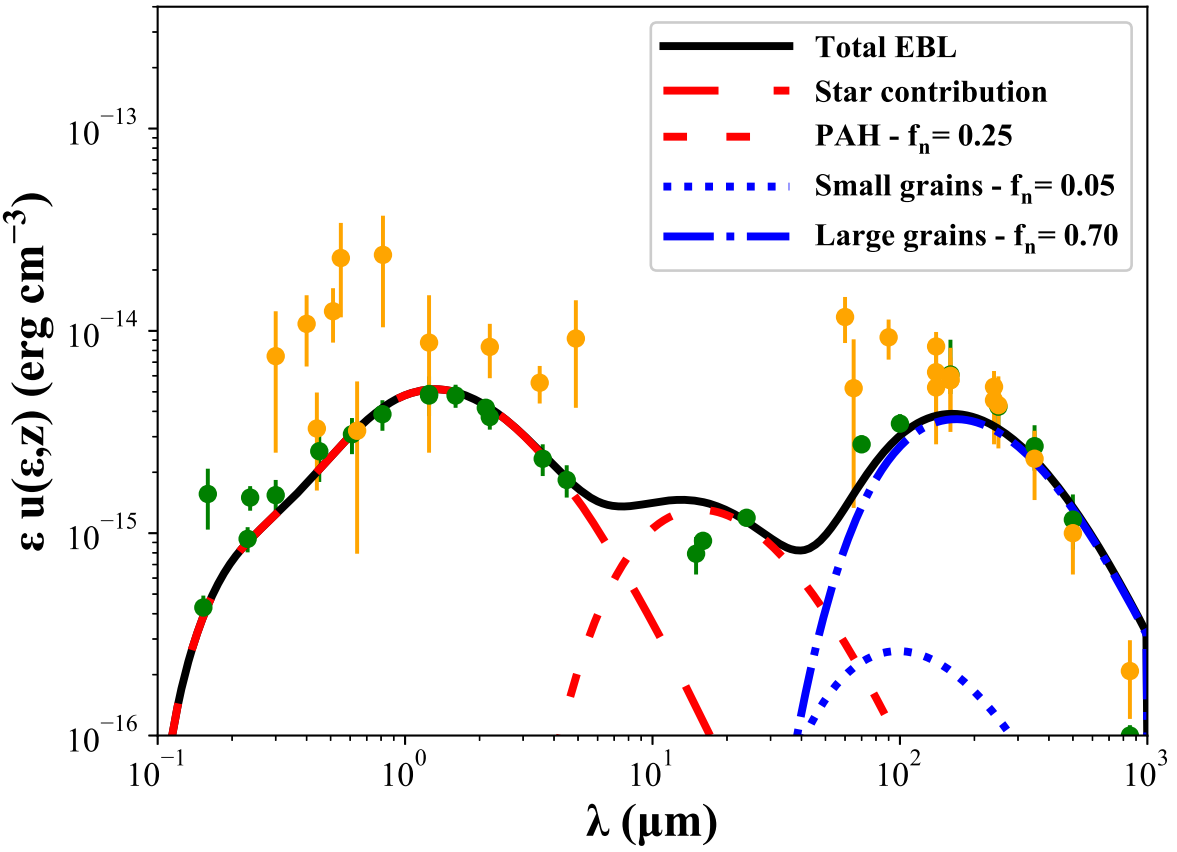

Figure 2.12: *EBL energy density in comoving coordinates as measured by an observer at redshift $z = 0$. In addition to the total (black) density, individual contributions are also shown: stellar (long-dashed red), small hot grains (dotted blue), large warm grains (dot-dashed blue) and PAHs (dashed red).*

2.4 Domínguez's model

The last model presented here is that elaborated by Domínguez et al. [20] which is classified as type (iv), according to the list previously described. This EBL model is based on three main ingredients:

(i) The luminosity function (LF) of galaxy at the rest-frame K-band (near-infrared, centered at 2.2 μm) described by Cirasuolo et al. [51];

(ii) the multiwavelength galaxy data from the All-wavelength Extended Groth Strip International Survey (AEGIS) of about 6000 galaxies in the redshift range of 0.2-1;

(iii) the galaxy SED SWIRE (Spitzer Wide-Area Infrared Extragalactic Survey) library with 25 templates available [52].

The galaxies in the sample are conveniently divided into three subsamples based on their magnitudes in the K-band (defined as faint, middle and bright). The division is done

so that the number of galaxies is approximately the same in each magnitude bin. Then, the comoving luminosity density for each galaxy population considered can be calculated by

$$\begin{aligned} j_i(\lambda, z) &= j_i^{faint} + j_i^{middle} + j_i^{bright} \\ &= \int_{M_2}^{M_1} \Phi(M_K^z, z)\, f_i\, T_i(M_K^z, \lambda)\,(1+z)\, dM_K^z + \int_{M_3}^{M_2} \Phi(M_K^z, z)\, m_i\, T_i(M_K^z, \lambda)\,(1+z)\, dM_K^z \\ &+ \int_{M_4}^{M_3} \Phi(M_K^z, z)\, b_i\, T_i(M_K^z, \lambda)\,(1+z)\, dM_K^z, \end{aligned} \tag{2.26}$$

where the index i refers to the galaxy population defined in the SWIRE SED library, f_i, m_i and b_i are the fractions of galaxies in each magnitude range, $T_i(M_K^z, \lambda) = L_\nu$ (in ergs s^{-1} Hz^{-1}) is the luminosity and M_K^z is the rest-frame absolute magnitude in the K-band at redshift z. Φ is the LF derived by Cirasuolo et al. [51], which assumes the shape of Schechter function in terms of magnitudes, given by

$$\Phi(M) = 0.4\,\ln(10)\Phi_0 10^{-0.4\,\Delta M(\alpha+1)} \exp(-0.4\Delta M), \tag{2.27}$$

where $\Delta M = M_K - M_K^*$ and the luminosity and density evolution are parameterized as

$$M_K^*(z) = M_K^*(z=0) - \left(\frac{z}{z_M}\right)^{k_M}, \tag{2.28}$$

and

$$\Phi_0 = \Phi_0(z=0)\, \exp\left[-\left(\frac{z}{z_\Phi}\right)^{k_\Phi}\right]. \tag{2.29}$$

The best-fit parameters found by Cirasuolo et al. are summarized in table 2.3.

Parameters	best-fit
α	-1.07 ± 0.1
$M_L^*(z=0)$	-22.26 (fixed)
z_M	1.78 ± 0.15
k_M	0.47 ± 0.2
z_Φ	1.70 ± 0.09
k_Φ	1.47 ± 0.1
$\Phi_0(z=0)$	$(3.5 \pm 0.4)\times10^{-3}$ (Mpc^{-3})

Table 2.3: *Best-fit LF parameters found by Cirasuolo et al. [51].*

The limits of integration in 2.26 are $M_1 = -16.6$, $M_2 = -21.0$, $M_3 = -23.0$ and $M_4 = -25.0$. So, the total comoving luminosity density is the sum of each galaxy population

contribution

$$j_c(\lambda, z) = \sum_i j_i(\lambda, z). \tag{2.30}$$

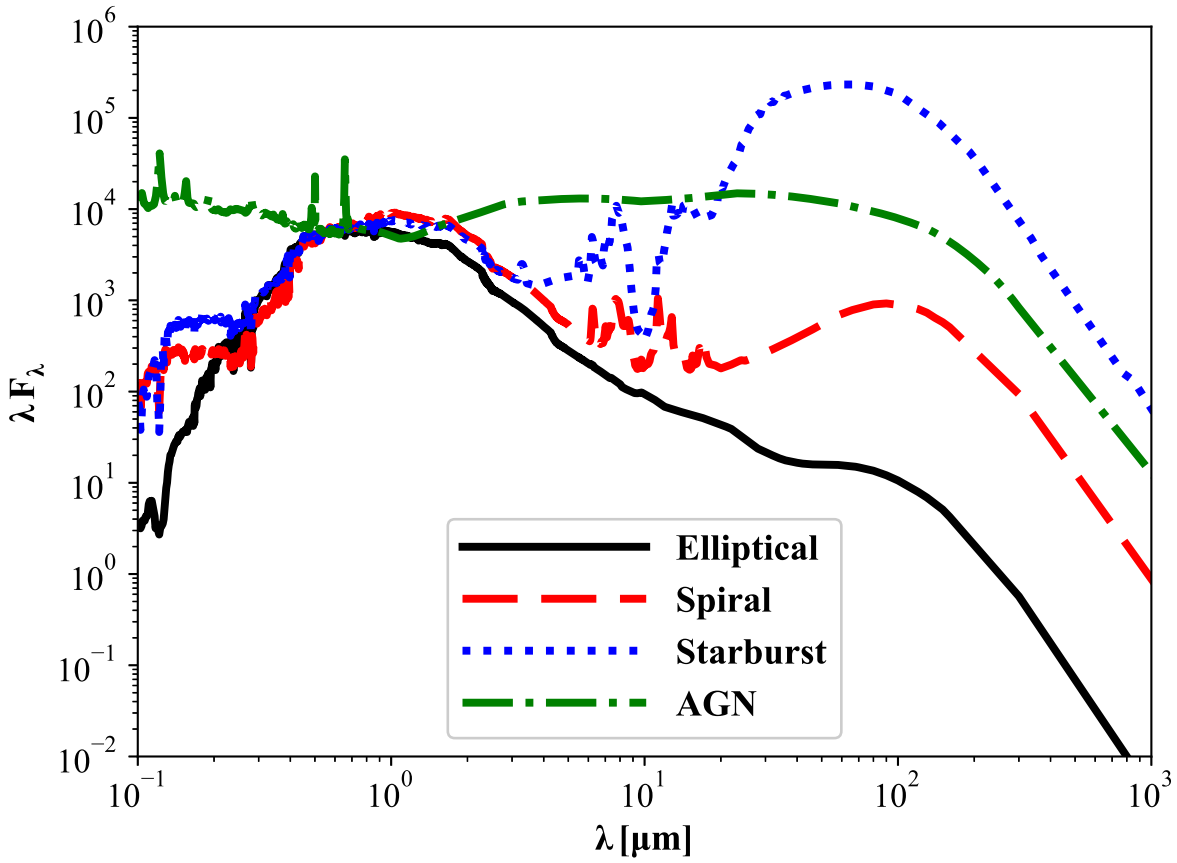

Figure 2.13: *Four examples of SED templates from the SWIRE library which are used in Domínguez et al. EBL model. The y-axis is shown in arbitrary units.*

Figure 2.13 shows some examples of templates of galaxy SED used in the construction of this EBL model. Considering all the 25 galaxy types and fitting the data collected, the authors found the fractional contribution to each galaxy class. Figure 2.14 presents the resulting local emissivity compared to data and a good agreement can be seen between model and data. As shown in equation 2.5, the EBL spectrum observed at some redshift z can be obtained integrating $j_c(z, \lambda)$ from a maximum redshift z_{max} up to redshift z of the observer. At $z = 0$ we expect to get the EBL spectrum measured today. This accumulated radiation spectrum is shown in figure 2.15 which was extracted from [20], where the black line represents the intensity obtained from Domínguez's model. Other models and EBL data are also shown in this plot for comparison. As we can seen, the spectrum obtained by Domínguez et al. is in agreement with the limits imposed by measurements. The stellar component, which peaks around 1.0 μm is close to lower limits, which as we saw previously comes from the resolved galaxy counts. In the region expected to be dominated

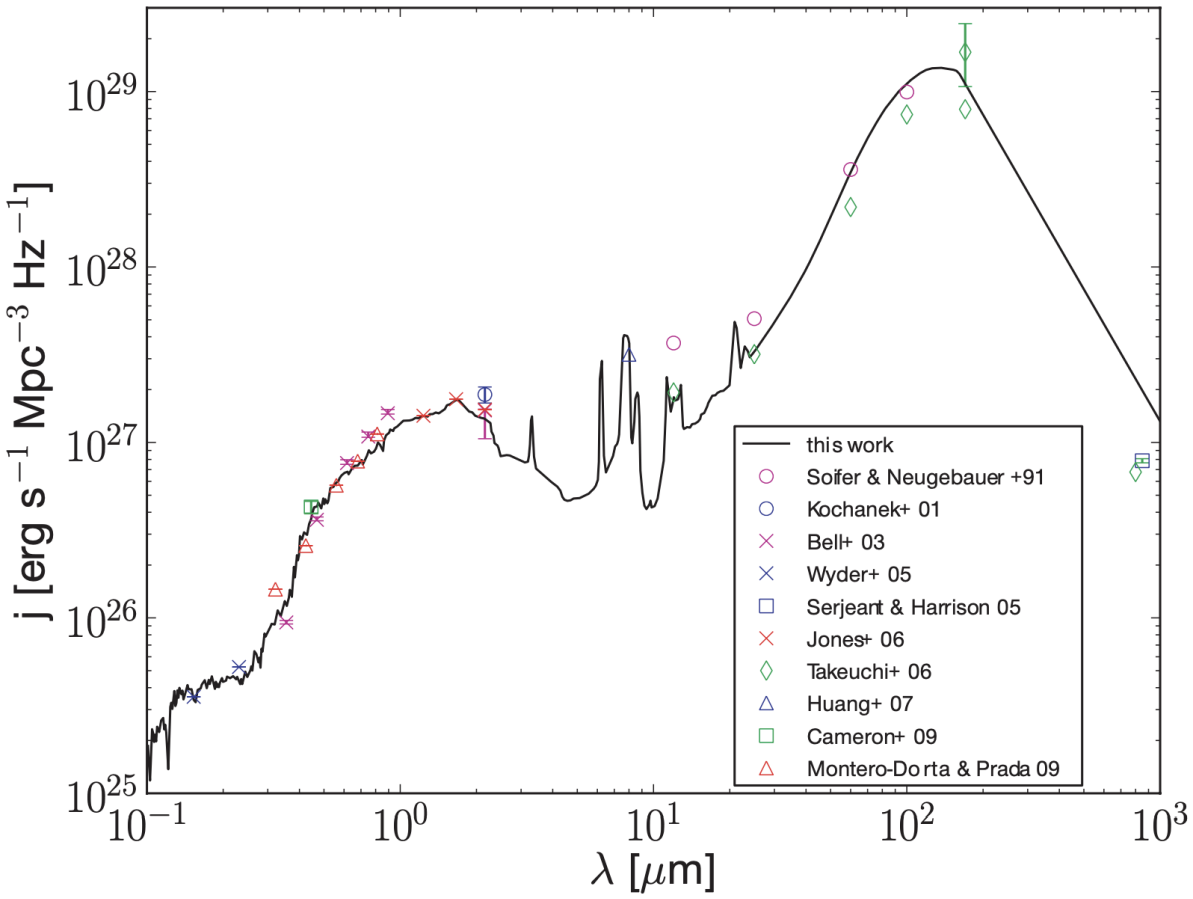

Figure 2.14: *The resulting local emissivity obtained by eq 2.30. Superimposed to the model are observational data from many different surveys at different electromagnetic bands [20]. Figure extracted from [20].*

by dust emission, at far-IR, Domínguez' model best agrees with upper limits, in general obtained from direct measurements.

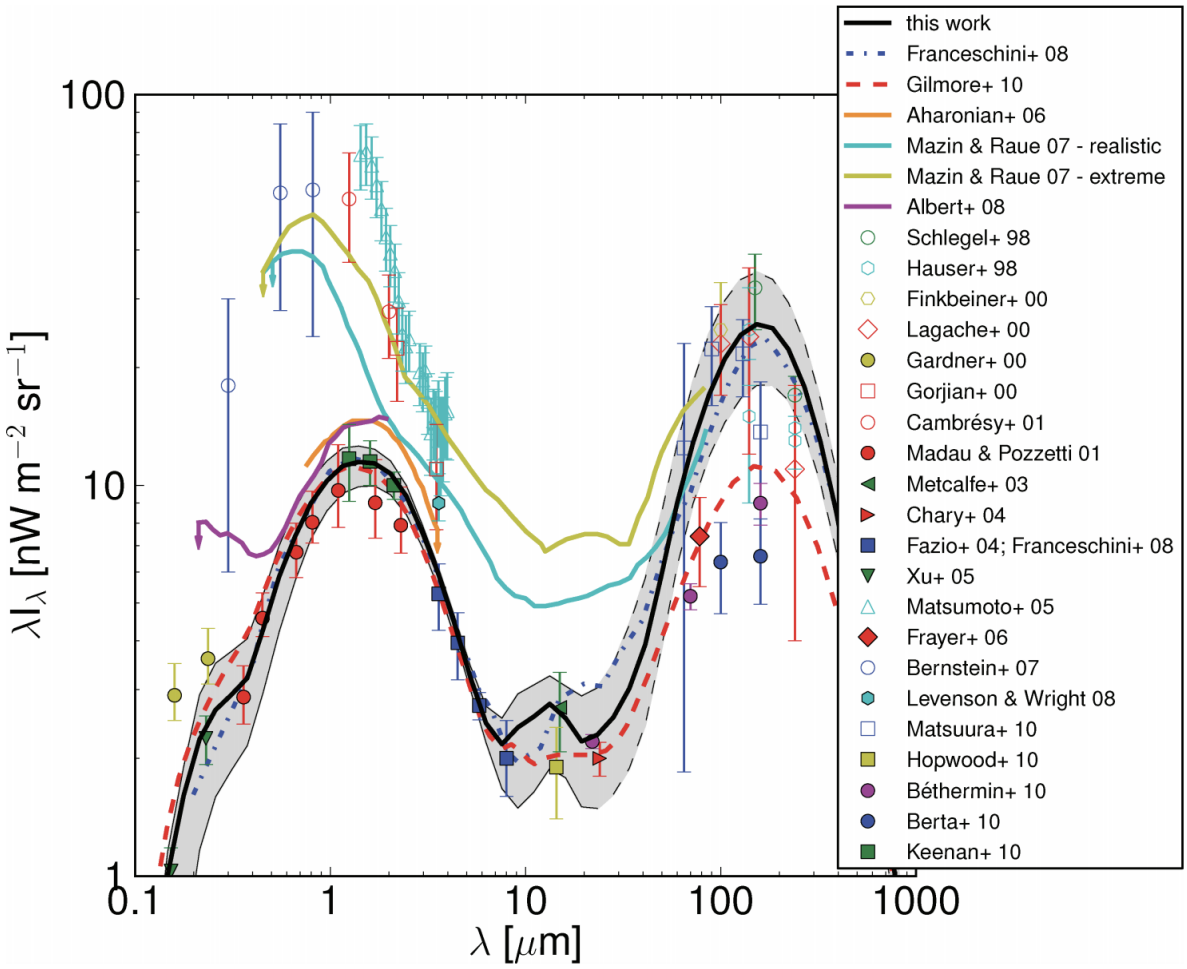

Figure 2.15: *EBL spectrum at $z = 0$ calculated from Domínguez et al. model (black line) and many other models and observational data superimposed. Figure extracted from [20].*

Chapter 3

Extragalactic gamma-ray sources and the EBL opacity

Although the focus of this thesis is not the theory/phenomenology of AGNs, a little overview on this subject is needed at this time. This chapter is dedicated to the description of the gamma-ray sources of our interest and the interaction between the photons from the EBL with the extremely energetic ones from these sources. The SED measured at Earth from these astrophysical objects undergoes attenuation at very high energy due to this interaction and such an effect could be deeply investigated only with the advent of the IACT instruments.

3.1 Active galactic nuclei

There are many astrophysical objects emitting gamma-rays, however, here we want to investigate just extragalactic sources, since in order to the EBL attenuation to become important for TeV photons, they have to propagate over distances much bigger than our galaxy's size. Among the extragalactic gamma-ray emitters, we can mention the gamma-ray bursts (GRB) and AGNs. In particular, blazars are one of the main extragalactic targets in gamma-ray astronomy.

In 1943, Carl Seyfert investigated a class of galaxies presenting strong and broad emission lines. The core of these galaxies exhibited an unsual intense brightness and since they were not spatially resolved in the optical band, an estimate of the maximum radius of their cores was found by Lodewijk Woltjer, in 1959, as $r \lesssim 100$ pc. In 1963, Maarten Schmidt identified the radio source 3C 273 as a point-like source with unusual strong and broad emission lines. Analyzing the position of these lines Schmidt found that 3C 273 had to be located at $z = 0.158$. For this distance, its absolute magnitude had to be ~ 100 times brighter than a normal galaxy. This large amount of energy had to be emitted from a small region of space, and such quasi-stellar radio sources became known as quasars [53].

Initially just radio sources were classified as quasars, however similar features were found in objects which did not have appreciable radio emission and were called as radio-quiet quasars. Quasi-Stellar Objects (QSOs) is the class encompassing these two types of AGNs. Another class are the Seyferts, which are less luminous compared to QSOs. They are commonly divided in subgroups due to spectral features. For example, Seyfert 1 presents both broad and narrower emission lines, while Seyfert 2 just the narrower ones. Optically Violently Variable (OVV) sources are quasars with strong and rapid variability in optical band, presenting high polarization at these wavelengths. Similar to OVVs, BL Lacs also exhibit high variability, but are featureless in the optical, making hard to determine their redshifts. At low luminosity epochs, emission lines can arise and BL Lacs become very similar to OVVs. Therefore, it is usual to refer to both as the same class, the blazars. These sources also present high energetic and strongly variable gamma-ray emission [53].

Despite all the differences among these objects, common properties motivated the development of a unified model of AGNs. These sources are supposed to contain a central supermassive black hole (SMBH) and a material accretion disk, therefore, the mass $M_\circ$ of the black hole and the accretion rate $\dot{m}$ could define the AGN classifications. It is believed that most of the energy emitted by AGNs is produced close to Schwarzschild radius through accretion of matter. The radiation in the outward direction can interact with matter falling into the black hole, therefore it is expected a minimum value of mass of the black hole $M_\circ$ in such way that the gravitational force wins over the radiation pressure in the opposite direction, hence the mass $M_\circ$ can set the maximum luminosity of the AGN in terms of Eddington luminosity [1], while the ratio $\dot{m}/\dot{m}_{edd}$ [2] describes the rate in which matter from the accretion disk falls into the black hole. In addition, the geometric structure of these objects suggests that the viewing angle can affect the observed spectrum and can be used in their classification. As said before, Seyfert 1 and Seyfert 2 basically differ by the presence of broad and narrow emission lines in the former and just narrow ones in the latter. Observations of NGC 1068 (Seyfert 2) have shown that, when just polarized light is detected, the narrow lines which appeared alone before, now are accompanied by broad ones (features of Seyfert 1). These apparently different objects could belong to the same class if a material, which is able to polarize the light, are in the line-of-sight of the Seyfert 2. Studies show that a thick torus of dust must be located at the accretion disk plane causing this polarization [53].

The unified model of AGNs provides also a good description of observed features of blazars, such as superluminal motions, strong variability and absence (or presence) of emisson lines. Apparent superluminal motions can be explained by relativistic velocities

[1] A maximum luminosity, L_{Edd}, which keeps the equilibrium between gravitational force and that from the radiation pressure on the material of the accretion disk.

[2] m is the falling mass from the accretion disk and $\dot{m}_{Edd} = L_{Edd}/\epsilon c^2$, where ϵ is the eficiency of energy conversion in the process.

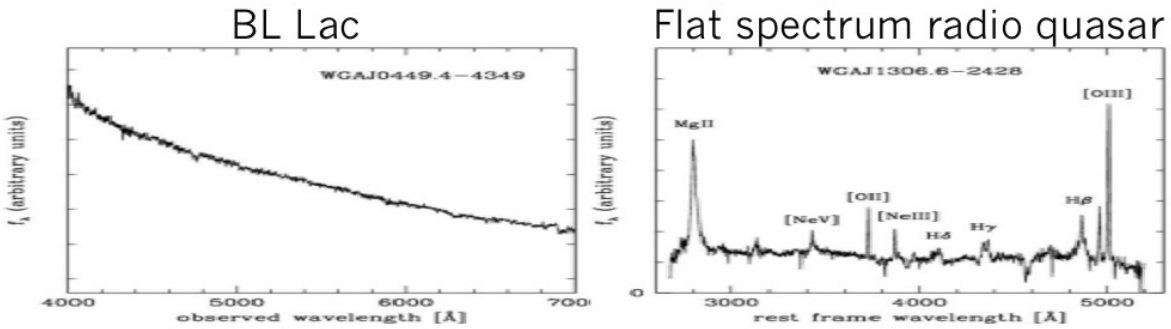

Figure 3.1: *Comparison between BL Lac and FSRQ spectra at the optical band evincing the lines features in FSRQ and the absence in BL Lacs. Figure extracted from fermi.gsfc.nasa.gov/science/mtgs/fermi_jansky/slides/PPadovani.pdf.*

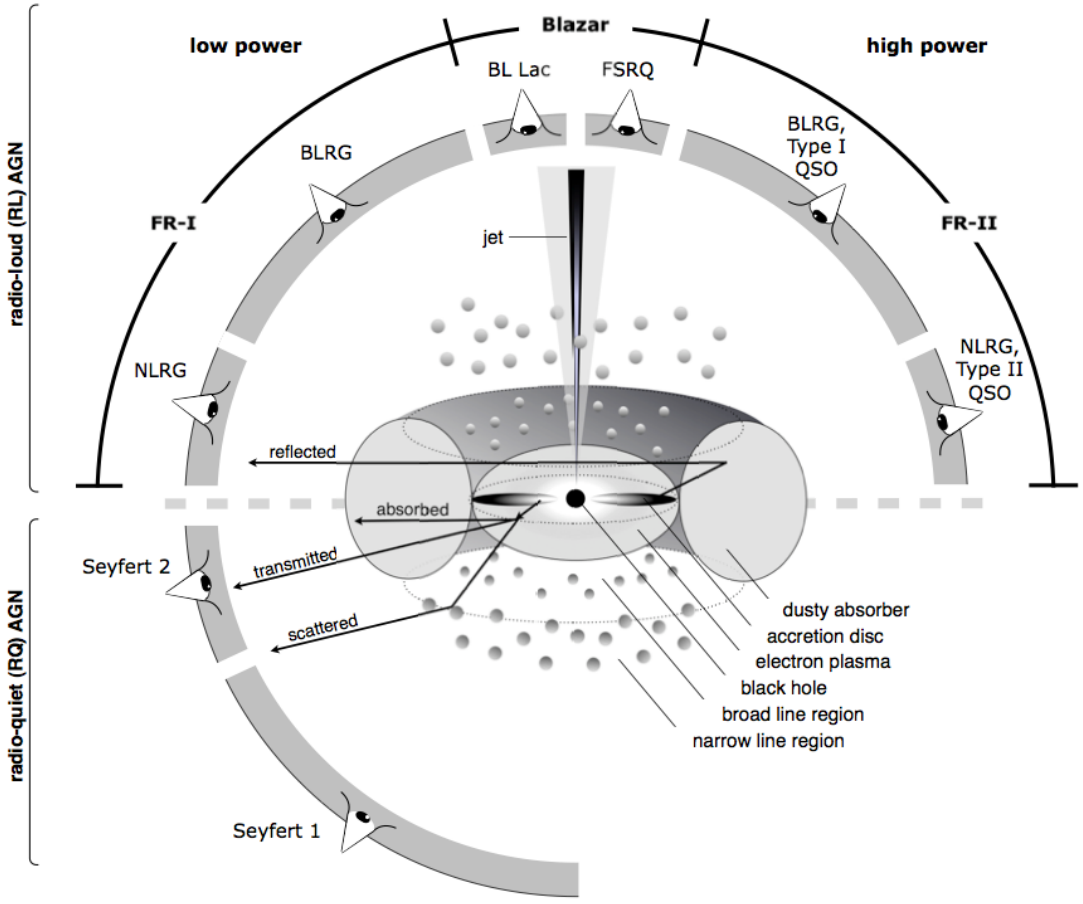

Figure 3.2: *Schematic illustration of the unified model for AGNs showing the classification to each mode of observation. Figure extracted from [54].*

of matter in a jet (present in some AGNs) closely aligned with the line-of-sight. The existence of particles accelerated close to the speed of light is a indicative of the presence of a compact and powerful object in its core, such as a SMBH. These relativistic motions in the jet must originate the beaming effect. A Doppler shift in the frequencies is expected and an isotropic emission in the rest-frame becomes anisotropic to the observer, amplifying

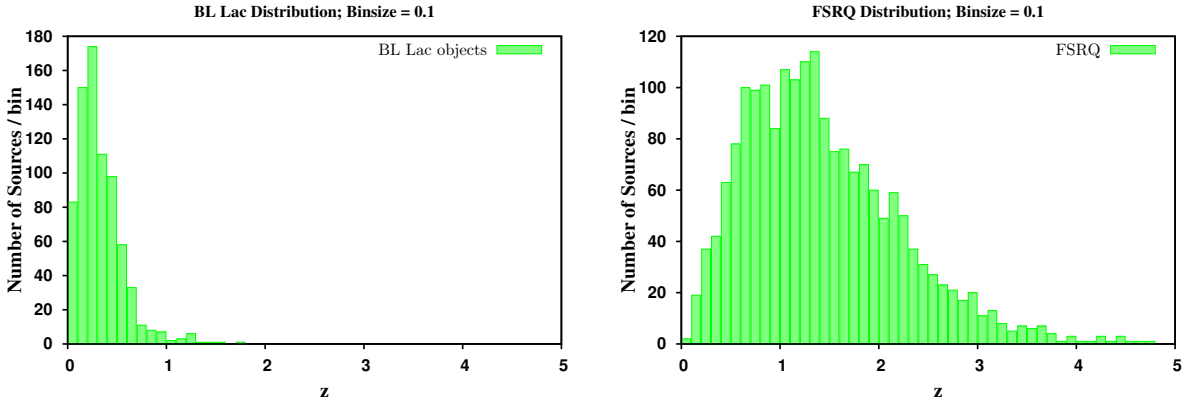

Figure 3.3: *Left: Redshift distribution of BL Lac-type blazars from the Roma-BZCAT catalog [55]. Right: Redshift distribution of FSRQ-type blazars from the Roma-BZCAT catalog [55].*

the measured intensity. When jet radiation extends at optical/UV band its intensity can hide emission lines, like in BL Lacs. On the other hand, when the intensity is not enough to outshine completely these lines, we have an OVV, sometimes called Flat Spectrum Radio Quasars (FSRQ). Figure 3.1 shows BL Lac and FSRQ spectra, where we can see clearly the spectral differences. The high variability can also be explained by beaming effect, since even smooth changes in the velocities of sources can amplify appreciably its brightness [53]. Figure 3.2 displays a cartoon summarizing the main ideas of the unified model of AGNs.

The histograms in figure 3.3 shows the redshift distribution of BL Lacs and FSRQ from Roma-BZCAT compilation [55]. The concentration of BL Lacs at low redshifts, as compared to the FSRQ distribution which extends up to $z \sim 5$, is likely to be a selection effect, due to difficulties in determining the redshift of the BL Lacs.

In general, the spectrum of a blazar presents two peaks, where the first one, located in UV/X-rays region, is believed to come from synchrotron emission by electrons. The second peak at gamma-ray energies is not very well understood and currently there are two main models trying to describe the observations: the leptonic models, in which the main contribution to gamma-ray emission comes from relativistic electrons and positrons; and the hadronic models, based on emission from protons and atomic nuclei. For leptonic models the high energy peak is interpreted as the radiation produced from target photons inversely Compton scattered by relativistic leptons in the jet [54, 57]. A possible origin of these target photons could be the synchrotron radiation produced by the same population of leptons which scatter them. This process is known as synchrotron self-Compton model (SSC). Another possibility is an external source of soft photons, such as the broad line region (region with gas clouds responsible for the broad emission lines observed in the Optical and UV in AGNs), a dusty torus, and/or the accretion disk. In fact, these two processes can be important for a given source and both contribution must be taken

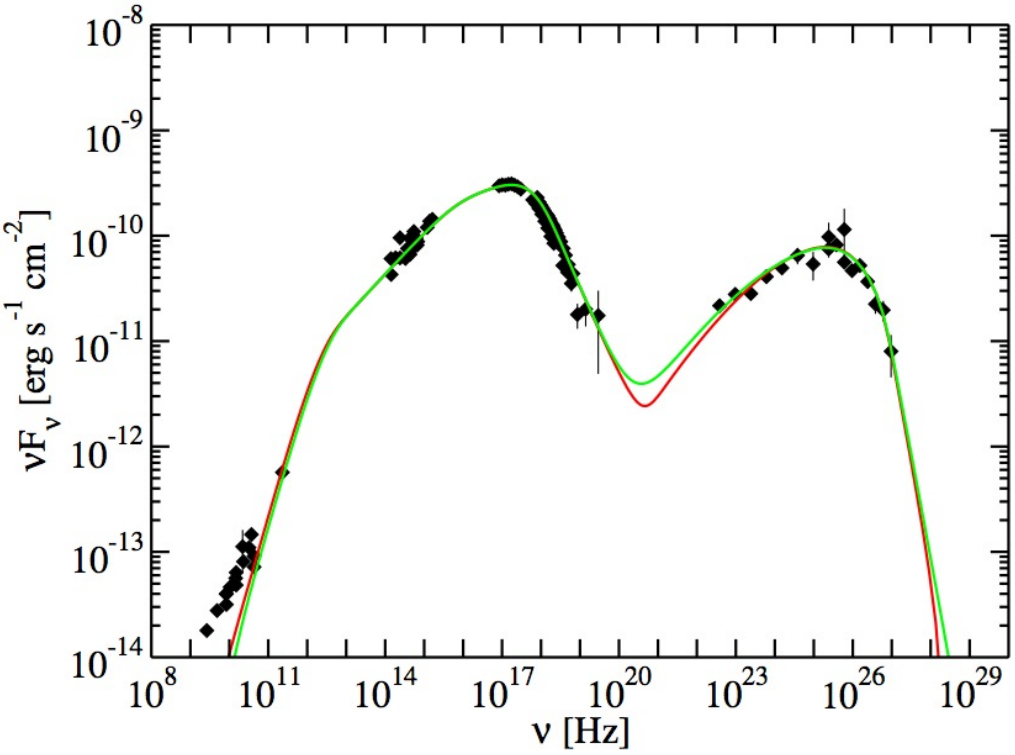

Figure 3.4: *Spectrum of BL Lac Markarian 421 with its two characteristics peaks. The first peak appears in the X-ray band and the second in TeVs. Figure extracted from [56].*

into account. Another possible scenario is a jet dominated by relativistic hadrons, instead of leptons. For hadronic models the high energy emission could come from proton synchrotron radiation or photopion production initiated when soft photons and protons interact [57]. As an example, figure 3.4 shows the spectrum of the BL Lac Markarian 412 described by the leptonic SSC model, where each curve uses different assumptions on the time scale variabilities: the red curve uses a minimum variability of 1 day and the green curve 1 hour [56].

The distributions in figure 3.3 contain blazars observed in many bands of the electromagnetic spectrum. However, we are particularly interested in TeV energy emissions, therefore, we have explored the TeVCat catalogue which provides information about TeV-sources [58]. Figure 3.5 shows a sky map in galactic coordinates of the sources available in TeVCat. This sky map contains both galactic and extragalactic emitters.

As of March 2019, TeVCat contained 54 extragalactic TeV-emitting sources, where the majority are blazars and just six of them are FSRQ. The sources with highest z are of this type, with $z \sim 1$ (an epoch when the universe had approximately half of its current age). All these sources were detected by IACTs, figure 3.6 shows their redshift distribution.

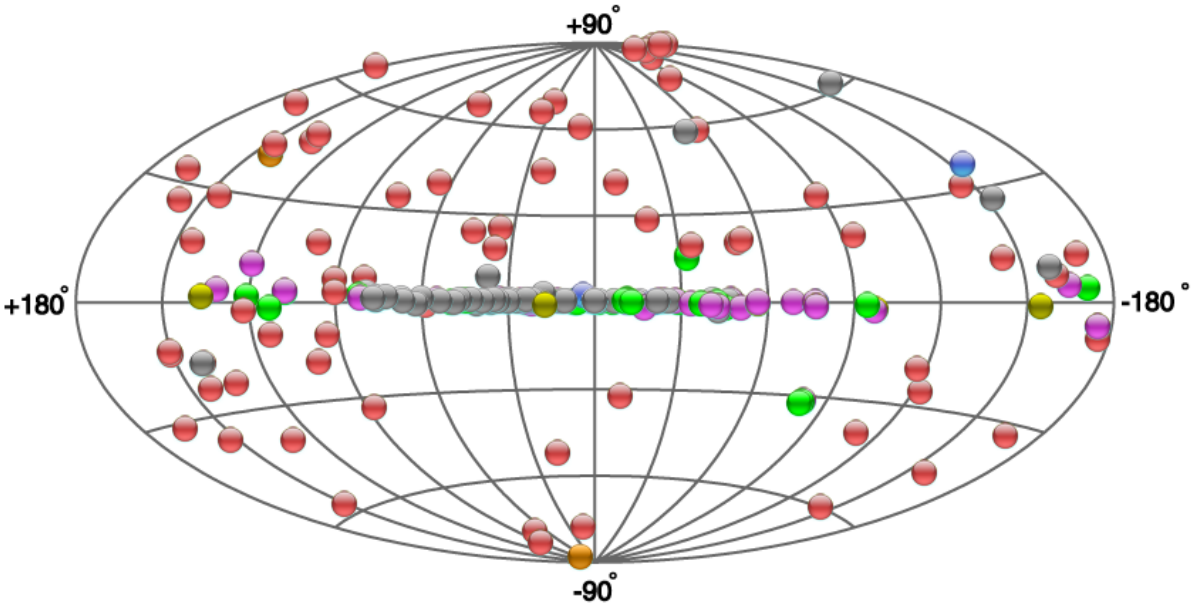

Figure 3.5: *Sky map in galactic coordinates showing the sources available in TeVCat [58]. The purple points are Pulsar Wind Nebulae (PWNe), orange are starbursts, red are blazars, blue are globular clusters, green are Supernova Remnant (SRN), yellow are binary and grey are unidentified sources. Some code colors represents many types of similar sources. To detailed color classification visit the webpage http://tevcat.uchicago.edu/.*

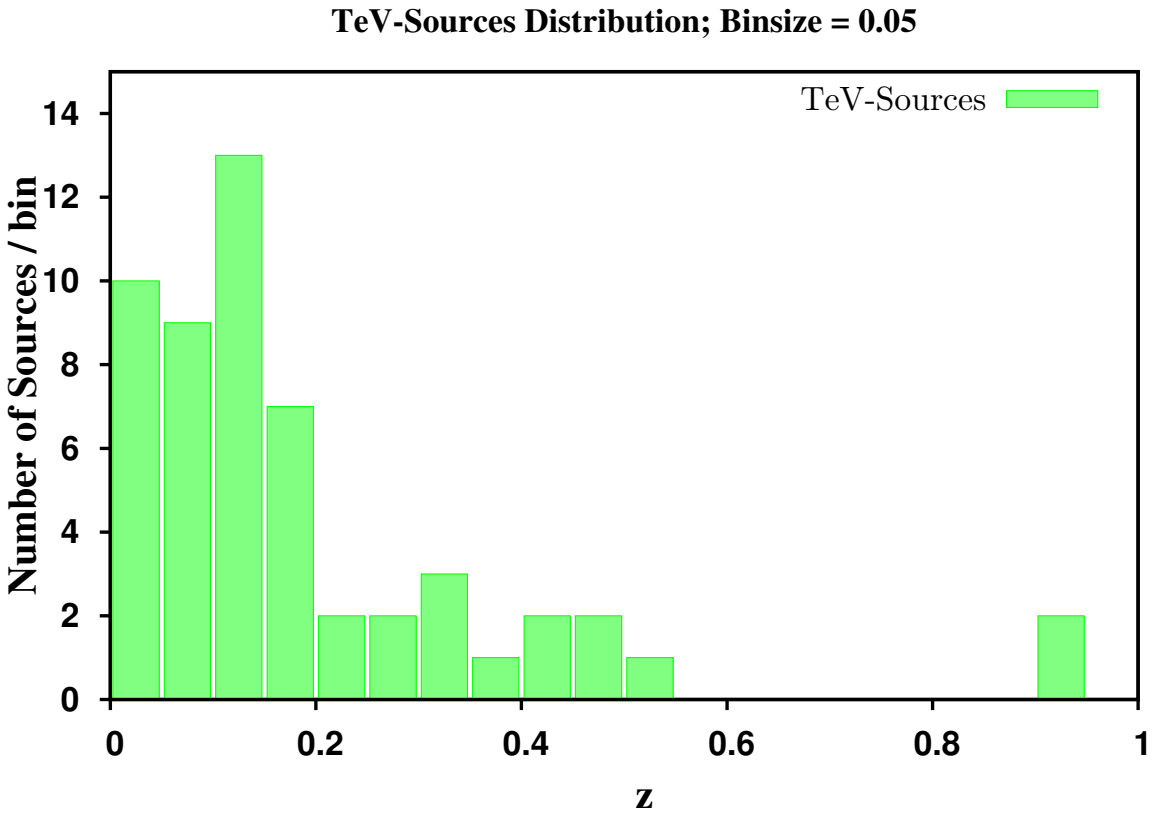

Figure 3.6: *Distribution in redshift of extragalactic sources from TeVCat [58].*

3.2 Gamma-ray Luminosity Function

There is an intense effort to describe how blazars are distributed in terms of their luminosities and how they evolved in time. As the number of observed blazars increases, different approaches are being used. In order to study the cosmic gamma-ray background, Narumoto and Totani [59] used data from EGRET to determine the gamma-ray luminosity function (GLF) based on a correlation between radio and X-rays bands with the gamma-ray luminosities. Similarly, Inoue and Totani [60] built a GLF from X-ray luminosity functions (XLF) relating the bolometric luminosity from the jet with its disc X-ray emission. Without assuming correlations between different bands of the spectrum, M. Ajello et al. built a GLF to FSRQ [61] and BL Lac [62] using the first year data collected by Fermi-LAT. In [61] the authors firstly test a parameterization for the LF called pure luminosity evolution (PLE) model given by

$$\Phi(L_\gamma, z) = \Phi(L_\gamma / e(z)) \tag{3.1}$$

where the term $e(z)$ describes the evolution of the LF.

When this model is applied to the sample of FSRQ detected by LAT, although good fits for the redshift and luminosity distributions are obtained, it does not provide a good description of the distribution of source counts. In this model the luminosity evolution $e(z)$ has a peak at a specific redshift z_c which is luminosity independent. In order to test if there is some luminosity dependence on z_c, two subsamples were considered, splitting the initial set of sources in low- and high-luminosity samples. Performing the fits the authors found different redshift peaks to each set of sources, evincing some luminosity dependece on z_c. Therefore, since the PLE model does not provide a good description of Fermi source counts and apparently the redshift peak evolves with the luminosity, a luminosity-dependent density evolution (LDDE) was proposed. In this model we can write the GLF as

$$\Phi(L_\gamma, z, \Gamma) = \Phi(L_\gamma, z = 0, \Gamma) \times e(z, L_\gamma), \tag{3.2}$$

where at redshift $z = 0$ we have $\Phi(L_\gamma, z = 0, \Gamma)$ given by the parameterization

$$\Phi(L_\gamma, z = 0, \Gamma) = \frac{A}{\ln(10) L_\gamma} \left[\left(\frac{L_\gamma}{L_*} \right)^{\gamma_1} + \left(\frac{L_\gamma}{L_*} \right)^{\gamma_2} \right]^{-1} e^{-0.5[\Gamma - \mu(L_\gamma)]^2/\sigma^2}, \tag{3.3}$$

where L_γ is the rest-frame gamma-ray luminosity at 0.1-100 GeV in units of erg s^{-1} and Γ is the photon index of the source. The photon index, which is the exponent of the power-law used to model the intrinsic flux of Fermi-LAT sources, is assumed to be distributed as a Gaussian function and μ and σ are its mean and dispersion, respectively. The mean μ is allowed to vary with luminosity as

$$\mu(L_\gamma) = \mu^* + \beta[\log(L_\gamma) - 46]. \tag{3.4}$$

The term which gives us how the GLF evolves is written as a double power law

$$e(z, L_\gamma) = \left[\left(\frac{1+z}{1+z_c(L_\gamma)} \right)^{-p_1(L_\gamma)} + \left(\frac{1+z}{1+z_c(L_\gamma)} \right)^{-p_2(L_\gamma)} \right]^{-1}, \tag{3.5}$$

and as we can see, it depends on the redshift peak z_c. Now, this redshift is a function on L_γ given by

$$z_c(L_\gamma) = z_c^*(L_\gamma/10^{48})^\alpha. \tag{3.6}$$

The parameters p_1 and p_2 in equation 3.5 are also allowed to depend on L_γ as

$$p_1(L_\gamma) = p_1^* + \tau(\log(L_\gamma) - 46), \tag{3.7a}$$

$$p_2(L_\gamma) = p_2^* + \delta(\log(L_\gamma) - 46). \tag{3.7b}$$

The definitions in equation 3.7 are written in a general way, but here we will use the results obtained in [61, 62], so $\delta = 0$ which implies $p_2 = p_2^*$. In order to determine the parameters of the model, a maximum likelihood procedure was performed over the Fermi-LAT data in the (L_γ, z, Γ) space. Table 3.1 shows the values for each parameter.

source	A [Gpc^{-3}]	γ_1	γ_2	L_* [erg/s]	p_1^*	p_2^*	τ	z_c^*	α	μ^*	β	σ
BL Lac	3.39	0.27	1.86	$10^{47.4472}$	2.24	-7.37	4.92	1.34	0.0453	2.10	0.0646	0.26
FSRQ	3.06	0.21	1.58	$10^{47.9243}$	7.35	-6.51	0.0	1.47	0.21	2.44	0.0	0.18

Table 3.1: *Parameters of LDDE model to gamma-ray luminosity function for FSRQ and BL Lac objects obtained in [61, 62].*

The data used are distributed between the following values, which are used as integration limits: For BL Lacs $z_{min} = 0.03$, $z_{max} = 6$, $L_{\gamma,min} = 7 \times 10^{43}$ erg s^{-1}, $L_{\gamma,max} = 10^{52}$ erg s^{-1}, $\Gamma_{min} = 1.45$ and $\Gamma_{max} = 2.80$, while for FSRQ were used $z_{min} = 0$, $z_{max} = 6$, $L_{\gamma,min} = 10^{44}$ erg s^{-1}, $L_{\gamma,max} = 10^{52}$ erg s^{-1}, $\Gamma_{min} = 1.8$ and $\Gamma_{max} = 3.0$. The number of sources expected in this limits can be obtained from

$$N = \int_{z_{min}}^{z_{max}} \int_{L_{min}}^{L_{max}} \int_{\Gamma_{min}}^{\Gamma_{max}} \Phi(L_\gamma, z, \Gamma) \frac{dV_c}{dz} d\Gamma dL_\gamma dz, \tag{3.8}$$

where the comoving volume per unit redshift is given by

$$\frac{dV_c}{dz} = D_H \frac{(1+z)^2 D_A^2}{E(z)} d\Omega \tag{3.9}$$

where $D_H = c/H_0$ is the Hubble distance, $E(z) = \sqrt{\Omega_M(1+z)^3 + \Omega(1+z)^2 + \Omega}$ and $D_A = \frac{D_H}{(1+z)} \int_0^z \frac{dz'}{E(z')}$ [63].

The distributions of the sources in redshift, luminosity and photon index can be calculated through appropriate marginalization over two parameter space variables

$$\frac{dN}{dz} = \int_{L_{min}}^{L_{max}} \int_{\Gamma_{min}}^{\Gamma_{max}} \Phi(L_\gamma, z, \Gamma) \frac{dV_c}{dz} d\Gamma dL_\gamma, \tag{3.10a}$$

$$\frac{dN}{dL_\gamma} = \int_{z_{min}}^{z_{max}} \int_{\Gamma_{min}}^{\Gamma_{max}} \Phi(L_\gamma, z, \Gamma) \frac{dV_c}{dz} d\Gamma dz, \tag{3.10b}$$

$$\frac{dN}{d\Gamma} = \int_{L_{min}}^{L_{max}} \int_{z_{min}}^{z_{max}} \Phi(L_\gamma, z, \Gamma) \frac{dV_c}{dz} dz dL_\gamma. \tag{3.10c}$$

Using equation 3.8 for BL Lacs we get 8033 sources and for FSRQ we obtain 1138, values similar to those found in [64] (8019 for BL Lacs and 1167 for FSRQ), where the authors use these GLF models to study the diffuse astrophysical neutrino emission. Figure 3.7 shows the redshift, luminosity and photon spectral index distribution for blazars. The column on the left side shows the distribution for the BL Lac population, while the right side displays the FSRQ one. These gamma-ray luminosity functions will be of particular interest in studies related to the performance of future observatories, such as CTA. An analysis involving the potential of CTA in detecting blazars and constraining EBL parameters will be described in Chapter 5 and the GLF will play an important role throughout the simulation process.

3.3 Interaction between EBL and gamma-rays

Gamma-rays coming from distant sources, such as GRBs and AGNs, can interact with low energy photons of the EBL during their travel through the universe, in a process that can be represented by

$$\gamma_{EBL} + \gamma \rightarrow e^+ + e^-. \tag{3.11}$$

The interaction creates an electron-positron pair, imparting some level of opacity to the extragalactic medium to gamma-rays. According to quantum electrodynamics (QED) the lowest order contribution in perturbation theory for this process is described by the Feynman diagram shown in figure (3.8). In order to be kinematically allowed, the energy of the photons must obey the condition

$$E' E'_\gamma (1 - \mu) \geq 2(m_e c^2)^2, \tag{3.12}$$

where E' and E'_γ are the EBL and gamma-ray photon energies, respectively. The prime in both energies means that they must be calculated in the center of mass of the collision. The energy evolution of a photon due the expansion of the universe is given by the relation $E' = E(1 + z')$, where z' is the redshift, m_e is the electron rest mass, c the speed of light

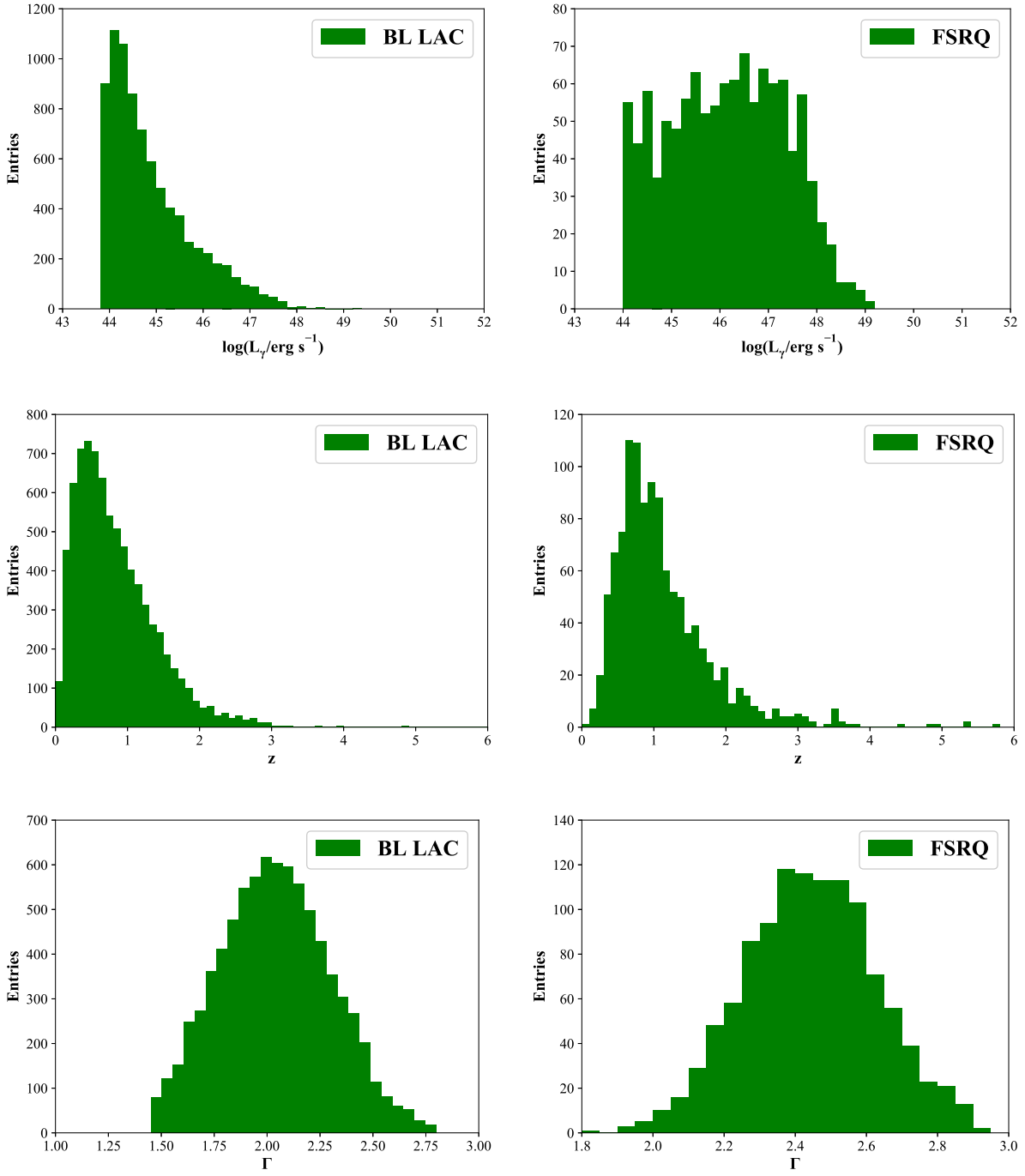

Figure 3.7: *Left: BL Lacs expected gamma-ray luminosity, redshift and photon index distributions for a LDDE GLF model (see text). Top: gamma-ray luminosity. Middle: redshift. Bottom: spectral index distribution. Right: the same distributions on the left side, but for FSQR population.*

in vacuum and $\mu = \cos\theta$, where θ is the angle between the photons momenta in the lab frame.

In 1967, Gould and Schréder [65] developed the approach described here to calculate the universe's opacity to gamma-rays and since then several works followed this method,

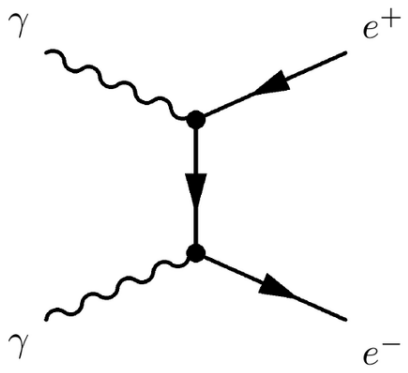

Figure 3.8: *The Feynman diagram of the lowest order contribution for the electron-positron pair creation.*

such as [26, 30, 66–68]. If condition (3.12) is satisfied, we can calculate the cross section

$$\sigma(E', E'_\gamma, \mu) = \frac{3}{16}\sigma_T(1-\beta^2)\left[2\beta(\beta^2-2) + (3-\beta^4)\ln\left(\frac{1+\beta}{1-\beta}\right)\right] \tag{3.13}$$

where σ_T [3] is the Thomson cross section and

$$\beta = \sqrt{1 - \frac{2m_e^2c^4}{E'E'_\gamma(1-\mu)}}. \tag{3.14}$$

Figures 3.9 and 3.10 display the behavior of the cross section of Eq. 3.13 in terms of β and for a few collision angles θ, respectively. When $\beta \to 0$ the photons are very close to the condition for electron-positron pair creation and, as we can see in figure 3.9, in this regime there is a low probability of interaction. The probability increases until it reaches a maximum at $\beta \sim 0.7$. In the limit $\beta \to 1$, the interaction probability also tends to zero. The cross section of this process depends also on the collision angle between the gamma-ray and the EBL photon. This dependence is presented in figure 3.10. In a frontal collision, $\theta = 180°$, $\sigma_{\gamma\gamma}$ is such that a broad range of photon-photon energy combinations can lead to the creation of an e^+/e^- pair. When $\theta = 0$, the photons are in the same direction of propagation and the process cannot occur.

The optical depth τ of the medium between the observer and the gamma-ray source can be obtained integrating the reciprocal of the mean free path λ^{-1} along the line-of-sight. We have that $\lambda^{-1} = \int \sigma dn$, where dn is the differential photon number density of the medium. As done by Gould and Schréder [65], one treats the EBL as an isotropic photon gas. The fraction of the EBL photons considered in the collisions are moving in the differential cone defined by θ and $\theta + d\theta$. For photons with energy E' we have

[3] $\sigma_T = 6.6524 \times 10^{-29}$ m^2

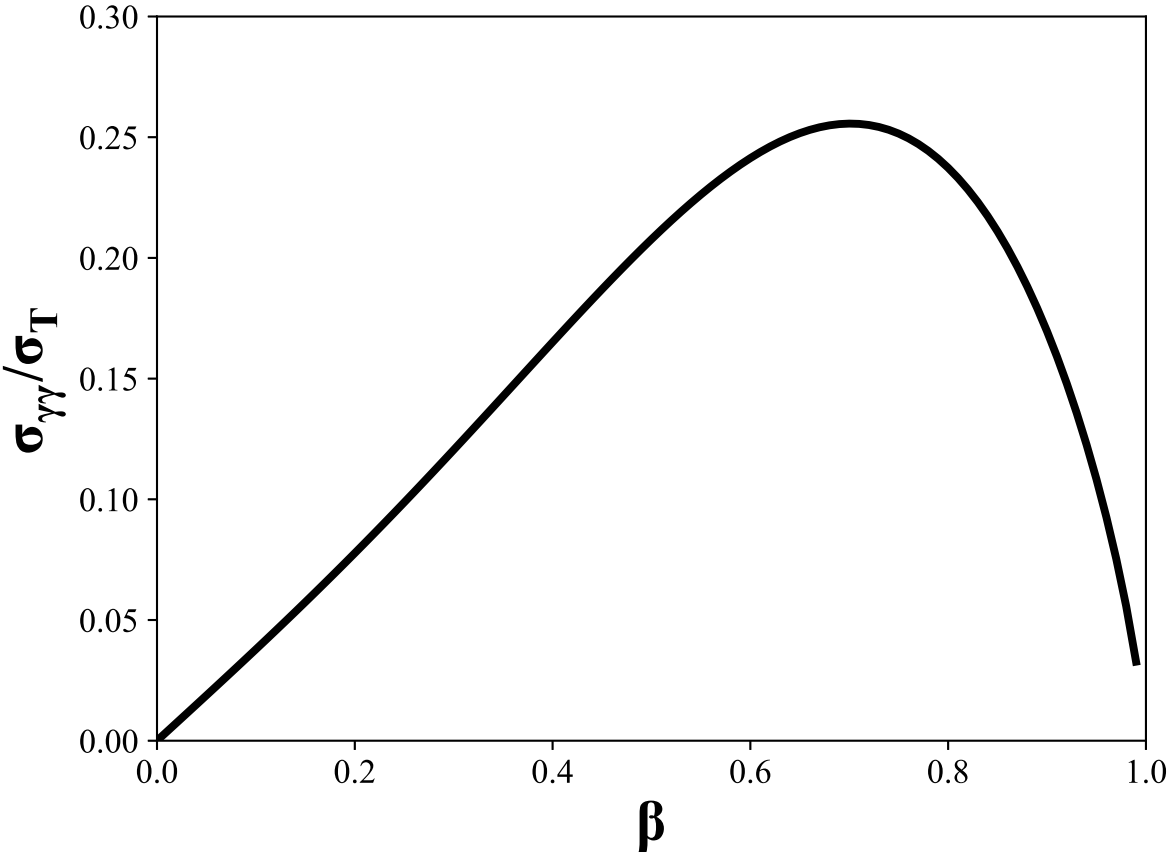

Figure 3.9: *Cross section for the e^-/e^+ pair creation as a function on β, defined in Eq. 3.14, in units of σ_T.*

$dn = \frac{1}{2}n(E', z)\sin\theta d\theta dE'$. Therefore, for the optical depth can be written as

$$\tau_{\gamma\gamma}(E_\gamma, z) = c\int_0^z \frac{dt'}{dz'}dz' \int_{-1}^{+1} \frac{(1-\mu)}{2}d\mu \int_{E'_{min}}^{\infty} \sigma(E', E'_\gamma, \mu)n(E', z)dE' \tag{3.15}$$

where $E'_{min} = \frac{2m_e c^2}{E'_\gamma(1-\mu)}$ is the minimum energy allowing the pair creation.

Figure 3.11 shows the mean free path generated by the CMB and EBL backgrounds at $z = 0$. As we can see, the pair creation process for gamma-rays with TeV energies is dominated by the EBL, while for PeV photons the CMB becomes the main contribution. Therefore, for our studies the CMB attenuation effect can be ignored, since the sensitivity of the current IACT allows to measure photons with energies up to tens of TeVs. It is worth noting that for PeV photons the mean free path is of the order of ~ 10 kpc. Since the radius of the Milky Way is of this order of magnitude, around PeV energies one expects only galactic sources and its nearby satellites to contribute to the flux measured at Earth.

The optical depth is a fundamental quantity to reconstruct the intrinsic spectrum of distant sources. The flux of gamma-ray emitters should obey a radiative transfer equation [73, 74] for the absorption-only case

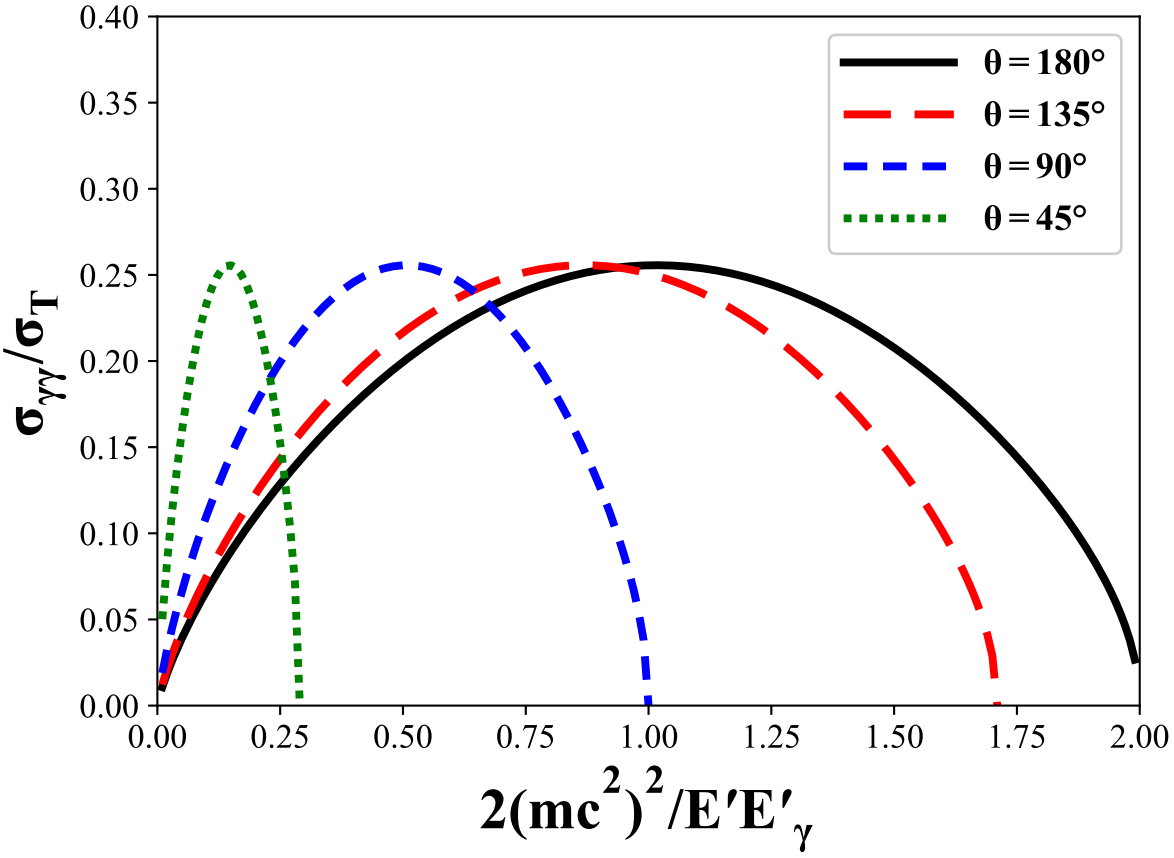

Figure 3.10: *Cross section for the e^-/e^+ pair creation as function on $2(mc^2)^2/E'E'_\gamma$, in units of σ_T, for several angles of collision.*

$$\frac{d\Phi}{ds} = -\alpha\,\Phi, \tag{3.16}$$

where $d\tau \equiv \alpha\, ds$ and s is the distance coordinate along the line-of-sight. So, the solution of the radiative transfer equation for a opaque medium gives us the relation between intrinsic ($\Phi(E)$) and observed ($\Phi_0(E)$) fluxes

$$\Phi(E) = e^{-\tau_{\gamma\gamma}}\Phi_0(E). \tag{3.17}$$

A first approximation to the intrinsic spectrum of AGNs at very high energies is given by a power-law model with spectral index ~ 2.5. In figure 3.12 we can see the intrinsic and attenuated spectrum of a hypothetical source with $\Gamma = 2.5$ and located at three different redshifts: 0.1, 0.3 and 0.5. For comparison, the convolution of the intrinsic spectrum was performed for two of the EBL models presented in Chapter 2, Helgason's and F10. As we can see, up to $\sim$ 100 GeV the attenuation effect is negligible independent of the redshift of the source, for both models. From 100 GeV the opacity caused by EBL becomes more and more important as energy increases. Here it is also possible to visualize the limitation of the Helgason model, with the red curves stopping before the blue ones, since for very

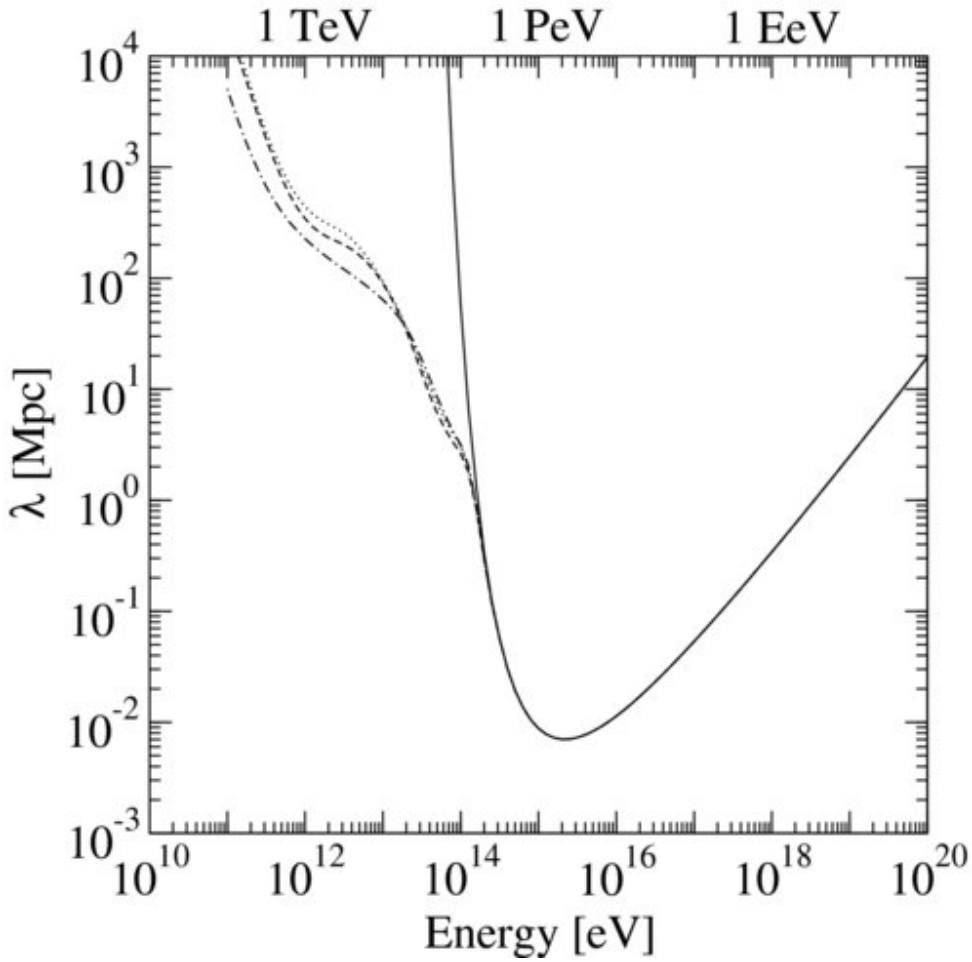

Figure 3.11: *The mean free path to the pair creation process for gamma-rays through the photon background at redshift $z = 0$. Solid line: CMB background. Dotted line: CMB plus EBL model from Gilmore [69]. Dot-dashed line: CMB and EBL model from Stecker et al. [70]. Dashed line: CMB and EBL model from Kneiske [71]. Figure extracted from [72].*

high energies the dust component of the EBL becomes important and such a model does not take it into account. On the other hand, the F10 model allows us to calculate the attenuated spectrum up to very high energies, essential for sources detected by IACTs.

For $\tau \sim 0$ equation (3.17) suggests that the intrinsic and observed spectra are essentially the same. However, for $\tau > 1$ the attenuation factor becomes significant, therefore it is usual to define the cosmic gamma-ray horizon (CGRH) which is the energy E_γ such that $\tau(E_\gamma, z) = 1$, where z is the redshift of the gamma-ray source.

Using Helgason's model we build the heat map of figure 3.13 showing the predicted color-coded optical depth in the $E_\gamma \times z$ plane and the curve relative to the CGRH. The limitation due to the lack of the dust component can again be seen at high energies, where the model is unable to predict the value of τ. F10 model [29] does not present this problem, since it calculates the EBL energy density for the whole relevant range of the spectrum. This is very important in the analysis which will be proposed in the next chapters, since the current available sample of gamma-ray sources is already quite limited.

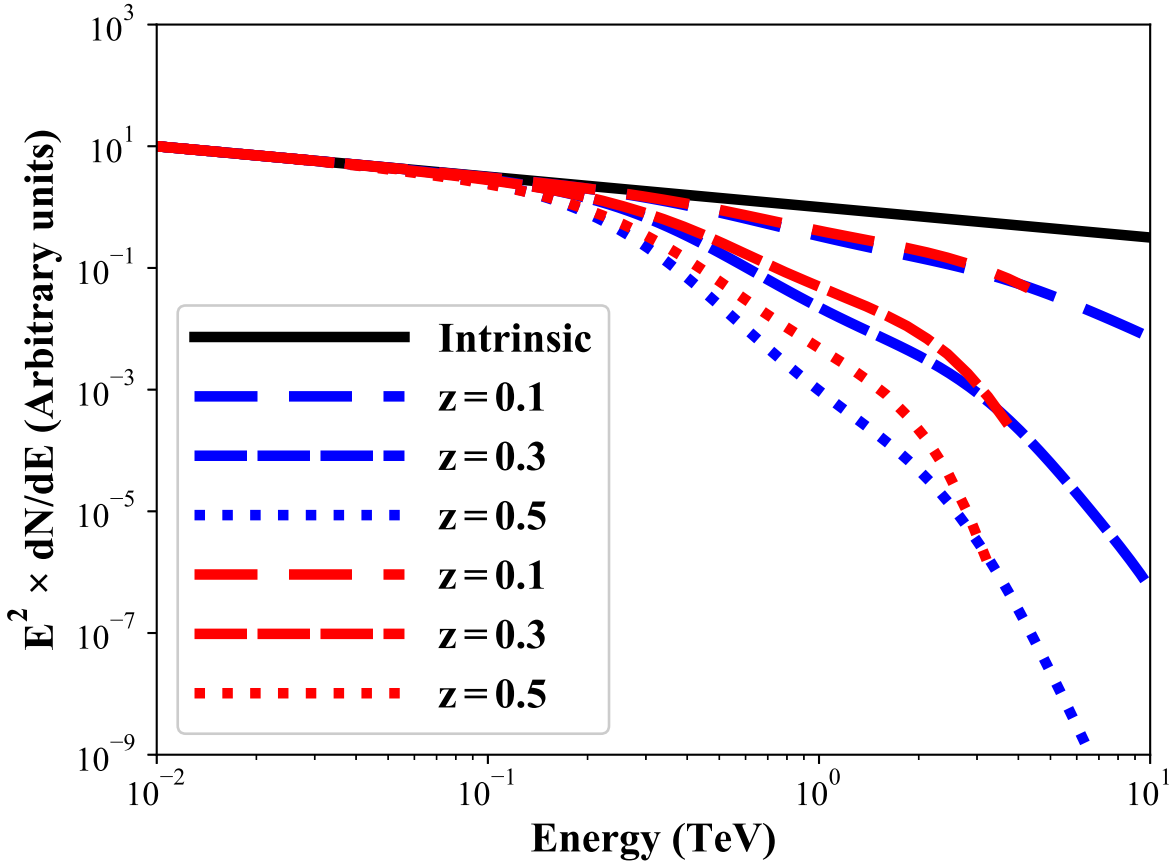

Figure 3.12: *Spectrum of a hypothetical source following a power-law intrinsic behavior with* $\Gamma = 2.5$. *Two EBL models were utilized to describe the opacity to the gamma-rays, the Helgason (red curves) and the F10 (blue curves) models. The three different line styles correspond each one to a different redshift of the source, as indicated in the inset.*

Figure 3.14 shows the optical depth from the F10 model in the plane $E_\gamma \times z$.

3.3.1 Gamma-ray detection and EBL constraints

With the advances in VHE gamma-ray detection by telescopes on-board satellites, such as Fermi-LAT, and ground-based facilities, represented by IACTs, the opacity of the universe to gamma-rays could be deeply investigated. An important step related to these investigations was given in 2006, when the IACT MAGIC detected a flare state of the FSRQ called 3C 279 [16]. This source is located at $z = 0.536$, which corresponds to a distance of more than 5 billion light-years. In this observation, MAGIC measured fluxes for photons with energies up to ~ 500 GeV. Before this detection, the most distant VHE gamma-ray source detected was 1ES 1011+496 with $z = 0.212$. For this source the level of attenuation expected is so high that it could be used to impose constraints on EBL. The authors used two EBL models to define the uncertainty on the EBL density: Primack et al. [75], which are close to the galaxy count, as the lower limit and the "fast-evolution" model from Stecker et al. [70], as the upper limit. The CGRHs from these two models

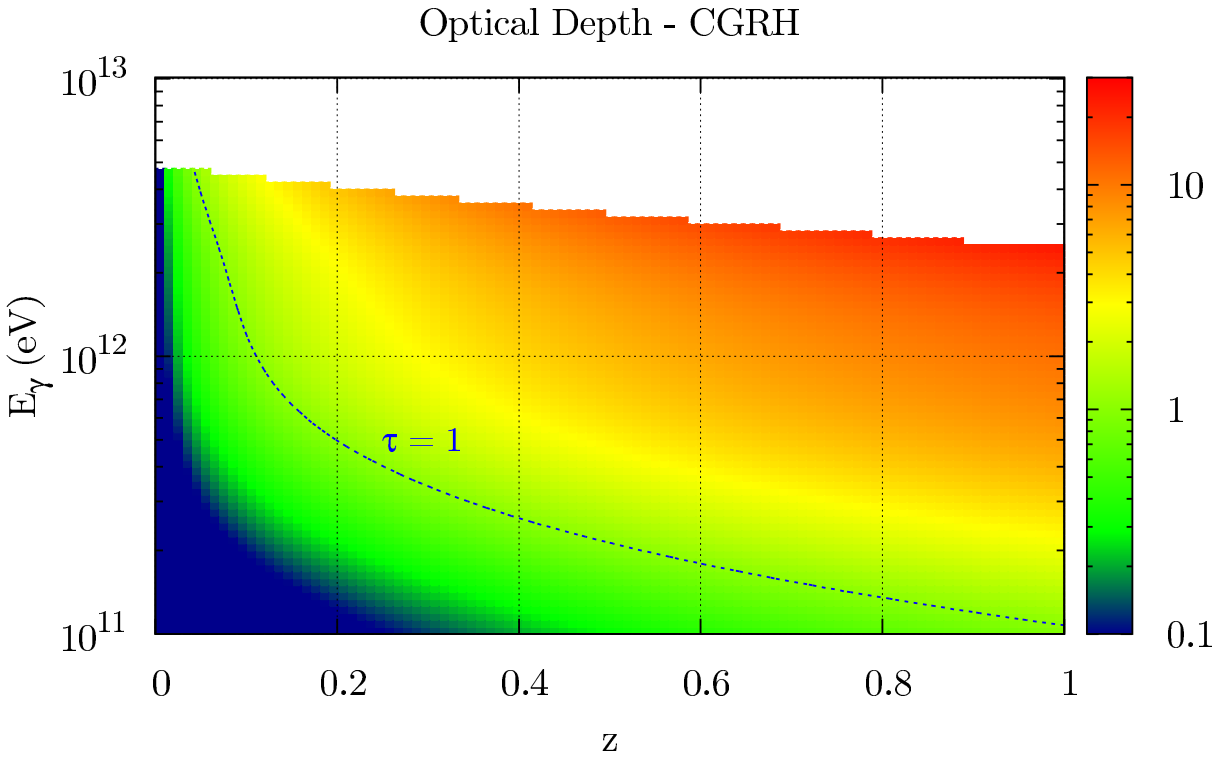

Figure 3.13: *Color map representing the optical depth to the Helgason's model [30]. The dashed line is the CGRH. This model does not make predictions at high energies.*

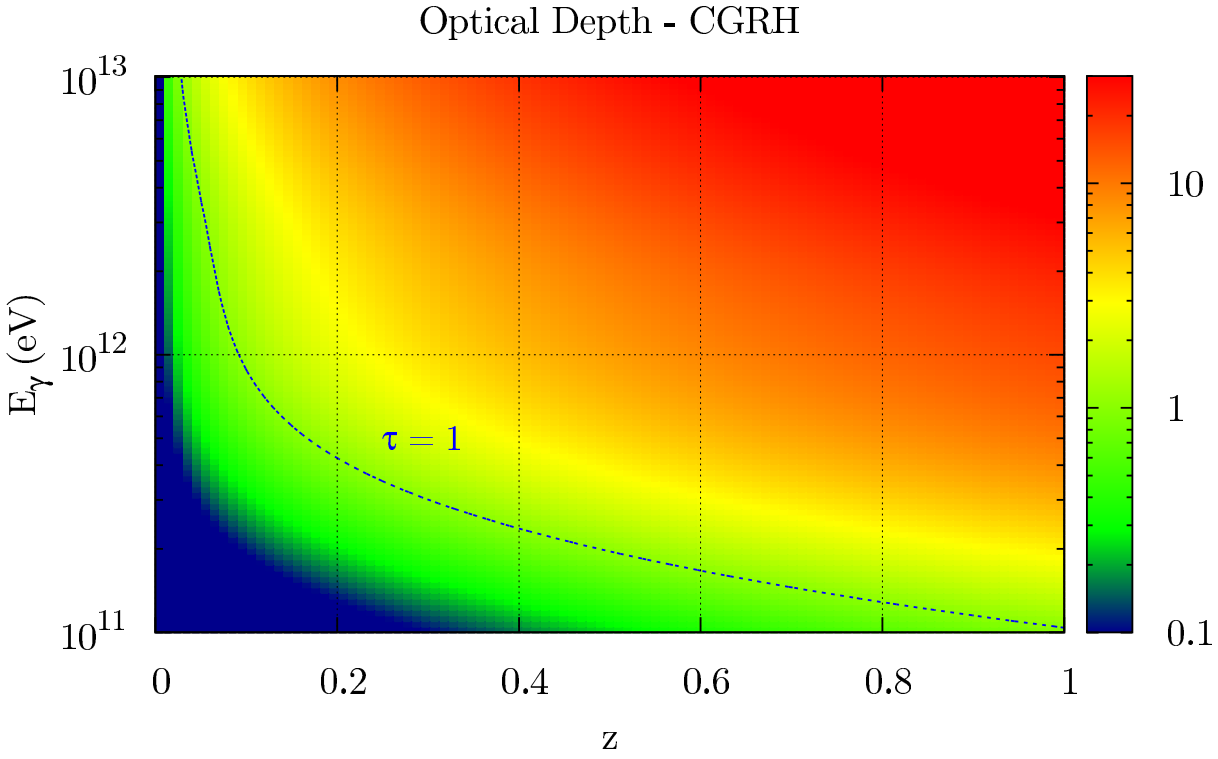

Figure 3.14: *Color map representing the optical depth from the F10 model [29]. The dashed line is the CGRH.*

define an uncertainty region on $E \times z$ space, as we can see in figure 3.15. Based on data of VHE sources not affected by EBL, the lower spectral index measured was $\Gamma = 1.5$,

representing the hardest intrinsic index. In order to get a maximum EBL density, the hardest intrinsic spectrum was assumed for 3C 279 and the EBL model from [27] was tuned in order to get the observed spectrum by MAGIC. The CGRH obtained from this procedure is shown in figure 3.15 in blue dashed line and defines a new upper limit to EBL models. Using other sources located at different redshifts we can see that almost all of them are consistent with the limit found.

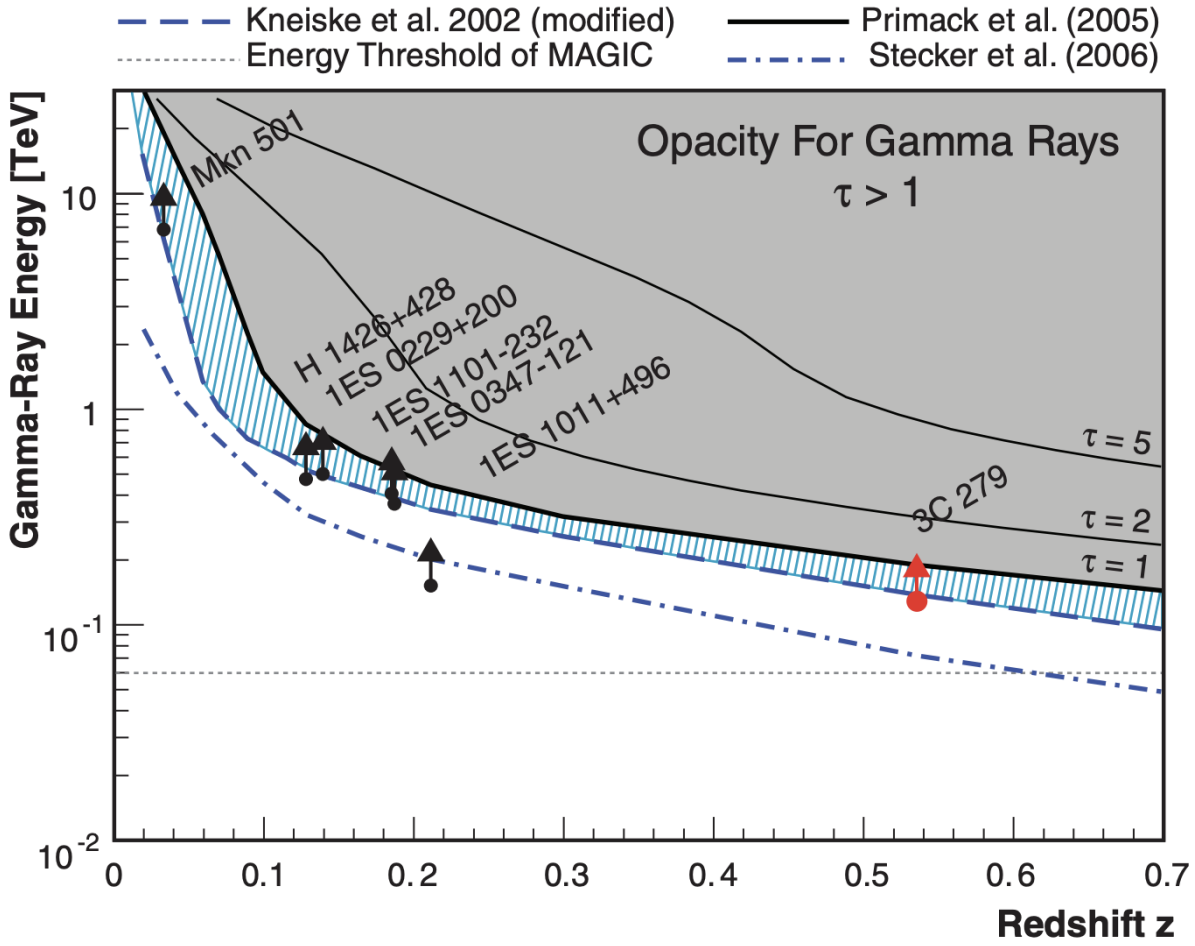

Figure 3.15: *Cosmic gamma-ray horizon from models considered as limit cases (see text) to the EBL levels. The arrows correspond to upper limits coming from gamma-ray sources. The narrow blue region defines the band between the minimum transparency described by [75] and the maximum EBL level coming the modified EBL model [27] based on hardest spectral index assumed to 2C 279. Dashed-dotted blue line is the CGRH based on Stecker et al. "fast evolution" model [70] and gives us a high level of opacity which is discarded by this analisys. Figure extracted from [16].*

Another remarkable EBL investigation coming from gamma-ray observations was done by Ackermman et al. [17] searching for an EBL imprint in a sample of blazar spectra observed by Fermi-LAT. With a set of 150 BL Lac spectra detected with high statistical significance above 3 GeV and located at redshifts ranging from 0.03 to 1.6, the authors were able to assess the unattenuated part of blazar spectra, representing the intrinsic behaviors of these sources and the attenuated one, where features of the EBL opacity are

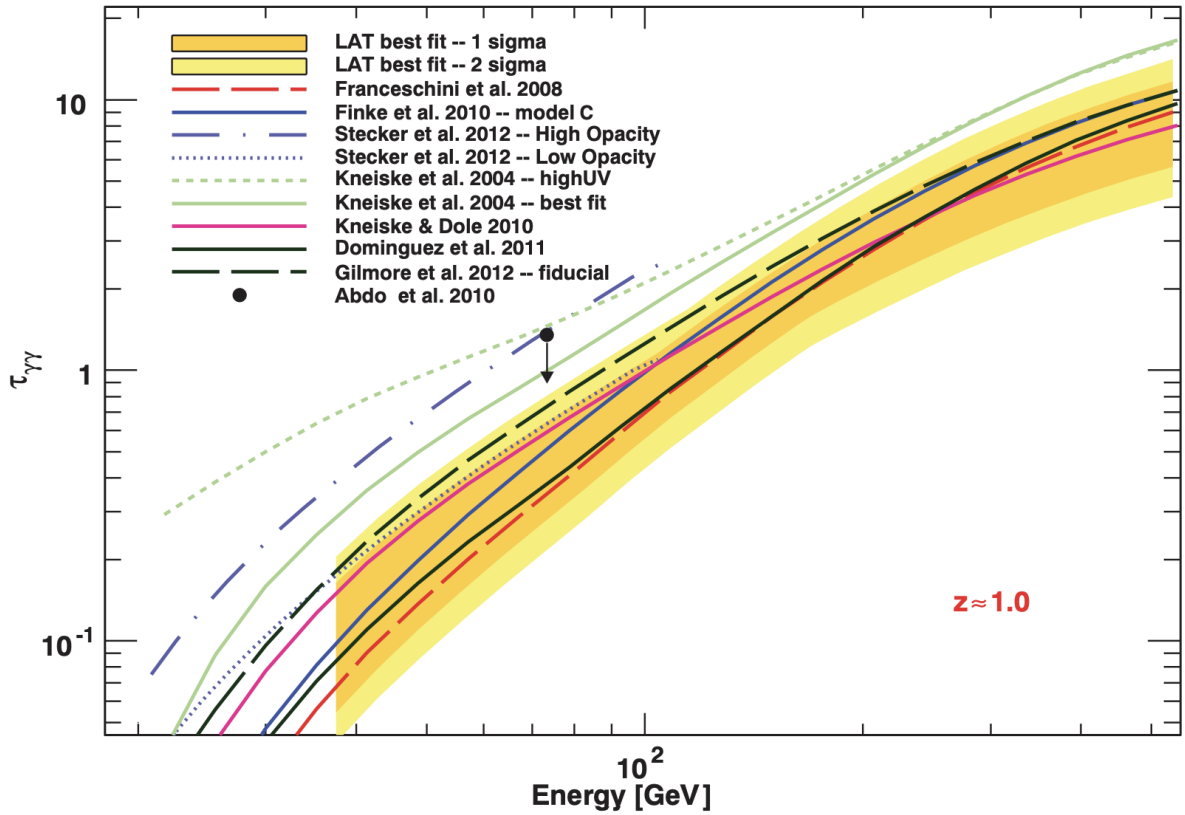

Figure 3.16: *Optical depth as a function on energy for $z \sim 1.0$. The 1- and 2-sigma confidence levels found by Fermi-LAT observation is shown with EBL models prediction superimposed. The downward arrow is the 95% upper limit found by [56] for $z - 1.05$. Figure extracted from [17].*

expected to be found. Extrapolating the intrinsic behavior up to high energies and taking into account the EBL attenuation factor, $e^{-\tau_{\gamma\gamma}}$, the Fermi data could be fitted in order to assess the attenuation signal. A likelihood maximization procedure was performed with $\tau_{\gamma\gamma}(E,z) = b\,\tau_{\gamma\gamma}^{\rm model}(E,z)$, where b was left free to fit the data and $\tau_{\gamma\gamma}^{\rm model}(E,z)$ are based on EBL models analyzed. When $b \sim 1$ we have a indicative that the data contain attenuation signal, while for $b \sim 0$ no attenuation is expected in the data. Actually, a characteristic attenuation was found in this sample and it was correctly described by all models in which the EBL density is consistent with the lower limits imposed by resolved galaxy counts, such as Domínguez's and F10 model among others considered by the authors. Models with high levels of EBL, mainly at the UV band, which is the responsible for attenuation at this energies and redshifts, such as [76] and [70], are incompatible with the signal found by the Fermi-LAT observations. Figure 3.16 shows the 1- and 2-sigma regions for the optical depth obtained from Fermi data and the curves of τ for many different EBL models.

In 2015, the Fermi-LAT colaboration released the Second Catalog of Hard Fermi-LAT sources (2FHL) [18], which contains sources detected with energies above 50 GeV. In this catalog some sources are located at very high redshifts, $z > 1.0$, enhancing the capability

to probe EBL attenuation. Figure 3.17 shows a clear dependence of the observed spectral index with redshift for different energy ranges. The 3LAC catalog ranges from 0.1 GeV to 100 GeV and 1FHL between 10 GeV and 500 GeV, while 2FHL extends from 50 GeV to 2 TeV. The increase of the observed index with redshift for high energies is a typical behavior of EBL attenuation. Figure 3.18 shows the CGRH for three different models, [20], [29] and [23]. The plot also shows the highest photon energy of sources from 2FHL. The majority of the photons are below of CGRH with a few cases near the horizon or above. The reader must bear in mind that the CGRH is not a limit impossible to be crossed by gamma-rays, but defines a frontier in the 2D space $E \times z$ from which the photon flux should be strongly suppressed by pair creation processes since the attenuation factor drops exponentially with τ. It is worth remembering that Domínguez and F10 models were treated in details in chapter 2, and as we could see, the EBL levels of these models are very close to the lower limits from source counts at UV/optical, which are the energy domains responsible for interaction with these Fermi-LAT sources.

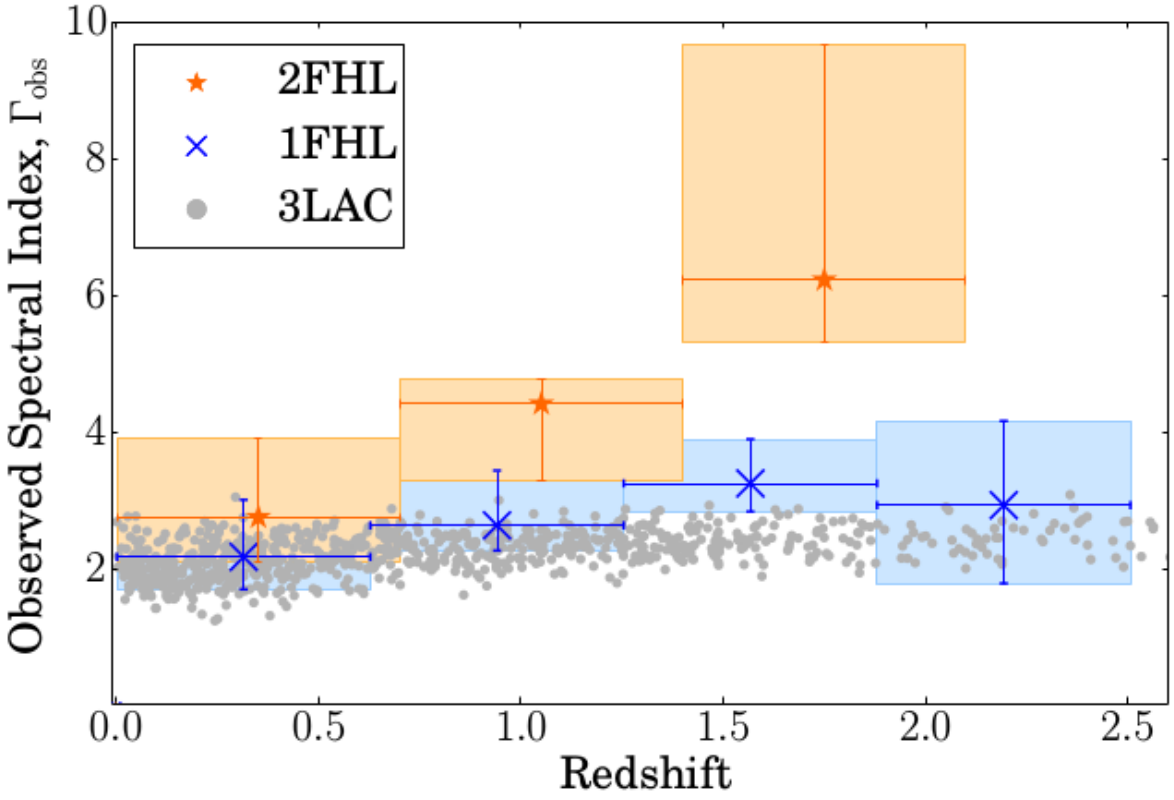

Figure 3.17: *Observed spectral index versus redshift for sources of three different catalogues: 3LAC, 1FHL and 2FHL. Figure extracted from [18].*

With the increase in the number of detections of extragalactic gamma-ray sources and the improvement of the telescopes dedicated to gamma-ray astronomy, one expects a corresponding decrease in the uncertainties on the EBL density. Upper limits coming from gamma-ray observations have been favoring models which are close to the resolved galaxy

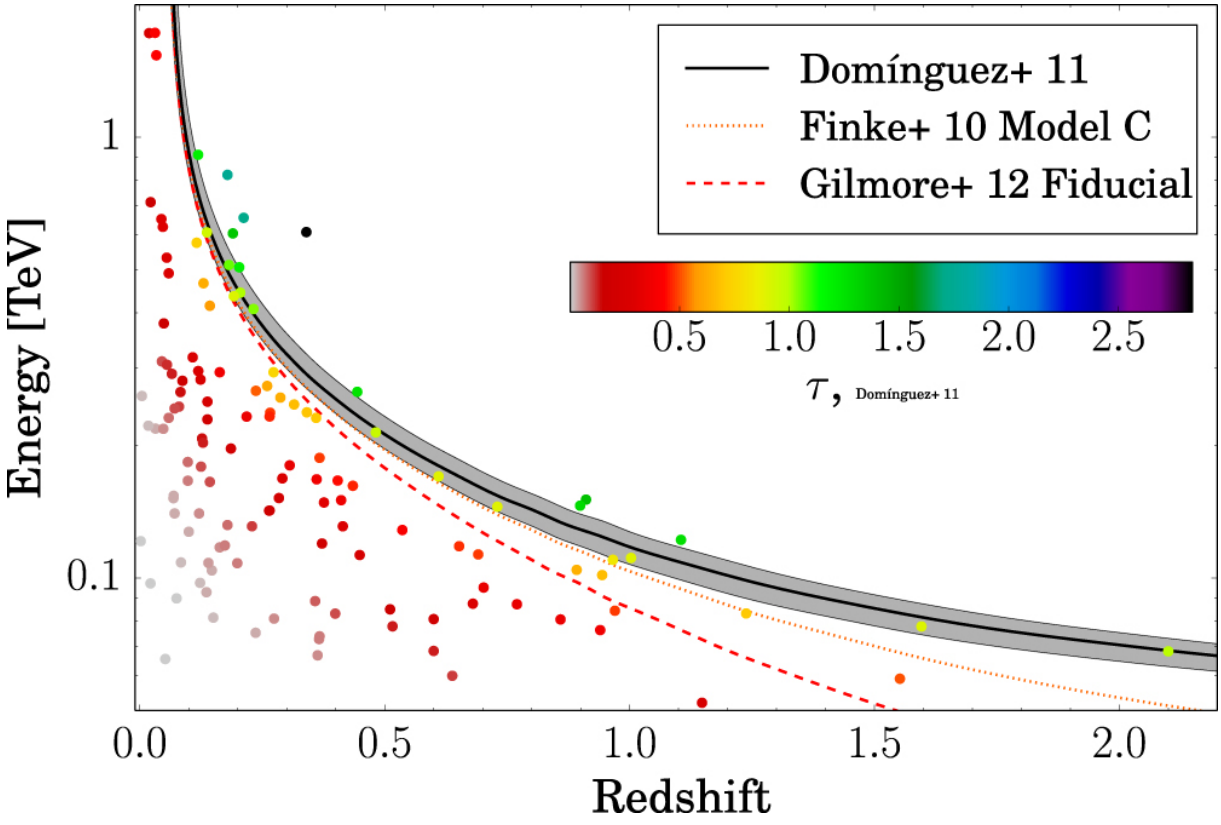

Figure 3.18: *Cosmic gamma-ray horizon for [20], [29] and [23] EBL models. Superimposed are the highest photon energy of sources from 2FHL. Figure extracted from [18].*

counts, indicating that the universe is more transparent than previous EBL descriptions predicted.

Chapter 4

Infrared emission from dust and spectral features of extragalactic gamma-ray sources

In this chapter the role of the EBL dust component in the attenuation of gamma-ray fluxes from extragalactic sources will be studied in more detail. Based on F10 model it was possible to explore separately each dust contribution in order to better understand the importance of them in the gamma-ray attenuation. The mid-IR emission is believed to dominate the attenuation of extragalactic fluxes up to around 10 TeV and the BL Lac Mkn 501 is particularly appropriate for this kind of study. Through the single source analysis adopted here it is already possible to see some sensitivity to dust parameters, giving rise to the possibility of constraining such quantities through well determined SEDs at TeV energies. Such a scenario is expected to be achieved with the start of CTA operation. The results presented in this chapter are based on those published in [77].

4.1 Markarian 501 exceptional flare

Most of the gamma-ray extragalactic sources observed nowadays have their spectra attenuated mainly by the direct starlight component of the EBL, however, some of them were observed around $\gtrsim 1$ TeV and in a redshift range in which the dust component plays an important role in the attenuation process. Mkn 501, a BL Lac located at $z = 0.034$, presented an exceptional flare in 1997, which made possible a precise determination of its SED at energies up to ~ 20 TeV by HEGRA [78]. Figure 4.1 shows the spectrum of Mkn 501 flare superimposed to the corresponding expected attenuation factor based on the optical depth from F10 model evincing each astrophysical contribution.

We can see the role played by each component across the SED. The starlight contribution to the opacity decreases slowly and steadily for energies above ~ 1 TeV, while

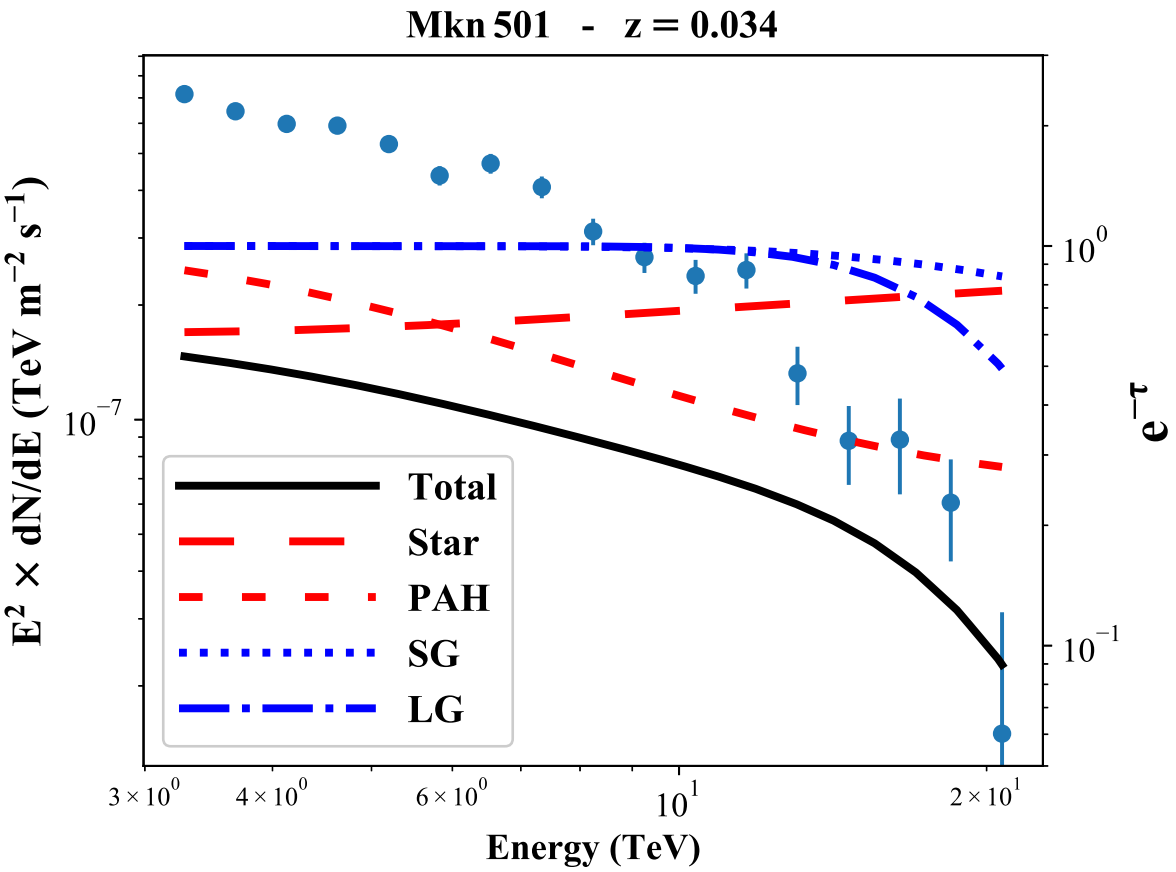

Figure 4.1: *Mkn 501 SED for the flare of in 1997. Also we plot the attenuation factor from the optical depth according to F10 model for a source located at $z = 0.034$ where the contribution from stars and individual dust components are also shown.*

the dust component increases monotonically up to $\sim$ 20 TeV. In special, we note the predominance of the PAH component between $10 \lesssim E \lesssim 20$ TeV. The large and small grains contributions are less significant, but increase fast above 10 TeV.

As we have seen in chapter 2, once the IMF and SFR are defined, the stellar contribution is totally determined. The photon escape fraction f_{esc} is based on the description of [79]. Model C was considered the best one in describing the UV/optical emissivity data, therefore, there is no free parameter in the stellar component. On the other hand, for the dust contribution, f_n and Θ_n still needs to be set. These parameters were chosen by F10 in such a way to approximately describe IR luminosity data at low redshifts. Here, we fit Mkn 501 SED allowing the dust relative contributions f_n as well as intrinsic parameters of the gamma-ray source to vary in order to study the potential of this kind of observation to constrain intrinsic spectra and EBL parameters. The temperatures Θ_n which characterize the Planck spectra of each dust component are kept fixed at the same values used by F10 (see table 2.1).

4.2 Intrinsic spectrum parameterization

For the intrinsic spectrum, three parameterizations will be used: a single power-law (PL), a log-parabola (LP) and a power-law with an exponential cutoff (PLC). Since this last function has an energy dependent curvature, it is more likely for a combined blazar spectrum+EBL fit to converge in this case to a solution where part of the flux drop at the high energy region of the measured SEDs is mimicked by the intrinsic source spectrum, instead of being created by EBL attenuation. Explicitly, we have

$$\Phi_0(E) = \begin{cases} N_0 \left(\frac{E}{E_0}\right)^{-\Gamma} & \text{(PL)} \\ N_0 \left(\frac{E}{E_0}\right)^{-a-b\log(E/E_0)} & \text{(LP)} \\ N_0 \left(\frac{E}{E_0}\right)^{-\Gamma} e^{-\left(\frac{E}{E_{\rm cut}}\right)} & \text{(PLC)} \end{cases} \tag{4.1}$$

where $E_0 = 1.0$ TeV is the reference energy which is kept fixed to minimize the correlations between the free parameters, N_0 is a flux normalization factor given in $\mathrm{TeV}^{-1}\ \mathrm{m}^{-2}\ \mathrm{s}^{-1}$ units, Γ is the spectral index of the power-law, a and b are, respectively, the spectral index and curvature for the log-parabola and $E_{\rm cut}$ is the energy cutoff for the power-law with an exponential cutoff.

Assuming gaussianity in the uncertainties of the Mkn 501 spectrum and a normalization condition for the dust fractions ($\sum_{n=1}^{3} f_n = 1$), we performed a χ^2 minimization to fit dust fractions and intrinsic parameters. Therefore, the fits have either 4 (PL) or 5 (LP and PLC) free parameters.

4.3 Fit results

As we can see in figure 4.2, all the three cases considered show values of f_n more than 3σ away from the fractions obtained in F10 model (henceforward, these values will be called as "nominal fractions"). It should be noted here that there is an important systematic uncertainty in the bestfit fractions due to the lack of knowledge on the exact intrinsic flux. In the PL case, for example, we note a larger contribution of PAH and small grains compared to the LP case which has an intrinsic curvature. Also, we call the attention to the somehow inverted hierarchy between small and large contributions. In general, it is believed that small grains should represent around 10% of the solid grains (small plus large) in the ISM [44]. In order to include this information in the analysis we also performed a minimization imposing an upper-bound on the mentioned fraction

$$\tilde{f}_{\rm sg} = \frac{f_{\rm sg}}{f_{\rm sg} + f_{\rm lg}} \leq 0.1. \tag{4.2}$$

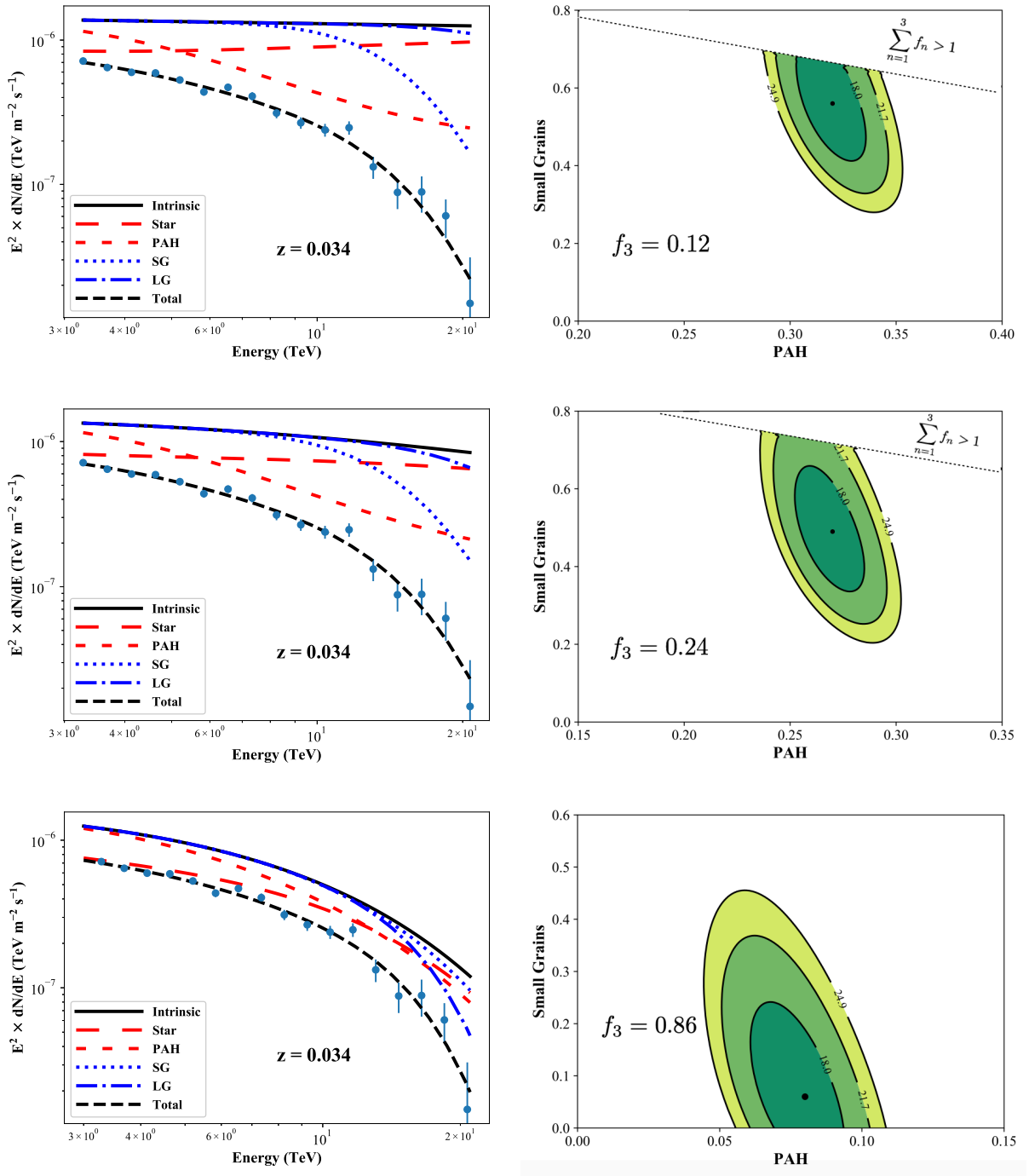

Figure 4.2: *Combined fits of the intrinsic spectrum and relative contributions of dust grains using Mkn 501 measured SED. Three different parameterizations are used for the intrinsic spectrum: power-law (top), log-parabola (middle) and power-law with an exponential cutoff (bottom). Left: measured SED superimposed to the convolution of the best-fit intrinsic spectrum with the attenuation factors of each EBL component, as well as the total attenuation. Right: χ^2 contours in the 2D space of dust parameters $f_{PAH} \times f_{SG}$ at confidence levels of 68%, 95% and 99%.*

These cases are included in tables 4.1 and 4.2. As we can see in the results obtained, the fits saturate the bound imposed on the the small fractions, in order to better describe

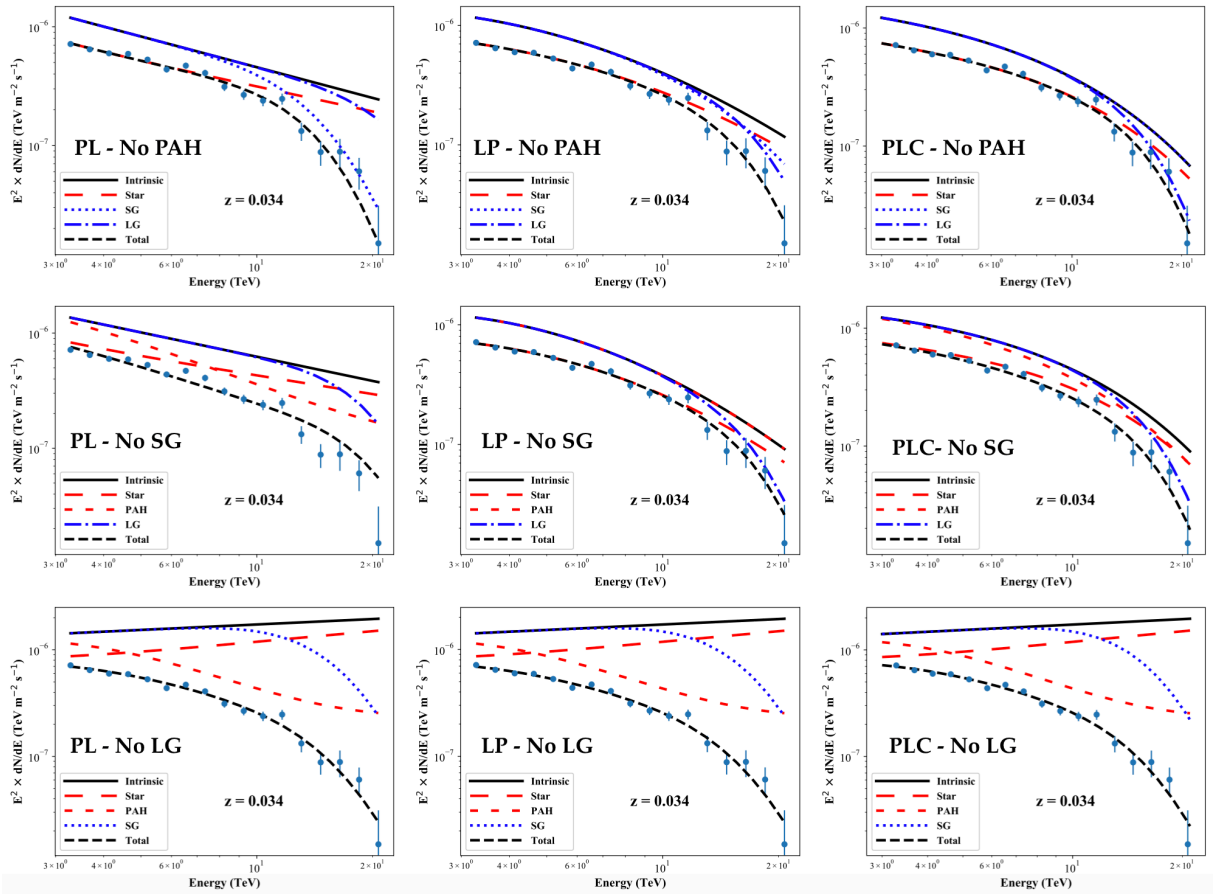

Figure 4.3: *Best fit curves superimposed to measurements for an effective 2-grain model. The intrinsic spectrum convoluted with the EBL attenuation factors of individual components is shown, as well as the total attenuation.*

the strong suppression at the end of the Mkn 501 spectrum. But in the case where the intrinsic spectrum lacks curvature, like the PL, the $\tilde{f}$-bounded fit is much worse than the unbounded case: $\chi^2/ndof = 37.6/13$ (bounded) against 15.7/13 (unbounded).

The left column in figure 4.2 shows the Mkn 501 SED and the intrinsic best-fit model convoluted with each EBL component and also the total attenuated spectrum. For the PL and LP models we can see that the different energy dependencies of small and large grains attenuation factors lead the fit to overestimate the small grains contribution compared to the large ones, in order to fit the tail of Mkn 501 SED. This does not occur for the PLC, for the strong curvature above the cutoff energy is enough to describe well the end of the spectrum. The importance of PAH molecules can be also appreciated, because it provides the correct attenuated spectral index in the region just below 10 TeV, which no other component is able to describe.

In order to better understand the role of each grain in fitting Mkn 501 SED, we also performed the χ^2 minimization for hypothetical cases where we have the EBL with just 1- and 2-grain dust components. Figures 4.3 and 4.4 show the results from the cases with

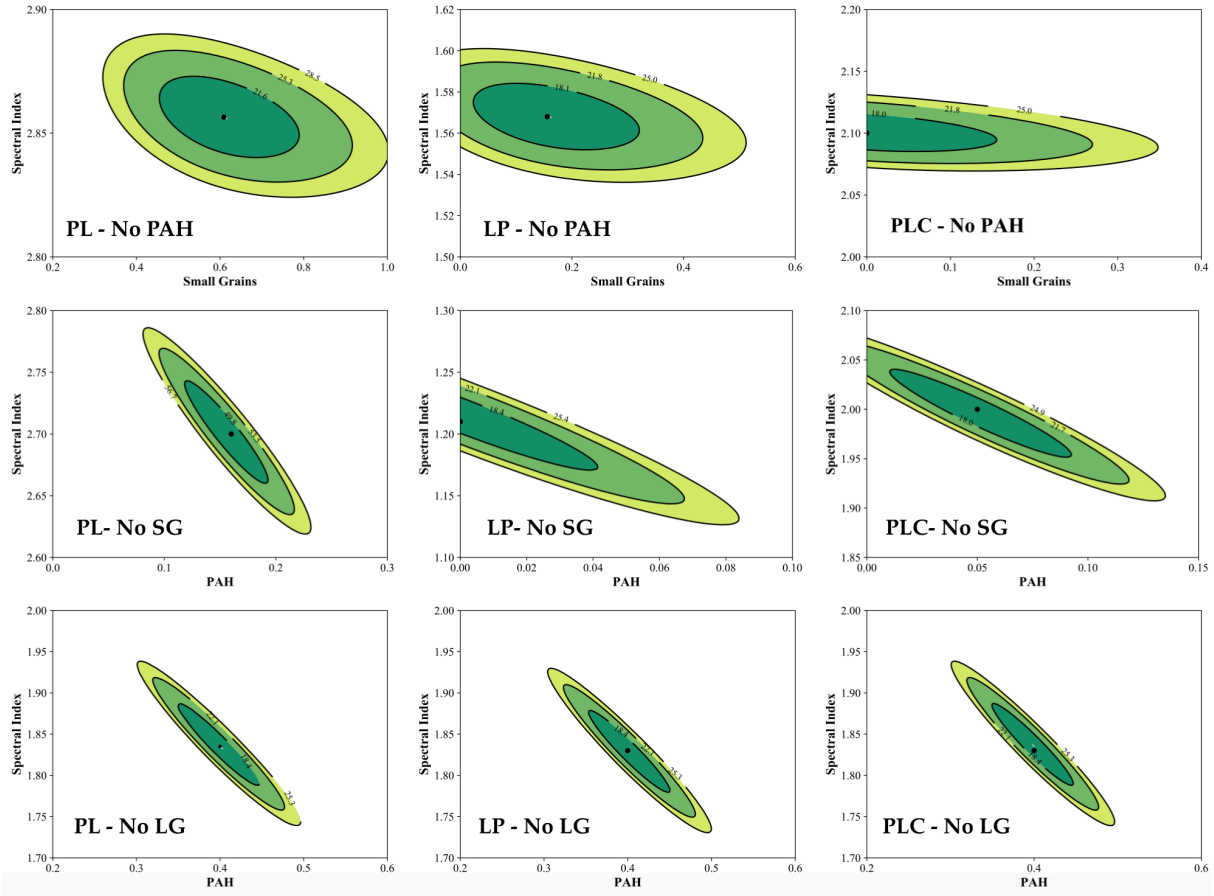

Figure 4.4: *Confidence level curves at 68%, 95% and 99% in a 2D parameter space with spectral index versus grain fraction:* $\Gamma \times f_n$ *(PL/PLC) or* $a \times f_n$ *(LP). All the curves are for an effective 2-grains model.*

an effective 2-grain model for the three intrinsic spectra defined in equation 4.1.

Tables 4.1 (PL), 4.2 (LP) and 4.3 (PLC) summarize the main information about the fits in each intrinsic case studied. It is possible to see that for the PL case, the fit prefers to rely on small grains to describe the spectrum tail at very high energies. One can see that in the absence of this kind of grain, the fit is the worst among the three effective 2-grain models. It is worth noting the fact that we kept the grain temperatures fixed at their nominal values (see table 2.1), and these quantities are important parameters to describe correctly the shape of the EBL, as we can see in figure 2.12. When a curvature is introduced we note that part of the dust attenuation can be transferred to the intrinsic emission and a reasonable quality in the fit is obtained. The contours in the space of parameters show a strong correlation between the spectral index and dust fractions in the cases where small or large grains are absent. The models with a single dust grain do not provide good fits in any case.

power-law					
EBL model	χ^2/ndof	$\Gamma \pm \sigma$	$f_{\rm PAH} \pm \sigma$	$f_{\rm sg} \pm \sigma$	$f_{\rm lg} \pm \sigma$
3 grains	15.7/13	2.05 ± 0.39	0.32 ± 0.15	0.56 ± 0.12	0.12
3 grains ($\tilde{f}_{\rm sg} \leq 0.1$)	37.6/13	2.75 ± 0.29	0.12 ± 0.12	0.09 ± 0.02	0.79
PAH+small	16.1/14	1.83 ± 0.23	0.40 ± 0.10	0.60	0.00
PAH+large	47.5/14	2.70 ± 0.29	0.16 ± 0.11	0.00	0.84
small+large	19.3/14	2.86 ± 0.06	0.00	0.61 ± 0.14	0.39
PAH	98.0/15	0.68 ± 0.04	1.00	0.00	0.00
small	25.1/15	2.76 ± 0.05	0.00	1.00	0.00
large	48.9/15	3.09 ± 0.04	0.00	0.00	1.00
F10	41.6/15	2.44 ± 0.04	0.25	0.05	0.70

Table 4.1: *Summary of EBL+spectrum combined fits for a power-law intrinsic spectrum and the observed SED of Mkn 501. Fractions without uncertainties were either kept fixed during the fit or obtained from fitted fractions by the normalization condition.*

log-parabola						
EBL model	χ^2/ndof	$a \pm \sigma$	$b \pm \sigma$	$f_{\rm PAH} \pm \sigma$	$f_{\rm sg} \pm \sigma$	$f_{\rm lg} \pm \sigma$
3 grains	15.7/12	1.96 ± 0.48	0.16 ± 0.60	0.27 ± 0.25	0.49 ± 0.28	0.24
3 grains ($\tilde{f}_{\rm sg} \leq 0.1$)	15.8/12	1.44 ± 0.14	1.01 ± 0.09	0.00 ± 0.14	0.10 ± 0.08	0.90
PAH+small	16.1/13	1.83 ± 0.23	0.00 ± 0.23	0.40 ± 0.10	0.60	0.00
PAH+large	16.1/13	1.21 ± 0.33	1.18 ± 0.21	0.00 ± 0.16	0.00	1.00
small+large	15.8/13	1.56 ± 0.56	0.92 ± 0.39	0.00	0.15 ± 0.20	0.85
PAH	62.4/14	-0.99 ± 0.29	1.00 ± 0.17	1.00	0.00	0.00
small	25.1/14	2.76 ± 0.04	0.00 ± 0.13	0.00	1.00	0.00
large	16.2/14	1.21 ± 0.33	1.18 ± 0.21	0.00	0.00	1.00
F10	18.8/14	0.93 ± 0.32	0.95 ± 0.20	0.25	0.05	0.70

Table 4.2: *Summary of EBL+spectrum combined fit for a log-parabola intrinsic spectrum and the observed SED of Mkn 501. Fractions without uncertainties were either kept fixed during the fit or obtained from fitted fractions by the normalization condition.*

4.4 Likelihood ratio hypotheses test

A nested log-likelihood ratio test was performed in order to compare the 1- and 2-grain models (the null hypotheses H_0) against the 3-grain scenario (the alternative hypothesis H_1). As test statistic we have used

$$-2\ln(\mathcal{L}_0/\mathcal{L}_1) = \Delta\chi^2. \tag{4.3}$$

The Wilks' theorem [80] states that, in the limit of a large data sample, the asymptotic probability distribution function (pdf) of $\Delta\chi^2$, when H_0 holds true, should be a χ^2_k distribution with number of degrees of freedom (k) equal to the difference in dimensionality between the parameter space of the two hypotheses. Therefore, we performed tests for

power-law with exponential cutoff						
EBL model	χ^2/ndof	$\Gamma \pm \sigma$	$E_{\rm cut} \pm \sigma$(TeV)	$f_{\rm PAH} \pm \sigma$	$f_{\rm sg} \pm \sigma$	$f_{\rm lg} \pm \sigma$
3 grains	15.7/12	2.00 ± 0.12	7.7 ± 2.1	0.08 ± 0.07	0.06 ± 0.17	0.86
PAH+small	16.1/13	1.83 ± 0.24	$(0.1 \pm 9.9) \times 10^7$	0.40 ± 0.10	0.60	0.00
PAH+large	15.7/13	2.00 ± 0.40	6.9 ± 1.5	0.05 ± 0.16	0.00	0.95
small+large	15.8/13	2.10 ± 0.19	6.7 ± 1.3	0.00	0.00 ± 0.78	1.00
PAH	50.4/14	-0.31 ± 0.16	7.6 ± 1.2	1.00	0.00	0.00
small	25.1/14	2.76 ± 0.05	$(0.1 \pm 5.3) \times 10^6$	0.00	1.00	0.00
large	15.8/14	2.10 ± 0.19	6.7 ± 1.3	0.00	0.00	1.00
F10	16.6/14	1.62 ± 0.18	8.3 ± 1.9	0.25	0.05	0.70

Table 4.3: *Summary of EBL+spectrum combined fit for a power law with an exponential cutoff intrinsic spectrum and the observed SED of Mkn 501. Fractions without uncertainties were either kept fixed during the fit or obtained from fitted fractions by the normalization condition.*

$k = 1$ (H_0 = "two grains") and $k = 2$ (H_0 = "single grain").

	power-law		log parabola		power-law × cutoff	
null hypothesis	$\Delta\chi^2$	$P(\geq \Delta\chi^2)$	$\Delta\chi^2$	$P(\geq \Delta\chi^2)$	$\Delta\chi^2$	$P(\geq \Delta\chi^2)$
PAH+small	0.4	0.53	0.4	0.53	0.4	0.53
PAH+large	31.8	1.7×10^{-8}	0.4	0.53	0.0	1.0
small+large	3.6	0.06	0.1	0.75	0.1	0.75
PAH	82.3	1.4×10^{-18}	46.7	7.2×10^{-11}	34.7	2.9×10^{-8}
small	9.4	0.01	9.4	0.01	9.4	0.01
large	33.2	6.2×10^{-8}	0.5	0.78	0.1	0.95

Table 4.4: *Summary of the nested likelihood ratio test for 2-grain and 1-grain models with power-law, log-parabola and power-law with an exponential cutoff intrinsic spectra. The 3-grains model was used as alternative hypothesis.*

The distributions of $\Delta\chi^2$ for PL, LP and PLC intrinsic models, using as null hypotheses the 1- and 2-grain best fits from tables 4.1, 4.2 and 4.3, are shown in figures 4.5, 4.6 and 4.7. In these plots the expected asymptotic pdf of $\Delta\chi^2$ is also superimposed, showing that for the number of points in the SED of Mkn 501, an excellent agreement with the asymptotic pdf is already obtained. Therefore, the p-values in table 4.4 were calculated using the asymptotic formula. As we can see the model with only the PAH component can be excluded at more than 5σ ($p = 2.9 \times 10^{-8}$), irrespective of the intrinsic model assumed. From figures 4.3 and 4.4 we can see clearly that the PAH-only attenuation is unable to account for the strong flux drop of Mkn 501 SED above 10 TeV.

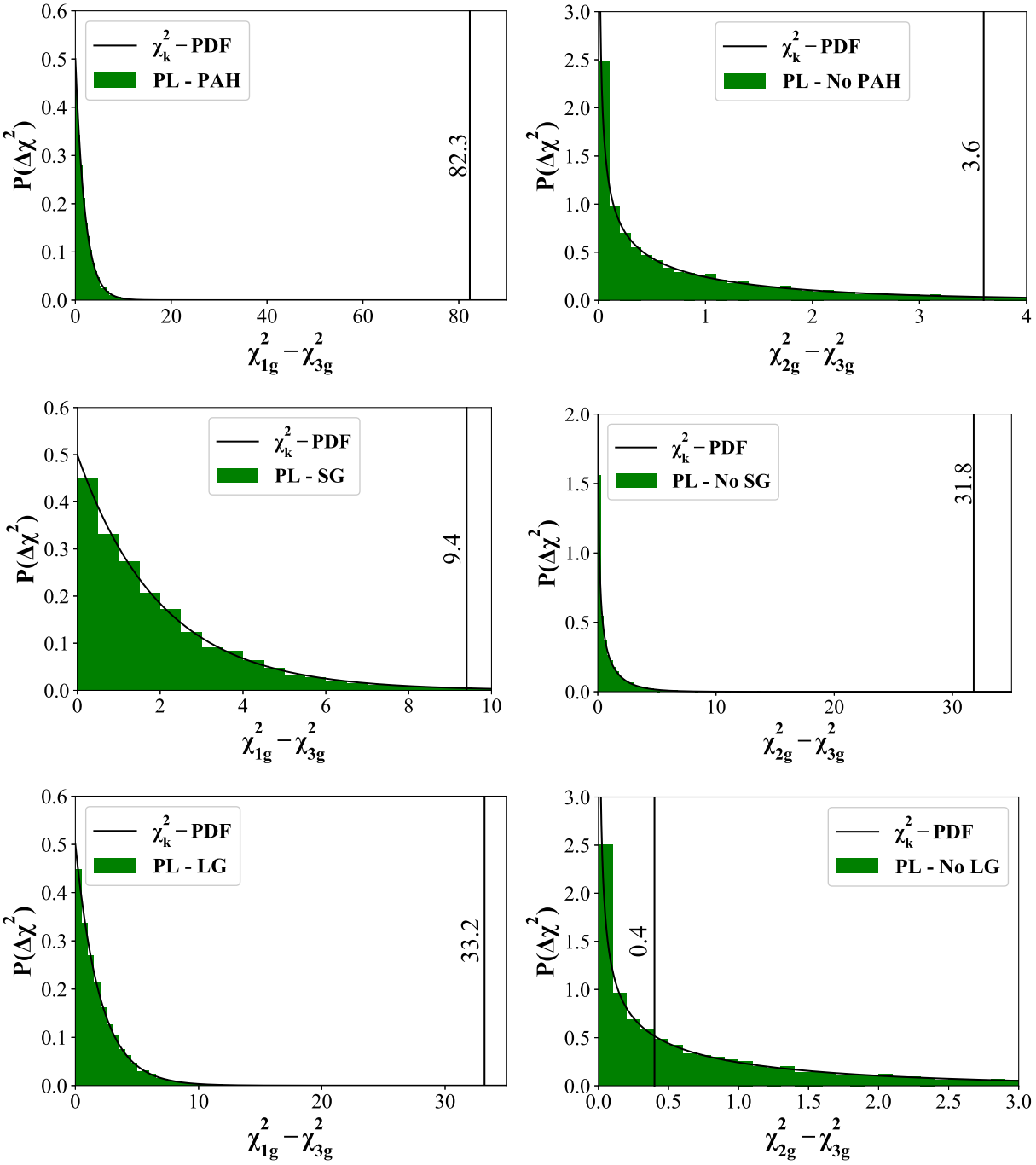

Figure 4.5: *Distribution of test statistic* $(-2\,ln(\mathcal{L}_0/\mathcal{L}_1) = \Delta\chi^2)$ *for a power-law intrinsic spectrum, 1- and 2-grain models as null hypotheses* (H_0) *and 3-grain model as alternative hypothesis* (H_1)*. Left: distribution for effective 2-grain models superimposed to the* χ^2_k *pdf with* $k = 1$ *dof. Right: distribution for single grain models superimposed to the* χ^2_k *pdf with* $k = 2$ *dofs. The vertical lines correspond to the test statistic value for the bestfits of table 4.1.*

4.5 Bolometric intensity and emissivity evolution: comparison with other models

In order to verify the consistency of the results obtained here with other models, we can use the bolometric intensity defined in 2.25.

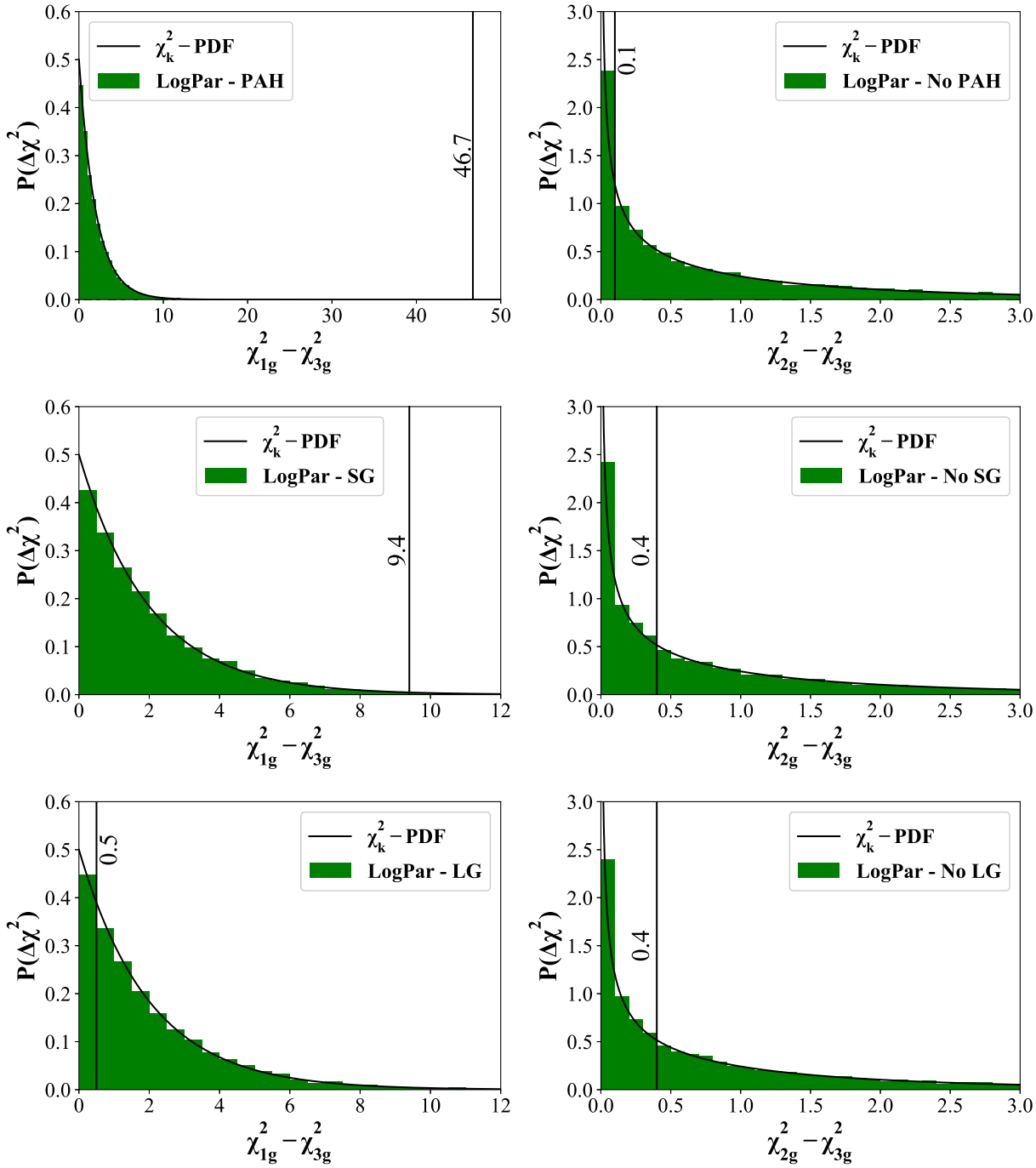

Figure 4.6: *Distribution of test statistic ($-2\,ln(\mathcal{L}_0/\mathcal{L}_1) = \Delta\chi^2$) for a log-parabola intrinsic spectrum, 1- and 2-grain models as null hypotheses (H_0) and 3-grain model as alternative hypothesis (H_1). Left: distribution for effective 2-grain models superimposed to the χ^2_k pdf with $k = 1$ dof. Right: distribution for single grain models superimposed to the χ^2_k pdf with $k = 2$ dofs. The vertical lines correspond to the test statistic value for the bestfits of table 4.2.*

The bolometric intensities for each best-fit shown in tables 4.1, 4.2 and 4.3 are around $I_{bol} = 48.0$ nW m^{-2} sr^{-1}, varying in the first digit, since the stellar contribution does not change and the broad range of redshifts over which the integration is performed dilute the dependence in the temperature of I_{bol}. For comparison, F10 model yields $I_{bol} = 46.8$

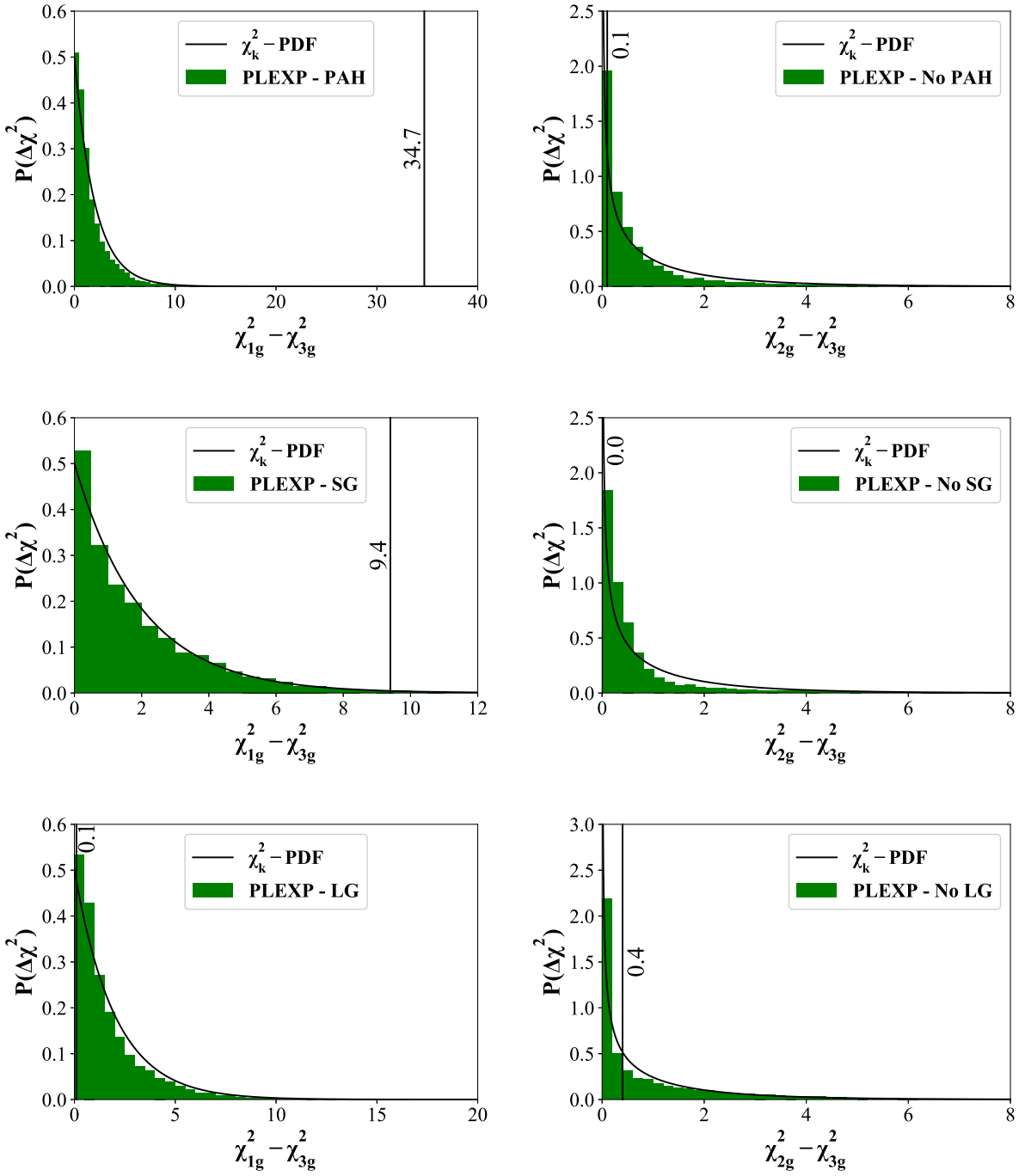

Figure 4.7: *Distribution of test statistic* $(-2\,ln(\mathcal{L}_0/\mathcal{L}_1) = \Delta\chi^2)$ *for a power-law with cutoff intrinsic spectrum, 1- and 2-grain models as null hypotheses* (H_0) *and 3-grain model as alternative hypothesis* (H_1)*. Left: distribution for effective 2-grain models superimposed to the* χ^2_k *pdf with* $k = 1$ *dof. Right: distribution for single grain models superimposed to the* χ^2_k *pdf with* $k = 2$ *dofs. The vertical lines correspond to the test statistic value for the bestfits of table 4.3.*

nW m^{-2} sr^{-1}. As a result, the best-fits found in this analysis correspond to conservative estimates of the EBL contribution, since the bolometric intensities obtained are very close to the lower bounds obtained from the resolved galaxy counts (see figure 2.12).

It is also interesting to compare emissivity measurements in the IR band with our predictions using the best-fit fractions found here. In [81] and [82] the authors developed empirical methods in order to get the evolution of the EBL emissivity over a broad range of wavelengths, all the way from the Lyman limit to far-IR (850 μm). Utilizing the 3-grain scenarios obtained in our analysis based on different assumptions for Mkn 501 intrinsic spectrum we calculate the luminosity density evolution for different wavelengths. Figure 4.8 displays the results obtained. As we can see, for 68% confidence level bands shown in [81,82], the emissivity calculated are in agreement within 1-2σ with the measurements.

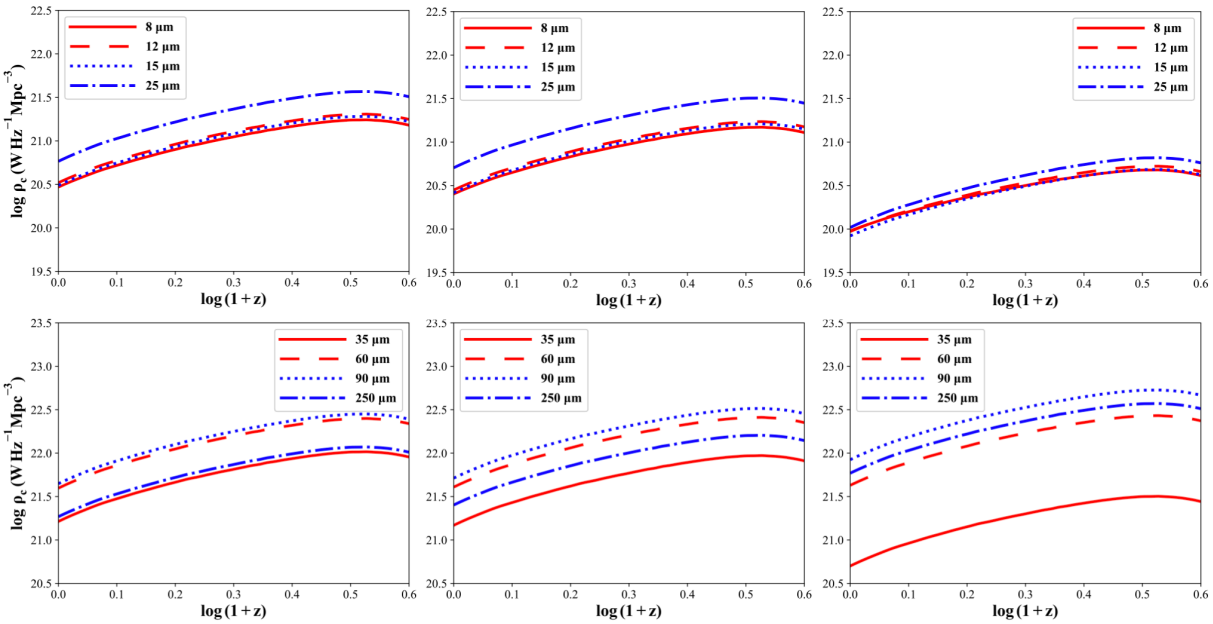

Figure 4.8: *EBL luminosity density (i.e. emissivity) as a function of redshift predicted by equation 2.20, using the best-fit fractions for the 3-grain cases. Left: emissivity with dust fractions obtained from the fit with power-law intrinsic spectrum; middle: dust fractions from the log-parabola; right: dust fractions from the power-law with cutoff.*

4.6 Global fit properties for an extended sample of gamma-ray sources

Here, we describe a statistical test made to compare two EBL scenarios: the nominal fractions and the model with Mkn 501 tuned fractions as presented before. We started the analysis by pre-selecting a sample of extragalactic gamma-ray sources from the TeVCat catalog [83]. From this initial sample, we were able to select 78 spectra of 41 different gamma-ray sources, all of them observed by IACTs. The main information about each one of these spectra is shown in tables 4.5 and 4.6. This set of spectra contains measurements of gamma-ray flux for which attenuation by EBL is expected to be non-negligible. This can be better visualized in figure 4.9 in which we show the optical depth map of F10

model in the 2D-parameter space $E_\gamma \times z$ with the lowest and highest energy bins for each spectrum superimposed. As we can see, several of these spectra have fluxes measured at energies above the CGRH.

Name	Redshift	Type	Survey	Period of Observ.	Reference
1ES 0229+200	0.14	BL Lac	HESS	2005-2006	[84]
			VERITAS	2010-2012	[85]
1ES 0347-121	0.188	BL Lac	HESS	2006	[86]
1ES 0414+009	0.287	BL Lac	HESS	2005-2009	[87]
			VERITAS	2008-2011	[88]
1ES 0806+524	0.138	BL Lac	MAGIC	2011	[89]
			VERITAS	2006-2008	[90]
1ES 1011+496	0.212	BL Lac	MAGIC	2007	[91]
1ES 1101-232	0.186	BL Lac	HESS	2004-2005	[92]
1ES 1215+303	0.13	BL Lac	MAGIC	2011	[89]
			VERITAS	2011	[93]
1ES 1218+304	0.182	BL Lac	VERITAS	2008-2009	[94]
			VERITAS	2007	[95]
			MAGIC	2005	[96]
1ES 1312-423	0.105	BL Lac	HESS	2004-2010	[97]
1ES 1727+502	0.055	BL Lac	VERITAS	2013	[98]
1ES 1741+196	0.084	BL Lac	VERITAS	2009-2014	[99]
1ES 1959+650	0.048	BL Lac	VERITAS	2007-2011	[100]
			MAGIC	2006	[101]
1ES 2344+514	0.044	BL Lac	VERITAS	2007-2008	[102]
				2007	[102]
			MAGIC	2008	[103]
			MAGIC	2005-2006	[104]
1RXS J101015.9	0.142639	BL Lac	HESS	2006-2010	[105]
3C 279	0.5362	FSRQ	MAGIC	2008	[16]
3C66A	0.34	BL Lac	VERITAS	2008	[106]
4C+2135	0.432	FSRQ	MAGIC	2010	[107]
AP Librae	0.049	BL Lac	HESS	2010-2011	[108]
BL Lacertae	0.069	BL Lac	VERITAS	2011	[109]
Centaurus A	0.00183	FR I	HESS	2004-2008	[110]
H 1426+428	0.129	BL Lac	HEGRA	1999-2000	[111]
				2002	[111]
H 2356-309	0.165	BL Lac	HESS	2004-2007	[112]
IC 310	0.0189	BL Lac	MAGIC	2012	[113]
				2009-2010	[114]
M87	0.0044	FR I	HESS	2005	[115]
				2004	[115]
			MAGIC	2005-2007	[116]
				2008	[117]
			VERITAS	2007	[118]
Markarian 180	0.045	BL Lac	MAGIC	2006	[119]
Markarian 421	0.031	BL Lac	MAGIC	2004-2005	[120]
				2006	[121]
			VERITAS	2008	[122]
Markarian 501	0.034	BL Lac	HEGRA	1997	[123]
			VERITAS	2009	[124]
NGC 1275	0.017559	FR I	MAGIC	2009-2014	[125]
PG 1553+113	0.49	BL Lac	VERITAS	2010-2012	[126]
			MAGIC	2008	[127]
				2006	[128]
			HESS	2013-2014	[129]
			HESS	2005-2006	[130]
			HESS	2012	[130]

Table 4.5: *Gamma-ray sources selected from TeVCat [83].*

This sample of spectra allows us to study the distribution of residuals obtained when we compare the measured flux (Φ_i) with the predicted flux at Earth ($\Phi(E) = e^{-\tau}\Phi_0$) from different EBL models defined in Section 4.3 and the intrinsic spectrum models considered in Section 4.2, taking into account the uncertainties on the measured flux $\Phi_i(\sigma_i)$:

Name	Redshift	Type	Survey	Period of Observ.	Reference
PKS 0301-243	0.2657	BL Lac	HESS	2009-2011	[131]
PKS 0447-439	0.343	BL Lac	HESS	2009	[132]
PKS 1441+25	0.939	FSRQ	MAGIC	2015	[133]
PKS 1510-089	0.361	FSRQ	HESS	2009	[134]
			MAGIC	2015-PeriodA	[135]
				2015-PeriodB	[135]
PKS 2005-489	0.071	BL Lac	HESS	2004-2007	[136]
PKS 2155-304	0.116	BL Lac	HESS	2006	[137]
				2005-2007	[138]
			MAGIC	2006	[139]
RBS 0413	0.19	BL Lac	VERITAS	2009	[140]
RGB J0152+017	0.08	BL Lac	HESS	2007	[141]
RGB J0710+591	0.125	BL Lac	VERITAS	2008-2009	[142]
RX J0648.7+1516	0.179	BL Lac	VERITAS	2010	[143]
S3 0218+35	0.954	FSRQ	MAGIC	2014	[144]
VER J0521+211	0.108	BL Lac	VERITAS	2009-2010	[145]

Table 4.6: *Continuation of Table 4.6.*

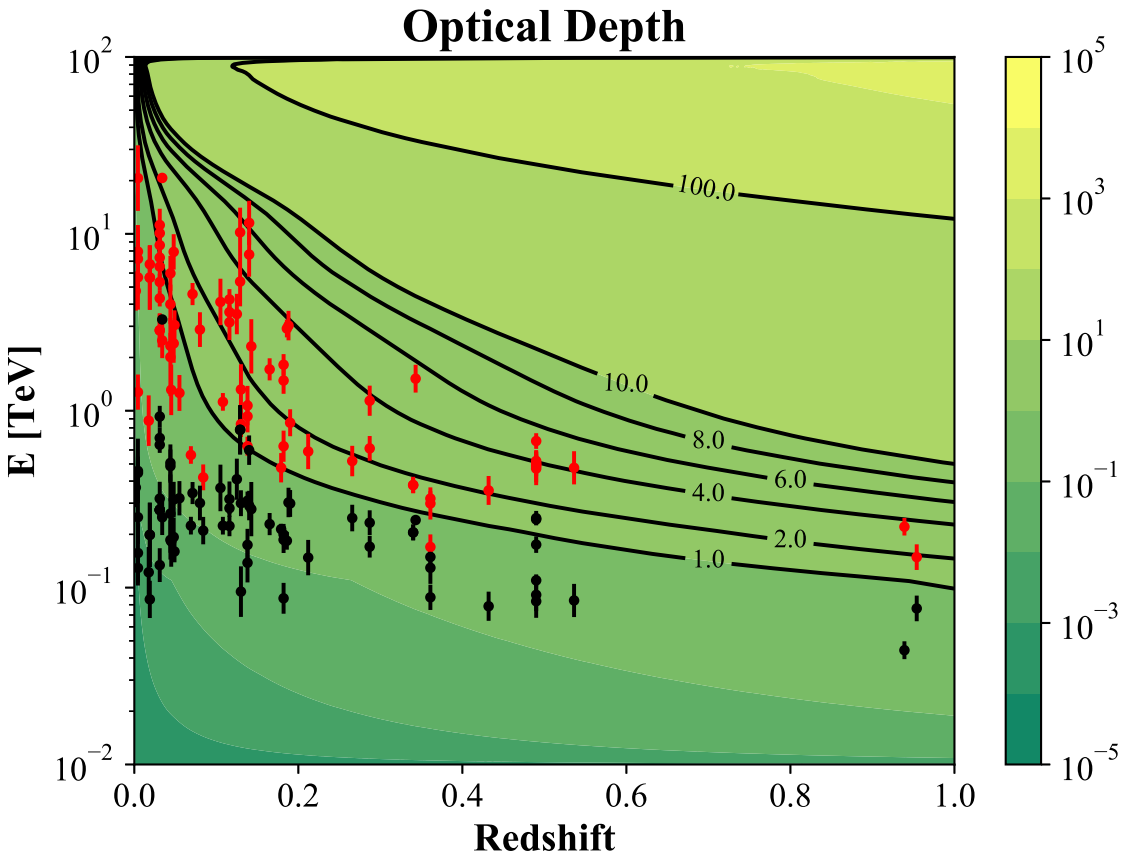

Figure 4.9: *Heat map showing the optical depth to gamma-rays according to F10 model in the $E_\gamma \times z$ parameter space. The lowest (black) and highest (red) energy bins for each observation shown in tables 4.5 and 4.6 are superimposed to the plot. Black curves at specific values of τ are shown. The curve corresponding to $\tau = 1$ is defined as the cosmic gamma-ray horizon (CGRH).*

$$\text{Flux residual}_i \equiv \frac{\Phi_i - \Phi(E_i)}{\sigma_i}, \tag{4.4}$$

which is expected to follow a normal distribution with mean equal to zero and unit

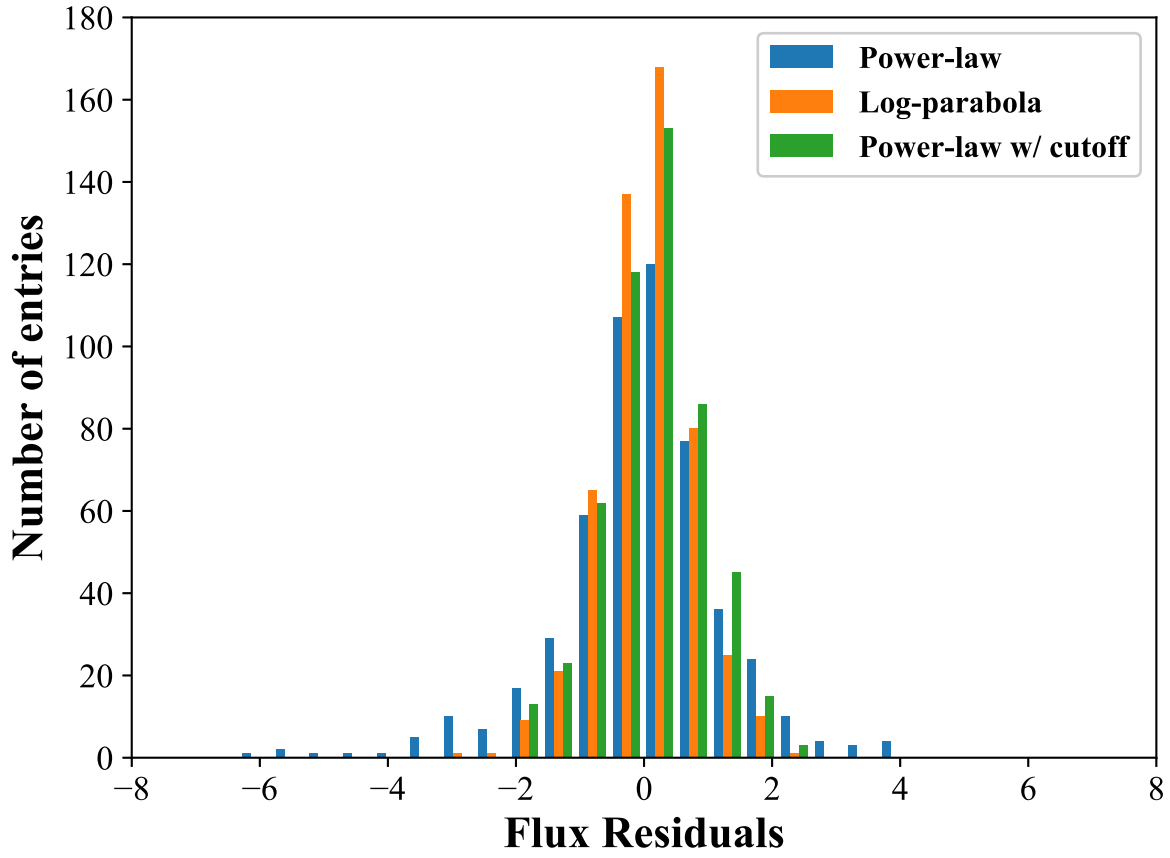

Figure 4.10: *Distribution of flux residuals for the EBL F10 model. Each histogram correspond to a different intrinsic spectrum model.*

variance when the errors σ_i are Gaussian and the model $\Phi(E)$ describes the measurements Φ_i appropriately. Therefore, this kind of analysis provides enough information on the quality of the fits and the estimated uncertainty since we get not just the reduced χ^2, but also the σ and μ which characterize the distribution. In order to ensure that all the fits have at least one degree of freedom, six sources with only three data points measured were eliminated from the initial sample. In appendix B the 72 spectra used for this analysis are shown with the bestfit for the power-law intrinsic spectrum and EBL with nominal dust fractions.

Figure 4.10 shows the distribution of flux residuals for the three intrinsic spectra and F10 model. By eye we can see a clear improvement in the distributions for log-parabola and power-law with a cutoff when compared to the power-law case. The number of outliers decreases significantly in these two cases. In table 4.7 we summarize a more quantitative analysis based on Gaussian fits to the distributions of flux residuals. The columns labeled as "nominal fractions" of this table show the fit results for the distributions in figure 4.10 and we can see that the reduced χ^2 for LP and PLC are closer to unity than PL case. Other tests were made by comparing two different EBL scenarios for a fixed intrinsic spectrum parameterization. For each parameterization we use F10 model and Mkn 501

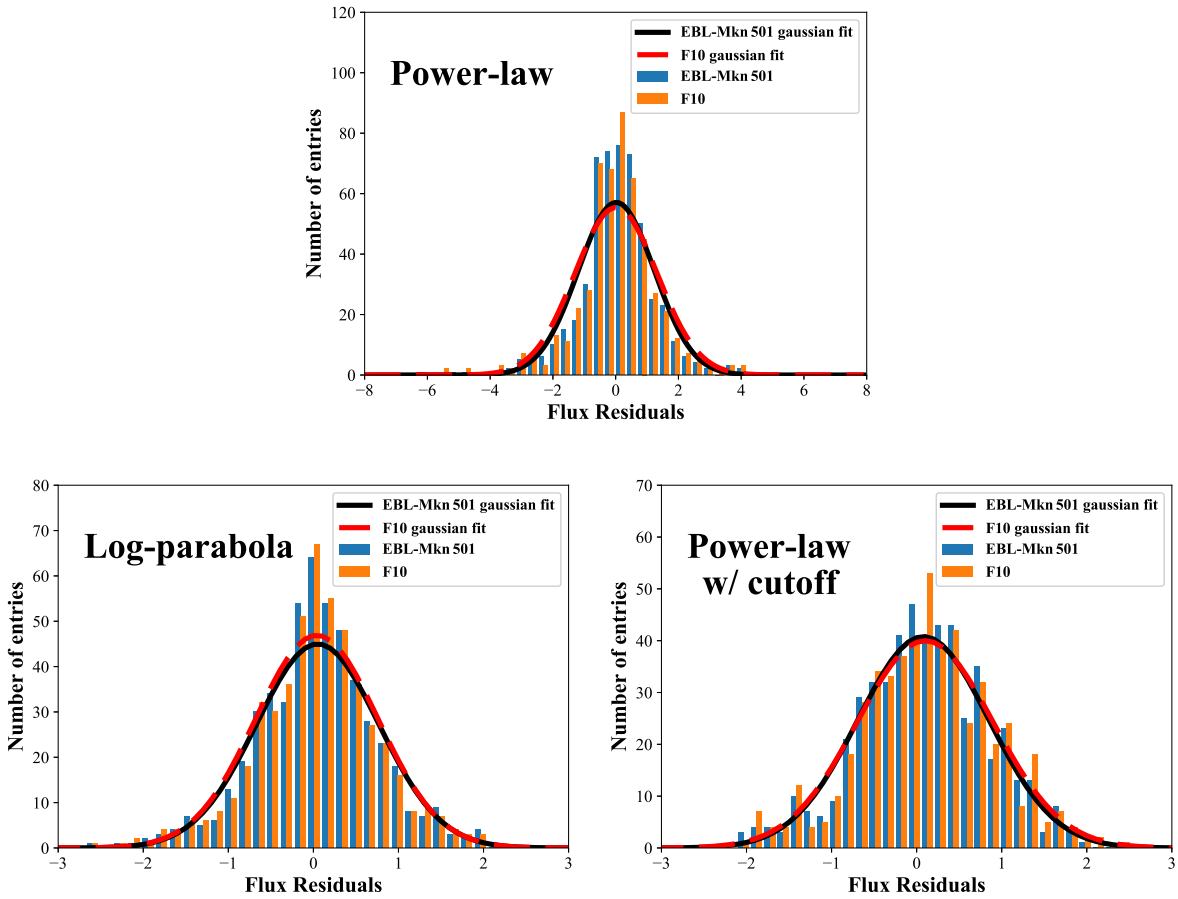

Figure 4.11: *Distributions of flux residuals for different combinations of EBL attenuation and intrinsic spectrum. Each plot displays two distributions of residuals: one for the nominal dust fractions and another for the tuned fraction case. (Top) power-law; (Left-bottom) log-parabola; (Right-bottom) power-law with an exponential cutoff.*

tuned one. Figure 4.11 shows these fits and in table 4.7 we can see again that the PL is the worst case with the reduced χ^2 greater than the other intrinsic cases. On the other hand, the small difference in χ^2 for the two spectra with curvature does not allow to conclude that one is better than the other.

4.6.1 Additional tests

In order to disentangle, at least partially, intrinsic spectrum effects from the EBL attenuation ones, we performed two additional tests. Firstly, we follow the approach used in [35], where the fit residuals for the nominal and Mkn 501-tuned fractions were calculated for each source using the intrinsic spectrum that lead to the best fit quality (the largest $P(> \chi^2)$ for a given ndof). Once again, we have worked with two scenarios of dust fractions: the nominal fractions and the ones tuned from Mkn 501 SED. Table 4.7 presents these results in the lines labeled as "best spec". All the three tuned EBL scenarios have

slightly smaller reduced χ^2.

For the second test, we have subdivided the initial sample using an attenuation estimator which generates stellar- and dust-dominated SED bins. The estimator used for this procedure is defined as

$$r = \frac{\tau_{star}(E,z)}{\tau_{star}(E,z) + \tau_{dust}(E,z)}, \tag{4.5}$$

where $\tau_{star}(E,z)$ and $\tau_{dust}(E,z)$ are the optical depth due to stellar and dust contributions, respectively, E is the energy of the photon and z the redshift of the source. In this equation we use the nominal dust fractions. We have verified that the use of Mkn 501 tuned fractions did not change the classification of EBL component dominance.

Figure 4.12 shows the distribution for 39 sources from the initial sample [1]. Clearly figure 4.12 shows us that the current sample of blazars observed by IACTs is attenuated predominantly by the stellar component of the EBL. When the estimator of equation 4.5 is applied to the highest energy bin of each source, we get that Mkn 501 is the blazar with the highest expected dust attenuation level in the sample. The distributions for the two subsamples ($r > 0.8$ and $r \leq 0.8$) are shown in figure 4.13 and in table 4.7 we can see the mean, the variance and the reduced χ^2 obtained in this analysis. We conclude that the quality of the fits does not show a systematic change when one goes from the nominal dust fractions to the tuned ones.

Excluding the cases with bad fit quality ($\chi^2/\mathrm{ndof} \gtrsim 10$), we can see that the mean values (μ) are consistent with zero at the 1- to 2-sigma level, whereas the standard deviation (σ) from the fits can be up to 30% smaller than the expected unit variance. This effect could be due to an overestimation of the uncertainties in the fluxes. Investigating this would require extra information at the telescopes and data processing levels, to which we do not have access to.

4.7 Summary

In this chapter a study of the role of the emission from the dust component of the EBL was performed. Such investigation was possible since the EBL utilized was separated in their stellar and dust contributions. The Mkn 501 SED shows some sensitivity to the relative contribution of different dust grains. It is important to keep in mind that in our analysis the temperatures were kept fixed in the fit at their nominal values. By performing a nested log-likelihood ratio test we were able to exclude with more than 5σ the scenario with just PAH contribution to the dust component. The PAH-only scenario is unable to account for the flux suppression in the tail of the spectrum, even if an exponential cutoff

[1] Two of the blazars in the input sample (CenA and M87) are too close that their optical depths due to starlight are negligible.

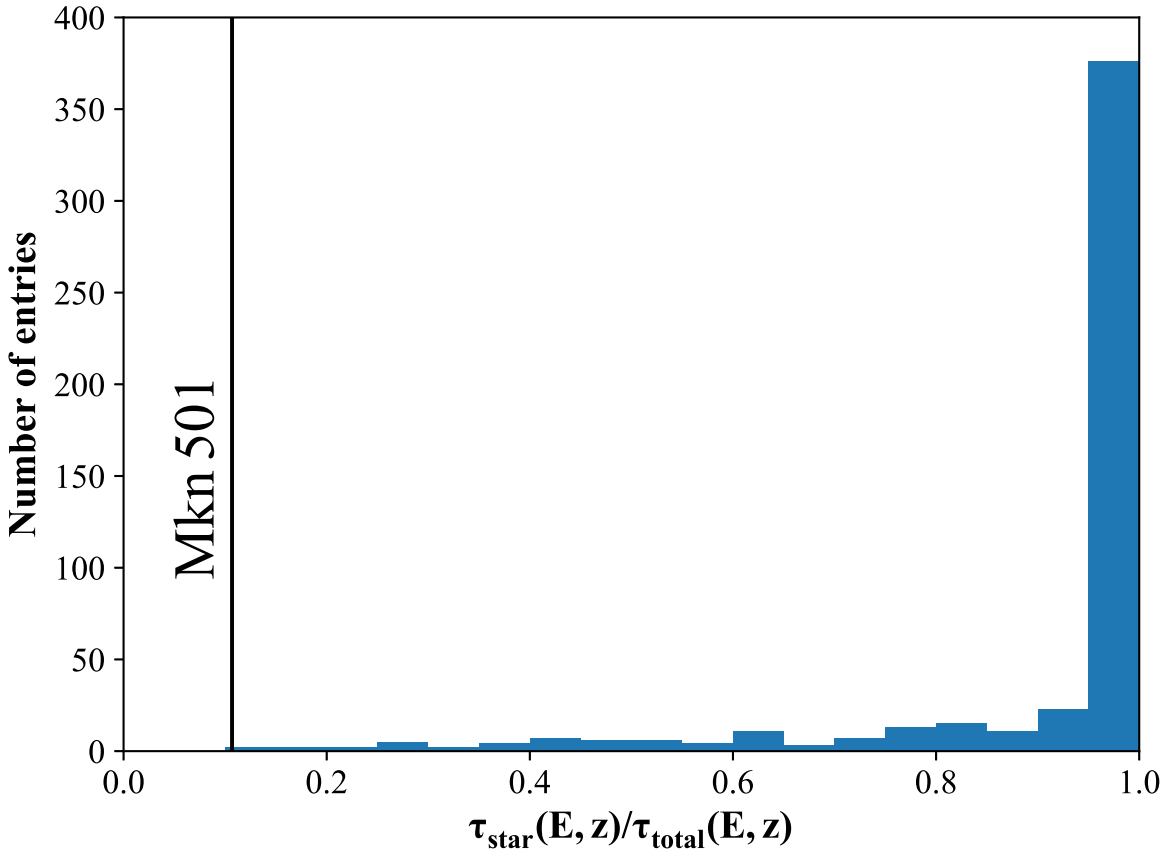

Figure 4.12: *Distribution of the optical depth estimator τ_{star}/τ_{total} for the sample of spectra shown in tables 4.5 and 4.6. The vertical line correspond to the highest energy bin of the Mkn 501 flare.*

is present in the intrinsic emission. On the other hand, the PAH molecules are essential in describing correctly the spectral index of the measured flux at energies below 10 TeV. With TeVCat sources a comparison between nominal and tuned fractions was possible. By splitting the measured energy bins into two subsamples, stellar and dust attenuation dominated, no systematic changes were identified in the quality of the fits of the residual distributions going from the nominal to the tuned fractions. This result is consistent with the fact that the sample of sources is dominated by stellar attenuation.

	nominal fractions			tuned fractions		
	μ	σ	χ^2/dof	μ	σ	χ^2/dof
PL	-0.01 ± 0.08	1.31 ± 0.06	61.23	0.02 ± 0.08	1.21 ± 0.05	97.79
LP	0.04 ± 0.05	0.72 ± 0.03	1.91	0.05 ± 0.05	0.72 ± 0.03	1.96
PLC	0.10 ± 0.05	0.80 ± 0.04	1.87	0.08 ± 0.05	0.77 ± 0.04	1.47
best spec. (PL)				0.06 ± 0.04	0.71 ± 0.03	2.25
best spec. (LP)	0.05 ± 0.04	0.71 ± 0.03	2.46	0.05 ± 0.04	0.71 ± 0.03	2.39
best spec. (PLC)				0.05 ± 0.04	0.71 ± 0.03	1.31
$r > 0.8$ (PL)	0.11 ± 0.09	1.24 ± 0.06	70.17	0.08 ± 0.08	1.18 ± 0.06	44.74
$r \leq 0.8$ (PL)	-0.40 ± 0.40	1.80 ± 0.30	2.12	-0.30 ± 0.30	1.50 ± 0.20	9.18
$r > 0.8$ (LP)	0.03 ± 0.05	0.70 ± 0.04	1.65	0.03 ± 0.05	0.70 ± 0.04	1.91
$r \leq 0.8$ (LP)	0.10 ± 0.20	0.90 ± 0.10	1.22	0.10 ± 0.10	0.90 ± 0.10	1.35
$r > 0.8$ (PLC)	0.06 ± 0.06	0.79 ± 0.04	1.77	0.06 ± 0.05	0.77 ± 0.04	1.35
$r \leq 0.8$ (PLC)	0.40 ± 0.20	1.00 ± 0.20	1.13	0.30 ± 0.20	0.90 ± 0.10	0.45

Table 4.7: *Mean, standard deviation and reduced χ^2 of Gaussian fits to the distributions of residuals for SED fits performed with different dust fractions and blazar intrinsic spectra: PL (power-law), LP (log-parabola) and PLC (power-law with cutoff).*

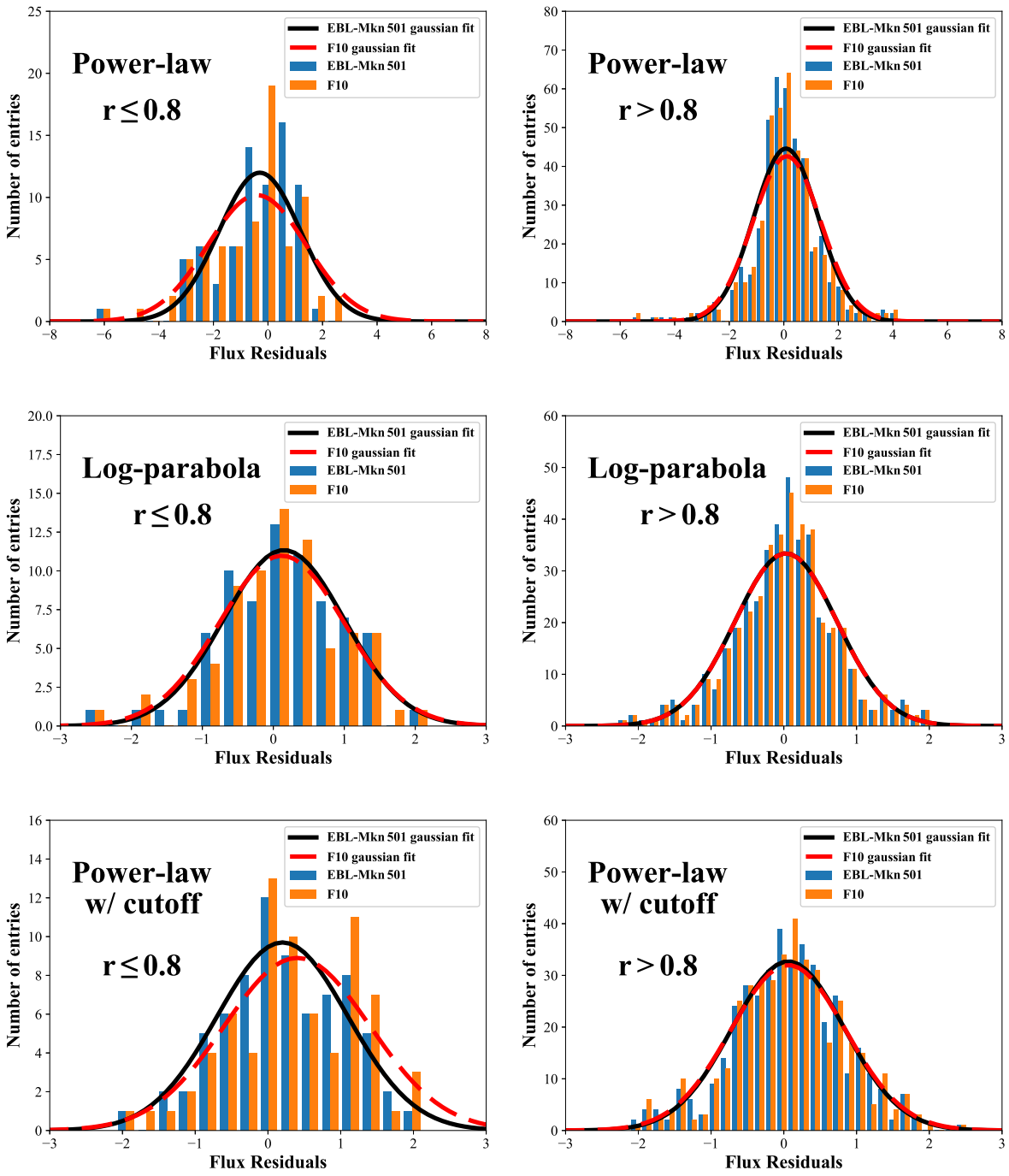

Figure 4.13: *Distributions of flux residuals for two distinct populations of SED bins and different blazar intrinsic spectra. Left: plots corresponding to the bins dominated by dust attenuation ($\tau_{star}/\tau_{total} \leq 0.8$) according to the estimator of equation 4.5. Right: bins dominated by stellar attenuation ($\tau_{star}/\tau_{total} > 0.8$). At each plot, two histograms are compared: nominal dust fractions and tuned ones.*

Chapter 5

Absorption forecasts for the Cherenkov Telescope Array

The third generation of IACTs will be represented by the CTA which is being constructed right now. In this chapter, forecast studies are made for the CTA in order to estimate the potential of this survey in determining EBL parameters, in particular, those important for the IR part of its spectrum, a region dominated by the contribution of dust grains in the interestellar medium, as discussed before. In order to do this, the behavior of a likelihood function that depends on the EBL parameters is studied for a sample of sources to be observed by CTA for several exposure times. This kind of study is possible thanks to the remarkable improvements in performance for this telescope array when compared to the current generation of IACTs.

5.1 IACT technique

Our atmosphere is opaque to photons with energies above ~ 10 MeV and in order to detect directly these gamma-rays, telescopes on-board satellites have been developed, such as Fermi-LAT. However, due to the limited collection area, the energy coverage reaches up to ~ 100 GeV. The IACT technique allows to observe gamma-rays with telescopes on the ground, but indirectly. Coincidentally, this technique measures gamma radiation with energies just above the maximum energy detected by satellites [7].

The main interaction between gamma-rays and atmospheric particles is the e^-/e^+ pair creation [7]. The newly created pair will travel, on average, one radiation length in air before emitting new photons through bremsstrahlung. These new gamma-rays repeat the initial cycle producing an extensive atmospheric shower (EAS). The number of particles increases until the cascade reaches its point of maximum development, this initial stage being characterized by the fact that cross sections for bremsstrahlung and pair production dominate over those of energy losses. After the point of maximum development, the

number of particles decreases as the cascade develops towards the ground. Charged particles in the EAS moving above the speed of light in air emit Cherenkov radiation, allowing the reconstruction of the main characteristics of the primary gamma-ray, such as energy, direction and arrival time, by mirrors located on the ground. Observations from IACTs are based on these processes.

The shower is accompanied by a cone of Cherenkov radiation as illustrated in figure 5.1. The region iluminated by Cherenkov photons covers an area of approximately 120 m of radius, known as the "Cherenkov light pool". For a gamma-ray of 1 TeV, approximately 100 photons m^{-2} arrive at the ground [7].

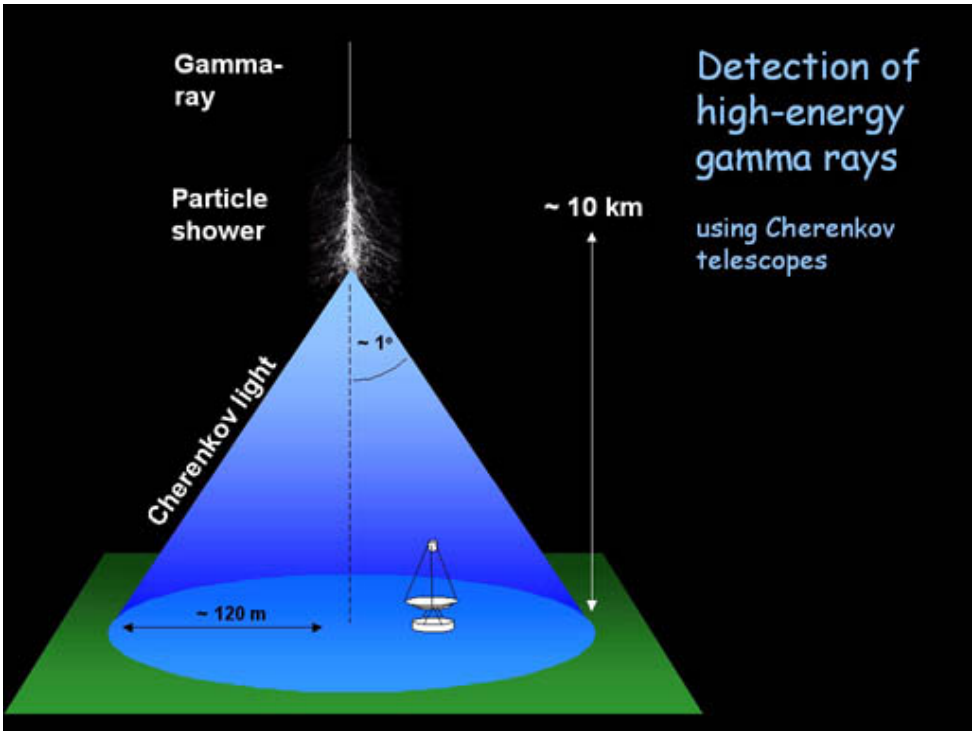

Figure 5.1: *Illustration of the Cherenkov cone emitted by the atmosphere resulting from a shower produced by a primary gamma-ray. Figure extracted from www.mpi-hd.mpg.de/hfm/HESS/pages/about/telescopes/#cherenkov.*

5.2 Hillas parameters

From the captured images it is possible to reconstruct the primary gamma-ray event. The main characteristics of these events are their direction, energy and time of arrival. In 1985, Hillas showed that from a few parameters of the captured image one can determine these quantities [146].

However, extensive air showers are not just produced by gamma-rays. Cosmic-rays such as protons, electrons, etc, also generate EAS producing Cherenkov emission which are collected by the mirrors. The large (for each gamma-ray there are about 1000 cosmic-rays

detected) number of relativistic atomic nuclei bombarding the Earth implies that hadronic showers are the main sources of background in gamma-ray detections. Hillas also showed that parameters associated to the shape of the images formed in the camera could be used for the gamma/hadron shower separation [146]. The image obtained from a shower initiated by a gamma-ray is more elliptical in shape, whereas for hadronic showers a more irregular image is recorded, as we can see in figure 5.2, which leads to the background reduction by the so-called gamma/hadron separation method.

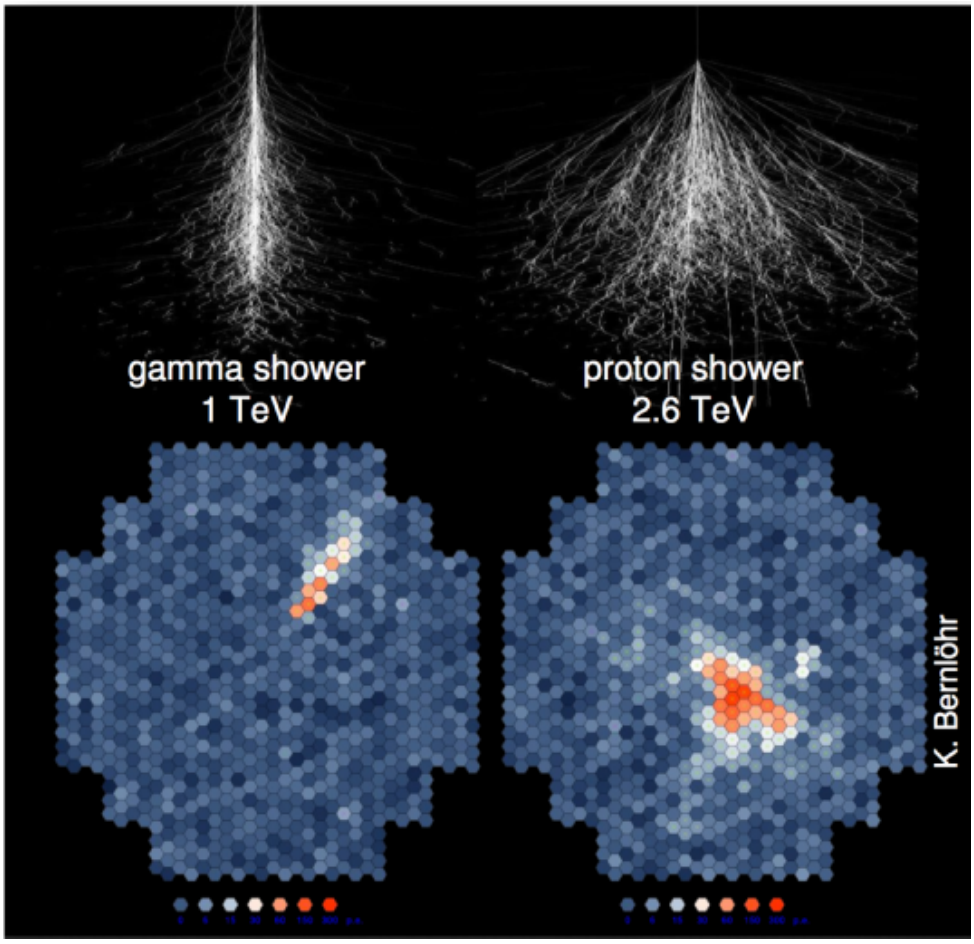

Figure 5.2: *Illustration of the image created in the camera of IACT detectors by showers of gamma-ray (left side) and proton (right side). Figure extracted from www.mpi-hd.mpg.de/hfm/∼bernlohr/sim_ telarray/Presentations/Corsika_ HESS.pdf.*

Figure 5.3 shows an illustration of the Hillas parameters: **size**, **width**, **length**, **alpha** and **distance**. The **size** is obtained from the total photons measured and depends on the energy and the impact parameter. The **width** and **length** carry information about the lateral and longitudinal development of the shower, respectively. The **distance** is defined as the space between the center of the field of view (FoV) and the center of gravity of the shower image, which is equivalent to the angle between the shower axis and the line that joins the shower maximum to the telescope. The **alpha** parameter, which is the angle between the major axis of the ellipse and the line jointing the center of the camera and

the center of the image, quantifies the parallelism between the shower and telescope axes. When the shower Cherenkov pool is imaged by more than one camera, the detection is called stereoscopic. In the right side of figure 5.3 this scheme is illustrated.

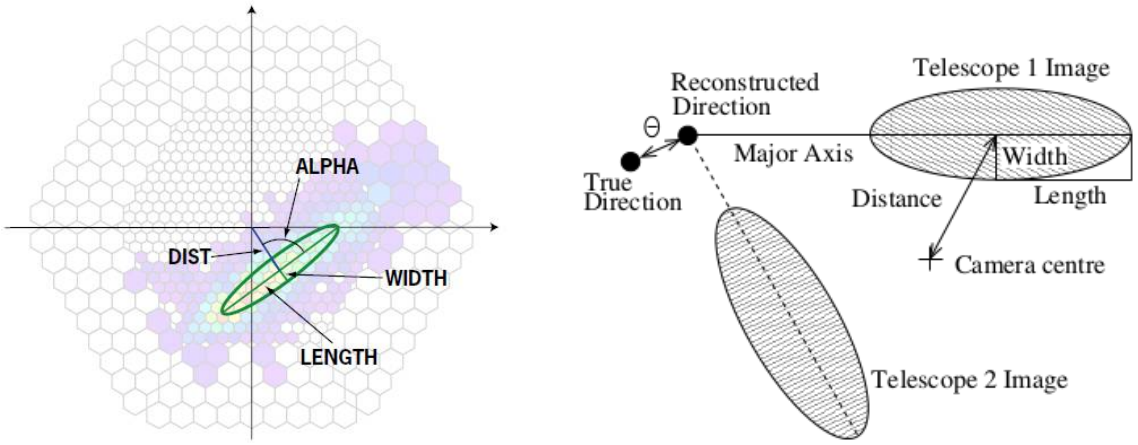

Figure 5.3: *Schemes showing the Hillas parameters describing the ellipse signal detected by IACTs. Left: a signal recorded by one camera (monoscopic mode). Right: a scheme of reconstruction of a signal detected by two cameras (stereoscopic mode). Figure extracted from [12].*

5.3 CTA instrument response functions

The next generation of IACTs is being built in two sites: in the Southern hemisphere, in Paranal, Chile, and in the Northern hemisphere, in one of the Canary Islands (La Palma), Spain. These two arrays of telescopes of different sizes will observe the sky in energies ranging approximately between 0.01 TeV up to 100 TeV. CTA will reach a flux sensitivity around one order of magnitude below the current IACT levels as we can see in figure 5.4. The sensitivity was obtained from Monte Carlo (MC) simulations and is defined as the minimum flux necessary for the CTA to get a detection with 5σ of significance from a point-like gamma-ray source. This figure also shows the sensitivity of other gamma-ray observatories that use different techniques, such as Fermi-LAT and HAWC [10].

The performance of an IACT observatory depends on the determination of several quantities, such as the energy and angular resolutions, effective collection area of the survey, etc. Such variables depend on several technical and design parameters. In order to meet the requirements suggested by the scientific community, intense MC simulations have been made to find the optimized array configuration [147]. These efforts are essential for the studies to be presented in the next sections.

Due to the finite resolution of the equipaments, the energy and direction primary photons measured are different from their true values. Figures 5.5 and 5.6 show the energy and angular resolutions obtained from the MC simulations for the third large simulation

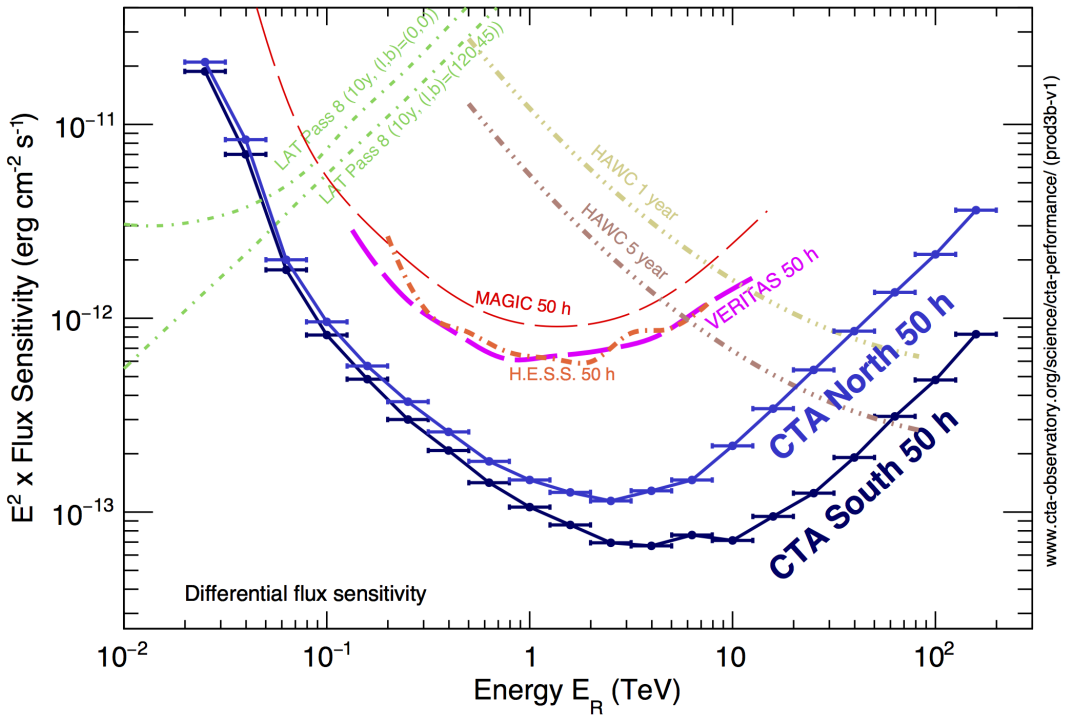

Figure 5.4: *Differential flux sensitivity as a function of the shower reconstructed energy E_R expected for the CTA for 50 hours of observation of a point-like source. For comparison, the sensitivity from other gamma-ray observatories are also shown.*

campaign, dubbed inside the CTA consortium as "prod3b-v1". Another important feature of an observatory is its effective collection area, which is energy dependent and was determined through simulations using observation campaigns of different durations, as shown in figure 5.7. These three quantities (angular and energy resolutions and effective area) play a fundamental role in essentially all the analyses since they define the instrument response function (IRF) of the CTA, which is responsible for making the connection between measured quantities and true ones. Mathematically, we can write for the event (primary photon) rate (in units of TeV^{-1})

$$m(\mathbf{d}) = \int d\mathbf{p}\, R(\mathbf{d}|\mathbf{p},\mathbf{a}) \times S(\mathbf{p}) \tag{5.1}$$

where $\mathbf{p}$ represents the true properties of the photon, such as energy, arrival time and direction. The observed quantities $\mathbf{d}$ are generally the measured energy, arrival time and direction. The source intensity (in units of TeV^{-1} m^{-2} s^{-1}) is represented by $S(\mathbf{p})$ and the IRF is described by $R(\mathbf{d}|\mathbf{p},\mathbf{a})$. The quantity $\mathbf{a}$ contains auxiliary parameters that the IRF may depend on, such as the telescopes pointing direction, subset of triggered telescopes, optical efficiencies, atmospheric conditions, etc. [148].

The CTA IRFs currently available were built for three optimized exposure times: 30

minutes, 5 hours and 50 hours. The IRFs are assumed to be factorized in the following way

$$R(\hat{\mathbf{n}}', E'|\hat{\mathbf{n}}, E) = A_{eff}(\hat{\mathbf{n}}, E) \times \mathrm{PSF}(\hat{\mathbf{n}}', E'|\hat{\mathbf{n}}) \times E_{disp}(E'|E) \tag{5.2}$$

where *prime* represents the measured quantities, whereas *unprime* variables are associated to true values.

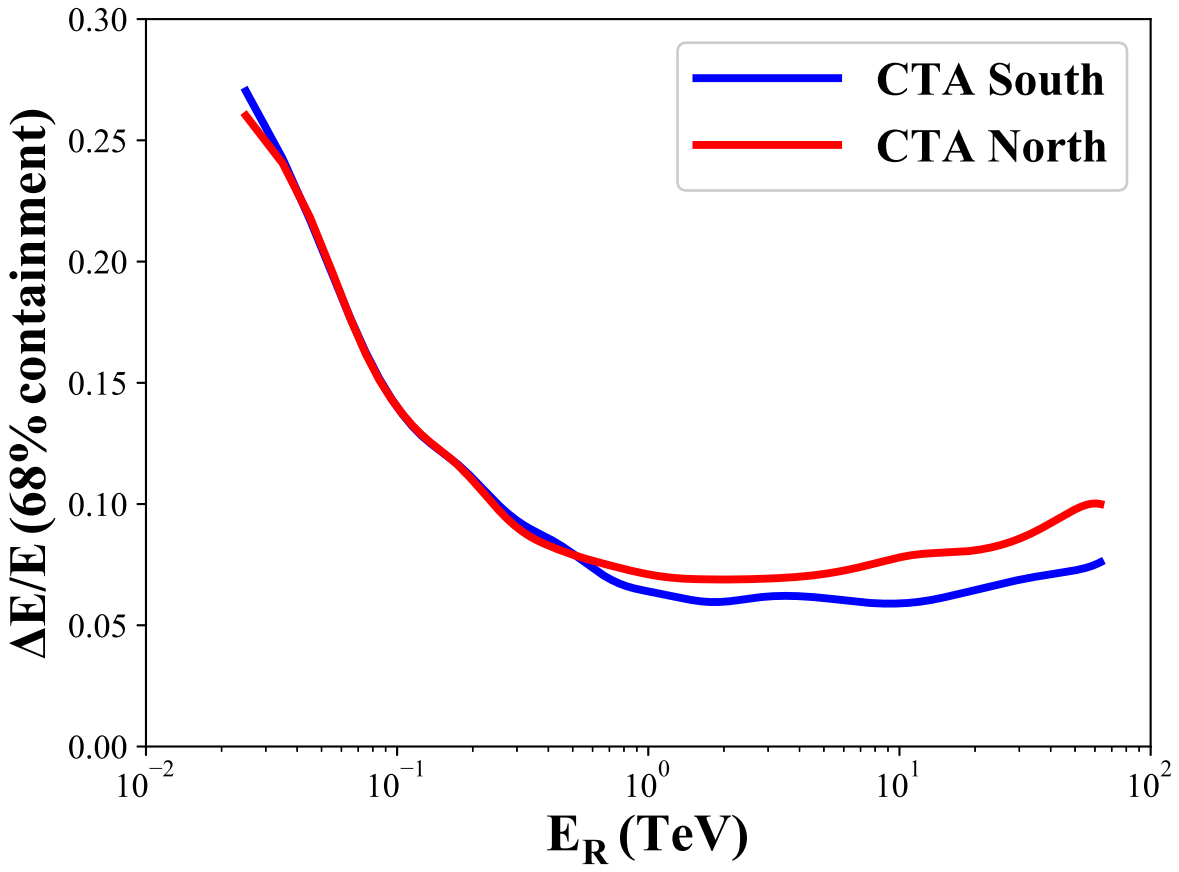

Figure 5.5: *Energy resolution of the CTA South and North as a function of reconstructed energies.*

The energy dispersion $E_{disp}(E'|E)$ and the point spread function $\mathrm{PSF}(\hat{\mathbf{n}}', E'|\hat{\mathbf{n}})$ represent a posteriori probabilities for the photon true energy and direction, respectively, given the measured values of those quantities. Here, we use a 2-dimensional symmetric Gaussian function to describe the PSF,

$$\mathrm{PSF}(\theta, E) = \frac{1}{2\pi\sigma_\theta^2(E)} e^{-\frac{1}{2}\frac{\theta^2}{\sigma_\theta^2(E)}} \tag{5.3}$$

where θ is the angular distance between the observed direction and the true VHE photon position, σ_θ is the angular resolution given in degrees. The energy dispersion is likewise

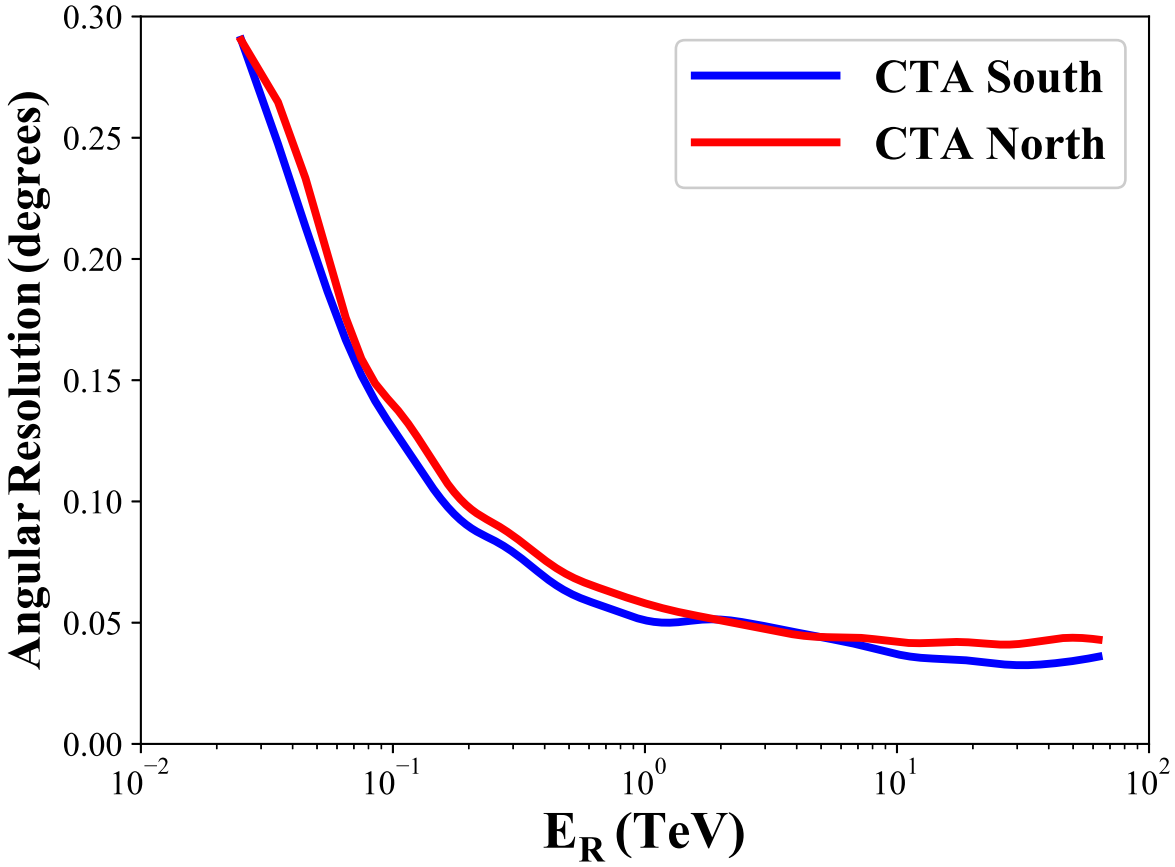

Figure 5.6: *Angular resolution of the CTA South and North as a function of reconstructed energies.*

modeled as

$$E_{disp}(E', E) = \frac{1}{\sqrt{2\pi}\sigma_E} e^{-\frac{1}{2}\frac{(E-E')^2}{\sigma_E^2}} \tag{5.4}$$

where σ_E is the energy resolution in units of TeV.

In addition to these parameters, another important quantity is the background rate. Residual cosmic-rays create a background which must be separated from the gamma-ray signal. Figure 5.8 shows the background rate expected for CTA in the southern array optimized for 50 hours of observation after gamma/hadron separation cuts [147].

The IRFs provided by the mass production "prod3b-v1" were obtained for point-like sources for two different zenith angles, 20 deg and 40 deg. For each one, two azimuth angles were simulated: in the directions of the magnetic North and South poles. Since the geomagnetic field affects the air shower development, differences in the performance were found between these two configurations. An azimuth-averaged IRF is also provided for each configuration. Since we will be interested in determining parameters of the dust component of the EBL, well determined SEDs at very high energies will be essential for our studies, thus we will focus in the southern array, which exhibits the best sensitivity of

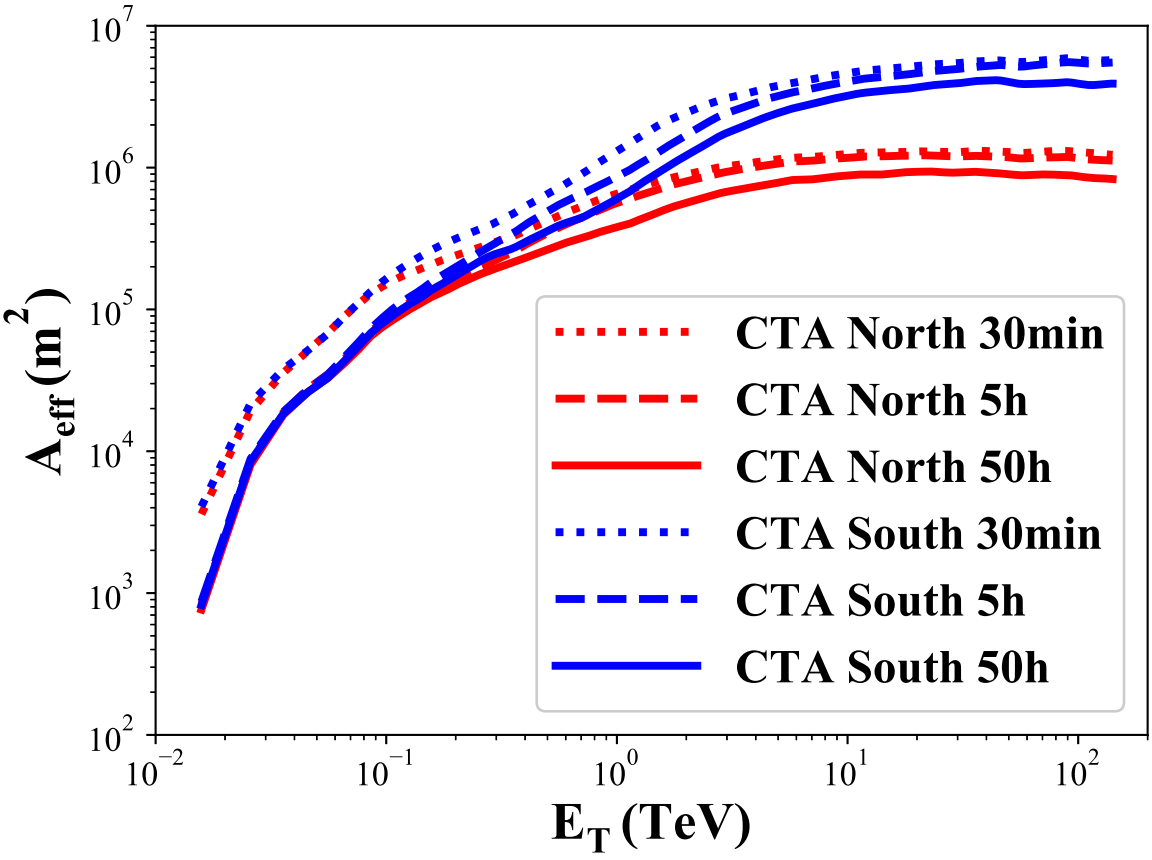

Figure 5.7: *Effective collection area of CTA South and South as a function of true energies. The optimized effective area is shown for three different exposure times: 30 minutes, 5 hours and 50 hours.*

the two arrays around tens of TeV, as we can see in figure 5.4. Figure 5.9 shows the layout of the telescopes used in our simulation. The analysis performed in the next sections is based on the South IRFs for zenith angle of 20 deg in the azimuth-averaged case.

For the determination of the quantities described here, which form the instrument response function for CTA optimized for specific exposure times, realistic and detailed simulations were performed in [147] including the EAS simulation for primary gamma-rays and cosmic ray showers as well as Cherenkov photons ray tracing across the telescope optical systems, response of the electronics, etc. Three different telescope sizes were treated in the simulation: LST (Large Size Telescope), MST (Middle Size Telescope) and SST (Small Size Telescope).

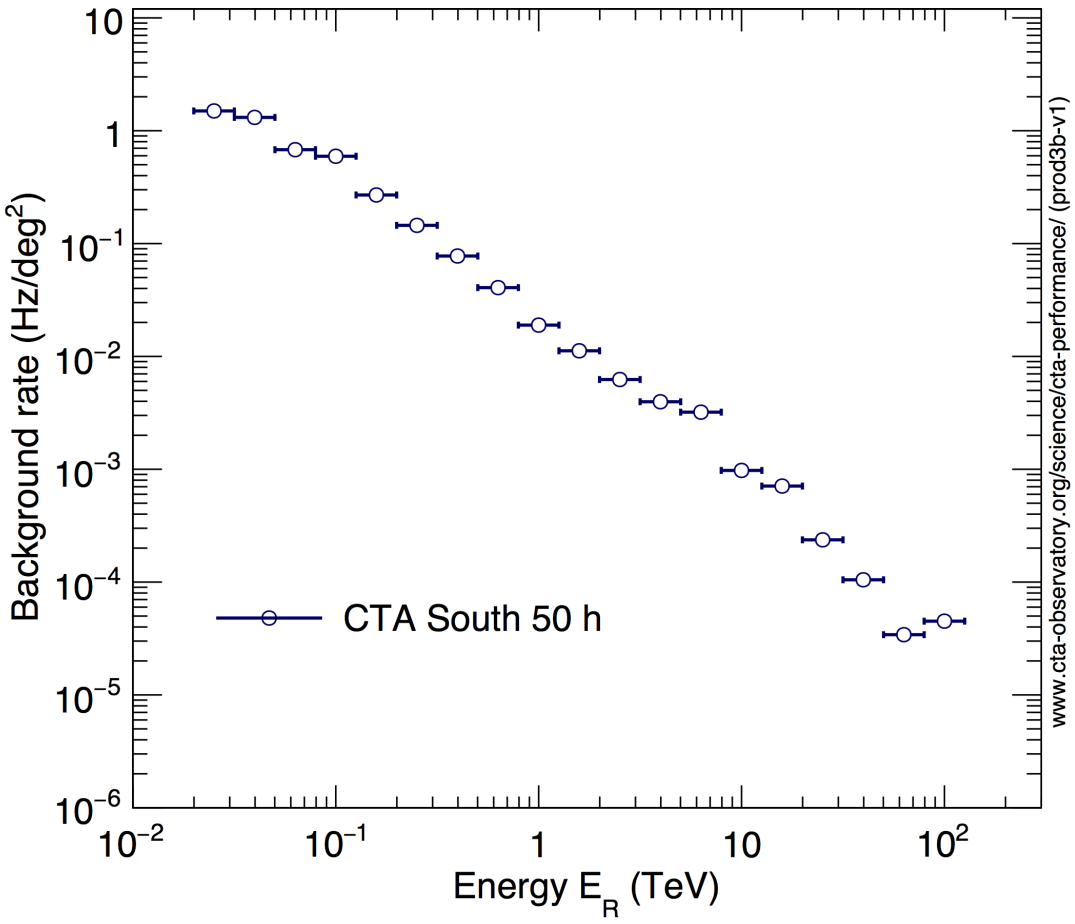

Figure 5.8: *Background rate from cosmic-rays estimated for CTA South with gamma/hadron separation cuts optimised for 50 hours of observation time.*

5.4 Simulating observational campaigns of extragalactic point sources

The IRFs determined during the mass production simulations described in the last section allow much faster physics simulations to be done. Ctools, for instance, is a free software which allows to do scientific analysis using CTA data [148]. It is based on GammaLib, a toolbox for high-level analysis in gamma-ray astronomy [148]. Gamma-ray events can be simulated [1] for a given source and background models. For this, some information must be provided, such as the region of interest (ROI), observation time, energy interval and IRF. The photon flux can be simulated for several intrinsic spectrum parameterizations, such as power-law, log-parabola, etc., including a customized flux as input. This is the ideal case for our studies, because the SED measured at Earth must be attenuated by EBL. By using the GLF elaborated by M. Ajello et al. for BL Lacs and FSRQs [61,62], which

[1] With the executable called "ctobssim"

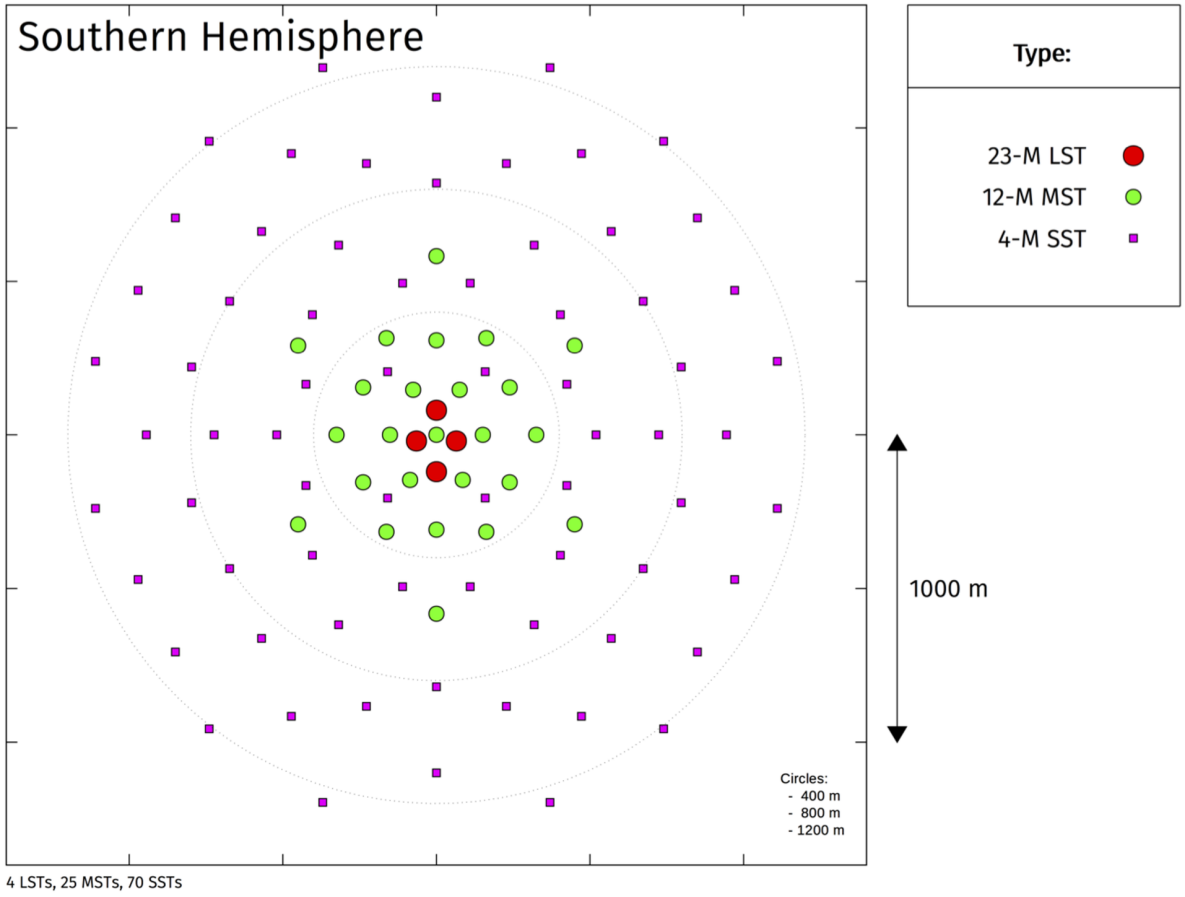

Figure 5.9: *Layout of telescopes simulated for observations from the southern hemisphere array. The different points correspond to the different mirrors. Red: Large Size Telescopes (LST). Green: Middle Size Telescopes (MST). Purple: Small Size Telescopes (SST). Figure extracted from www.cta-observatory.org/project/technology/.*

was shown in Chapter 3, with the EBL model developed by F10 [29], it was possible to build these attenuated spectra. The intrinsic source spectrum parameterization behavior assumed is the power-law flux with spectral index Γ sampled from the GLF.

In order to select sources with high statistical significance of detection, we have fitted the data collected in the simulation with Ctools [2] using a specific model of interest. The statistical significance associated to the observation is determined through a likelihood ratio test where the null hypothesis (the detected photons are coming from background cosmic rays) was compared to an alternative one (the photons are coming from a gamma-ray point-like source). The corresponding test statistic (TS) is given by

$$TS = -2(\ln \mathcal{L}_0 - \ln \mathcal{L}_1), \tag{5.5}$$

where $\mathcal{L}_0$ is the null hypothesis and $\mathcal{L}_1$ the alternative one.

[2] With the "ctlike" executable.

Based on the recipe usually adopted by Fermi-LAT observations [149], we use a power-law spectrum with fixed spectral index, $\Gamma = 2.48$ (typical value). Therefore, just the normalization is allowed to vary. From Wilks's theorem [80], the TS must be asymptotically distributed as χ^2_n (where n is the difference between the dimensionality of the parameter spaces of the two hypotheses) when the null hypothesis is assumed to be true. With $n = 1$, $\sqrt{\mathrm{TS}}$ can be immediatelly identified as the number of Gaussian standard deviations. Here, sources presenting TS<25 (5σ) for 30 minutes of observation are excluded from our analysis. With an initial set containing 36 sources sampled from Ajello's BL Lacs GLF, 16 of them were detected with at least 5σ of significance. Such sources define the sample used in the analysis proposed in this chapter. Table 5.1 shows the main information of each source.

It is worth mentioning that the TS could be calculated if the spectral index were also free to vary. In this case, the value of the test statistic corresponding to 5σ of detection significance would be TS=28.8. Due to the long computation times required when the spectral index is included in the fit, we decided to perform the fits at the source selection level with a fixed index.

Name	z	$\log(L_\gamma/erg\,s^{-1})$	Γ	TS_{30m}	$\mathrm{TS}_{30m}(>1$ TeV)
src1	0.0982	45.3331	1.9913	1307.8	1060.3
src2	0.0965	44.0213	1.8087	56.5	45.8
src6	0.0581	44.0214	2.1006	69.4	31.6
src10	0.0968	45.0219	1.9177	670.5	736.0
src11	0.0558	44.2770	2.0971	58.2	101.6
src12	0.0478	43.9742	2.1414	49.5	65.3
src13	0.0344	43.9385	1.9012	1271.2	957.1
src19	0.0808	44.0241	1.5489	692.8	542.9
src21	0.0459	44.2640	1.9330	943.5	932.4
src22	0.0475	44.2443	1.6912	3858.7	4088.2
src23	0.0853	44.1772	1.8887	52.3	86.0
src26	0.0873	44.1389	1.6319	355.2	422.0
src27	0.0367	44.3515	1.9808	1976.1	2092.5
src28	0.0949	44.4405	2.0016	26.6	65.6
src31	0.0611	44.3077	1.6680	2340.0	2341.2
src32	0.0447	44.4493	1.6810	10988.7	10989.1

Table 5.1: *Summary of the source parameters generated by GLF for Bl Lacs. The two last columns are the calculated test statistic for 30min case, where TS_{30min} regards the whole energy range measured, 0.1 TeV - 100.0 TeV. TS_{30min}(>1 TeV) is calculated from 1.0 TeV up to 100.0 TeV.*

5.5 Construction of a likelihood

We are interested in estimating the potential of the CTA regarding the determination of EBL and source intrinsic parameters. In particular, the relative contribution of the dust grains, the spectral index and the gamma-ray luminosity will be the work variables of the analysis performed here.

For gamma-ray observations, the probability of detection is generally assumed to follow a Poisson distribution. For a given energy bin k, the probability of observing n_k photons when a given model predicts a corresponding number count m_k is

$$P_k = \frac{m_k^{n_k} e^{-m_k}}{n_k!}. \tag{5.6}$$

The product of the probabilities over all the bins gives us the probability of getting the data collected, which is the likelihood

$$\mathcal{L} = \prod_k \frac{m_k^{n_k} e^{-m_k}}{n_k!}. \tag{5.7}$$

Usually, it is more convenient to work with $\ln \mathcal{L}$, so we have

$$\ln \mathcal{L} = \sum_k^{N_{bins}} (n_k \ln m_k - \ln(n_k!)) - N_{pred}, \tag{5.8}$$

where N_{pred} is the total number of photons predicted by the model.

As we saw in Section 5.3, equation 5.1 shows how to build the counting rate model m_i. Firstly, it must be the combination of source and background

$$m_i = s_i + b_i \tag{5.9}$$

where s_i is the signal from a point-like source convoluted with the CTA IRF and b_i is the background counting rate estimated by Monte Carlo simulations, as we saw in Section 5.3. We write the source signal as

$$S(E, \hat{\mathbf{n}}) = \Phi(E; L_\gamma, z, \Gamma)\, e^{-\tau(E,z)}\, \delta(\hat{\mathbf{n}}). \tag{5.10}$$

Therefore, the predicted signal contribution obtained by marginalizing the incoming flux 5.10 over the primary photon true energy and direction is

$$s(E', \hat{\mathbf{n}}' | z, \Gamma, L_\gamma, \hat{\mathbf{n}}) = \int\int dE\, d\Omega R(E', \hat{\mathbf{n}}'; E, \hat{\mathbf{n}})\, S(E, \hat{\mathbf{n}}). \tag{5.11}$$

The number of expected photons in a bin k is given by integrating 5.9 over the measured quantities of such bin. The total number of expected photons is obtained integrating 5.9

over the whole range of the measured quantities

$$N_{pred} = \int \int dE'\, d\Omega'\, m(E', \hat{\mathbf{n}}'). \tag{5.12}$$

Once the likelihood is constructed, we can find the set of parameters that maximizes such function. It is worth noting that the term $\ln(n_k!)$ in equation 5.8 is model independent, in such a way that the function which we will maximize is

$$\ln \mathcal{L} = \sum_{k}^{N_{bins}} n_k \ln m_k - N_{pred}. \tag{5.13}$$

5.6 Forecasts for the sensitivity to dust grain fractions

Here, we present the results of forecasts for the CTA sensitivity to dust grain fractions as well as intrinsic spectrum parameters. The core of the analysis is based on the binned likelihood previously described which is fed by photons collected by telescopes with IRFs given by CTA prod3 during simulated observation campaigns of extragalactic point sources.

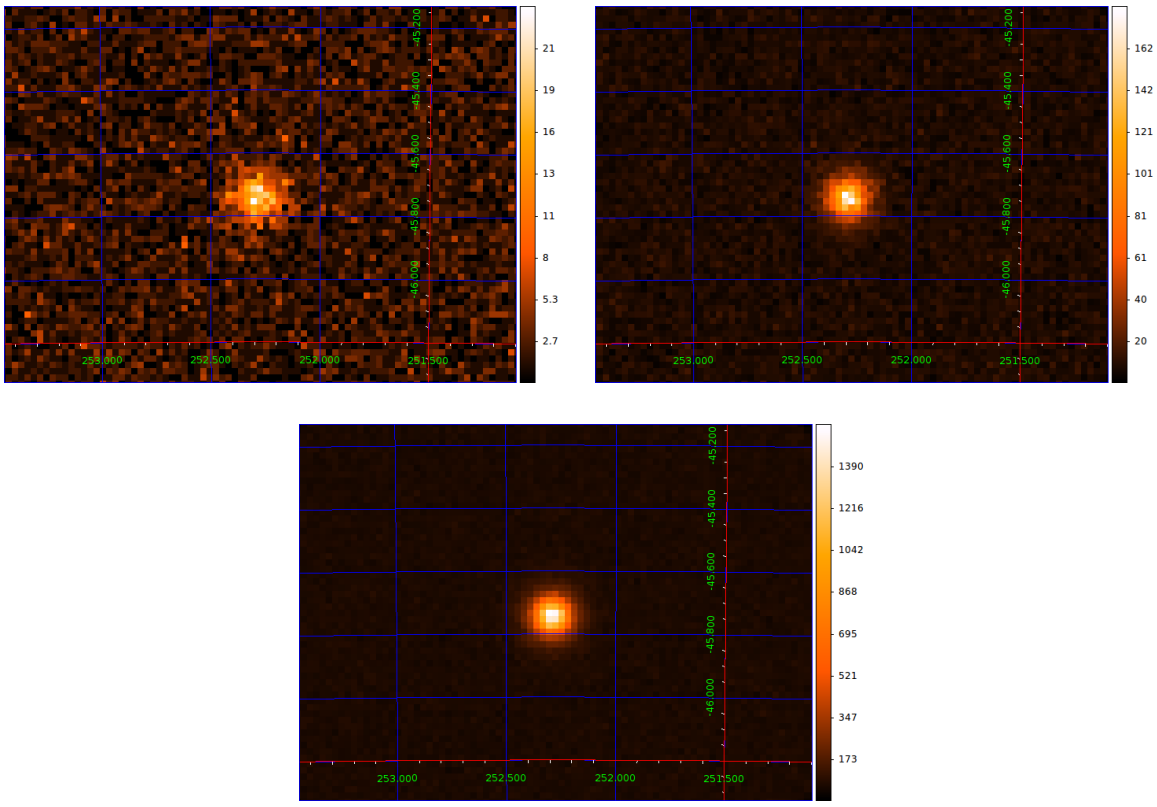

Figure 5.10: *Sky maps generated from the simulated observation of the src27 for the three exposure times studied. In the left-top we have the case of 30 minutes of observation, while in top-right the 5 hours case is shown. The 50 hours case is exhibited in the bottom. The color axis corresponds to the photon counting.*

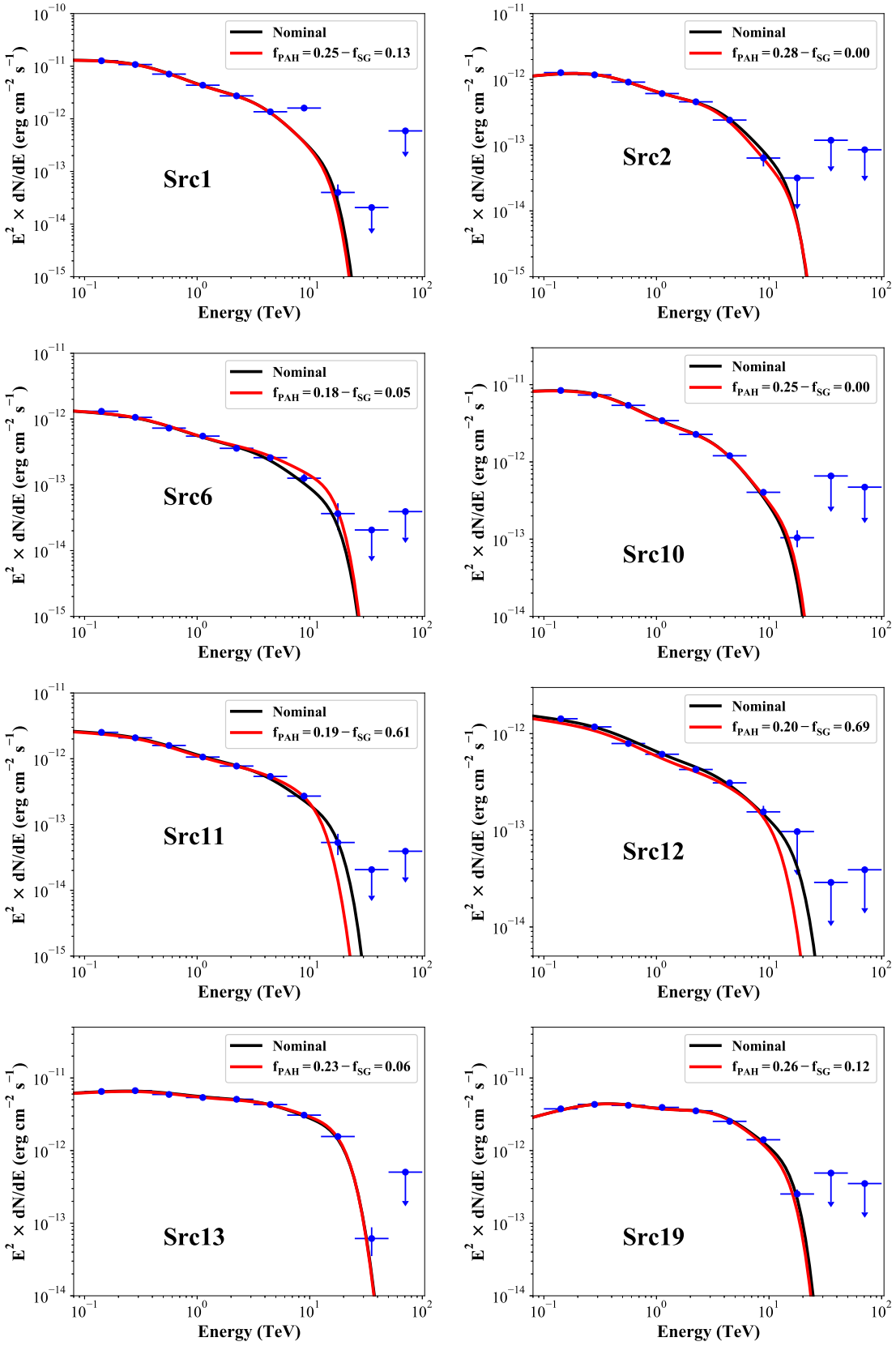

Figure 5.11: *Spectra of the sources. The SED with EBL nominal fractions (black line) and those determined by the likelihood maximization (red line) are superimposed to the spectra.*

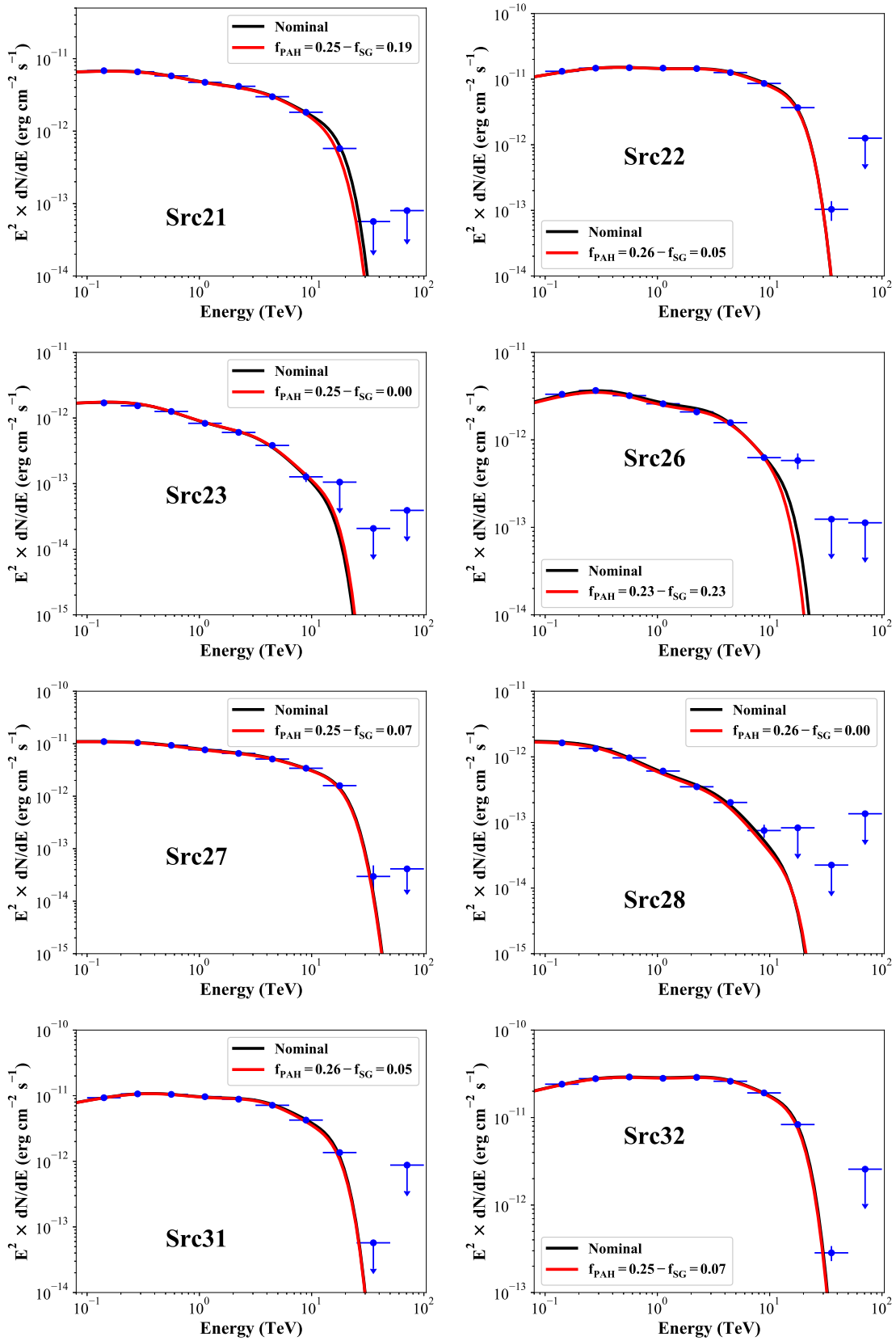

Figure 5.12: *Continuation of figure 5.11.*

Three different observation times were simulated for the sources in the sample defined in table 5.1: 30 minutes (30min), 5 hours (5h) and 50 hours (50h). The photon counts sky maps observed for these three exposure times for one of the sources (Src27) are shown in figure 5.10 providing the spatial distribution of primary photons in the ROI. In order to visualize the energy dependence of the flux, figures 5.11 and 5.12 show the spectra of the whole sample for the 50h case. Two solid curves are superimposed to the binned flux: the SED attenuated by EBL with nominal dust fractions (black) and the SED attenuated by EBL with fractions obtained from the maximum likelihood solution (red). The reader interested in visualizing the spectra for 30min and 5h cases should go to the Appendix C.

As we can see, all the spectra are reasonably described by the parameters obtained from the likelihood maximization, even for sources presenting a low photon counting around tens of TeV, where for some bins only flux upper limits could be established. These, in turn, are low detection TS sources for TeV energies (TS(>1 TeV)) as we can see in table 5.1. In general, these gamma-ray sources have a soft spectrum ($\Gamma > 1.8$) and just a few photons can be detected in energies where the EBL dust component becomes important. Sources with harder spectra, such as src22 and src32, exhibit a large TS(>1 TeV) and hence the dust parameters can be better determined. The likelihood function

$$\mathcal{L} \equiv \mathcal{L}(\alpha_i) \tag{5.14}$$

where

$$\alpha_i = \{f_{PAH}, f_{SG}, \Gamma\}^3 \tag{5.15}$$

can quantify the resolution of the CTA to the parameters α_i. From the Bayes' theorem, we can write

$$P(\alpha|data)P(data) = P(data|\alpha)P(\alpha). \tag{5.16}$$

If nothing about the a priori probability $P(\alpha)$ is assumed (i.e. $P(\alpha) = 1$ for a flat prior), the a posteriori probability $P(\alpha|\text{data})$ is equal to the likelihood $P(\text{data}|\alpha)$.

Figures 5.13 and 5.14 show the posterior (i.e. the likelihood, since we have adopted flat priors on all parameters of interest) as a function of the PAH fraction. The curves shown are not marginalized probability distributions, but instead they correspond to the likelihood conditioned to the fitted values of the $n-1$ remaining parameters, to know: f_{SG}, Γ. For the 30min case, the width of the likelihood is the largest compared to the curves for 5h and 50h cases. Increasing the exposure time the likelihood becomes narrower and its maximum goes towards the nominal value. For 50h, a good determination of the f_{PAH} is obtained with almost all cases within 1σ from the true value. Figures 5.15, 5.16, 5.17 and 5.18 show the likelihood as a function of the small and large grain fractions. The determination of these fractions is not as good as the PAH case since the photon

[3]Since the dust fractions must obey de normalization condition $\sum f_i = 1$, just two fractions are being taken into account in the fit.

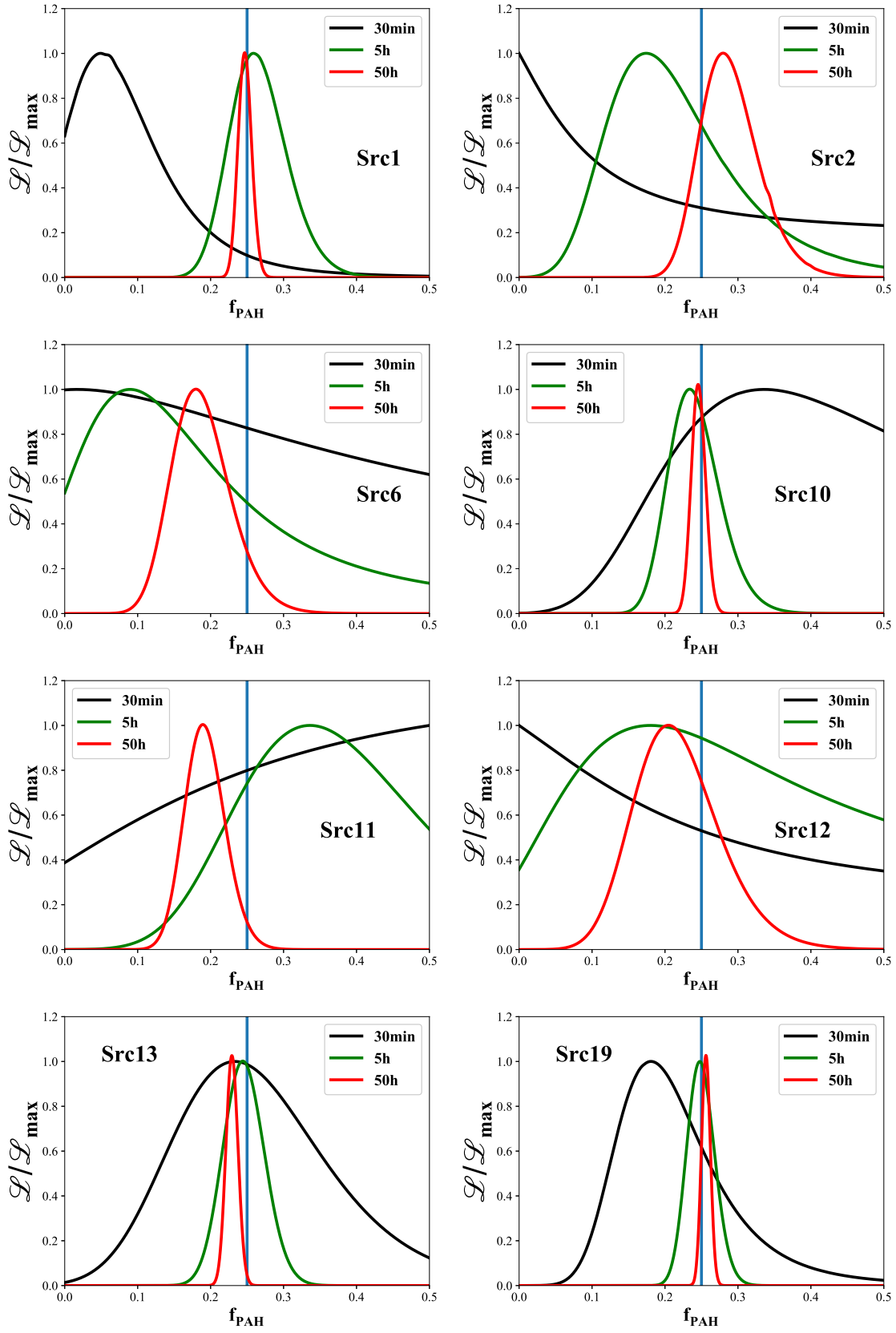

Figure 5.13: *Likelihood as a function of f_{PAH}. The black curves correspond to the 30min, green lines to the 5h and red to the 50h case. The vertical line corresponds to the true solution.*

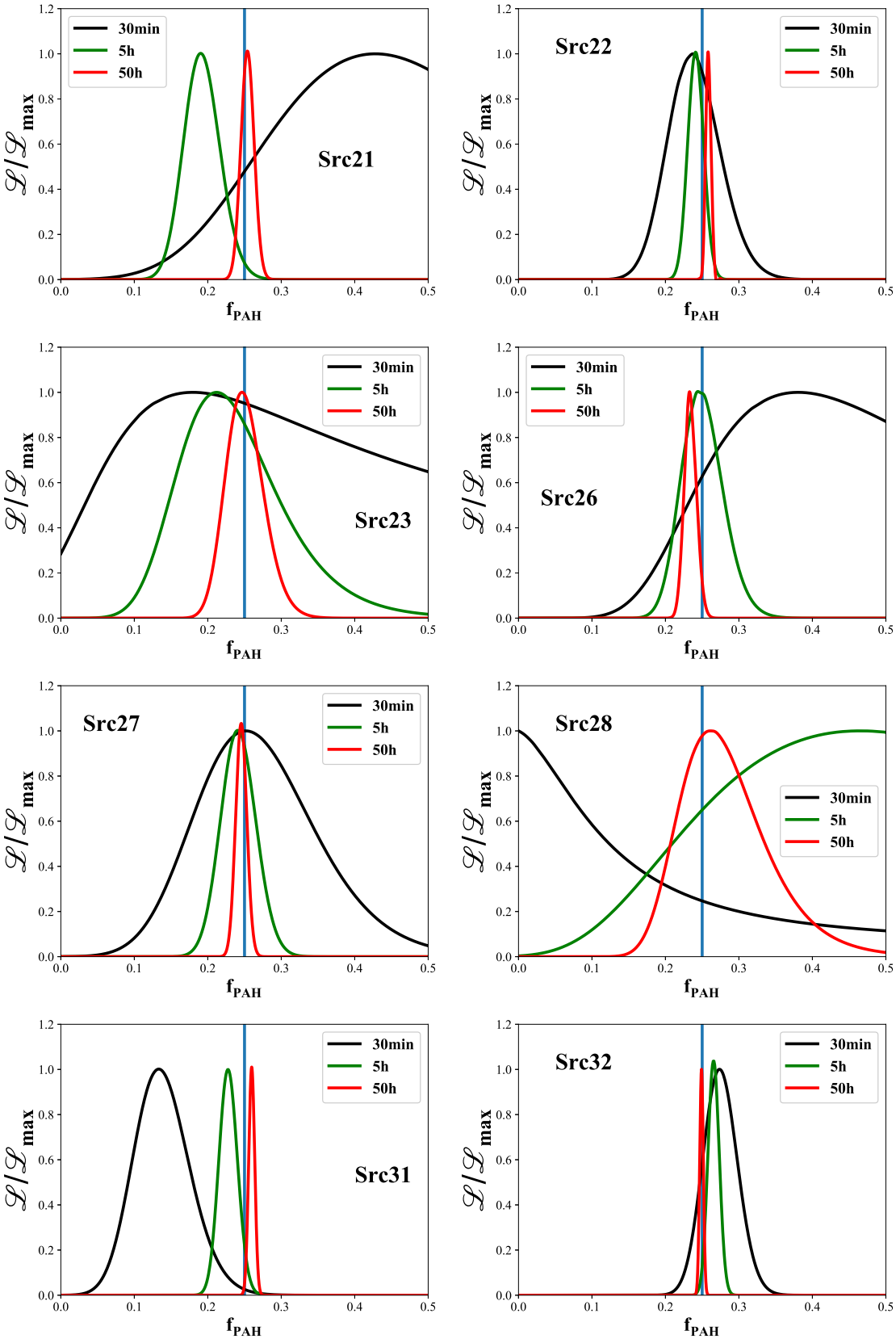

Figure 5.14: *Continuation of figure 5.13.*

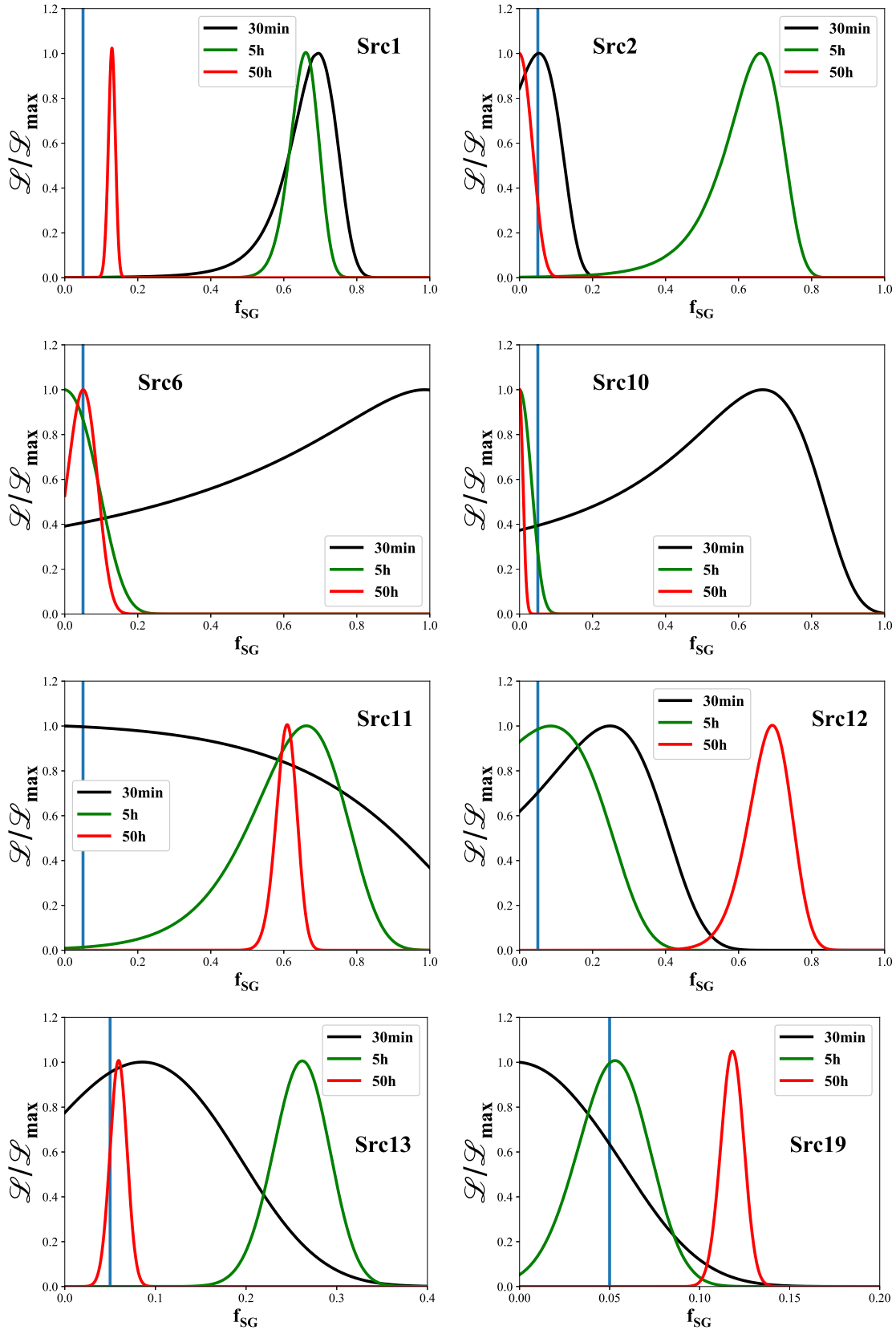

Figure 5.15: *Likelihood as a function of f_{SG}. The black curves correspond to the 30min, green lines to the 5h and the 50h case with red ones. The vertical line corresponds to the true solution.*

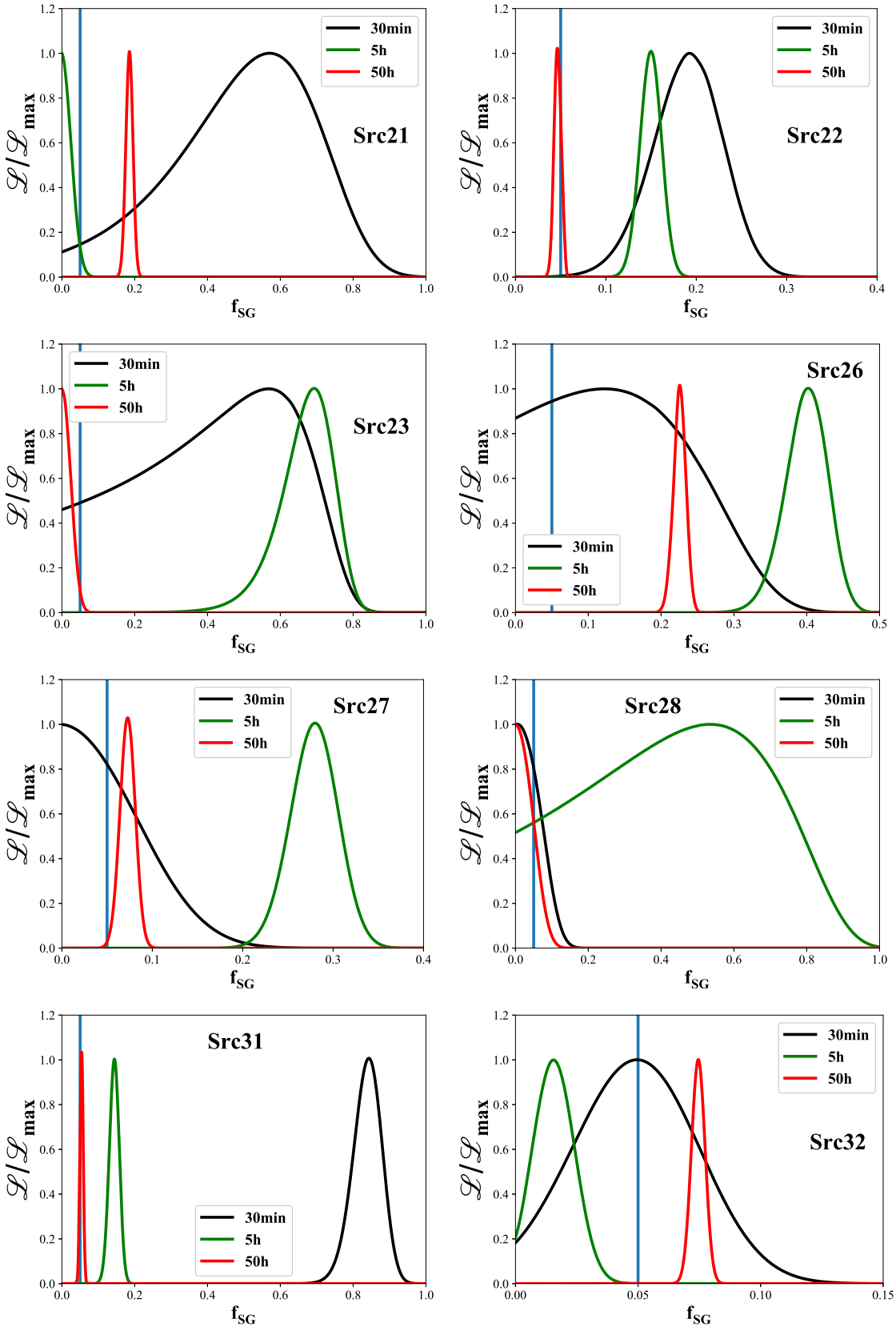

Figure 5.16: *Continuation of figure 5.13.*

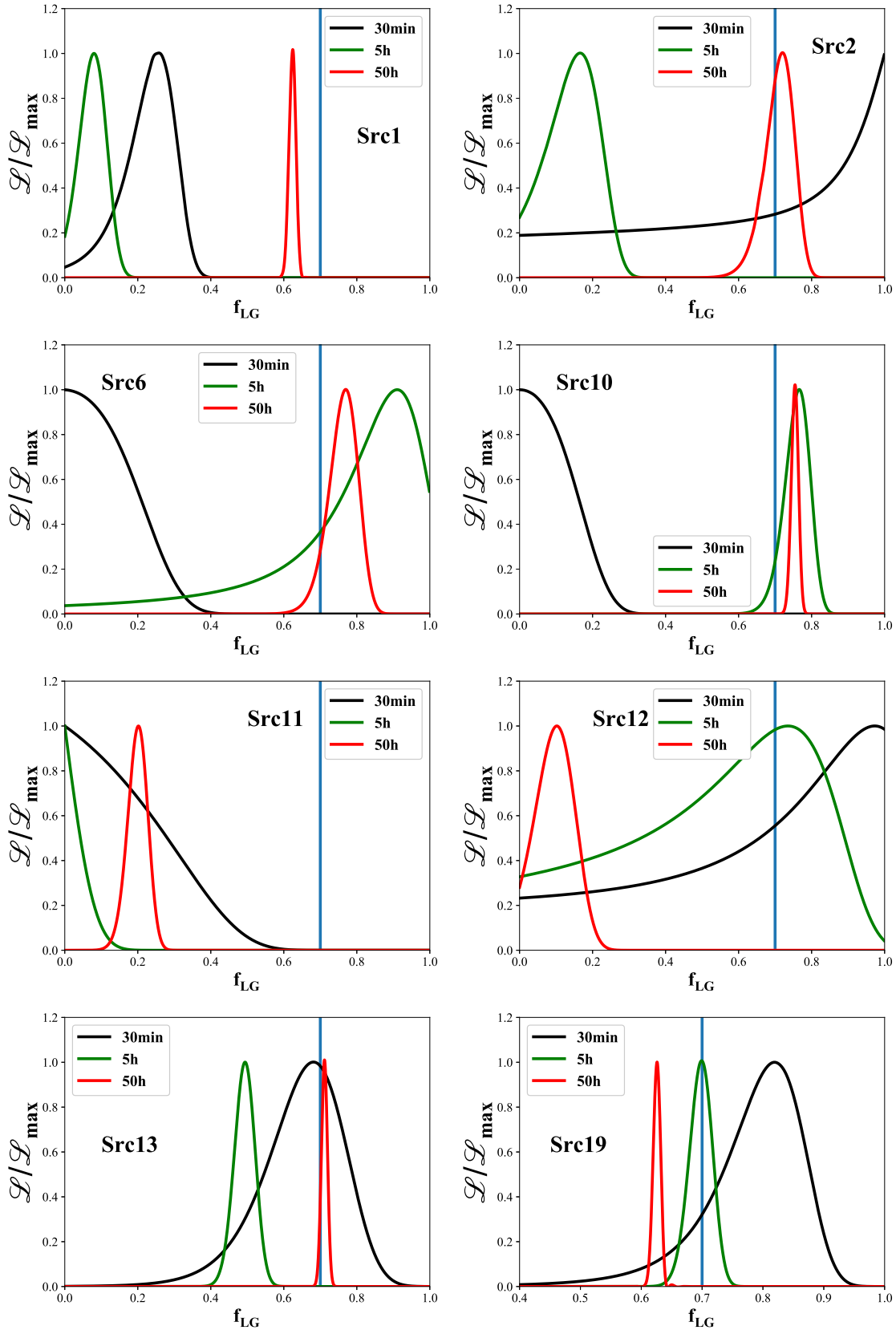

Figure 5.17: *Likelihood as a function of f_{LG}. The black curves correspond to the 30min, green lines to the 5h and the 50h case with red ones. The vertical line corresponds to the true solution.*

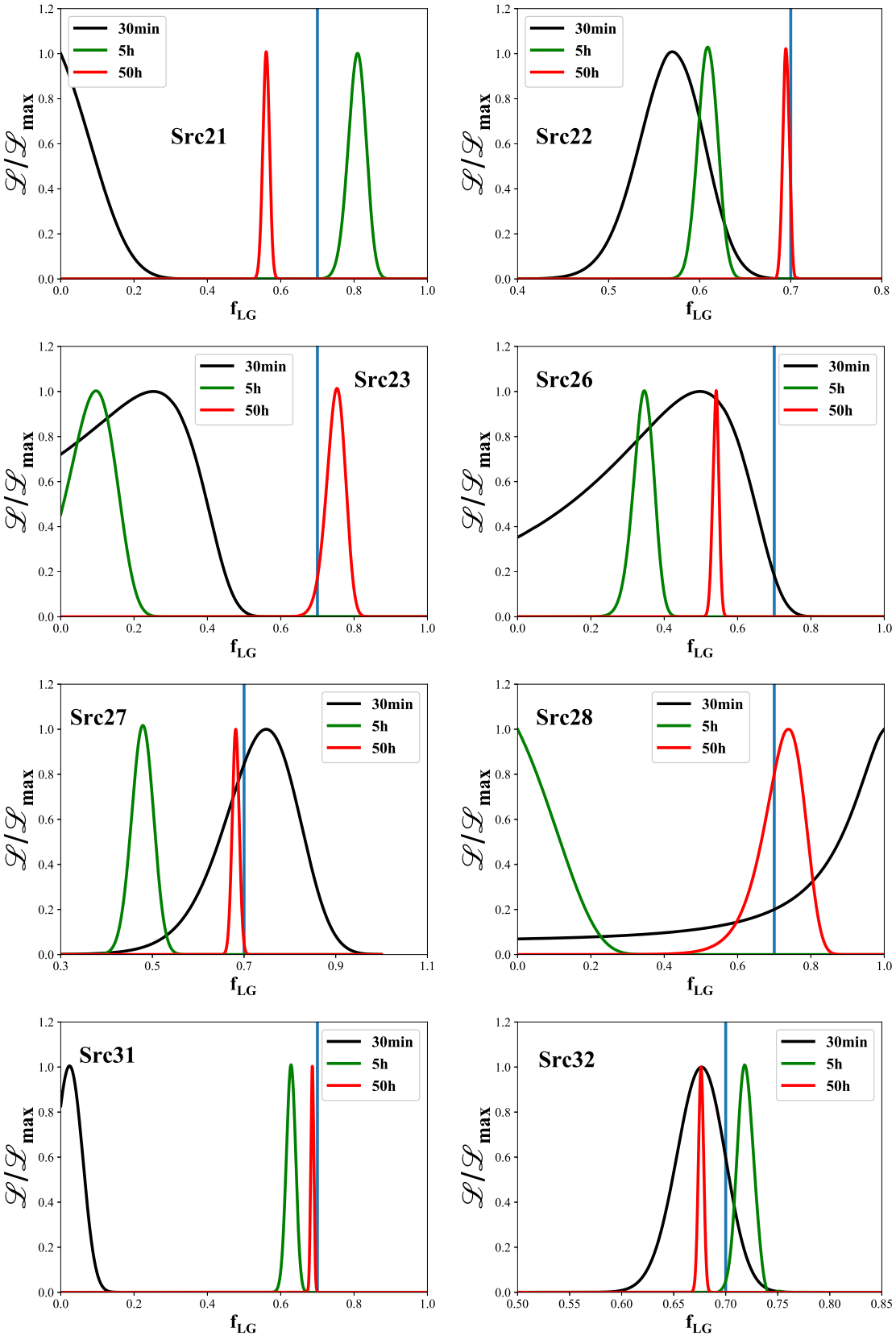

Figure 5.18: *Continuation of figure 5.13.*

counts are still low, for all observations times, in the energy range in which SG and LG are important.

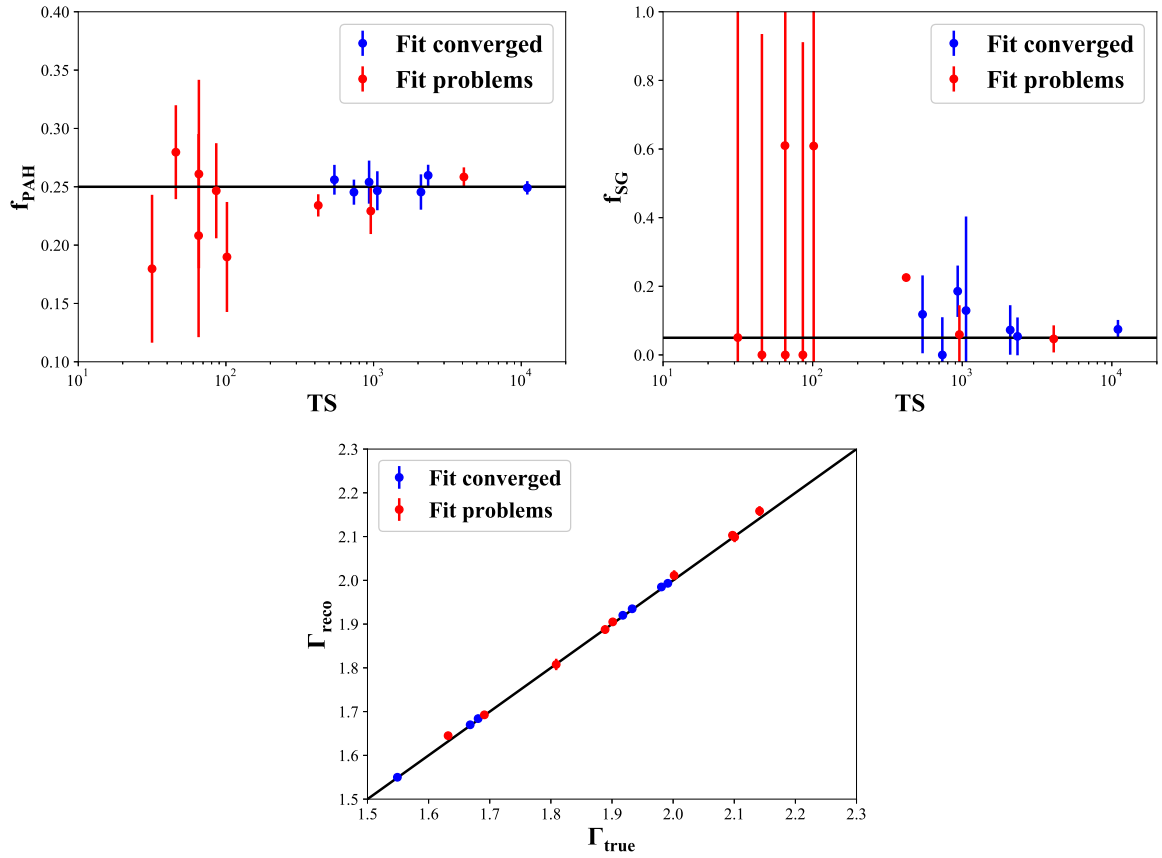

Figure 5.19: *Analysis for the 50h case with three free parameters assuming L_γ fixed in the true value. Top-left: PAH dust fraction. Top-right: Small grains. Bottom: Spectral index. The black lines represent the expected value of each parameter.*

The results obtained through the likelihood maximization with these three free parameters ($\alpha_i = \{f_{PAH}, f_{SG}, \Gamma\}$) for the 50h case can be visualized in figure 5.19. As we can see, the uncertainties on the fitted small grain fractions are, on average, larger than those associated to the PAH relative contribution, but for sources with large TS the SG dust fraction can also be determined with a good resolution. Differently from the relative dust contributions, the reconstructed spectral index are well determined independently of the detection significance of the source. This should be expected since the spectral index is responsible for the description of the intrinsic flux in the whole energy range considered, including the region dominated by the stellar attenuation. On the other hand, the determination of dust fractions are conditioned to a good measurement of the SEDs at specific energy regions. During the fit procedures, which were made with the Minuit package of ROOT [150], problems of convergence in some sources were detected and the reason of such problems must be understood.

A second case is performed considering also the gamma-ray luminosity of the source

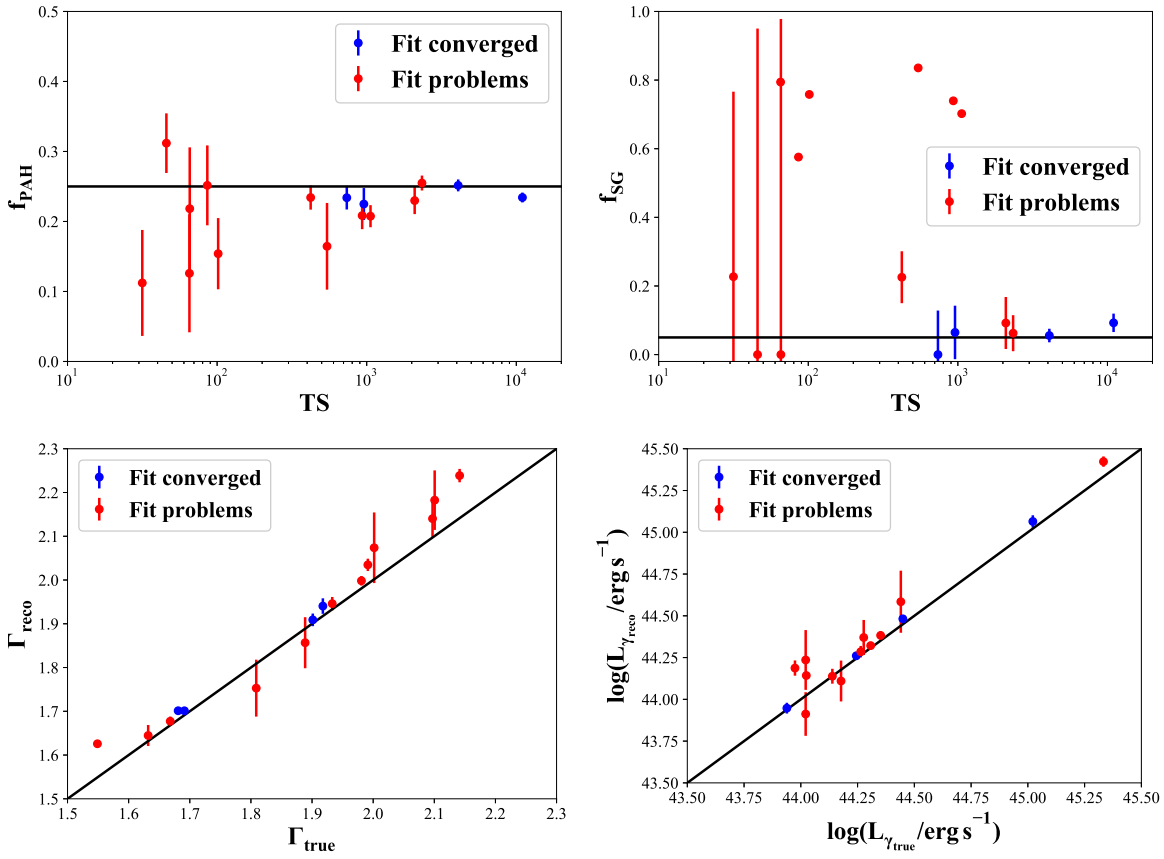

Figure 5.20: *Analysis for the 50h case with four free parameters. Top-left: PAH dust fraction. Top-right: Small grains. Bottom-left: Spectral index. Bottom-right: Luminosity. The black lines represent the expected value of each parameter.*

in the fit, $\alpha_i = \{f_{PAH}, f_{SG}, \Gamma, L_\gamma\}$. Figure 5.20 shows the values found from the likelihood maximization. We can see that in this case, the uncertainties of f_{PAH} and Γ become, on average, larger than the case with the luminosity fixed at its true value. For the f_{SG} parameter the fits are even worse than in the previous 3-parameter fit. The red points in figure 5.20 indicate fits with problem where either the minimization of $f = -\ln\mathcal{L}$ did not converge or the uncertainties could not be properly estimated. In fact, we can see this behavior also in the case previously considered ($\alpha_i = \{f_{PAH}, f_{SG}, \Gamma\}$). The attenuation by small grains becomes important at energies above that where PAH are dominant, therefore, the fits performed were unable to determine correctly the small grains for several of the sources in our sample.

In order to get around the problem of the lack of sensitivity to SG fractions in the fit, a last case is considered, now fixing the SG fraction in the nominal value, $f_{SG} = 0.05$, and leaving free in the fit the parameters $\alpha_i = \{f_{PAH}, \Gamma, L_\gamma\}$. Figure 5.21 shows the results obtained for each quantity. For the PAH fraction, the behavior is similar to the previous cases, the higher the TS the better the determination of f_{PAH}. A good resolution is also obtained in the determination of the spectral index and the gamma-ray luminosity,

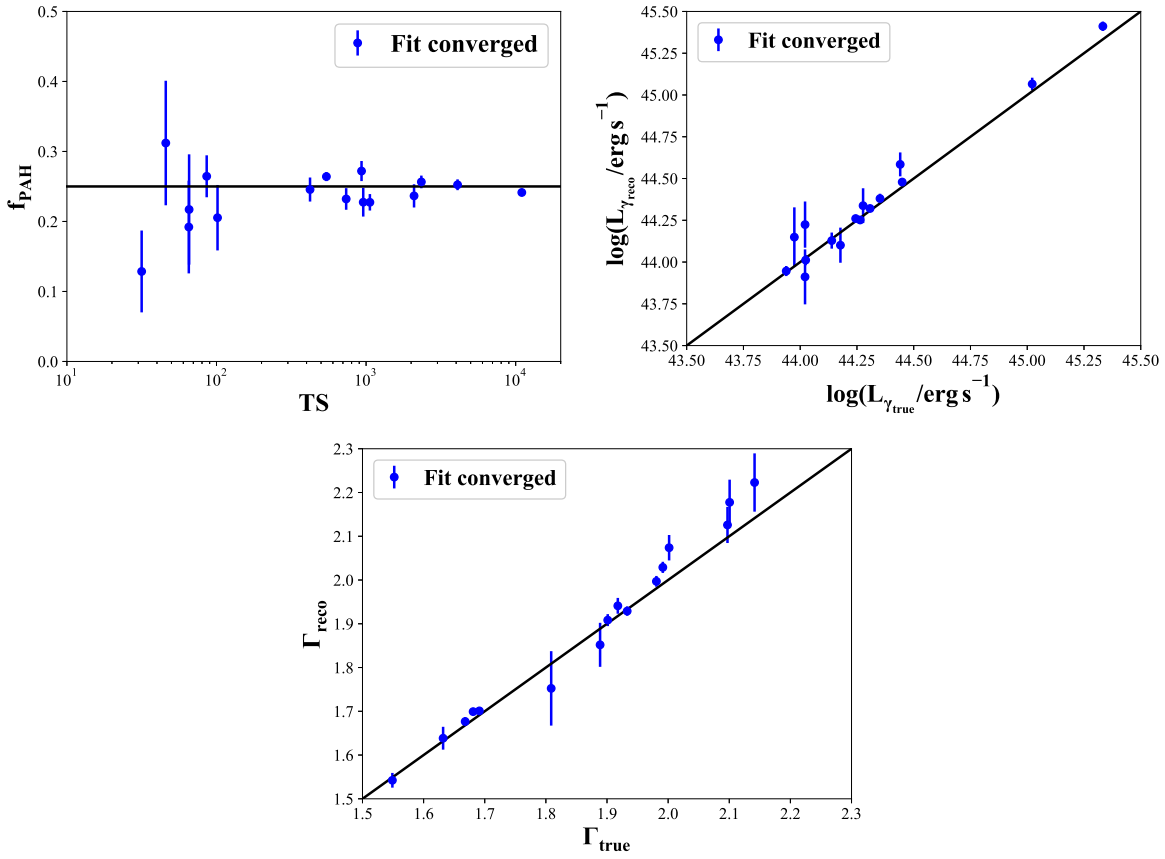

Figure 5.21: *Analysis for the 50h case with three free parameters assuming f_{SG} fixed in the true value. Top-left: PAH dust fraction. Top-right: Luminosity. Bottom: Spectral index. The black lines represent the expected value of each parameter.*

with the reconstructed parameters within 1σ, on average, from the true values. Special attention should be paid to the parameter Γ since a clear bias can be identified in figure 5.21 for soft spectral indices ($\Gamma \gtrsim 2.0$). These sources exhibit a low number of photons around tens of TeV, in such way that f_{PAH} cannot be well determined and higher values of Γ_{reco} are obtained in comparison to Γ_{true}, which is the case of src6 and src12, for example (see table 5.2). In this case (i.e., when the set of fit parameters is given by $\alpha_i = \{f_{PAH}, \Gamma, L_\gamma\}$), the fits for all the sources converged with no problems and the fit values obtained are shown in table 5.2.

As we can see from these three different analyses, the sample of sources considered are not suitable to study the relative contribution of the small grains in the attenuation process. On the other hand, the PAH fraction is well determined for sources presenting large TS. A good resolution is also found in the determination of the spectral index and the gamma-ray luminosity in the sample considered.

This single source analysis can be extended to include combination of several sources, because even though they have different intrinsic spectra, the EBL is common to all of them. The different redshifts of the sources being included in the likelihood bring extra

Source	$\log(L_\gamma/erg\,s^{-1}) \pm \Delta\log(L_\gamma/erg\,s^{-1})$	$\Gamma \pm \Delta\Gamma$	$f_{PAH} \pm \Delta f_{PAH}$
src1	45.41 ± 0.03	2.03 ± 0.01	0.23 ± 0.01
src2	43.91 ± 0.16	1.75 ± 0.09	0.31 ± 0.09
src6	44.22 ± 0.14	2.18 ± 0.05	0.13 ± 0.06
src10	45.07 ± 0.04	1.94 ± 0.02	0.23 ± 0.02
src11	44.34 ± 0.10	2.13 ± 0.04	0.21 ± 0.05
src12	44.15 ± 0.18	2.22 ± 0.07	0.19 ± 0.07
src13	43.95 ± 0.03	1.91 ± 0.01	0.23 ± 0.02
src19	44.01 ± 0.03	1.54 ± 0.02	0.26 ± 0.01
src21	44.25 ± 0.02	1.93 ± 0.01	0.27 ± 0.01
src22	44.26 ± 0.01	1.70 ± 0.01	0.25 ± 0.01
src23	44.10 ± 0.11	1.85 ± 0.05	0.26 ± 0.03
src26	44.13 ± 0.05	1.64 ± 0.03	0.25 ± 0.02
src27	44.38 ± 0.03	2.00 ± 0.01	0.24 ± 0.02
src28	44.58 ± 0.07	2.07 ± 0.03	0.22 ± 0.08
src31	44.32 ± 0.02	1.68 ± 0.01	0.26 ± 0.01
src32	44.48 ± 0.01	1.699 ± 0.004	0.24 ± 0.01

Table 5.2: *Summary of the values obtained through the likelihood maximization for the 50h case with three free parameters: gamma-ray luminosity, spectral index and PAH fraction.*

information to break some of the degeneracy between the intrinsic source spectral index and the EBL attenuation. Figure 5.22 shows the combination of all the sources studied for the three exposure times assumed. It is interesting to see that even the 30min case, where single source observations could not determined very well the PAH fraction, now exhibits a good resolution for f_{PAH}. As expected, the combinations for 5h and 50h cases present great resolutions in the determination of the PAH dust fraction. As we can see, combining all the source, the statistical uncertainty in the PAH fraction are better than 0.5% for the 50h case.

So far, all the analyses performed here were based on the assumption that the redshift of the sources is precisely known. In fact, this assumption is not true since an error is associated to each redshift. For sources with considerable uncertainty in the redshift, an a priori probability must be taken into account in equation 5.16. As we saw, the PAH is the dust grain best determined in our analysis, thus we will study the impact of the redshift uncertainties on the determination of this grain. Therefore, we have compared the posterior probabilities for f_{PAH} conditioned to values of all the other parameters fixed at their true values with and without marginalizing over the redshift of the source. The a priori probability for the source redshift in the marginalized case was written as

$$P(z) \propto z^2 e^{-\frac{(z-z_{src})^2}{2\sigma_z^2}}, \tag{5.17}$$

where z_{src} is the measured redshift (here taken to be simply the true value) of the source and σ_z is its uncertainty. This function is a Gaussian probability weighted by a quadratic

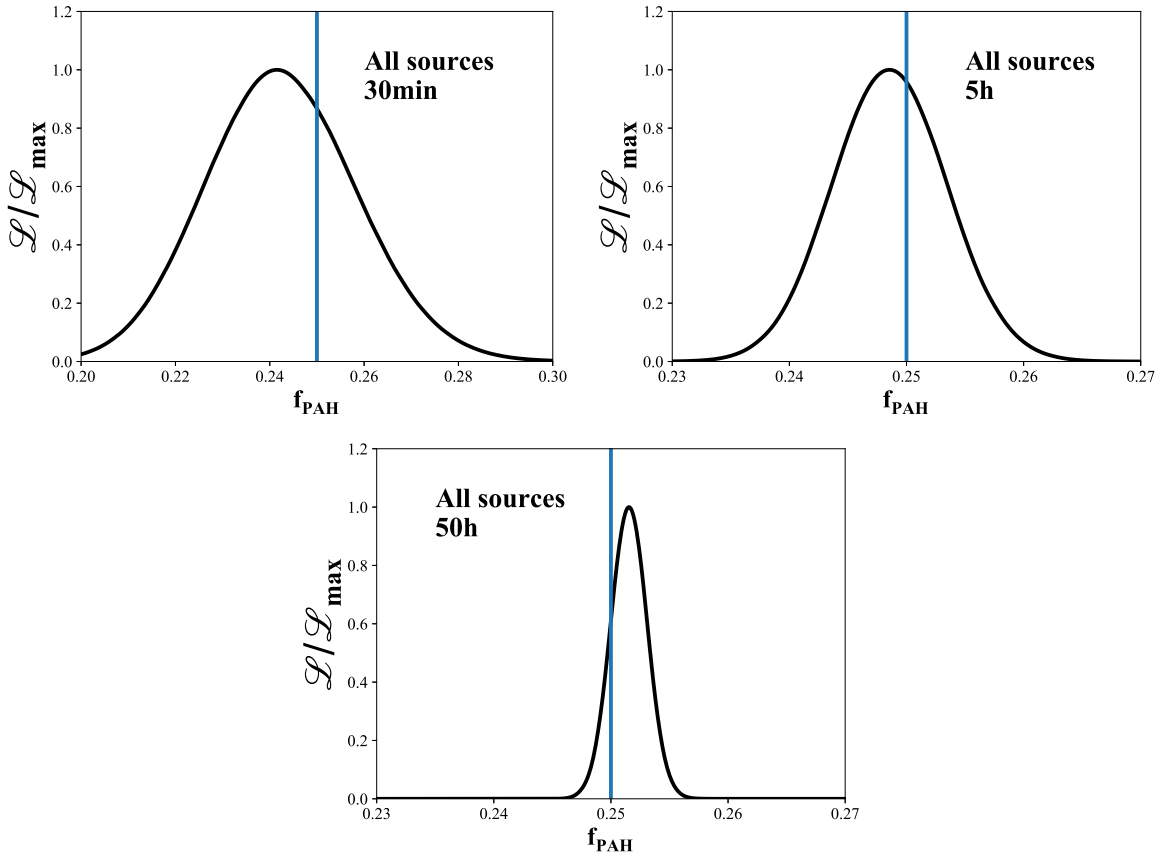

Figure 5.22: *Likelihood resulting from the combination of all the sources studied for the exposure time considered. Top-left: 30min case. Top-right: 5h case. Bottom: 50h case. The vertical line corresponds to the true solution.*

term in redshift. Since in the local universe the Hubble flow is constant, $H_0 \sim 70$ km s^{-1} Mpc^{-1}, the distance is given by $d \simeq (c/H_0)z$. Therefore, as a first approximation, we can consider that, for low redshifts, the number of BL Lacs increases with the square of the distance. Figure 5.23 shows the z^2 curve superimposed to the corresponding Ajello's GLF distribution being used to sample the sources in our analysis.

Figures 5.24 and 5.25 show that assuming a prior in the redshift with uncertainties corresponding to 10% of the central value, the width of the likelihood becomes slightly larger than the case without prior. An uncertainty of 10% can be considered quite large for sources with spectroscopic redshifts. However, we have adopted such a value both to probe the limiting uncertainties on f_{PAH} and also to embrace situations where a spectroscopic redshift is not available as can be the case of newly discovered sources at high redshifts. Therefore, the prior in redshift does not affect substantially the results obtained previously.

A possible extension of the analysis performed here would be the inclusion of the redshift as a free parameter in the likelihood maximization.

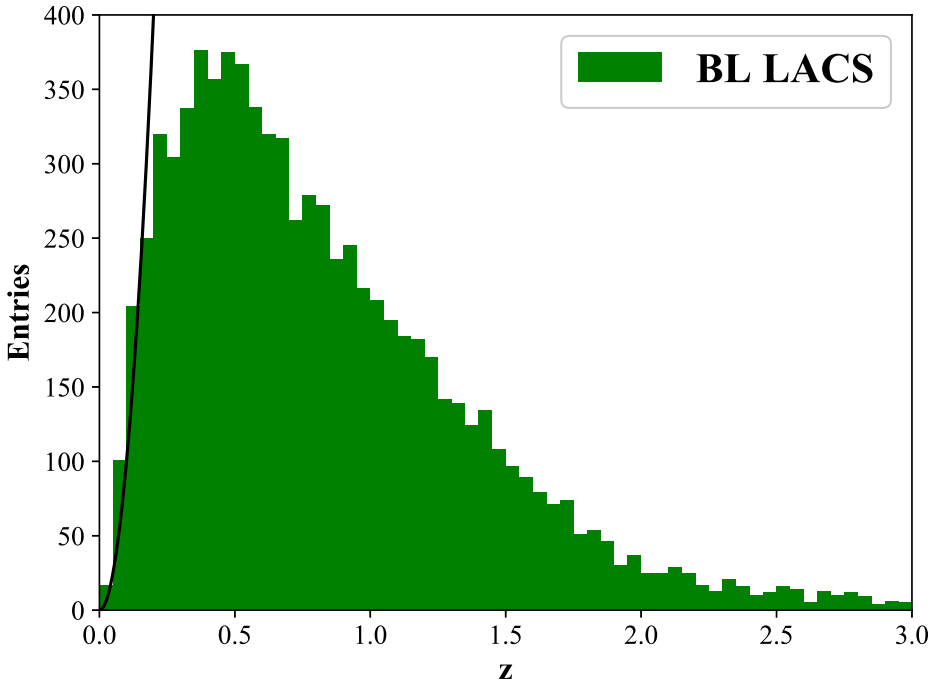

Figure 5.23: *Redshift distribution for BL Lacs from the GLF by M. Ajello et al. and a curve of the type z^2.*

5.7 Summary

Here, we have studied the potential of the CTA in determining parameters of the EBL and of the source spectrum. Simulating observations of 30 minutes, 5 hours and 50 hours for 16 sources sampled from M. Ajello et al. GLF, we could see that for the single source analysis, 50 hours of observation determines the PAH fraction with a good resolution (12%), in special for sources with high detection significance at TeV energies. The sensitivity to SG is low, mainly because there are not enough photons detected in the tens of TeV region of the SEDs. Since the spectral index and the gamma-ray luminosity are important parameters for the whole energy range of the spectra, they are well determined also for sources with low TS, however, a clear bias can be identified in figure 5.21 for the Γ_{reco} of soft spectra. The low photon counting around tens of TeV for such spectra makes the determination of f_{PAH} difficult, more precisely, the lack of photons is such that the reconstructed spectral indices are biased towards softer spectra. The combination of observations improves the resolution of the parameter determination and combining all the 16 spectrum studied, we can see that the PAH fraction is well determined even for 30 minutes of observation. A fine resolution is obtained for 5h and 50h exposure times. Assuming an uncertainty of 10% in the redshift of the sources, we have studied its impact in the determination of the PAH fraction. A small enlargement of the likelihood is observed, implying in an increase in the errors of the f_{PAH}. However, this effect is not pronounced even for such

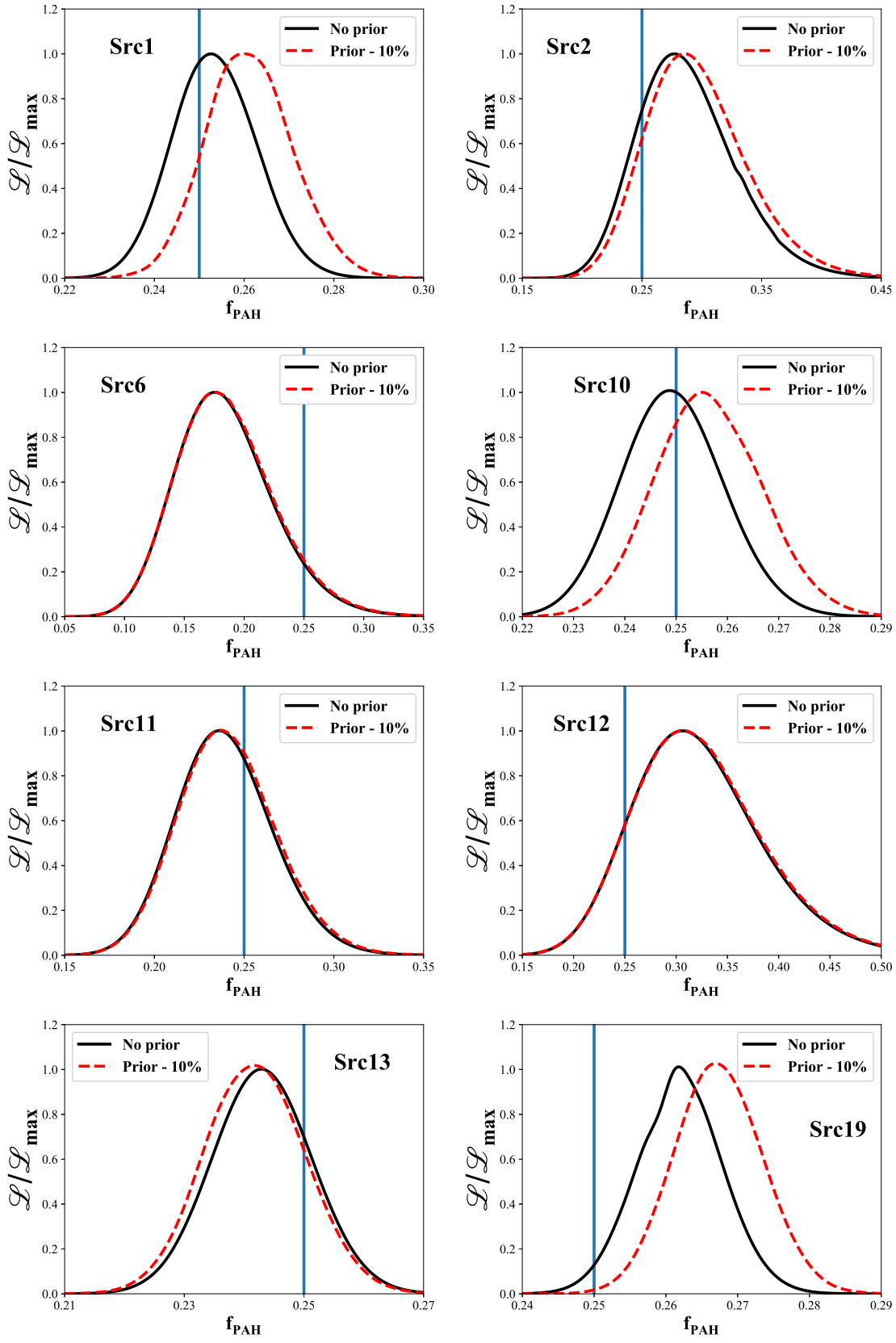

Figure 5.24: *Likelihood as a function of f_{PAH}. Black curves correspond to the case with no prior and red lines with a prior on the redshift. The vertical line shows the nominal value.*

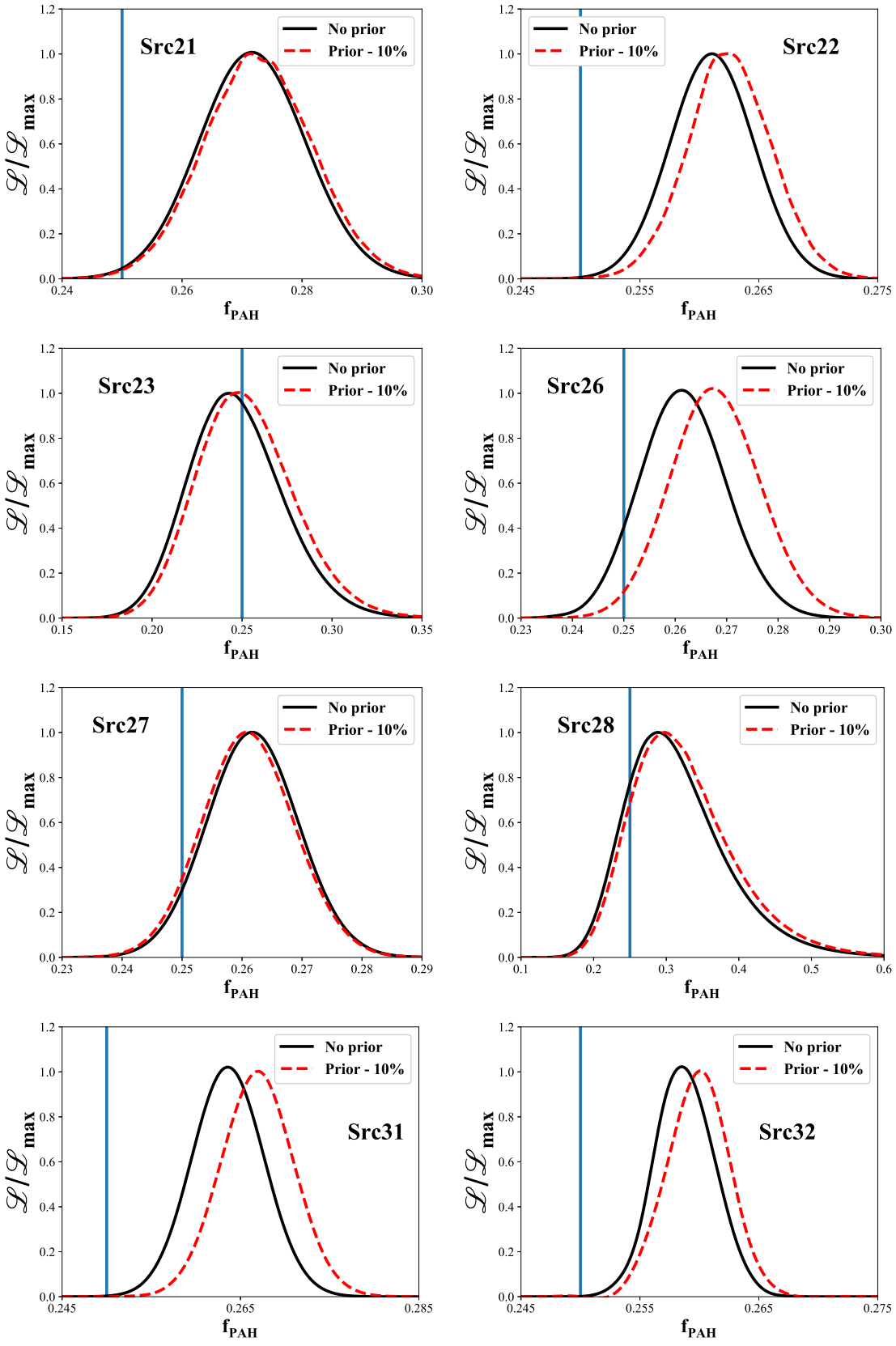

Figure 5.25: *Continuation of figure 5.24.*

large uncertainty (compared to typical spectroscopic values) in the redshift.

Chapter 6

Conclusions

We have investigated here the importance of the EBL in gamma-ray astronomy given that the spectrum of AGNs must undergo attenuation due to the quantum nature of the interaction between matter and radiation. The complex spectral energy and time evolutions of the EBL carry information on galaxy evolution because stars and dust are their main sources of radiation. In order to investigate the role of each of these contributions in the attenuation of SEDs of distant gamma-ray sources, we have based our study mainly in the F10 model [29], which was implemented in this thesis from scratch in a C++ code. F10 treats the EBL as the result of a combination of four components: 1 stellar and 3 types of dust. We have been able to separate each one of these contributions, which allowed studying the impact of them in the spectra of blazars observed at TeV energies by IACTs.

The IACTs and gamma-ray detectors on-board satellites have been observing AGNs (in general, blazars) in energies where a substantial attenuation by EBL is expected. In one decade of operation, Fermi-LAT has detected a considerable number of AGNs at energies up to hundreds of GeV. The third catalog of AGNs detected by Fermi-LAT, published in 2015 [151], contains 1563 gamma-ray sources associated with AGNs, where 98% of them are identified as blazars. Sources observed at TeV energies have been catalogued in the TeVCat [58], which currently provides information from 41 extragalactic gamma-ray emitters with determined redshift, all of them observed by IACTs. These two samples of sources were very important for the studies performed in this thesis. Thanks to the large amount of objects detected by Fermi-LAT, the distribution of blazars could be described through the gamma-ray luminosity functions, an essential piece of information to feed the simulation chain described in Chapter 5 which included also the CTA IRFs.

Sources observed by IACTs allowed a detailed investigation of the role of the EBL dust component in the attenuation process, since some of these sources present a well determined spectrum around tens of TeV, as we saw in Chapter 4. Mkn 501 flare state observed in 1997 by HEGRA allowed the detection of photon flux at energies up to $\sim$ 20 TeV. At these energies, the SED of a source located in a redshift like that of Mkn 501

($z = 0.034$) must be subject to non-negligible attenuation by IR radiation emitted by cosmic dust. In particular, the role of the PAH contribution, responsible for emission mainly in mid-IR, could be better understood. We showed that this dust component is essential for the correct description of the spectral index of the SED of Mkn 501 in the region below 10 TeV, for neither the stellar component nor the emission from other dust grains provided the correct slope for the measured SED at these energies. This becomes clear when we isolate the attenuation contribution of each EBL component in the Mkn 501 spectrum. On the other hand, based on the likelihood ratio test comparing an effective 1-grain model (null hypothesis) against the 3-grain one (alternative hypothesis), the scenario with just PAH as dust contribution can be excluded with more than 5σ independent of the intrinsic spectrum used, provided the grain temperatures are fixed a priori. The attenuation caused by the PAH grains has an effective energy dependence as a single spectral index over a broad energy range, thus the strong decrease of the Mkn 501 flux at energies above 10 TeV cannot be described in this PAH-only scenario, even if an intrinsic spectrum with an exponential cutoff, which can mimic part of the attenuation by EBL, is assumed. Therefore, this single source analysis showed the potential that a well measured SED have in constraining both spectral and EBL parameters. It is important to note the presence of degeneracies between some grains (small and large fractions) and intrinsic curvature of the spectrum in the fit of the SED. In the cases of zero (power-law) and constant curvature (log-parabola), small grains are overestimated compared to large ones since in the former the attenuation factor is slightly harder. However, with an energy dependent curvature (like in the power-law with exponential cutoff), at least part of the flux suppression can be accounted for already at the intrinsic spectrum level.

The extention of this single source analysis to a combination of many sources well measured at different redshifts can eliminate the degeneracies since the number of degrees of freedom of the fit increases. With this purpose, a first step was taken by checking the consistency of the EBL parameters tuned by Mkn 501 in describing the attenuation of the sample of SEDs collected from TeVCat. For several combinations of EBL dust fractions and intrinsic spectra we were able to study the distributions of flux residuals. When the uncertainties on the flux measurements are Gaussian and the model describing the observed spectrum is suitable, these flux residuals must follow a normal distribution. By fitting a Gaussian function to these data it is possible to see that the power-law intrinsic case has the worse fit compared to the cases with an intrinsic curvature, independent of the dust fractions used. By adding an intrinsic curvature to the spectra the quality of the fit is improved since the reduced χ^2 of the distributions becomes closer to unity compared to the PL case. Based on the estimator defined in equation 4.5, we also separated the measured SED bins into two groups, stellar and dust attenuation dominated subsamples, and we could not observed a systematic change in the quality of the Gaussian fits of these distributions when going from nominal to tuned fractions. This is consistent with the fact

that the sample of sources measured today by IACTs is dominated by stellar attenuation, as shown by the appropriated estimator in figure 4.12.

Finally, we made some forecast studies for the CTA in order to verify the potential of this observatory in determining EBL and intrinsic source parameters. Since the CTA will measure fluxes at tens of GeV, the unattenuated part of the SEDs will be obtained, providing the intrinsic behavior of the source. However, fluxes up to hundreds of TeV are also expected to be observed by CTA, therefore, an investigation of the role of the dust component of the EBL in the opacity of the universe to the gamma-rays must be possible. Based on the IRFs provided by the simulation mass production of the CTA consortium, known as "prod3b-v1", we simulated observations of 16 gamma-ray sources with high TS by the CTA South. This array is the one with best performance for our studies since the flux sensitivity expected for the CTA South around tens of TeV is better than the site located in the North. The 16 sources sampled from the GLF for BL Lacs developed by M. Ajello et al. have their redshifts in the interval [0.0, 0.1] and each spectrum is measured between 0.1 TeV and 100 TeV. Considering a power-law as the intrinsic flux and the F10 model, a likelihood maximization procedure was performed leaving the dust fractions of the EBL and intrinsic parameters free to fit the data collected by the CTA. We showed that the PAH fraction can be determined with good resolution already for the single source analysis using 50 hours of exposure time. As expected, sources with high detection significance present a better determination of the PAH relative contribution. Due to the finite observation time, on average, high TS sources will tend to be associated to hard intrinsic spectra, implying in a reasonable photon flux at very high energies, essential for studies of the EBL dust component. The sample of spectra considered could not determine the small grains very well since the opacity caused by this grain plays an important role for photons with energies greater than tens of TeV. Intrinsic parameters, as the spectral index and the gamma-ray luminosity could be well determined when they were included in the fit. This was expected since these quantities are important in the description of the observed SED in the entire energy range covered by the observations, unlike the dust components, whose determination are conditioned to measurements of specific regions of the spectrum. The combination of the sources improves the resolution obtained for single observations. Taking into account all the 16 sources, we can see that the PAH is already well determined for 30 minutes of observation. It is worth mentioning that the estimated errors for the f_{PAH} through the likelihood represent a posteriori statistical uncertainties given the a priori information that F10 provides the correct description of the EBL energy density. The contributions to the statistical uncertainty of f_{PAH} coming from the corresponding uncertainties in the others parameters of the F10 model, such as grain temperatures, IMF, SFR, etc, were not taken into account in this thesis, but should certainly be incorporated in a future work.

It is important to mention that the variability of the sources was not take into account

in our simulations. Since we have noted a bias for soft spectra and a source with high variability can exhibit appreciable changes in its spectral index, a final bias in the Γ_{reco} could be generated considering a time average of the spectrum.

In order to incorporate in the EBL absorption forecasts the effect of the source redshift uncertainties, we have marginalized the likelihood over the redshifts using an appropriate a priori probability for z, which includes both the effect of the uncertainties on this parameter, as well as the dependence of the local density of gamma-ray sources. Considering an error of 10% (considerably large for typical spectroscopic redshifts) in the redshift of the sources, we observed a small increase in the width of the posterior for the PAH fraction. The uncertainty on the redshift implies in an increase on the errors of f_{PAH}, however, this effect is relatively small.

Appendices

Appendix A

Boltzmann equation to a smooth CMB distribution

One of the most remarkable result in cosmology certainly is the discovery of the Cosmic Microwave Background by Penzias and Wilson, confirming the predictions about a radiation emitted at the beginning of the universe and which could travel freely in a future time after the decoupling between matter and radiation. This observation was a crucial evidence in favor of the Big Bang theory [1, 19].

Before the photons decouple from the matter the interaction between them was sufficiently strong to keep the photons, protons and electrons in thermodynamics equilibrium, so that the photon energy distribution is well described by a blackbody. In order to solve for the time evolution of their emissivity from the last scattering surface (LSS) until now, we can use the mathematical artifice of multiplying a blackbody term by de Dirac delta function centered at the LSS

$$j(t,\nu) = \delta(t - t_{lss})\frac{8\pi h}{c^3}\frac{\nu^3}{e^{h\nu/k_BT} - 1}, \tag{A.1}$$

the Boltzmann equation becomes

$$\frac{dI(t,\nu)}{dt} = -3\frac{\dot{a}}{a}I(t,\nu) + \delta(t - t_{lss})\frac{2h}{c^2}\frac{\nu_{lss}^3}{e^{h\nu_{lss}/k_BT_{lss}} - 1}. \tag{A.2}$$

As we have seen in Chapter 2, the solution for this equation takes the following form

$$I(t,\nu) = \int_0^t dt' \left(\frac{a(t')}{a(t)}\right)^3 \delta(t' - t_{lss})\frac{2h}{c^2}\frac{\nu_{lss}^3}{e^{h\nu_{lss}/k_BT_{lss}} - 1}. \tag{A.3}$$

Performing the integral and remembering that the emitted photon frequency ν_{lss} scales with the cosmological factor $a(t)$ as $a(t_{lss})\nu_{lss} = a(t)\nu$ and a similar scaling applies to temperature $a(t_{\rm lss})T_{\rm lss} = a(t)T$, we get

$$I(t,\nu) = \frac{1}{a(t)^3}\frac{2h}{c^2}\frac{a(t)^3\nu^3}{e^{h\nu/k_BT} - 1}, \tag{A.4}$$

the spectrum measured today from the CMB is given by

$$I(T,\nu) = \frac{2h}{c^2}\frac{\nu^3}{e^{h\nu/k_BT}-1}, \tag{A.5}$$

where $T = 2.725$ K is the current ($a = 1$) temperature of the CMB.

Figure A.1 shows the CMB intensity as a function on wave number. The theoretical curve are superimposed to dozens of measured data.

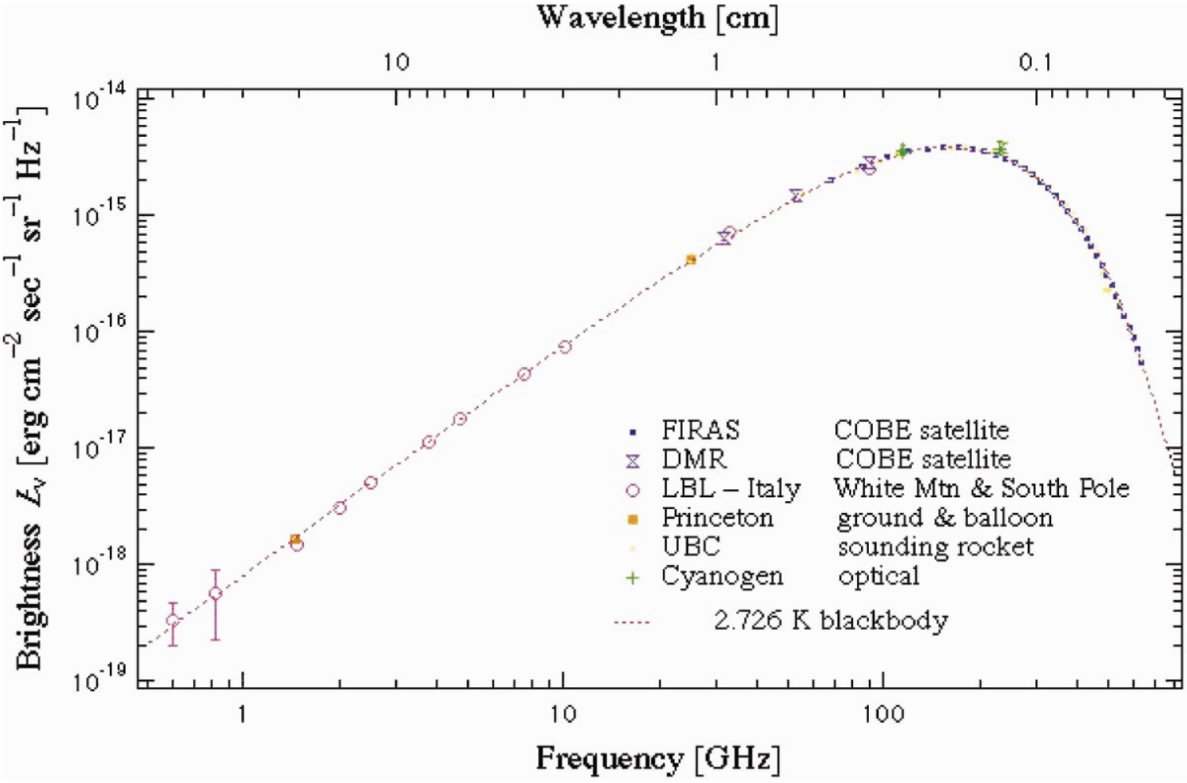

Figure A.1: *Intensity of CMB as a function of the frequency. The theoretical blackbody prediction and data points are displayed for comparison. Figure extracted from [152].*

The total energy flux due to photons traversing the cross section of a detector is then given by

$$F = \int\int I(T,\nu)\cos(\theta)\,d\nu\,d\Omega = \pi\int_0^\infty \frac{2h}{c^2}\frac{\nu^3}{e^{h\nu/k_BT}-1}d\nu. \tag{A.6}$$

Here we can do a convenient change of variable with $x = h\nu/k_BT$,

$$F = \frac{2\pi h}{c}\left(\frac{k_BT}{h}\right)^4\int_0^\infty \frac{x^3}{e^x-1}dx. \tag{A.7}$$

The integral in A.7 can be solved remembering the definition of the Riemann zeta function $\zeta(s)$ [153]

$$\zeta(s) = \frac{1}{\Gamma(s)}\int_0^\infty \frac{x^{s-1}}{e^x-1}dx \tag{A.8}$$

where $\Gamma(s)$ is the gamma function. For $s = 4$, $\zeta(4) = \pi^4/90$ and $\Gamma(4) = 15$, therefore we can writte

$$F = \sigma T^4 \tag{A.9}$$

where $\sigma = \frac{2k_B\pi^5}{15h^3c^2} = 5.67 \times 10^{-5}$ erg cm^{-2} K^{-4} s^{-1} is the Stefan-Boltzmann constant and A.9 is known as the Stefan-Boltzmann law.

Appendix B

SEDs and bestfits

B.1 Power-law intrinsic spectrum and F10 model

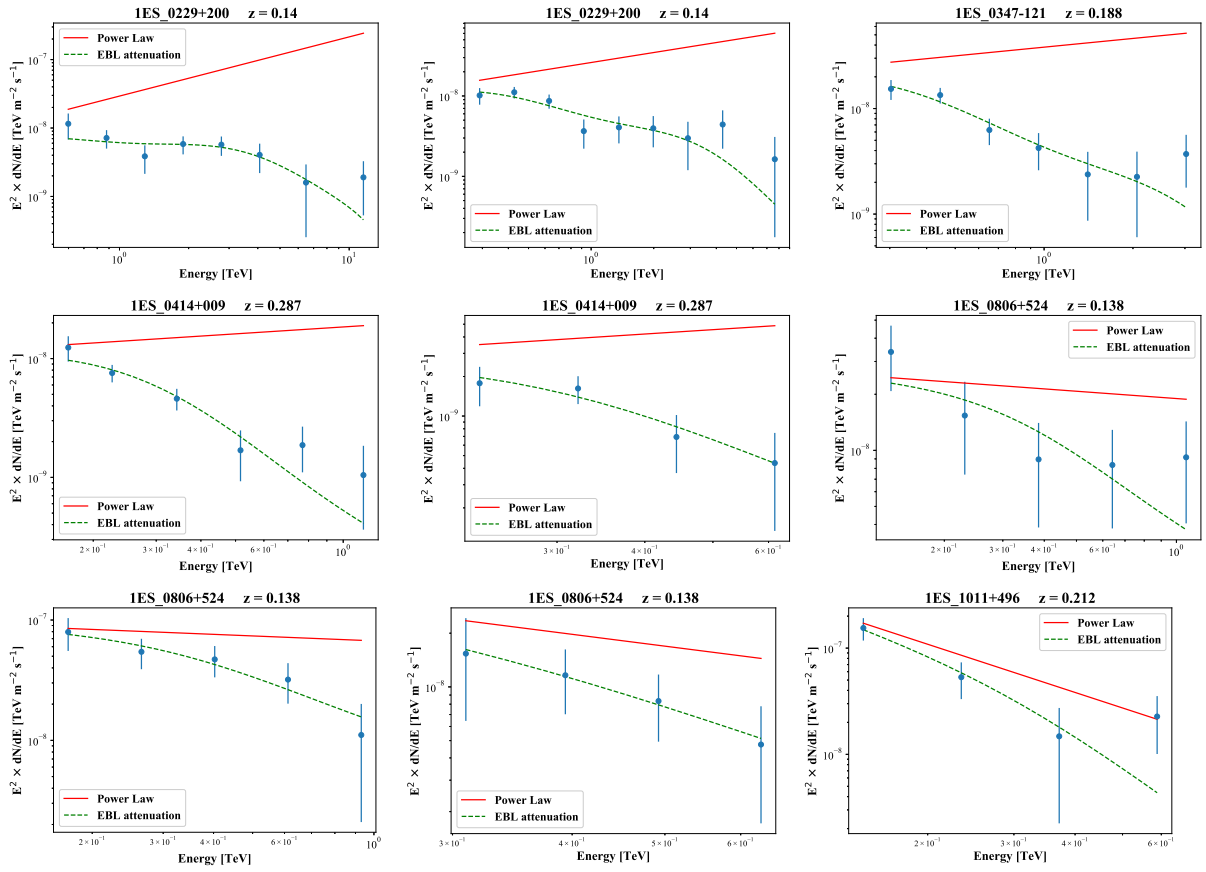

Figure B.1: *Spectra measured by IACTs fitted by an intrinsic power-law with F10 model.*

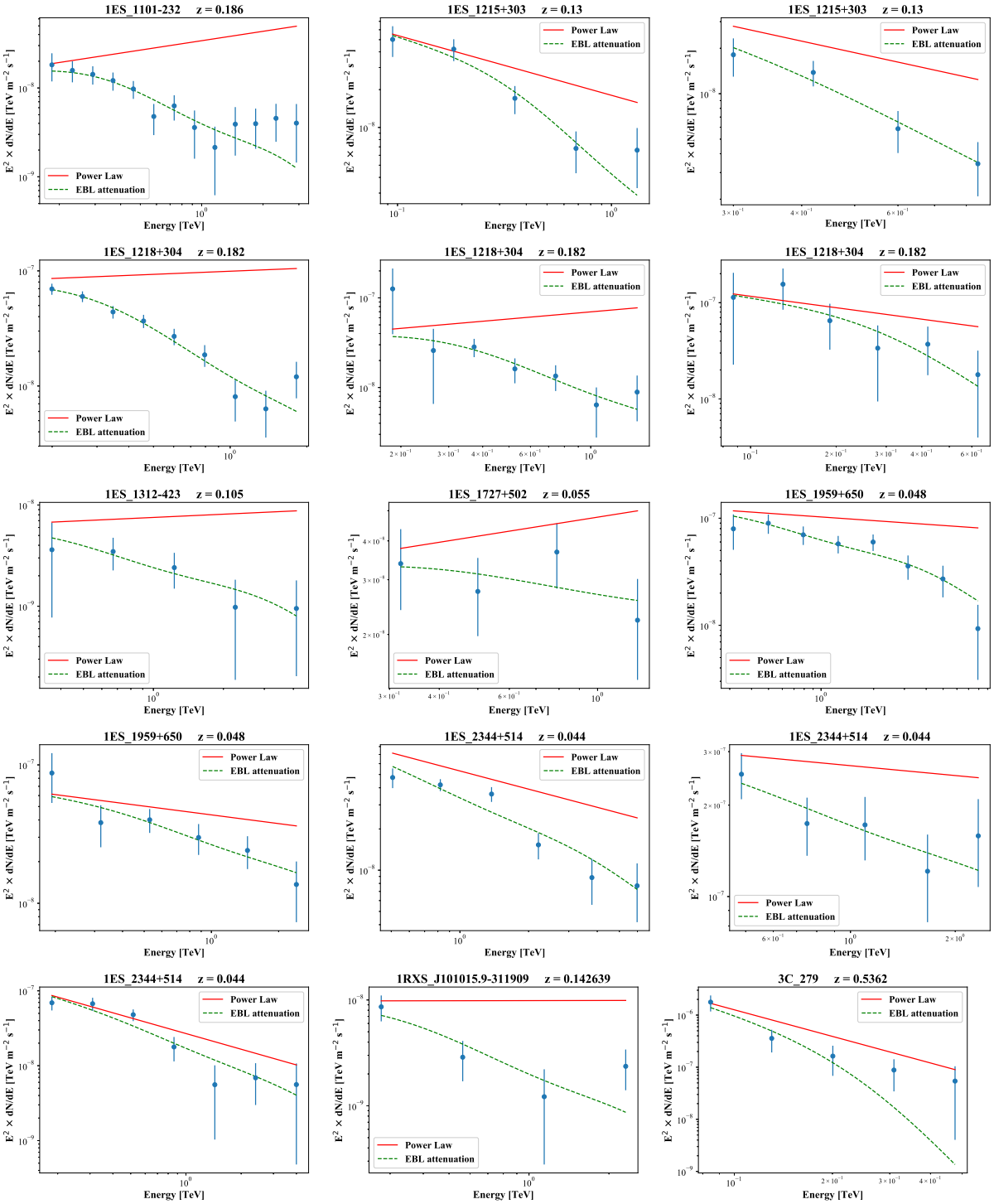

Figure B.2: *Continuation of figure B.1.*

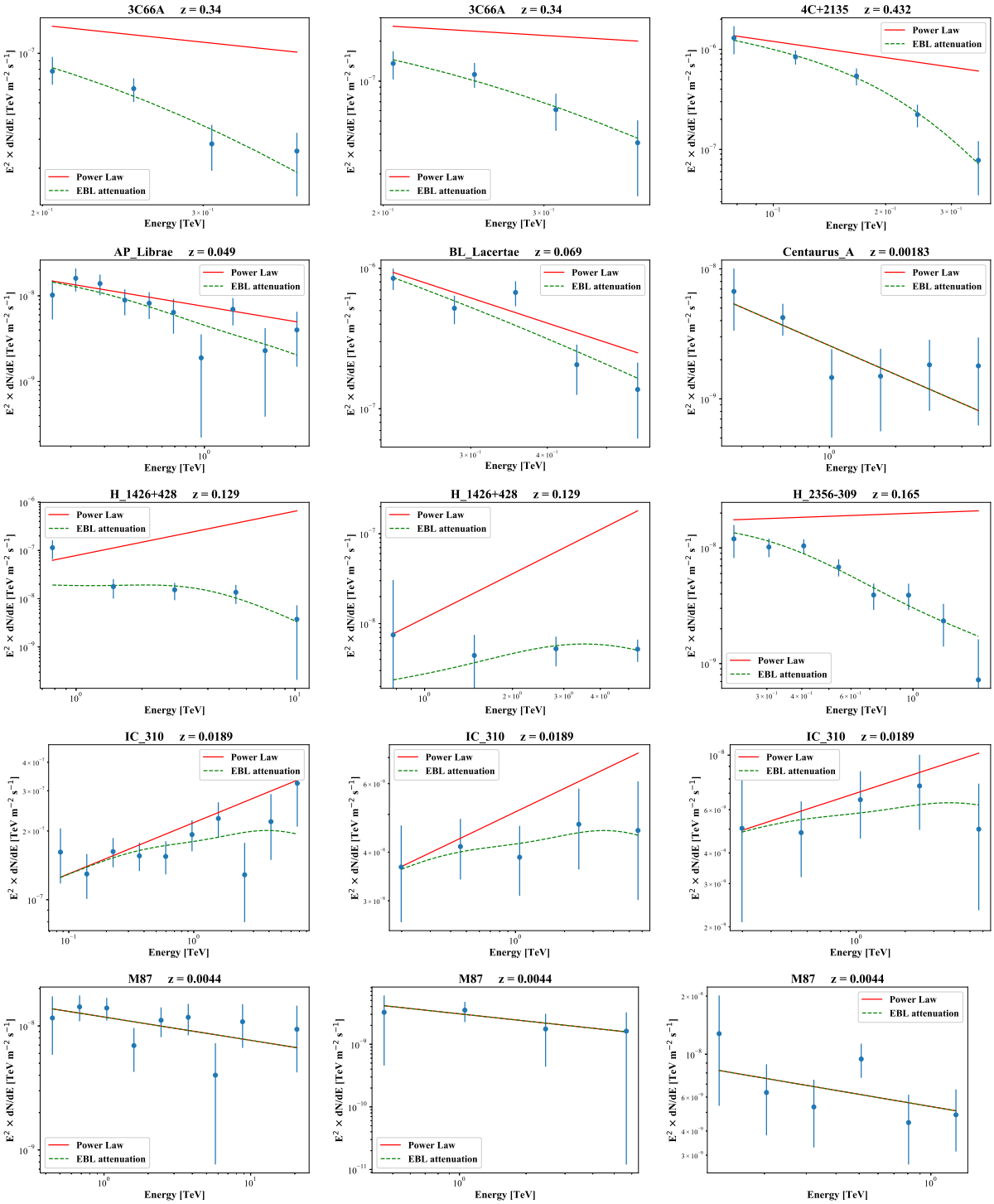

Figure B.3: *Continuation of figure B.2.*

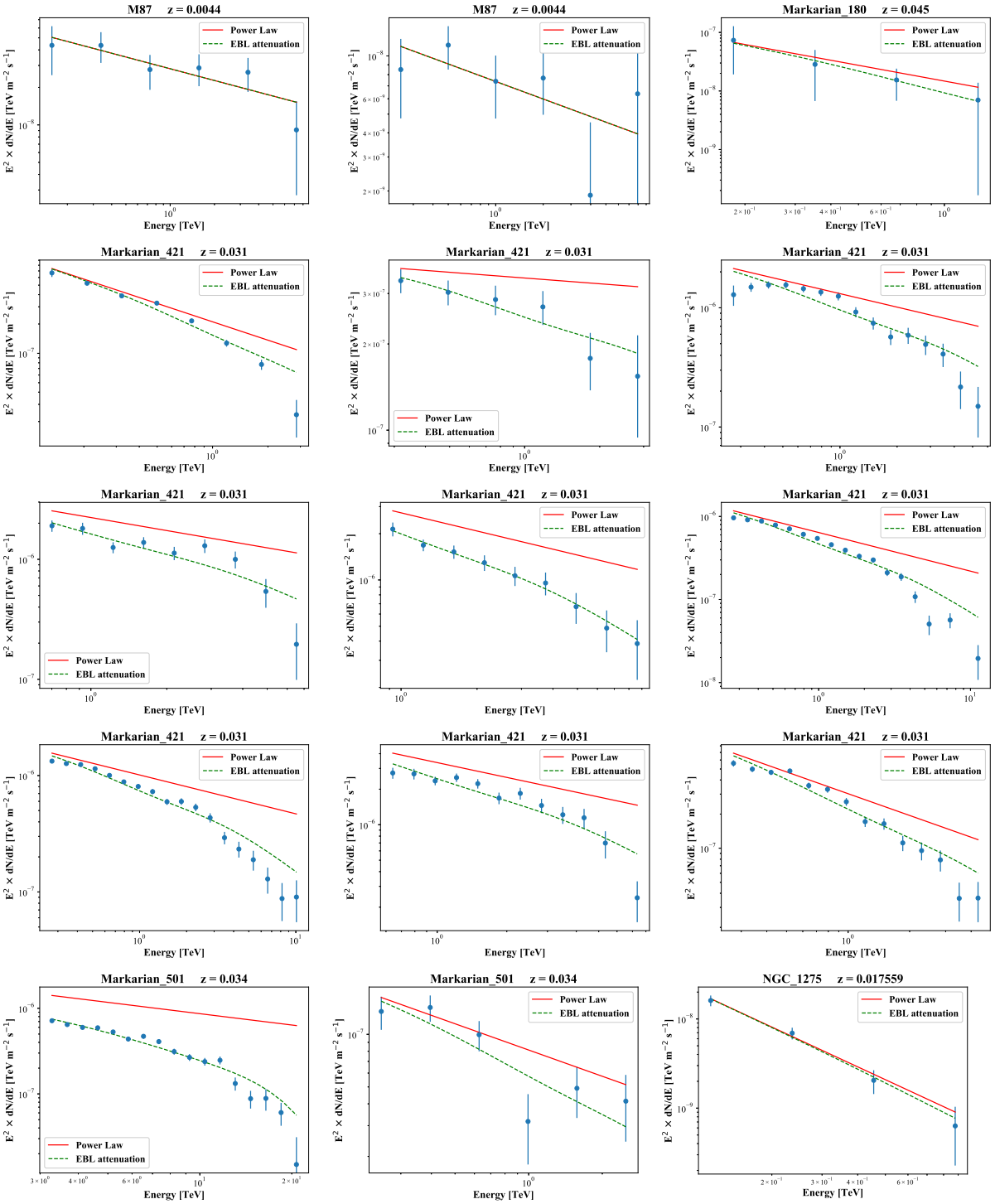

Figure B.4: *Continuation of figure B.3.*

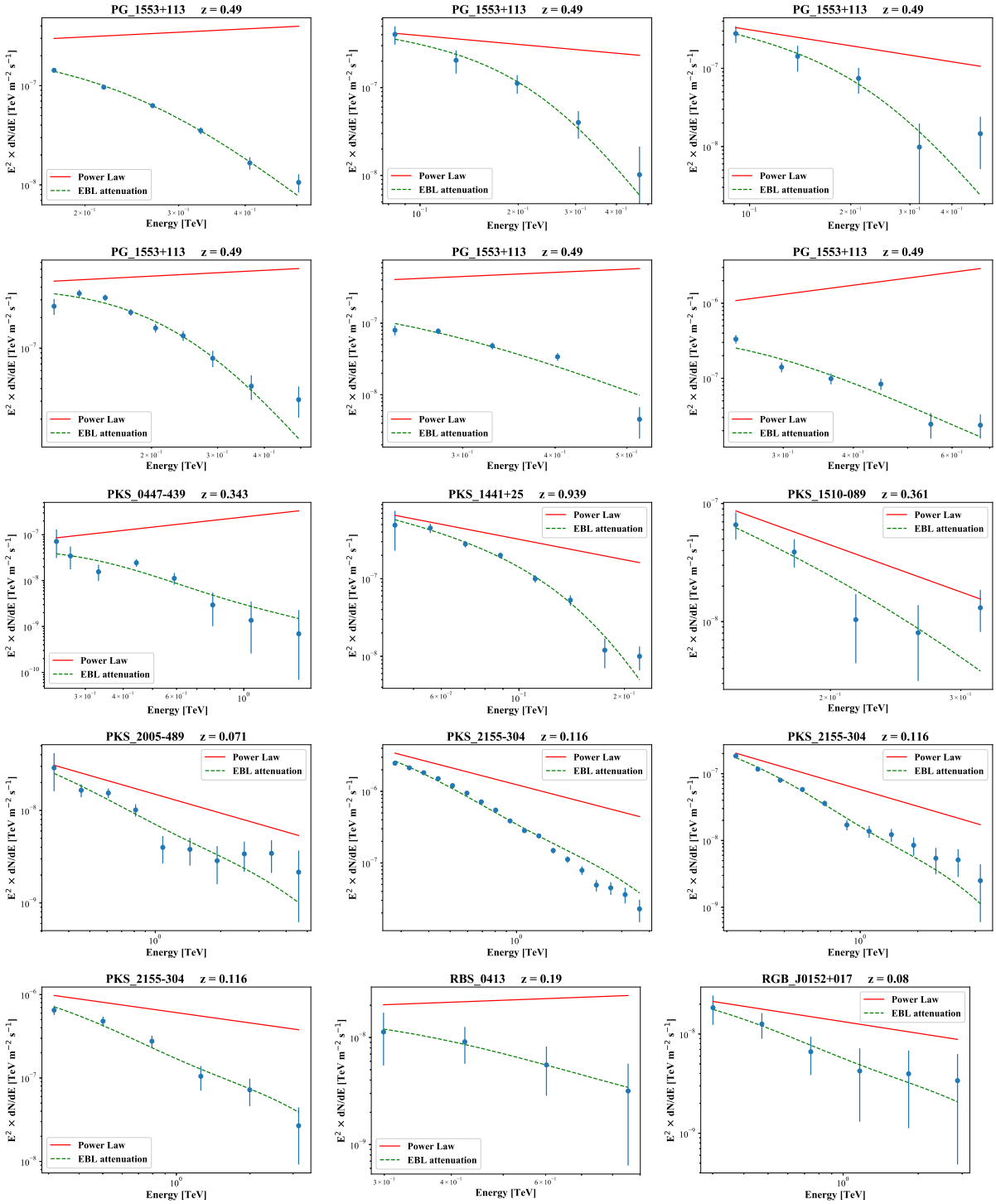

Figure B.5: *Continuation of figure B.4.*

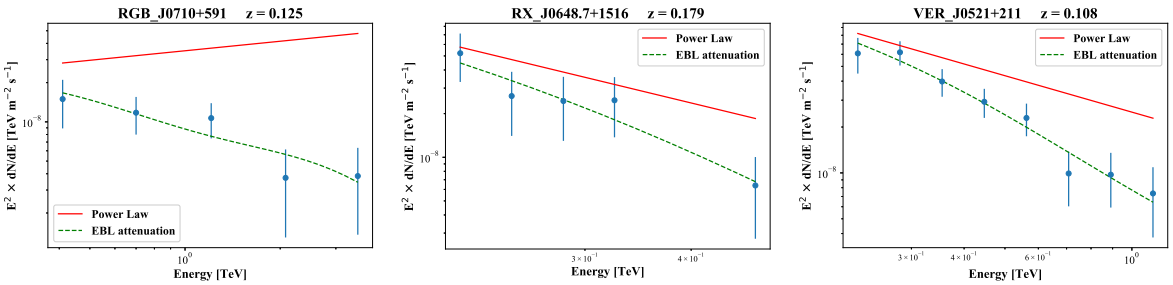

Figure B.6: *Continuation of figure B.5.*

Appendix C

Spectra simulated for 30min and 5h cases

All spectra of the 16 sources analyzed in Chapter 5 are shown in figures C.1 and C.2 for 30 minutes of observation and in C.3 and C.4 for 5 hours.

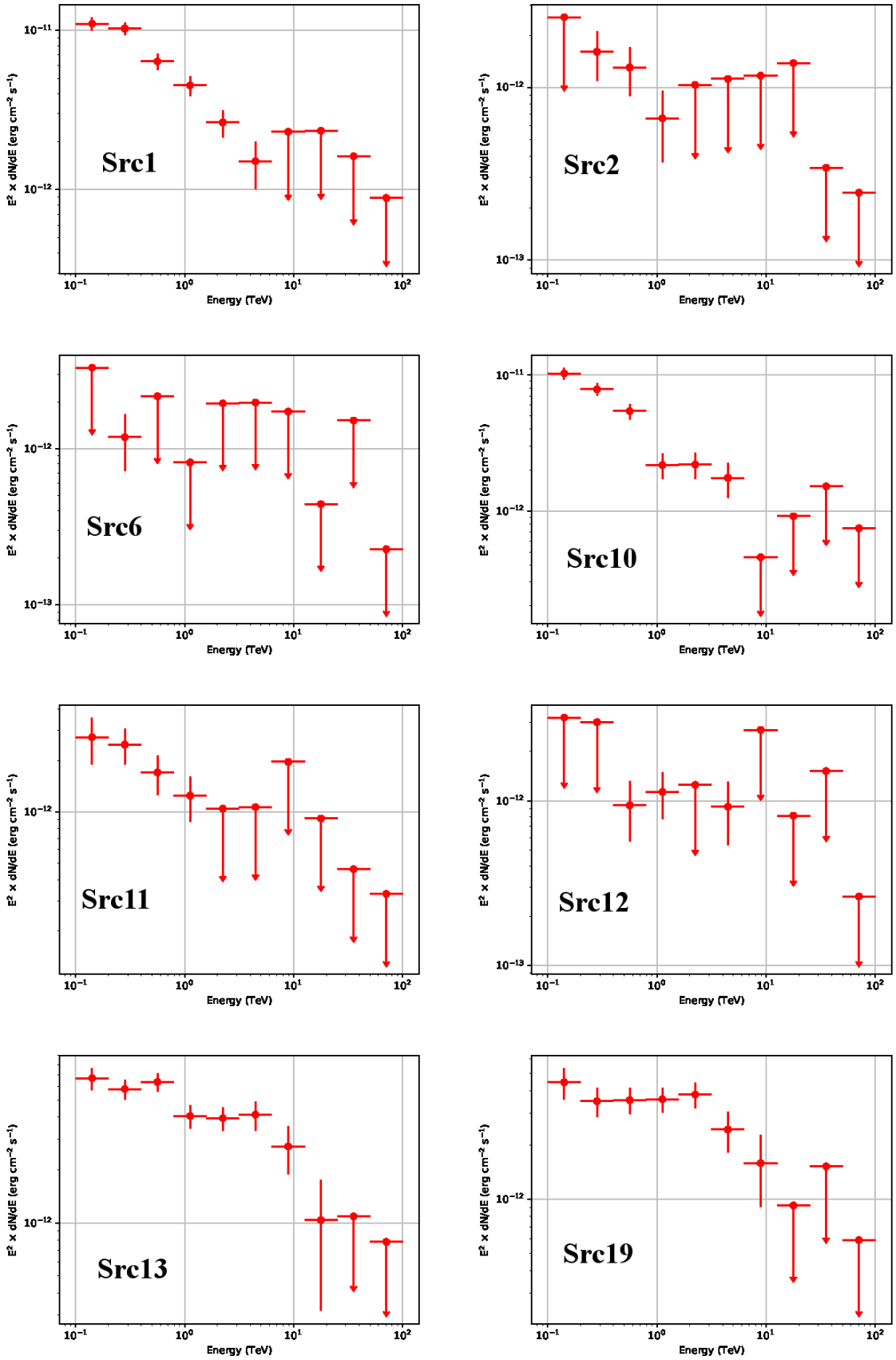

Figure C.1: *Spectra of the sources with 30 minutes of observation by CTA south.*

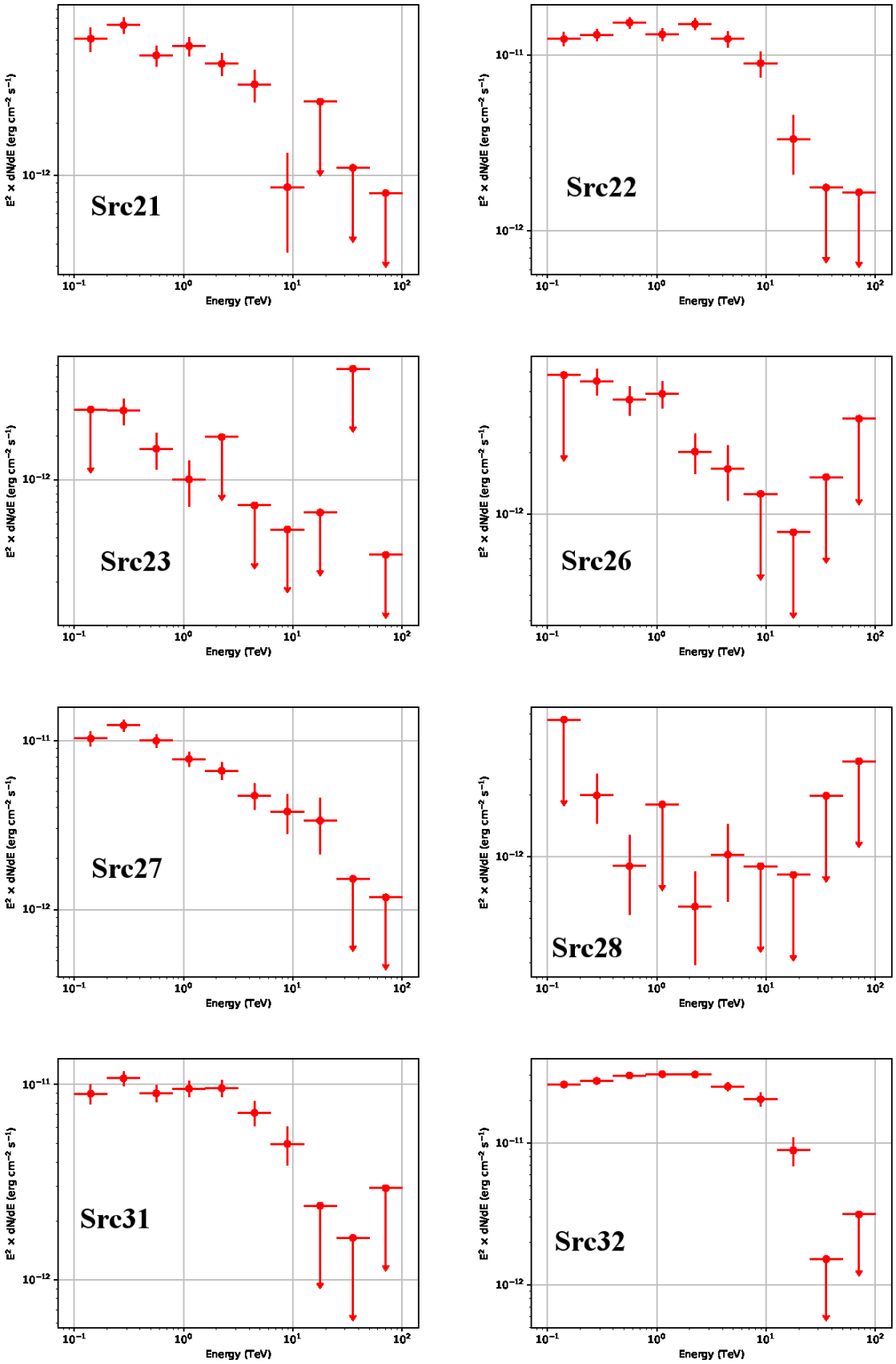

Figure C.2: *Continuation of figure C.1.*

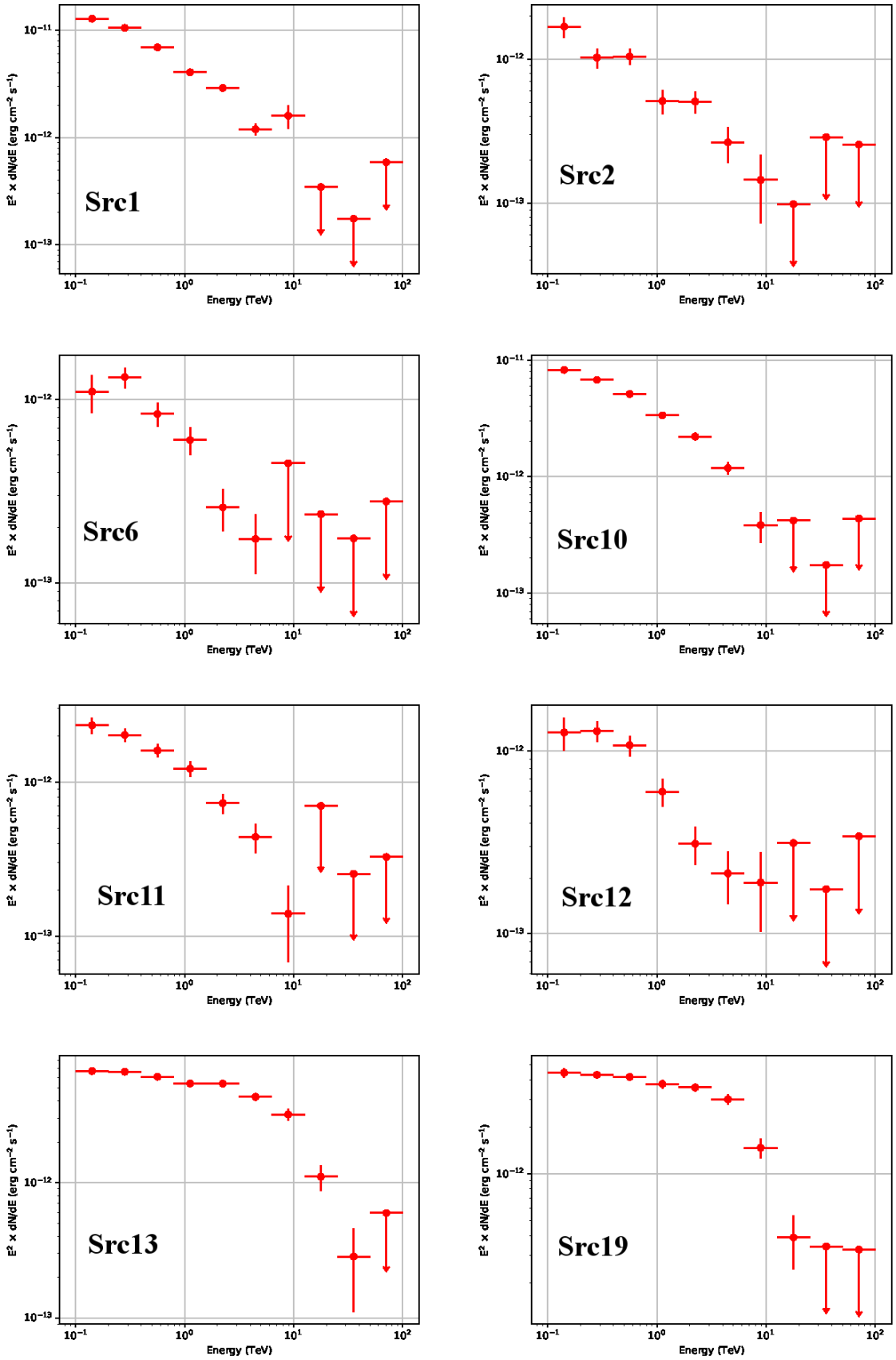

Figure C.3: *Spectra of the sources with 5 hours of observation by CTA south.*

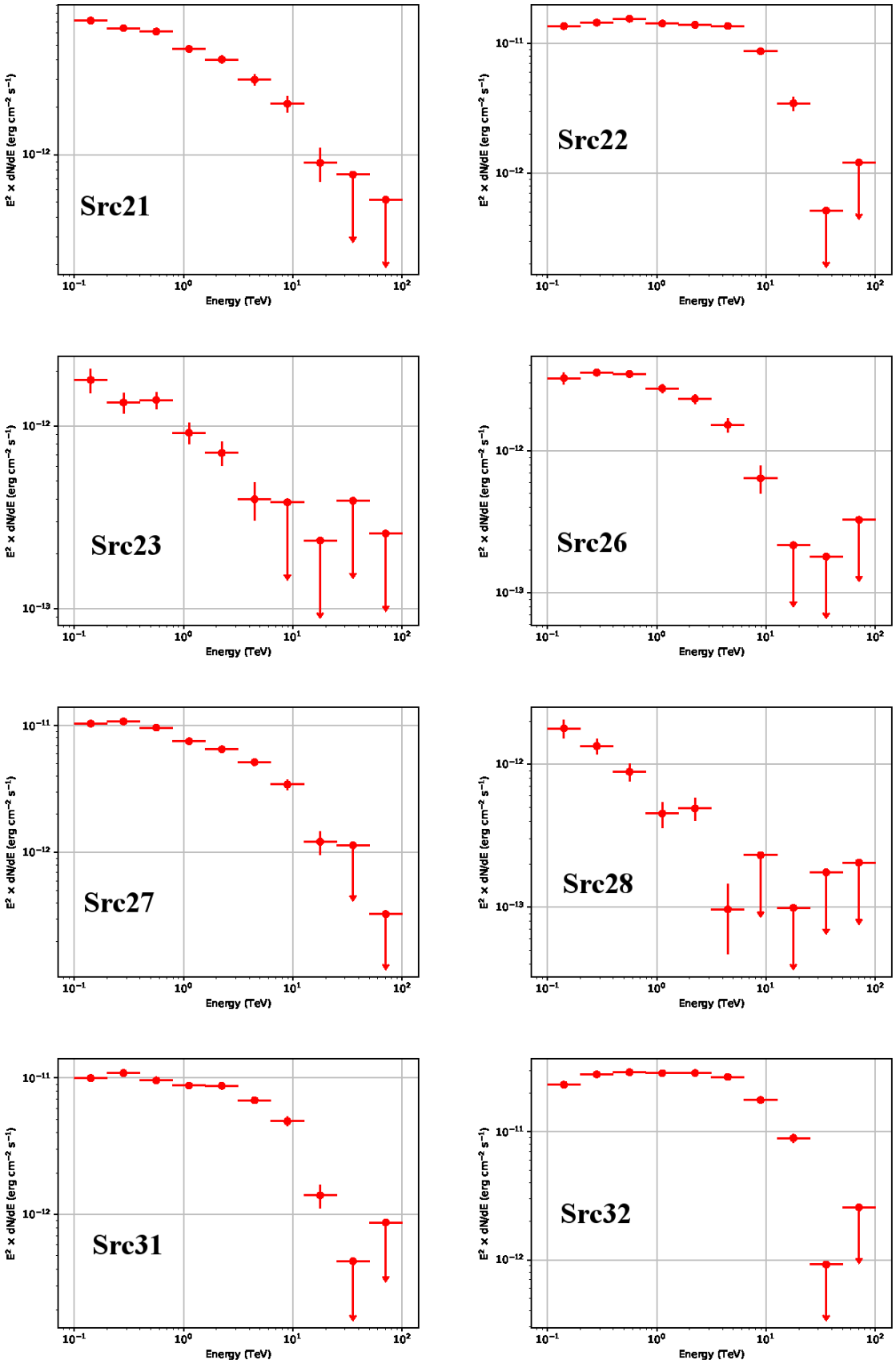

Figure C.4: *Continuation of figure C.3.*

Bibliography

[1] Scott Dodelson. *Modern cosmology*. Academic press, 2003.

[2] Arno A Penzias and Robert Woodrow Wilson. A measurement of excess antenna temperature at 4080 mc/s. *The Astrophysical Journal*, 142:419–421, 1965.

[3] Robert J. Gould and Gerard P. Schreder. Opacity of the Universe to High-Energy Photons. *Phys. Rev.*, 155:1408–1411, 1967.

[4] Robert J. Gould and Gerard P. Schreder. Pair Production in Photon-Photon Collisions. *Phys. Rev.*, 155:1404–1407, 1967.

[5] Victor Francis Hess. Über beobachtungen der durchdringenden strahlung bei sieben freiballonfahrten. *Z. Phys.*, 13:1084, 1912.

[6] Trevor C Weekes, MF Cawley, DJ Fegan, KG Gibbs, AM Hillas, PW Kowk, RC Lamb, DA Lewis, D Macomb, NA Porter, et al. Observation of tev gamma rays from the crab nebula using the atmospheric cerenkov imaging technique. *The Astrophysical Journal*, 342:379–395, 1989.

[7] Trevor C Weekes. *Very high energy gamma-ray astronomy*. CRC Press, 2003.

[8] G Kanbach, DL Bertsch, A Favale, CE Fichtel, RC Hartman, R Hofstadter, EB Hughes, SD Hunter, BW Hughlock, DA Kniffen, et al. The project egret (energetic gamma-ray experiment telescope) on nasa's gamma-ray observatory gro. *Space Science Reviews*, 49(1):69–84, 1989.

[9] AA Moiseev. Gamma-ray large area space telescope: mission overview. *Nuclear Instruments and Methods in Physics Research Section A: Accelerators, Spectrometers, Detectors and Associated Equipment*, 588(1):41–47, 2008.

[10] AU Abeysekara, A Albert, R Alfaro, C Alvarez, JD Álvarez, R Arceo, JC Arteaga-Velázquez, HA Ayala Solares, AS Barber, N Bautista-Elivar, et al. Observation of the crab nebula with the hawc gamma-ray observatory. *The Astrophysical Journal*, 843(1):39, 2017.

[11] M Amenomori, YW Bao, XJ Bi, D Chen, TL Chen, WY Chen, Xu Chen, Y Chen, SW Cui, LK Ding, et al. First detection of photons with energy beyond 100 tev from an astrophysical source. *Physical Review Letters*, 123(5):051101, 2019.

[12] Felix Aharonian, AG Akhperjanian, AR Bazer-Bachi, M Beilicke, Wystan Benbow, David Berge, K Bernlöhr, C Boisson, Oliver Bolz, V Borrel, et al. Observations of the crab nebula with hess. *Astronomy & Astrophysics*, 457(3):899–915, 2006.

[13] TC Weekes, H Badran, SD Biller, I Bond, S Bradbury, J Buckley, D Carter-Lewis, M Catanese, S Criswell, W Cui, et al. Veritas: the very energetic radiation imaging telescope array system. *Astroparticle Physics*, 17(2):221–243, 2002.

[14] Jürgen Albert, Ester Aliu, H Anderhub, Pedro Antoranz, Alexandre Armada, Cármen Baixeras, Juan A Barrio, Hendrik Bartko, D Bastieri, Julia K Becker, et al. Vhe γ-ray observation of the crab nebula and its pulsar with the magic telescope. *The Astrophysical Journal*, 674(2):1037, 2008.

[15] B. S. Acharya et al. Science with the Cherenkov Telescope Array. 2017.

[16] Jordı Albert, E Aliu, H Anderhub, LA Antonelli, P Antoranz, M Backes, C Baixeras, JA Barrio, H Bartko, D Bastieri, et al. Very-high-energy gamma rays from a distant quasar: how transparent is the universe? *Science*, 320(5884):1752–1754, 2008.

[17] Markus Ackermann, M Ajello, A Allafort, P Schady, Luca Baldini, Jean Ballet, Guido Barbiellini, D Bastieri, R Bellazzini, RD Blandford, et al. The imprint of the extragalactic background light in the gamma-ray spectra of blazars. *Science*, 338(6111):1190–1192, 2012.

[18] Markus Ackermann, Marco Ajello, William B Atwood, Luca Baldini, J Ballet, Guido Barbiellini, D Bastieri, J Becerra Gonzalez, R Bellazzini, E Bissaldi, et al. 2fhl: the second catalog of hard fermi-lat sources. *The Astrophysical Journal Supplement Series*, 222(1):5, 2016.

[19] Phillip James Edwin Peebles. *Physical cosmology*. Princeton University Press, 1971.

[20] Alberto Dominguez, Joel R Primack, DJ Rosario, F Prada, RC Gilmore, SM Faber, DC Koo, RS Somerville, MA Pérez-Torres, P Pérez-González, et al. Extragalactic background light inferred from aegis galaxy-sed-type fractions. *Monthly Notices of the Royal Astronomical Society*, 410(4):2556–2578, 2011.

[21] Joel R Primack, James S Bullock, Rachel S Somerville, and Donn MacMinn. Probing galaxy formation with tev gamma ray absorption. *Astroparticle Physics*, 11(1):93–102, 1999.

[22] Rachel S Somerville, Rudy C Gilmore, Joel R Primack, and Alberto Domínguez. Galaxy properties from the ultraviolet to the far-infrared: λ cold dark matter models confront observations. *Monthly Notices of the Royal Astronomical Society*, 423(3):1992–2015, 2012.

[23] Rudy C Gilmore, Rachel S Somerville, Joel R Primack, and Alberto Domínguez. Semi-analytic modelling of the extragalactic background light and consequences for extragalactic gamma-ray spectra. *Monthly Notices of the Royal Astronomical Society*, 422(4):3189–3207, 2012.

[24] MA Malkan and FW Stecker. An empirically based calculation of the extragalactic infrared background. *The Astrophysical Journal*, 496(1):13, 1998.

[25] Floyd W Stecker, MA Malkan, and STm Scully. Intergalactic photon spectra from the far-ir to the uv lyman limit for $0< z< 6$ and the optical depth of the universe to high-energy gamma rays. *The Astrophysical Journal*, 648(2):774, 2006.

[26] Alberto Franceschini, Giulia Rodighiero, and Mattia Vaccari. Extragalactic optical-infrared background radiation, its time evolution and the cosmic photon-photon opacity. *Astronomy & Astrophysics*, 487(3):837–852, 2008.

[27] Tanja M Kneiske, Karl Mannheim, and Dieter H Hartmann. Implications of cosmological gamma-ray absorption-i. evolution of the metagalactic radiation field. *Astronomy & Astrophysics*, 386(1):1–11, 2002.

[28] Tanja M Kneiske and Herve Dole. A lower-limit flux for the extragalactic background light. *Astronomy & Astrophysics*, 515:A19, 2010.

[29] Justin D. Finke, Soebur Razzaque, and Charles D. Dermer. Modeling the Extragalactic Background Light from Stars and Dust. *Astrophys. J.*, 712:238–249, 2010.

[30] Kari Helgason and Alexander Kashlinsky. Reconstructing the γ-ray photon optical depth of the universe to $z \sim 4$ from multiwavelength galaxy survey data. *The Astrophysical Journal Letters*, 758(1):L13, 2012.

[31] G Neugebauer, HJ Habing, R Van Duinen, HH Aumann, B Baud, CA Beichman, DA Beintema, N Boggess, PE Clegg, T De Jong, et al. The infrared astronomical satellite (iras) mission. *The Astrophysical Journal*, 278:L1–L6, 1984.

[32] MG Hauser, Richard G Arendt, T Kelsall, E Dwek, N Odegard, Janet L Weiland, Henry T Freudenreich, William T Reach, Robert F Silverberg, Samuel Harvey Moseley, et al. The cobe diffuse infrared background experiment search for the cosmic infrared background. i. limits and detections. *The Astrophysical Journal*, 508(1):25, 1998.

[33] Manabu Noda, Toshio Matsumoto, Shuji Matsuura, Kunio Noguchi, Masahiro Tanaka, Mark A Lim, and Hiroshi Murakami. Near-infrared spectrometer on the infrared telescope in space. *The Astrophysical Journal*, 428:363–369, 1994.

[34] Eli Dwek and Frank Krennrich. The extragalactic background light and the gamma-ray opacity of the universe. *Astroparticle Physics*, 43:112–133, 2013.

[35] Jonathan Biteau and David A Williams. The extragalactic background light, the hubble constant, and anomalies: conclusions from 20 years of tev gamma-ray observations. *The Astrophysical Journal*, 812(1):60, 2015.

[36] Michael G Hauser and Eli Dwek. The cosmic infrared background: measurements and implications. *Annual Review of Astronomy and Astrophysics*, 39(1):249–307, 2001.

[37] Paul Schechter. An analytic expression for the luminosity function for galaxies. *The Astrophysical Journal*, 203:297–306, 1976.

[38] Kari Helgason, Massimo Ricotti, and Alexander Kashlinsky. Reconstructing the near-infrared background fluctuations from known galaxy populations using multi-band measurements of luminosity functions. *The Astrophysical Journal*, 752(2):113, 2012.

[39] Ejnar Hertzsprung. Über die verwendung photographischer effektiver wellenlaengen zur bestimmung von farbenäquivalenten. *Publikationen des Astrophysikalischen Observatoriums zu Potsdam*, 63, 1911.

[40] Henry Norris Russell. Relations between the spectra and other characteristics of the stars. *Popular Astronomy*, 22:331–351, 1914.

[41] P. P. Eggleton, M. J. Fitchett, and C. A. Tout. The distribution of visual binaries with two bright components. *Astrophys. J.*, 347:998–1011, December 1989.

[42] G. Bruzual and Stephane Charlot. Stellar population synthesis at the resolution of 2003. *Mon. Not. Roy. Astron. Soc.*, 344:1000, 2003.

[43] F-X Desert, F Boulanger, and JL Puget. Interstellar dust models for extinction and emission. *Astronomy and Astrophysics*, 237:215–236, 1990.

[44] Endrik Krügel. *The Physics of Interstellar Dust*. Institute of Physics, 2003.

[45] Soebur Razzaque, Charles D Dermer, and Justin D Finke. The stellar contribution to the extragalactic background light and absorption of high-energy gamma rays. *The Astrophysical Journal*, 697(1):483, 2009.

[46] Simon P Driver, Cristina C Popescu, Richard J Tuffs, Alister W Graham, Jochen Liske, and Ivan Baldry. The energy output of the universe from 0.1 to 1000 μm. *The Astrophysical Journal Letters*, 678(2):L101, 2008.

[47] Edwin E Salpeter. The luminosity function and stellar evolution. *The Astrophysical Journal*, 121:161, 1955.

[48] Shaun Cole, Peder Norberg, Carlton M Baugh, Carlos S Frenk, Joss Bland-Hawthorn, Terry Bridges, Russell Cannon, Matthew Colless, Chris Collins, Warrick Couch, et al. The 2df galaxy redshift survey: near-infrared galaxy luminosity functions. *Monthly Notices of the Royal Astronomical Society*, 326(1):255–273, 2001.

[49] Andrew M Hopkins and John F Beacom. On the normalization of the cosmic star formation history. *The Astrophysical Journal*, 651(1):142, 2006.

[50] Ivan K Baldry and Karl Glazebrook. Constraints on a universal stellar initial mass function from ultraviolet to near-infrared galaxy luminosity densities. *The Astrophysical Journal*, 593(1):258, 2003.

[51] M Cirasuolo, RJ McLure, JS Dunlop, O Almaini, S Foucaud, and C Simpson. A new measurement of the evolving near-infrared galaxy luminosity function out to z $\simeq$ 4: a continuing challenge to theoretical models of galaxy formation. *Monthly Notices of the Royal Astronomical Society*, 401(2):1166–1176, 2010.

[52] M Polletta, M Tajer, L Maraschi, G Trinchieri, CJ Lonsdale, L Chiappetti, S Andreon, M Pierre, O Le Fevre, G Zamorani, et al. Spectral energy distributions of hard x-ray selected active galactic nuclei in the xmm-newton medium deep survey. *The Astrophysical Journal*, 663(1):81, 2007.

[53] Peter Schneider. *Extragalactic astronomy and cosmology: an introduction*. Springer, 2014.

[54] Volker Beckmann and Chris Shrader. *Active galactic nuclei*. John Wiley & Sons, 2013.

[55] E Massaro, P Giommi, C Leto, P Marchegiani, Alessandro Maselli, M Perri, S Piranomonte, and S Sclavi. Roma-bzcat: a multifrequency catalogue of blazars. *Astronomy & Astrophysics*, 495(2):691–696, 2009.

[56] Aous A Abdo, M Ackermann, M Ajello, L Baldini, J Ballet, G Barbiellini, D Bastieri, K Bechtol, R Bellazzini, B Berenji, et al. Fermi large area telescope observations of markarian 421: The missing piece of its spectral energy distribution. *The Astrophysical Journal*, 736(2):131, 2011.

[57] Justin D Finke, Charles D Dermer, and Markus Böttcher. Synchrotron self-compton analysis of tev x-ray-selected bl lacertae objects. *The Astrophysical Journal*, 686(1):181, 2008.

[58] SP Wakely and D Horan. Tevcat: An online catalog for very high energy gamma-ray astronomy. In *International Cosmic Ray Conference*, volume 3, pages 1341–1344, 2008.

[59] Takuro Narumoto and Tomonori Totani. Gamma-ray luminosity function of blazars and the cosmic gamma-ray background: evidence for the luminosity-dependent density evolution. *The Astrophysical Journal*, 643(1):81, 2006.

[60] Yoshiyuki Inoue and Tomonori Totani. The blazar sequence and the cosmic gamma-ray background radiation in the fermi era. *The Astrophysical Journal*, 702(1):523, 2009.

[61] M Ajello, MS Shaw, RW Romani, CD Dermer, L Costamante, OG King, W Max-Moerbeck, A Readhead, A Reimer, JL Richards, et al. The luminosity function of fermi-detected flat-spectrum radio quasars. *The Astrophysical Journal*, 751(2):108, 2012.

[62] Marco Ajello, RW Romani, D Gasparrini, Michael S Shaw, J Bolmer, G Cotter, J Finke, J Greiner, SE Healey, O King, et al. The cosmic evolution of fermi bl lacertae objects. *The Astrophysical Journal*, 780(1):73, 2013.

[63] David W Hogg. Distance measures in cosmology. *arXiv preprint astro-ph/9905116*, 1999.

[64] Andrea Palladino, Xavier Rodrigues, Shan Gao, and Walter Winter. Interpretation of the diffuse astrophysical neutrino flux in terms of the blazar sequence. *The Astrophysical Journal*, 871(1):41, jan 2019.

[65] Robert J Gould and Gérard P Schréder. Pair production in photon-photon collisions. *Physical Review*, 155(5):1404, 1967.

[66] Daniel Mazin, Martin Raue, Bagmeet Behera, Susumu Inoue, Yoshiyuki Inoue, Takeshi Nakamori, Tomonori Totani, CTA Consortium, et al. Potential of ebl and cosmology studies with the cherenkov telescope array. *Astroparticle physics*, 43:241–251, 2013.

[67] Lars Bergström. Dark matter and imaging air cherenkov arrays. *Astroparticle Physics*, 43:44–49, 2013.

[68] Floyd W Stecker, Matthew A Malkan, and Sean T Scully. A determination of the intergalactic redshift-dependent ultraviolet-optical-nir photon density using deep galaxy survey data and the gamma-ray opacity of the universe. *The Astrophysical Journal*, 761(2):128, 2012.

[69] Rudy C Gilmore, Piero Madau, Joel R Primack, Rachel S Somerville, and Francesco Haardt. Gev gamma-ray attenuation and the high-redshift uv background. *Monthly Notices of the Royal Astronomical Society*, 399(4):1694–1708, 2009.

[70] Floyd W. Stecker, M. A. Malkan, and S. T. Scully. Intergalactic photon spectra from the far ir to the uv lyman limit for $0 < Z < 6$ and the optical depth of the universe to high energy gamma-rays. *Astrophys. J.*, 648:774–783, 2006.

[71] Tanja M Kneiske. Gamma-ray background: a review. *arXiv preprint arXiv:0707.2915*, 2007.

[72] Tonia M Venters. Contribution to the extragalactic gamma-ray background from the cascades of very high energy gamma rays from blazars. *The Astrophysical Journal*, 710(2):1530, 2010.

[73] Subrahmanyan Chandrasekhar. *Radiative transfer*. Courier Corporation, 2013.

[74] George B Rybicki and Alan P Lightman. *Radiative processes in astrophysics*. John Wiley & Sons, 2008.

[75] Joel R Primack, James S Bullock, and Rachel S Somerville. Observational gamma-ray cosmology. In *AIP Conference Proceedings*, volume 745, pages 23–33. AIP, 2005.

[76] Tanja M Kneiske, T Bretz, K Mannheim, and DH Hartmann. Implications of cosmological gamma-ray absorption-ii. modification of gamma-ray spectra. *Astronomy & Astrophysics*, 413(3):807–815, 2004.

[77] D.R. de Matos Pimentel and E. Moura-Santos. Infrared emission from dust and the spectral features of extragalactic gamma-ray sources. *Journal of Cosmology and Astroparticle Physics*, 2019(04):043–043, apr 2019.

[78] F. Aharonian. The time averaged TeV energy spectrum of mkn 501 of the extraordinary 1997 outburst as measured with the stereoscopic Cherenkov telescope system of hegra. *Astron. Astrophys.*, 349:11–28, 1999.

[79] Simon P. Driver, Cristina C. Popescu, Richard J. Tuffs, Alister W. Graham, Jochen Liske, and Ivan Baldry. The energy output of the Universe from 0.1 micron to 1000 micron. *Astrophys. J.*, 678:L101, 2008.

[80] S. S. Wilks. The large-sample distribution of the likelihood ratio for testing composite hypotheses. *Ann. Math. Statist.*, 9(1):60–62, 03 1938.

[81] Sean T. Scully, Matthew A. Malkan, and Floyd W. Stecker. An Empirical Determination of the Intergalactic Background Light Using Near-infrared Deep Galaxy Survey Data out to $5\mu m$ and the Gamma-Ray Opacity of the Universe. *Astrophys. J.*, 784:138, 2014.

[82] Floyd W. Stecker, Sean T. Scully, and Matthew A. Malkan. An Empirical Determination of the Intergalactic Background Light from UV to FIR Wavelengths Using FIR Deep Galaxy Surveys and the Gamma-ray Opacity of the Universe. *Astrophys. J.*, 827(1):6, 2016. [Erratum: Astrophys. J.863,no.1,112(2018)].

[83] S. P. Wakely and D. Horan. TeVCat: An online catalog for Very High Energy Gamma-Ray Astronomy. *International Cosmic Ray Conference*, 3:1341–1344, 2008.

[84] F Aharonian, AG Akhperjanian, U Barres De Almeida, AR Bazer-Bachi, B Behera, M Beilicke, W Benbow, K Bernlöhr, C Boisson, O Bolz, et al. New constraints on the mid-ir ebl from the hess discovery of vhe γ-rays from 1es 0229+ 200. *Astronomy & Astrophysics*, 475(2):L9–L13, 2007.

[85] E Aliu, S Archambault, T Arlen, T Aune, B Behera, M Beilicke, W Benbow, K Berger, R Bird, A Bouvier, et al. A three-year multi-wavelength study of the very-high-energy γ-ray blazar 1es 0229+ 200. *The Astrophysical Journal*, 782(1):13, 2014.

[86] F Aharonian, AG Akhperjanian, U Barres De Almeida, AR Bazer-Bachi, B Behera, M Beilicke, W Benbow, K Bernlöhr, C Boisson, O Bolz, et al. Discovery of vhe γ-rays from the distant bl lacertae 1es 0347-121. *Astronomy & Astrophysics*, 473(3):L25–L28, 2007.

[87] A Abramowski, Fabio Acero, F Aharonian, AG Akhperjanian, G Anton, A Balzer, A Barnacka, U Barres De Almeida, Yvonne Becherini, J Becker, et al. Discovery of hard-spectrum γ-ray emission from the bl lacertae object 1es 0414+ 009. *Astronomy & Astrophysics*, 538:A103, 2012.

[88] E Aliu, S Archambault, T Arlen, T Aune, M Beilicke, W Benbow, M Böttcher, A Bouvier, V Bugaev, A Cannon, et al. Multiwavelength observations of the agn 1es 0414+ 009 with veritas, fermi-lat, swift-xrt, and mdm. *The Astrophysical Journal*, 755(2):118, 2012.

[89] Jelena Aleksić, S Ansoldi, LA Antonelli, P Antoranz, A Babic, P Bangale, JA Barrio, J Becerra González, W Bednarek, E Bernardini, et al. Magic detection of

short-term variability of the high-peaked bl lac object 1es 0806+ 524. *Monthly Notices of the Royal Astronomical Society*, 451(1):739–750, 2015.

[90] V Acciari, E Aliu, T Arlen, M Bautista, M Beilicke, W Benbow, M Böttcher, SM Bradbury, JH Buckley, V Bugaev, et al. Discovery of very high energy gamma-ray radiation from the bl lac 1es 0806+ 524. *The Astrophysical Journal Letters*, 690(2):L126, 2008.

[91] J Albert, E Aliu, H Anderhub, P Antoranz, A Armada, C Baixeras, JA Barrio, H Bartko, D Bastieri, JK Becker, et al. Discovery of very high energy γ-rays from 1es 1011+ 496 at z= 0.212. *The Astrophysical Journal Letters*, 667(1):L21, 2007.

[92] F Aharonian, AG Akhperjanian, AR Bazer-Bachi, M Beilicke, W Benbow, D Berge, K Bernlöhr, C Boisson, O Bolz, V Borrel, et al. A low level of extragalactic background light as revealed by γ-rays from blazars. *Nature*, 440(7087):1018, 2006.

[93] E Aliu, S Archambault, T Arlen, T Aune, M Beilicke, W Benbow, R Bird, A Bouvier, JH Buckley, V Bugaev, et al. Long term observations of b2 1215+ 30 with veritas. *The Astrophysical Journal*, 779(2):92, 2013.

[94] VA Acciari, E Aliu, M Beilicke, W Benbow, D Boltuch, M Böttcher, SM Bradbury, V Bugaev, K Byrum, A Cesarini, et al. Discovery of variability in the very high energy γ-ray emission of 1es 1218+ 304 with veritas. *The Astrophysical Journal Letters*, 709(2):L163, 2010.

[95] VA Acciari, E Aliu, T Arlen, M Beilicke, W Benbow, SM Bradbury, JH Buckley, V Bugaev, Y Butt, KL Byrum, et al. Veritas observations of the bl lac object 1es 1218+ 304. *The Astrophysical Journal*, 695(2):1370, 2009.

[96] J Albert, E Aliu, H Anderhub, P Antoranz, A Armada, M Asensio, C Baixeras, JA Barrio, M Bartelt, H Bartko, et al. Discovery of vhe gamma-ray emission from 1es1218+ 30.4. *arXiv preprint astro-ph/0603529*, 2006.

[97] HESS Collaboration, A Abramowski, F Acero, Felix Aharonian, AG Akhperjanian, E Angüner, G Anton, S Balenderan, A Balzer, A Barnacka, et al. Hess and fermi-lat discovery of γ-rays from the blazar 1es 1312- 423. *Monthly Notices of the Royal Astronomical Society*, 434(3):1889–1901, 2013.

[98] S Archambault, A Archer, M Beilicke, W Benbow, R Bird, J Biteau, A Bouvier, V Bugaev, JV Cardenzana, M Cerruti, et al. Veritas detection of γ-ray flaring activity from the bl lac object 1es 1727+ 502 during bright moonlight observations. *The Astrophysical Journal*, 808(2):110, 2015.

[99] AU Abeysekara, S Archambault, A Archer, W Benbow, R Bird, J Biteau, M Buchovecky, JH Buckley, V Bugaev, K Byrum, et al. Veritas and multiwavelength observations of the bl lacertae object 1es 1741+ 196. *Monthly Notices of the Royal Astronomical Society*, 459(3):2550–2557, 2016.

[100] E Aliu, S Archambault, T Arlen, T Aune, M Beilicke, W Benbow, R Bird, M Böttcher, A Bouvier, V Bugaev, et al. Multiwavelength observations and modeling of 1es 1959+ 650 in a low flux state. *The Astrophysical Journal*, 775(1):3, 2013.

[101] G Tagliaferri, L Foschini, G Ghisellini, L Maraschi, G Tosti, J Albert, E Aliu, H Anderhub, P Antoranz, C Baixeras, et al. Simultaneous multiwavelength observations of the blazar 1es 1959+ 650 at a low tev flux. *The Astrophysical Journal*, 679(2):1029, 2008.

[102] VA Acciari, E Aliu, T Arlen, T Aune, M Beilicke, W Benbow, D Boltuch, V Bugaev, A Cannon, L Ciupik, et al. Multiwavelength observations of the very high energy blazar 1es 2344+ 514. *The Astrophysical Journal*, 738(2):169, 2011.

[103] Jelena Aleksić, Lucio Angelo Antonelli, Pedro Antoranz, M Asensio, Michael Backes, U Barres De Almeida, Juan Abel Barrio, Włodek Bednarek, Karsten Berger, Elisa Bernardini, et al. The simultaneous low state spectral energy distribution of 1es 2344+ 514 from radio to very high energies. *Astronomy & Astrophysics*, 556:A67, 2013.

[104] J Albert, E Aliu, H Anderhub, P Antoranz, A Armada, C Baixeras, JA Barrio, H Bartko, D Bastieri, JK Becker, et al. Observation of very high energy γ-rays from the agn 1es 2344+ 514 in a low emission state with the magic telescope. *The Astrophysical Journal*, 662(2):892, 2007.

[105] A Abramowski, Fabio Acero, F Aharonian, AG Akhperjanian, G Anton, A Balzer, A Barnacka, Yvonne Becherini, J Becker, K Bernlöhr, et al. Discovery of vhe γ-ray emission and multi-wavelength observations of the bl lacertae object 1rxs j101015. 9- 311909. *Astronomy & Astrophysics*, 542:A94, 2012.

[106] AA Abdo, Markus Ackermann, Marco Ajello, Luca Baldini, J Ballet, Guido Barbiellini, D Bastieri, K Bechtol, R Bellazzini, B Berenji, et al. Multi-wavelength observations of the flaring gamma-ray blazar 3c 66a in 2008 october. *The Astrophysical Journal*, 726(1):43, 2010.

[107] Jelena Aleksić, LA Antonelli, P Antoranz, M Backes, JA Barrio, D Bastieri, J Becerra González, W Bednarek, A Berdyugin, K Berger, et al. Magic discovery of

very high energy emission from the fsrq pks 1222+ 21. *The Astrophysical Journal Letters*, 730(1):L8, 2011.

[108] A Abramowski, F Aharonian, F Ait Benkhali, AG Akhperjanian, E Angüner, G Anton, M Backes, S Balenderan, A Balzer, Anna Barnacka, et al. The high-energy γ-ray emission of ap librae. *Astronomy & Astrophysics*, 573:A31, 2015.

[109] T Arlen, T Aune, M Beilicke, W Benbow, A Bouvier, JH Buckley, V Bugaev, A Cesarini, L Ciupik, MP Connolly, et al. Rapid tev gamma-ray flaring of bl lacertae. *The Astrophysical Journal*, 762(2):92, 2012.

[110] F Aharonian, AG Akhperjanian, G Anton, U Barres De Almeida, AR Bazer-Bachi, Yvonne Becherini, B Behera, W Benbow, K Bernlöhr, C Boisson, et al. Discovery of very high energy γ-ray emission from centaurus a with hess. *The Astrophysical Journal Letters*, 695(1):L40, 2009.

[111] F Aharonian, A Akhperjanian, M Beilicke, K Bernlöhr, H-G Börst, H Bojahr, O Bolz, T Coarasa, JL Contreras, J Cortina, et al. Observations of h1426+ 428 with hegra-observations in 2002 and reanalysis of 1999&2000 data. *Astronomy & Astrophysics*, 403(2):523–528, 2003.

[112] A Abramowski, Fabio Acero, F Aharonian, AG Akhperjanian, G Anton, U Barres De Almeida, AR Bazer-Bachi, Yvonne Becherini, B Behera, W Benbow, et al. Multi-wavelength observations of h 2356–309. *Astronomy & Astrophysics*, 516:A56, 2010.

[113] Jelena Aleksić, S Ansoldi, LA Antonelli, P Antoranz, A Babic, P Bangale, JA Barrio, J Becerra González, W Bednarek, E Bernardini, et al. Black hole lightning due to particle acceleration at subhorizon scales. *Science*, 346(6213):1080–1084, 2014.

[114] Jelena Aleksić, LA Antonelli, P Antoranz, A Babic, U Barres de Almeida, JA Barrio, J Becerra González, W Bednarek, K Berger, E Bernardini, et al. Rapid and multiband variability of the tev bright active nucleus of the galaxy ic 310. *Astronomy & Astrophysics*, 563:A91, 2014.

[115] Felix Aharonian, AG Akhperjanian, AR Bazer-Bachi, M Beilicke, Wystan Benbow, David Berge, K Bernlöhr, C Boisson, Oliver Bolz, V Borrel, et al. Fast variability of tera–electron volt γ rays from the radio galaxy m87. *Science*, 314(5804):1424–1427, 2006.

[116] Jelena Aleksić, EA Alvarez, LA Antonelli, P Antoranz, M Asensio, M Backes, JA Barrio, D Bastieri, J Becerra González, W Bednarek, et al. Magic observations of the giant radio galaxy m 87 in a low-emission state between 2005 and 2007. *Astronomy & Astrophysics*, 544:A96, 2012.

[117] J Albert, E Aliu, H Anderhub, LA Antonelli, P Antoranz, M Backes, C Baixeras, JA Barrio, H Bartko, D Bastieri, et al. Very high energy gamma-ray observations of strong flaring activity in m87 in 2008 february. *The Astrophysical Journal Letters*, 685(1):L23, 2008.

[118] VA Acciari, M Beilicke, G Blaylock, SM Bradbury, JH Buckley, V Bugaev, Y Butt, O Celik, A Cesarini, L Ciupik, et al. Observation of gamma-ray emission from the galaxy m87 above 250 gev with veritas. *The Astrophysical Journal*, 679(1):397, 2008.

[119] J Albert, E Aliu, H Anderhub, P Antoranz, A Armada, M Asensio, C Baixeras, JA Barrio, H Bartko, D Bastieri, et al. Discovery of very high energy γ-rays from markarian 180 triggered by an optical outburst. *The Astrophysical Journal Letters*, 648(2):L105, 2006.

[120] J Albert, E Aliu, H Anderhub, P Antoranz, A Armada, M Asensio, C Baixeras, JA Barrio, H Bartko, D Bastieri, et al. Observations of markarian 421 with the magic telescope. *The Astrophysical Journal*, 663(1):125, 2007.

[121] VA Acciari, E Aliu, T Aune, M Beilicke, W Benbow, M Böttcher, SM Bradbury, JH Buckley, V Bugaev, Y Butt, et al. Simultaneous multiwavelength observations of markarian 421 during outburst. *The Astrophysical Journal*, 703(1):169, 2009.

[122] VA Acciari, E Aliu, T Arlen, T Aune, M Beilicke, W Benbow, D Boltuch, SM Bradbury, JH Buckley, V Bugaev, et al. Tev and multi-wavelength observations of mrk 421 in 2006-2008. *The Astrophysical Journal*, 738(1):25, 2011.

[123] FA Aharonian, AG Akhperjanian, JA Barrio, K Bernlöhr, O Bolz, H Börst, H Bojahr, JL Contreras, J Cortina, S Denninghoff, et al. Reanalysis of the high energy cutoff of the 1997 mkn 501 tev energy spectrum. *Astronomy & Astrophysics*, 366(1):62–67, 2001.

[124] VA Acciari, T Arlen, T Aune, M Beilicke, W Benbow, M Böttcher, D Boltuch, SM Bradbury, JH Buckley, V Bugaev, et al. Spectral energy distribution of markarian 501: Quiescent state versus extreme outburst. *The Astrophysical Journal*, 729(1):2, 2011.

[125] Max L Ahnen, S Ansoldi, LA Antonelli, P Antoranz, A Babic, B Banerjee, P Bangale, U Barres De Almeida, JA Barrio, J Becerra González, et al. Deep observation of the ngc 1275 region with magic: search of diffuse γ-ray emission from cosmic rays in the perseus cluster. *Astronomy & Astrophysics*, 589:A33, 2016.

[126] E Aliu, A Archer, T Aune, A Barnacka, B Behera, M Beilicke, W Benbow, K Berger, R Bird, JH Buckley, et al. Veritas observations of the bl lac object pg 1553+ 113. *The Astrophysical Journal*, 799(1):7, 2015.

[127] Jelena Aleksić, H Anderhub, LA Antonelli, P Antoranz, M Backes, C Baixeras, S Balestra, JA Barrio, D Bastieri, J Becerra González, et al. Simultaneous multi-frequency observation of the unknown redshift blazar pg 1553+ 113 in march-april 2008. *Astronomy & Astrophysics*, 515:A76, 2010.

[128] J Albert, E Aliu, H Anderhub, P Antoranz, C Baixeras, JA Barrio, H Bartko, D Bastieri, JK Becker, W Bednarek, et al. Magic observations of pg 1553+ 113 during a multiwavelength campaign in july 2006. *Astronomy & Astrophysics*, 493(2):467–469, 2009.

[129] H Abdalla, A Abramowski, F Aharonian, F Ait Benkhali, AG Akhperjanian, T Andersson, EO Angüner, M Arrieta, P Aubert, M Backes, et al. Gamma-ray blazar spectra with hess ii mono analysis: The case of pks 2155- 304 and pg 1553+ 113. *Astronomy & Astrophysics*, 600:A89, 2017.

[130] A Abramowski, F Aharonian, F Ait Benkhali, AG Akhperjanian, EO Angüner, M Backes, S Balenderan, A Balzer, Anna Barnacka, Yvonne Becherini, et al. The 2012 flare of pg 1553+ 113 seen with hess and fermi-lat. *The Astrophysical Journal*, 802(1):65, 2015.

[131] A Abramowski, Fabio Acero, F Aharonian, F Ait Benkhali, AG Akhperjanian, E Angüner, G Anton, S Balenderan, A Balzer, Anna Barnacka, et al. Discovery of very high energy γ-ray emission from the bl lacertae object pks 0301- 243 with hess. *Astronomy & Astrophysics*, 559:A136, 2013.

[132] A Abramowski, Fabio Acero, AG Akhperjanian, G Anton, S Balenderan, A Balzer, Anna Barnacka, Yvonne Becherini, J Becker Tjus, B Behera, et al. Discovery of tev γ-ray emission from pks 0447-439 and derivation of an upper limit on its redshift. *Astronomy & Astrophysics*, 552:A118, 2013.

[133] Max Ludwig Ahnen, S Ansoldi, LA Antonelli, P Antoranz, A Babic, B Banerjee, P Bangale, U Barres De Almeida, JA Barrio, W Bednarek, et al. Very high energy γ-rays from the universe's middle age: Detection of the z= 0.940 blazar pks 1441+ 25 with magic. *The Astrophysical Journal Letters*, 815(2):L23, 2015.

[134] A Abramowski, Fabio Acero, F Aharonian, AG Akhperjanian, G Anton, S Balenderan, A Balzer, Anna Barnacka, Yvonne Becherini, J Becker Tjus, et al. Hess discovery of vhe γ-rays from the quasar pks 1510- 089. *Astronomy & Astrophysics*, 554:A107, 2013.

[135] Max L Ahnen, S Ansoldi, LA Antonelli, C Arcaro, Ana Babić, B Banerjee, P Bangale, U Barres De Almeida, JA Barrio, W Bednarek, et al. Multiwavelength observations of a vhe gamma-ray flare from pks 1510- 089 in 2015. *Astronomy & Astrophysics*, 603:A29, 2017.

[136] Fabio Acero, F Aharonian, AG Akhperjanian, G Anton, U Barres De Almeida, AR Bazer-Bachi, Yvonne Becherini, B Behera, W Benbow, K Bernlöhr, et al. Pks 2005-489 at vhe: four years of monitoring with hess and simultaneous multiwavelength observations. *Astronomy & Astrophysics*, 511:A52, 2010.

[137] A Abramowski, Fabio Acero, F Aharonian, F Ait Benkhali, AG Akhperjanian, E Angüner, G Anton, S Balenderan, A Balzer, Anna Barnacka, et al. Constraints on axionlike particles with hess from the irregularity of the pks 2155- 304 energy spectrum. *Physical Review D*, 88(10):102003, 2013.

[138] Attila Abramowski, Fabio Acero, F Aharonian, AG Akhperjanian, G Anton, U Barres De Almeida, AR Bazer-Bachi, Yvonne Becherini, B Behera, W Benbow, et al. Vhe γ-ray emission of pks 2155–304: spectral and temporal variability. *Astronomy & Astrophysics*, 520:A83, 2010.

[139] Jelena Aleksić, EA Alvarez, LA Antonelli, P Antoranz, M Asensio, M Backes, U Barres de Almeida, JA Barrio, D Bastieri, J Becerra González, et al. High zenith angle observations of pks 2155-304 with the magic-i telescope. *Astronomy & Astrophysics*, 544:A75, 2012.

[140] E Aliu, S Archambault, T Arlen, T Aune, M Beilicke, W Benbow, M Böttcher, A Bouvier, SM Bradbury, JH Buckley, et al. Discovery of high-energy and very high energy γ-ray emission from the blazar rbs 0413. *The Astrophysical Journal*, 750(2):94, 2012.

[141] F Aharonian, AG Akhperjanian, U Barres de Almeida, AR Bazer-Bachi, B Behera, M Beilicke, W Benbow, K Bernlöhr, C Boisson, V Borrel, et al. Discovery of vhe γ-rays from the high-frequency-peaked bl lacertae object rgb j0152+ 017. *Astronomy & Astrophysics*, 481(3):L103–L107, 2008.

[142] VA Acciari, E Aliu, T Arlen, T Aune, M Bautista, M Beilicke, W Benbow, M Böttcher, D Boltuch, SM Bradbury, et al. The discovery of γ-ray emission from the blazar rgb j0710+ 591. *The Astrophysical Journal Letters*, 715(1):L49, 2010.

[143] E Aliu, T Aune, M Beilicke, W Benbow, M Böttcher, A Bouvier, SM Bradbury, JH Buckley, V Bugaev, A Cannon, et al. Multiwavelength observations of the previously unidentified blazar rx j0648. 7+ 1516. *The Astrophysical Journal*, 742(2):127, 2011.

[144] Max Ludwig Ahnen, S Ansoldi, LA Antonelli, P Antoranz, C Arcaro, A Babic, B Banerjee, P Bangale, U Barres de Almeida, JA Barrio, et al. Detection of very high energy gamma-ray emission from the gravitationally lensed blazar qso b0218+ 357 with the magic telescopes. *Astronomy & Astrophysics*, 595:A98, 2016.

[145] S Archambault, T Arlen, T Aune, B Behera, M Beilicke, W Benbow, R Bird, A Bouvier, JH Buckley, V Bugaev, et al. Discovery of a new tev gamma-ray source: Ver j0521+ 211. *The Astrophysical Journal*, 776(2):69, 2013.

[146] A Michael Hillas. Cerenkov light images of eas produced by primary gamma. 1985.

[147] K Bernlöhr, A Barnacka, Yvonne Becherini, O Blanch Bigas, E Carmona, P Colin, G Decerprit, F Di Pierro, F Dubois, Christian Farnier, et al. Monte carlo design studies for the cherenkov telescope array. *Astroparticle Physics*, 43:171–188, 2013.

[148] Jea Knödlseder, M Mayer, C Deil, J-B Cayrou, E Owen, N Kelley-Hoskins, C-C Lu, R Buehler, F Forest, T Louge, et al. Gammalib and ctools-a software framework for the analysis of astronomical gamma-ray data. *Astronomy & Astrophysics*, 593:A1, 2016.

[149] AA Abdo, Markus Ackermann, Marco Ajello, E Antolini, Luca Baldini, Jean Ballet, Guido Barbiellini, D Bastieri, BM Baughman, K Bechtol, et al. The fermi-lat high-latitude survey: source count distributions and the origin of the extragalactic diffuse background. *The Astrophysical Journal*, 720(1):435, 2010.

[150] Fred James. Minuit function minimization and error analysis: reference manual version 94.1. Technical report, 1994.

[151] M Ackermann, M Ajello, WB Atwood, Luca Baldini, J Ballet, G Barbiellini, D Bastieri, J Becerra Gonzalez, R Bellazzini, E Bissaldi, et al. The third catalog of active galactic nuclei detected by the fermi large area telescope. *The Astrophysical Journal*, 810(1):14, 2015.

[152] Eric Gawiser and Joseph Silk. The cosmic microwave background radiation. *Physics Reports*, 333:245–267, 2000.

[153] Milton Abramowitz and Irene A Stegun. Handbook of mathematical functions with formulas, graphs, and mathematical table. In *US Department of Commerce*. National Bureau of Standards Applied Mathematics series 55, 1965.